KINETIC, SPECTROSCOPIC, AND MUTAGENESIS STUDIES OF HOMOPROTOCATECHUATE 2,3-DIOXYGENASE

A DISSERTATION
SUBMITTED TO THE FACULTY OF THE GRADUATE SCHOOL
OF THE UNIVERSITY OF MINNESOTA
BY

MICHAEL MKONDO MBUGHUNI

IN PARTIAL FULFILLMENT OF THE REQUIREMENTS
FOR THE DEGREE OF
DOCTOR OF PHILOSOPHY

ADVISOR: JOHN D. LIPSCOMB

JUNE 2012

Acknowledgments

I would like to thank my advisor, Prof. John D. Lipscomb, for his guidance and support throughout my graduate career. His undying pursuit of biochemical excellence and endless wisdom as an advisor were instrumental to my success and growth as a biochemist. Also, none of the work presented in this thesis would have been possible without contributions from his collaborators, Prof. Eckard Münck and Prof. Michael P. Hendrich, who provided quantitative Mössbauer and EPR expertise.

There are several other scientists with significant contributions to the work presented in this thesis. Dr. Mrinmoy Chakrabarti who worked with Prof. Eckard Münck in analyzing the Mössbauer samples presented in Chapters 1-2. Likewise, Katlyn Meier who analyzed the Mössbauer data presented in Chapters 2-3 and Dr. Emile Bominaar, who oversaw the computational study of Int-1 as presented in Chapter 1. Many thanks to Dr. Joshua Hayden who enthusiastically accepted rapid freeze-quenched EPR samples and worked with Prof. Michael Hendrich to provide simulations and temperature dependent measurements of parallel mode EPR spectra in Chapters 1-2.

Thank you to past and present members of the Lipscomb lab, Prof. Lawrence Que, Prof. Carrie Wilmot, and members of the Que lab whom I have worked with. There was never a shortage of insightful discussions or technical help. Special thanks to Dr. Thomas Makris, his improvements on our rapid freeze quench device made some of this work possible.

I would also like to thank my entire family in Tanzania and here in the states, they are my inspiration. Additionally, graduate school would not have been fun if it were not for a remarkable group of friends who made the Twin-Cities feel like a second home. Caroline, thank you for your support. Your beautiful spirit and undying love are now a permanent part of me. Most importantly, I would like to thank my parents for creating many opportunities for us and for never failing to open my eyes.

To my parents

Abstract

Homoprotocatechuate 2,3-Dioxygenase (2,3-HPCD) from *Brevibacterium fuscum* catalyzes the O_2-dependent extradiol ring-opening reaction of its catecholic substrate homoprotocatechuate (HPCA) to yield a α-hydroxy-δ-carboxymethyl *cis*-muconic semialdehyde. In this process, both O_2 and HPCA are first coordinated to a mononuclear Fe(II) in the active site. The Fe(II) cofactor is postulated to act as an electronic conduit for facile electron transfer between the bound substrates, working in concert with second sphere amino acids to guide the formation of a reactive $\cdot$HPCA-Fe(II)-$O_2^{\cdot -}$ intermediate. The work presented in this thesis focuses on developing tools for solution trapping of reaction intermediates from 2,3-HPCD for spectroscopic studies, in particular mutagenesis of key active site residues and use of a novel rapid-freeze-quench apparatus (RFQ). 2,3-HPCD is found to catalyze the oxygen activation and radical recombination reactions on the sub-millisecond time scale at 4 °C, forming the Fe(II)-alkylperoxo (or lactone) intermediate in the dead time of the RFQ apparatus. The reaction was slowed to reveal intermediates in this important phase of the catalytic cycle by mutating the postulated second sphere acid/base catalyst His200 to Asn200 (H200N). This results in formation of a $\cdot$HPCA-Fe(III)-(H)peroxo intermediate that decays slowly through an Fe(II) intermediate to form ring-cleaved product. When H200N reacts with the electron deficient 4-nitrocatechol (4NC) substrate, a 4NC-Fe(III)-$O_2^{\cdot -}$ intermediate is formed. Both this species and the Fe(II)-alkylperoxo species described above represent the first time such species have been trapped from the solution reaction of a mononuclear non-heme iron enzyme. The 4NC-Fe(III)-$O_2^{\cdot -}$ intermediate decays to form an $\cdot$4NC-Fe(III)-(Hydro)peroxo species and then releases 4NC quinone without ring cleavage. These studies demonstrate facile electron transfer between substrates and reveal important roles for His200 in promoting efficient O_2 binding and rapid reaction between the O_2 and organic

substrate. Mutation of Tyr257 to Phe257 (Y257F) results in an enzyme that forms a HPCA-Fe(II)-O_2 intermediate. This initial oxygenated complex decays to form a Quinone-Fe(II)-(Hydro)peroxo intermediate which slowly forms ring-cleaved product. Tyr257 hydrogen bonds to the HPCA C3-O^- coordinated to the iron. This may stabilize both the substrate semiquinone state and the Fe(II)-alkylperoxo state because the HPCA C3-O^- would move closer to Tyr257 in both intermediates. Consequently, in the absence of Y257, both electron transfer and radical recombination are slowed, leading to the accumulation of the observed intermediates. The six new types of trapped reaction intermediates described in this thesis reveal the range of catalytic strategies used by 2,3-HPCD. However, the very rapid reactions of the native enzyme using its natural substrate suggest that the enzyme has evolved to prevent accumulation of any of these intermediates, thereby ensuring high flux and specificity.

Table of Contents

LIST OF TABLES ..... **VIII**

LIST OF FIGURES ..... **IX**

LIST OF SCHEMES ..... **XI**

INTRODUCTION **1**

THE CARBON CYCLE AND AEROBIC LIFE 3
HOMOPROTOCATECHUATE 2,3-DIOXYGENASE 6
O_2 ACTIVATION BY MONONUCLEAR NON-HEME FE OXYGENASES, PERSPECTIVE AND OVERVIEW 10
MONONUCLEAR NON-HEME IRON OXYGENASE FAMILIES 137
Aromatic ring-cleaving dioxygenases. *13*
Rieske mono- and dioxygenases. *19*
2-Oxo acid-dependent mononuclear non-heme Fe(II) dioxygenases. *22*
Tetrahydropterin-dependent mononuclear non-heme Fe(II) oxygenases. *26*
Related enzymes. *28*
Research directions. *29*
Research directions for 2,3-HPCD. *30*

CHAPTER 1 ..... **34**

TRAPPING AND SPECTROSCOPIC CHARACTERIZATION OF AN FE(III)-SUPEROXO INTERMEDIATE FROM A NON-HEME MONONUCLEAR IRON-CONTAINING ENZYME.

SUMMARY 35
INTRODUCTION 36
MATERIALS AND METHODS 40
Reagents. *40*
Over expression of the H200 variant, purification and ^{57}Fe incorporation. *40*
Preparation of fully reduced 2,3-HPCD. *40*
Rapid freeze quench (RFQ) methods. *41*
Enzyme and metal quantification. *42*
Spectroscopy. *42*
DFT calculation. *42*
RESULTS 44
Absorption spectra show that an intermediate precedes substrate oxidation. *44*
$H200N_{Int1}^{4NC}$ and $H200N_{Int2}^{4NC}$ exhibit EPR signals from S_1 = 5/2 Fe(III) that is antiferromagnetically coupled to S_2 = 1/2 species. *44*
Mössbauer spectroscopy shows that the iron of $H200N_{Int1}^{4NC}$ is an S_1 = 5/2 Fe(III) AF coupled to an S_2 = 1/2 species. *52*
^{17}O-Hyperfine coupling shows that an oxygen radical is present in $H200N_{Int1}^{4NC}$. *53*
$H200N_{Int2}^{4NC}$ may contain a bound peroxo and a product radical. *54*
$H200N_{Int1}^{4NC}$ structure from DFT calculations. *58*
DISCUSSION 64
Electronic Structure of $H200N_{Int1}^{4NC}$. *64*
Comparison of $H200N_{Int1}^{4NC}$ with Fe(III)-$O_2^{\bullet-}$ species from heme-containing enzymes. *66*
Significance for nonheme mononuclear iron-containing enzymes. *67*
Electronic structure of $H200N_{Int2}^{4NC}$ *67*
Implications for the mechanism of extradiol dioxygenases. *68*
CONCLUSION 69

Chapter 1 contributions. *69*

CHAPTER 2 ..... **71**

OXY-INTERMEDIATES OF HOMOPROTOCATECHUATE 2,3-DIOXYGENASE: FACILE ELECTRON TRANSFER BETWEEN SUBSTRATES.

SUMMARY 72
INTRODUCTION 73
EXPERIMENTAL PROCEDURES 76
Reagents and enzymes. *76*
Stopped-flow and spectroscopy. *76*
RFQ methods. *76*
Synthesis of HPCA enriched with ^{17}O at the C3 hydroxyl functional group. *77*
Liquid chromatography electrospray ionization-tandem mass spectrometry of ^{17}OH-C3-HPCA. *78*
Preparation of HPCA quinone. *79*
RESULTS 81
Single-turnover studies of the H200N-HPCA + O_2 reaction reveal a transient intermediate. *81*
RFQ EPR and Mössbauer studies show that H200N$_{Int1}^{HPCA}$ has an S_1=5/2 Fe(III) site coupled to an S_R =½ radical. *84*
^{17}O-Hyperfine coupling suggests that H200N$_{Int1}^{HPCA}$ contains an Fe-peroxo and a substrate radical moiety. *95*
Stopped-flow spectroscopy of the FeHPCA + O_2 reaction reveals no evidence for an intermediate similar to H200N$_{Int1}^{HPCA}$. *98*
RFQ samples from the FeHPCD + O_2 reaction reveal an Fe(II) reaction intermediate. *98*
DISCUSSION 103
Identity of H200N$_{Int1}^{HPCA}$. *103*
Identity of H200N$_{Int2}^{HPCA}$. *109*
Identity of FeHPCD$_{Int1}^{HPCA}$. *110*
Mechanistic implications of the observed intermediates. *111*
CONCLUSION 114
Chapter 2 contributions. *115*

CHAPTER 3 ..... **116**

DETECTION OF NOVEL RING-CLEAVING OXYGENATED INTERMEDIATES FROM A TYROSINE 257 MUTANT OF 2,3-HPCD.

SUMMARY 117
INTRODUCTION 118
MATERIALS AND METHODS 120
Y257F mutant. *120*
Iron quantification using ICP-OES. *121*
Steady-state kinetic experiments. *121*
Estimation of K_d for HPCA binding to Y257F and WT enzymes. *122*
Transient kinetic experiments. *122*
Rapid freeze quench (RFQ) methods. *123*
Preparation of HPCA semiquinone and HPCA quinone. *123*
RESULTS. 125
The Y257F mutation causes a significant decrease in the rate of HPCA turnover. *125*
Substrate binds tightly to Y257F. *125*
Single-turnover studies of the Y257F-HPCA+O_2 reaction reveals 2 intermediates *129*
Photochemical conversion of the enzyme-product complex. *131*
Rate constants for the formation and decay of the intermediates. *131*
Mössbauer reveals Y257F$_{Int1}^{HPCA}$ and Y257F$_{Int2}^{HPCA}$ both contain Fe(II). *139*

Rate-limiting step. *141*
DISCUSSION 143
Kinetic model for catalysis. *143*
Chemical nature of $Y257F_{Int1}^{HPCA}$. *147*
Chemical nature of $Y257F_{Int2}^{HPCA}$. *148*
energy band, and the presences of the intense feature near 425 nm suggest that $Y257F_{Int2}^{HPCA}$ is most likely a HPCA Q-Fe(II)-(H)peroxo complex. *150*
Basis for slow substrate binding in the rate limiting step while retaining high affinity. *150*
Origin of rate constant decreases in reaction cycle steps – mechanistic significance. *151*
Basis for pH effects on O_2 binding. *152*
CONCLUSION 154
Chapter 3 contributions. *155*
PERSPECTIVE 156
REFERENCES 164

List of Tables

Table 1: Electronic and nuclear parameters of $H200N_{Int1}^{4NC}$ and $H200N_{Int1}^{4NC}$ obtained from EPR (italics) and Mössbauer spectroscopy. 49
Table 2: Hyperfine parameters and exchange coupling constants for $H200N_{Int1}^{4NC}$. 60
Table 3: Mulliken spin populations. 62
Table 4: Mass spec Analysis of ^{17}O-C3-HPCA. 80
Table 5: Spin-Hamiltonian parameters for exchange coupled intermediates from EPR (italics) and Mössbauer spectroscopy. 90
Table 6: Comparison of quadrupole splitting and isomer shift parameters for the Mössbauer spectra of FeHPCD and its variants and complexes. 102
Table 7: Electronic parameters for quinone, semiquinone and peroxo model complexes. 106
Table 8: Steady state parameters for 2,3-HPCD-HPCA and Y257F-HPCA reaction with O_2 126
Table 9: Reciprocal relaxation times and amplitudes obtained from fitting single wavelength data from the Y257F-HPCA + O_2 reaction 135
Table 10: Intermediates formed by 2,3-HPCD and its variants with HPCA and alternative substrates. 159

List of Figures

Figure 1: Simplified representations of lignin and cellulose structures. 5
Figure 2: 3,4-dihydroxyphenylacetate or homoprotocatechuic acid (HPCA) as an intermediate in the O_2-dependent degradation pathway for aromatic compounds such as lignin constituents and tyrosine. 7
Figure 3: Molecular orbital diagram of ground state, triplet O_2. 11
Figure 4: Reactions and the 2-His + 1-Asp/Glu Fe binding motif of representative aromatic ring cleaving dioxygenases 14
Figure 5: Proposed reaction cycle for Fe(II) extradiol dioxygenases. 16
Figure 6: Proposed reaction cycle for Fe(III) intradiol dioxygenases. 18
Figure 7: Proposed reaction cycle for redox-cycling Rieske oxygenases. 20
Figure 8: Proposed reaction cycle for 2-oxo acid dependent dioxygenases. 24
Figure 9: Proposed reaction cycle for tetrahydropterin-dependent oxygenases. 27
Figure 10: Intermediates observed *in-crystallo* for FeHPCD and its variants. 31
Figure 11: Proposed superoxo complex in mechanism for extradiol dioxygenases. 37
Figure 12: Absorption spectra of species occuring in the H200N-4NC + O_2 reaction 45
Figure 13: EPR spectra of reaction intermediates from H200N-4NC + O_2 reaction.. 46
Figure 14: Parallel-mode EPR spectra of $H200N_{Int1}{}^{4NC}$ and $H200N_{Int2}{}^{4NC}$ and simulations 48
Figure 15: Time dependence of $H200N_{Int1}{}^{4NC}$ EPR signal decay. 50
Figure 16: Energy level diagram for the spin system of $H200N_{Int1}{}^{4NC}$. 51
Figure 17: Detailed $H200N_{Int2}{}^{4NC}$ EPR result. 55
Figure 18: 4.2 K Mössbauer spectra of H200N variants recorded for B = 0. 56
Figure 19: 4.2 K Mössbauer spectra in parallel applied magnetic fields, $H200N_{Int1}{}^{4NC}$ and $H200N_{Int2}{}^{4NC}$ 57
Figure 20: 4.2 K Mössbauer spectra of the single turnover time course in the presence of 2 X 4NC at 4 °C. 59
Figure 21: DFT result for $H200N_{Int1}{}^{4NC}$. 63
Figure 22: DFT geometry optimization of $H200N_{Int1}{}^{4NC}$. 65
Figure 23: Proposed O_2 activation by extradiol dioxygenases 74
Figure 24: H200N-HPCA + O_2 reaction monitored by stopped-flow. 82
Figure 25: The time course of the reaction of H200N-HPCA + O_2 monitored at 610 nm 83
Figure 26: Time dependent parallel mode EPR spectra from the H200N-HPCA + O_2 reaction 85
Figure 27: Parallel-mode EPR spectra and simulations for H200N-HPCA frozen 40 ms after reaction with O_2. 87
Figure 28: 4.2 K, zero field Mössbauer spectra of H200N-HPCA complexes 89
Figure 29: Numerical integration simulation of the time course of the H200N-HPCA + O_2 reaction. 93
Figure 30: 4.2 K Mössbauer spectra of $H200N_{Int1}{}^{HPCA}$ in applied magnetic fields. 94
Figure 31: EPR spectra of isotopically enriched $H200N_{Int1}{}^{HPCA}$. 96
Figure 32: FeHPCD-HPCA + O_2 reaction monitored by stopped-flow. 99
Figure 33: Mössbauer spectra from the FeHPCD-HPCA + O_2 reaction at 4.2K for B = 0.. 100
Figure 34: Intermediates from the FeHPCD and H200N turnover cycles. 112

Figure 35: Michaelis-Menten plot from the reaction of Y257F with HPCA and O_2 saturated buffer at 4 °C. 127
Figure 36: Estimation of K_d for HPCA binding to Y257F.. 128
Figure 37: The Y257F-HPCA + O_2 reaction time-course followed using diode-array detection . 130
Figure 38: Photochemistry of the ring-cleavage product.. 133
Figure 39: The Y257F-HPCA + O_2 reaction time course followed using single-wavelength detection at 450 nm and 350 nm 134
Figure 40: O_2 dependence of the three kinetically competent reciprocal relaxation times from the Y257F-HPCA + O_2 reaction 138
Figure 41: Mössbauer spectra from the Y257F-HPCA + O_2 reaction series 140
Figure 42: Simulations for the reaction time course based on Scheme 2 142
Figure 43: Second sphere residues which are proposed to participate in catalysis.. 144
Figure 44: Simulation of expected time-dependent yields for reaction intermediates from the Y257F-HPCA + O_2 reaction. 146
Figure 45: Comparison of UV-vis spectra of unbound HPCA quinone and HPCA semiquinone to those of $Y257F_{Int1}^{HPCA}$. 149
Figure 46: Proposed reaction intermediates in the native 2,3-HPCD reaction cycle.. 163

List of Schemes

Scheme 1: Kinetic model from stopped-flow studies of the H200N-HPCA + O_2 reaction..... 109
Scheme 2: Model for steps in the Y257F-HPCA + O_2 reaction..... 141
Scheme 3: Kinetic models for rate constant associated with species that occurring in the Y257F-HPCA + O_2 single-turnover reaction 145

INTRODUCTION

Abbreviations for introduction:

2,3-HPCD and FeHPCD, wild-type or recombinant homoprotocatechuate 2,3-dioxygenase from *Brevibacterium fuscum*.

4NC, 4-nitrocatechol; WT, wild type.

3,4-PCD, protocatechuate 3,4-dioxygenase from *Pseudomonas arvilla* C-1.

DFT, Density Functional Theory.

EPR, Electron Paramagnetic Resonance.

RFQ, Rapid Freeze Quench.

SQ, semiquinone radical.

MnHPCD, recombinant homoprotocatechuate 2,3-dioxygenase from *Brevibacterium fuscum* in which the Fe(II) is replaced by Mn(II).

CoHPCD, recombinant homoprotocatechuate 2,3-dioxygenase from *Brevibacterium fuscum* in which the Fe(II) is replaced by Co(II)

Life in all its complexity is sustained by metabolic reactions. These reactions are divided into two broad categories, anabolic and catabolic. Anabolic reactions are biosynthetic in nature, consuming energy to synthesize cellular constituents, whereas, catabolic reactions are degradative in nature, often but not always, resulting in the release of energy that is captured in the form of high energy bonds in ATP or other organic molecules. These high-energy molecules are used to drive thermodynamically unfavorable reactions such as anabolic metabolism, muscle function, and a myriad of regulatory, signaling, and cellular maintenance processes. Moreover, the catabolic processes themselves often require high-energy molecules to provide the activation energy to initiate their reactions. As a result, living organisms exist in a steady state, sustaining a balance between anabolic and catabolic reactions but also requiring a net input of energy in some form to keep cellular metabolism from achieving thermodynamic equilibrium.

In many ways, life on earth represents a competition for energy and life's building blocks. This competition has nurtured intricate relationships amongst living systems and also between living systems and their environment. Energy relationships between living systems have set forth a global metabolism that depends on the metabolic activities of autotrophic and heterotrophic organisms. This global metabolism affects all living systems and has transformed earth's atmosphere by defining cycles of elements which are useful to life, including; O_2, N_2 and CO_2 (*1-4*). Because carbon is the ultimate building block for life on earth, perhaps the most remarkable of these cycles is the global carbon cycle (*4-6*).

The carbon cycle and aerobic life

From the perspective of living systems, the global carbon cycle is essentially the process in which earth's limited source of carbon is cycled between organic and inorganic reservoirs. The flux of carbon into biomass is powered by available free energy and catalyzed by metabolic enzymes in anaerobic and aerobic environments alike. Because living organisms obtain energy through oxidation-reduction reactions, the global carbon cycle also resembles the flux of reducing equivalents from the environment into biomass. In aerobic environments, the exchange of carbon and reducing equivalents between biomass and the environment is most apparent in the balance between opposed metabolic processes such as oxygenic photosynthesis and aerobic respiration (*7*). In brief, oxygenic photosynthesis oxidizes water to O_2, using the protons and reducing equivalents to reduce CO_2 and synthesize an overwhelming diversity of organic molecules, whereas aerobic respiration couples oxidation of organic molecules to CO_2 with reduction of O_2 to yield water. In addition, aerobic organisms have also evolved many other O_2-dependent metabolic reactions by incorporating "oxygenase"[a] chemistry as a vital component of cellular processes. These include O_2-dependent post-translational modifications, DNA repair, O_2 sensing, detoxification of xenobiotics, biosynthesis, and biodegradation (*8-14*).

Up until 2.4 billion years ago, it appears the globe was devoid of both O_2 and aerobic organisms (*3, 15*). The appearance of atmospheric O_2 is commonly attributed to blue-green algae that are thought to have initiated oxygenic photosynthesis some 3.5 billion years ago (*2, 3, 16*). As a result, emergence of fossils from early aerobic eukaryotes has been closely linked to rising atmospheric O_2 levels (*17*), and the accumulation of O_2 to current levels of ~20% is thought to reflect an initial imbalance between photosynthesis and aerobic respiration (*2, 3*). Because photosynthesis requires ~ 450 kJ of photon energy to

[a] The transfer of one or two oxygen atoms from O_2 into organic molecules.
[b] The origin of the two enzyme-substrate species remains unknown. Crystal structures of

oxidize 2 moles of water to yield O_2 and protons, the rise of stable atmospheric O_2 means the corresponding reducing equivalents were sequestered in earth's crust as biomass, fossil fuels, and organic sediments, generating a large chemical potential energy between biomass and the potent electron acceptor, O_2, in earth's atmosphere (*2, 3*).

In one aspect, accumulation of atmospheric O_2 was possible partially because a majority of organic molecules in plant biomass are relatively stable molecules such as lignin and cellulose, which will not easily reduce O_2 under conditions that are conducive to life (Figure 1) (*18*). This is so because the direct transfer of reducing equivalents from organic molecules such as lignin and cellulose to O_2 involves spin-forbidden chemistry that is highly unfavorable at ambient temperatures (*14, 18-22*). To our benefit, the electronic stability of O_2 is thought to have played a role in allowing the large chemical potential energy to build up in earth's atmosphere as O_2 and reduced biomass accumulated, providing the necessary driving force for evolution of aerobic respiration and the rich oxygenase chemistry found in metabolic reactions of aerobic heterotrophs which include all animals (*4-6, 23*).

Unlike animals, microorganisms generally have short lifetimes and are often permeable to small molecules from their environment. This allows for constant experimentation with xenobiotic carbon sources which can permeate or be transported into single cell organisms (*7, 24, 25*). Specifically, aerobic microorganisms have demonstrated the ability for rapid evolution of peripheral metabolic processes that channel new carbon sources into central metabolic pathways where the carbon can be re-oxidized to CO_2 (*7*). This "catabolic" evolutionary paradigm towards metabolism of xenobiotics is in direct contrast to the "detoxification" paradigm adopted by higher organisms such as animals, making aerobic microorganisms champions of biodegradation wherever O_2 is available on earth.

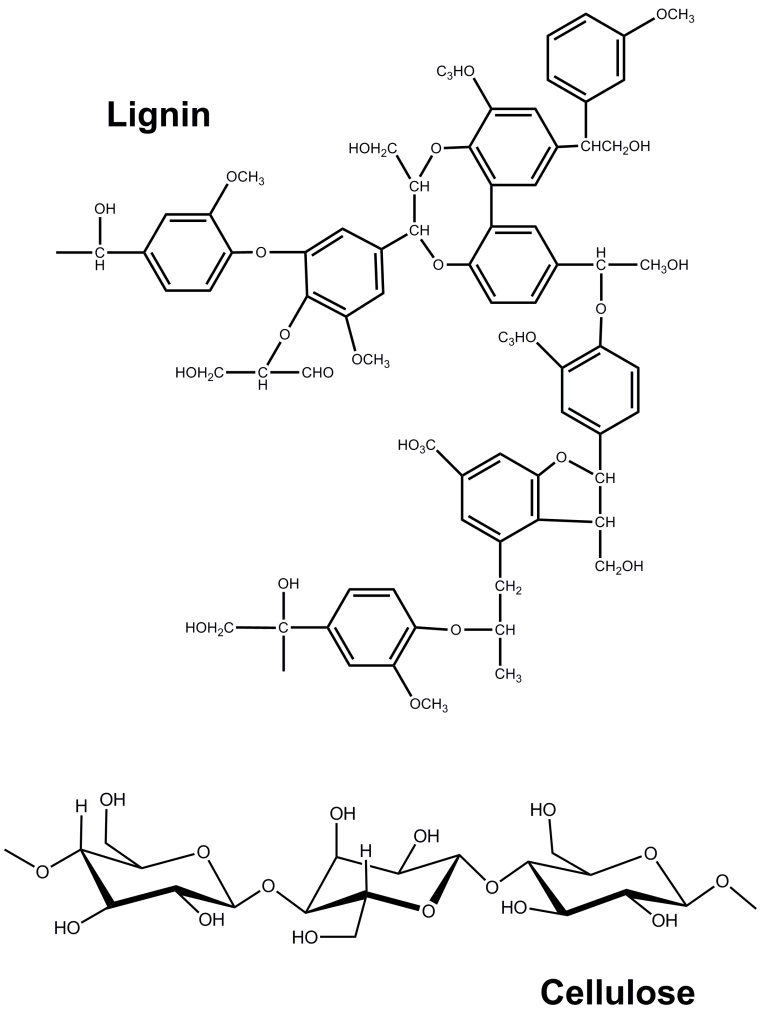

Figure 1: Simplified representations of lignin and cellulose structures.
.

Homoprotocatechuate 2,3-dioxygenase

As it pertains to the research presented in this thesis, the study of metabolic enzymes and pathways for aerobic catabolism of naturally occurring and man-made carbon compounds holds a promise of developing bioremediation technologies and biofuels from renewable energy sources such as biomass (*7, 26, 27*). The contents of this thesis will focus on detailed mechanistic studies on the catechol ring-cleaving enzyme Homoprotocatechuate 2,3-Dioxygenase (or 2,3-HPCD) from the gram (+) soil bacterium *Brevibacterium fuscum* (*B. fuscum*). 2,3-HPCD (EC 1.13.11.15) from *B. fuscum* is a non-heme mononuclear Fe(II)-dependent dioxygenase which belongs to the extradiol dioxygenase family**,** a diverse family of enzymes that use a mononuclear non-heme Fe(II) (or rarely Mn(II)) cofactor to catalyze the O_2-dependent ring-opening reaction of catecholic substrates (*28*). In nature, this reaction participates in the carbon cycle by allowing aerobic microorganisms to channel large amounts of naturally occurring and man-made aromatic compounds into central metabolic pathways, facilitating their complete oxidation to CO_2 (Figure 2).

The extradiol dioxygenases along with other well characterized mononuclear (non-heme) Fe(II)-dependent dioxygenase families such as Rieske dioxygenases, α-keto acid-dependent dioxygenases, and pterin-dependent dioxygenases, use the ubiquitous 2-His + 1-Asp/Glu Fe binding motif, a mode of binding Fe which rivals the heme paradigm in nature (*29*). Generally, non-heme oxygenases are distinct from their heme counterparts primarily by the set of ligands used to coordinate the catalytic iron atom. Common ligands to non-heme catalytic iron sites are protein derived amino-acids (e.g. His, Asp, Glu and Asn) along with several displaceable solvent molecules which compose a more flexible coordination environment compared to the porphyrin ring of heme irons. Consequently, the non-heme oxygenases accommodate a wider range of organic substrates and cofactors, many of which coordinate directly to or very

near the iron, allowing a remarkably diverse range of O_2-dependent reactions to be catalyzed.

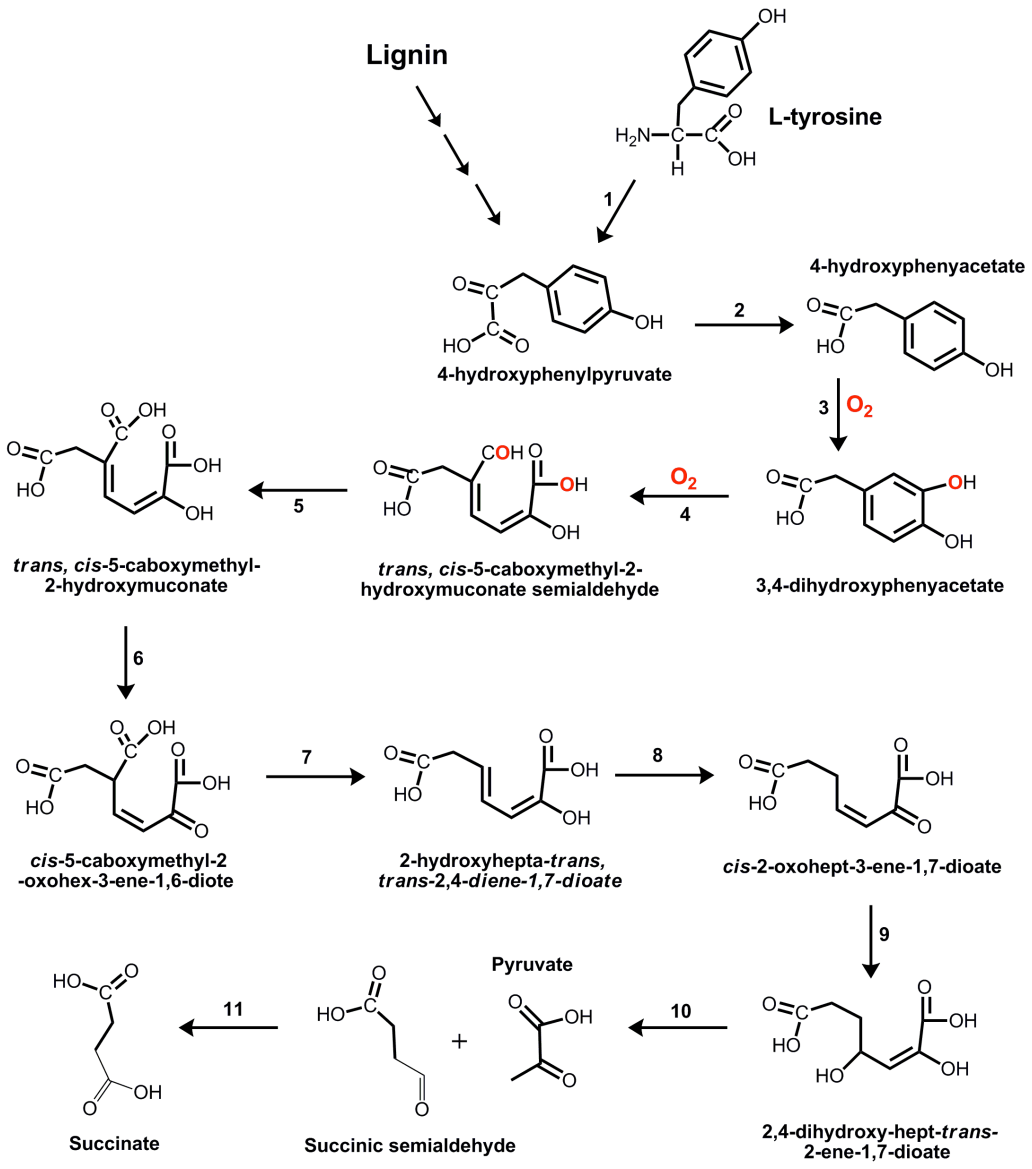

Figure 2: 3,4-dihydroxyphenylacetate or homoprotocatechuic acid (HPCA) as an intermediate in the O_2-dependent degradation pathway for aromatic compounds such as lignin constituents and tyrosine.

In contrast, heme oxygenases usually do not bind substrates directly to the iron. Instead, the heme iron is used almost exclusively to bind and activate O_2. Similarly, the non-heme oxygenases can use the iron to bind and activate O_2, but they can also use it to activate the substrate or even to bind and activate both O_2 and the organic substrate simultaneously. Because nature has evolved far more enzymes and proteins than there are novel folds, most oxygenase enzymes can be associated with structurally related ancestors that share the same overall fold, but catalyze different reactions (*30*). This is true for α-ketoglutarate dioxygenases, Rieske dioxygenases (α-subunit), and pterin-dependent dioxygenases among the non-heme oxygenases, as well at the P450 class of heme oxygenases (*11*) (*31*) (*32*) (*33*). However, structurally unrelated families of oxygenases which catalyze the same reaction are also known and this includes the extradiol dioxygenases (*34*). The members of the extradiol dioxygenase family can be grouped into three distinct structural classes which converged to the common 2-His + 1-Glu/Asp Fe binding motif in order to catalyze the extradiol ring-opening reaction (*34*). *B. fuscum* 2,3-HPCD belongs to the Class I extradiol dioxygenases. This class folds into paired $\beta\alpha\beta\beta\beta$ domains, a structural motif used by enzymes in the functionally diverse Vicinal Oxygen Chelate (VOC) superfamily to bind divalent metal ions such as; Fe(II), Mn(II), Co(II), Mg(II), Ni(II) or Zn(II) (*34*) (*30*).

The paired $\beta\alpha\beta\beta\beta$ structural motif exhibits remarkable mechanistic plasticity, using the bound metal to chelate vicinal oxygen atoms from substrates, reaction intermediates, or transition-states of reaction intermediates in order to provide electrophilic assistance and/or facilitate redox chemistry during catalysis (*35*) (*30*). Indeed, members of the VOC superfamily catalyze reactions which fall into entirely different classes, including: oxidoreductases such as the Fe(II)-dependent 2,3-HPCD or the Fe(II)-dependent dioxygenase 4-hydroxyphenylpyruvate dioxygenase (HPPD), isomerases such as Zn(II)-dependent Glyoxylase or Co(II)-dependent Methylmalonyl-CoA epimerase, and transferases such as the Mn(II)-dependent Fosfomycin resistance protein, FosA

(*30*).

In the VOC superfamily of enzymes, 2,3-HPCD and HPPD provide an opportunity to study the mode of O_2 activation by mononuclear non-heme Fe-dependent enzymes and the diverging mechanistic aspects of this structural superfamily. The value of mechanistic studies reported in this thesis are therefore two-fold. First, these studies are a part of the ongoing effort among biochemists and chemists to understand how biology activates a kinetically inert molecule (O_2), to react with highly stable organic compounds and effect stereo- and regio-specific oxygen atom transfer reactions. Second, the detailed study of electronic structures of trapped reaction intermediates from wild type 2,3-HPCD and selected mutants sheds light on mechanistic plasticity of the paired $\beta\alpha\beta\beta\beta$ fold and the 2-His + 1-Asp/Glu Fe binding motif, allowing 2,3-HPCD mutants to search the energy landscape for reaction intermediates that effect desired ring-cleaving chemistry.

O_2 activation by mononuclear non-heme Fe oxygenases, perspective and overview

O_2 is a unique reagent for biology because it combines availability and high potential reactivity with inertness at ambient (*18, 22, 36*). The latter is true because the molecular structure of O_2 would cause a violation of a quantum mechanical rule governing the conservation of spin angular momentum if it were to react with most biological molecules (*22*). The reaction is thus termed "spin forbidden". This is so because under physiological conditions, O_2 has a triplet ground state (with two unpaired electrons in the degenerate $2p\pi^*$ orbitals, Figure 3) whereas the organic substrates and products of oxygenase reactions are singlets (with no unpaired electrons). As such, the direct reaction of triplet O_2 with singlet organic molecules violates the spin conservation law which dictates that a spin flip must not occur as O_2 accepts electrons from suitable donors at ambient temperatures (*22*). Even so, once O_2 became available in the biosphere, life evolved various mechanisms to "activate" triplet O_2 for oxidation-reduction reactions with unactivated organic molecules under conditions which support life (*11, 20, 36-38*). A common theme for enzymes that activate O_2 for oxygenase or oxidase chemistry is the use of redox active transitional metal ions that have unpaired electrons and can react with triplet O_2 in a spin allowed process (*22, 39, 40*). Another strategy has been the use of organic cofactors or substrates that have the ability to stabilize unpaired electron density and can react with triplet O_2 via a radical mechanism under physiological conditions (*22*). Both strategies can generate highly reactive oxygen species, consequently, an important aspect of oxygenase mechanisms is the manner in which the enzymes regulate O_2 activation to unleash the inherent free energy stored in the O–O bond when and where it is required. This assures specificity and avoids the release of activated oxygen species that would randomly attack biological molecules.

In broad terms, there are two types of oxygenase reactions catalyzed by the mononuclear non-heme iron oxygenases, namely dioxygenase and

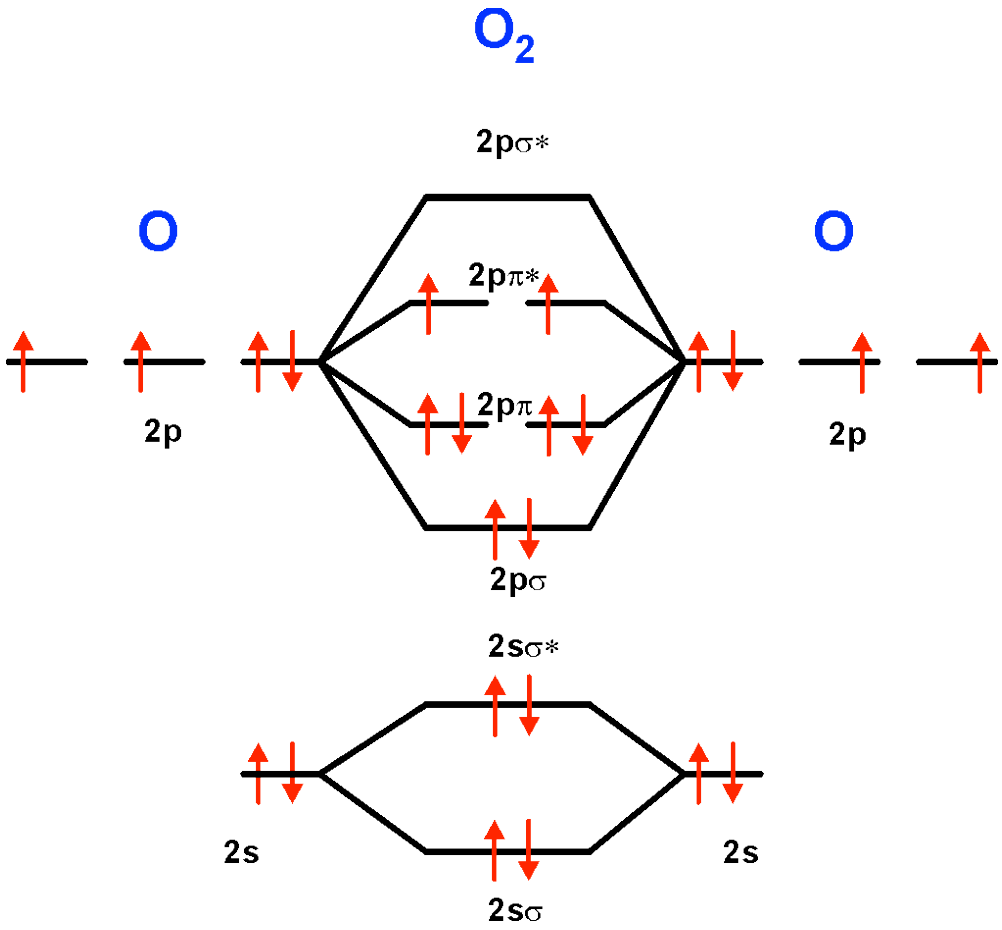

Figure 3: Molecular orbital diagram of ground state, triplet O_2.

monooxygenase chemistry. Dioxygenases transfer both atoms of oxygen from O_2 into one or more of the organic substrates or cofactors (*13, 34, 41*), whereas monooxygenases transfer one atom of oxygen from O_2 into the organic substrate with reduction of the second atom to water (*42, 43*). A few subfamilies can catalyze both types of oxygenase reactions using a shared reaction scheme (*44*). However, most of the time, monooxygenases and dioxygenases use significantly different mechanistic strategies.

Oxygenases usually function by using a reductive strategy for activation of O_2, but the source of the required electrons varies significantly. Common sources include oxidation of the substrate itself or of a specific cofactor, and use of the energy stored in universal metabolic cofactors such as NAD(P)H. One electron reduction of O_2 in and of itself overcomes the spin forbidden nature of the reaction with common biological molecules. However, it may also be a precursor to O–O bond cleavage to yield highly reactive oxidizing species containing only a single oxygen atom.

For mononuclear non-heme oxygenases, the iron plays many different roles in the process of O_2 activation through its ability to bind O_2 and/or organic substrates, to assume multiple oxidation and spin states, and promote electron spin exchange via the unpaired electrons in its d-orbitals (*13, 45*). Here these strategies are illustrated for the most prevalent families of the mononuclear non-heme iron oxygenases.

Mononuclear non-heme iron oxygenase families

Aromatic ring-cleaving dioxygenases.

Plants convert a significant portion of the global CO_2 reservoir into stable aromatic polymers which compose structural scaffolds in woody tissue (Figure 1). The aromatic fraction is returned to the global carbon cycle by the action of fungi and bacteria that first breakdown the aromatic polymer and then metabolize the individual aromatic molecules for growth (*10*). A key step in this process is the opening of the aromatic ring, which is catalyzed in the aerobic biosphere by one of two types of dioxygenases that bind Fe(II) or Fe(III), respectively, in their active site (*34, 46*). Both types result in the complete incorporation of oxygen from O_2 into the ring open product. The Fe(II) class is divided into enzymes that cleave catechols (1,2-dihydroxybenzene adducts) and those that cleave gentisates (2,5-dihydroxybenzoate adducts). The extradiol dioxygenases use the Fe(II) to open the catechol ring adjacent to the vicinal hydroxyl functions, yielding yellow muconic semialdehyde products (Figure 4 A). If the aromatic ring has another substituent, then the extradiol dioxygenase class can be further divided into proximal- and distal-cleaving members depending upon the relation of the cleavage site to the position of the substituent. Gentisate dioxygenases cleave between the carboxylate and 2-OH substituents to yield maleylpyruvic acid (*47*) . Other types of substrates such as hydroquinones and salicylates are ring opened by similar Fe(II) dioxygenases. The Fe(III) class is largely composed of enzymes that catalyze ring cleavage between the vicinal hydroxyls of catechol adducts to yield muconate derivatives and thus are called intradiol dioxygenases (Figure 4 B).

As mentioned above, the Fe(II) atom of extradiol dioxygenases is bound by the 2-His + 1-Asp/Glu Fe binding motif. The enzyme derived ligands are oriented on one side of the metal coordination sphere (Figure 4 A). The opposite side is bound by displaceable solvents and can be used to bind substrates upon

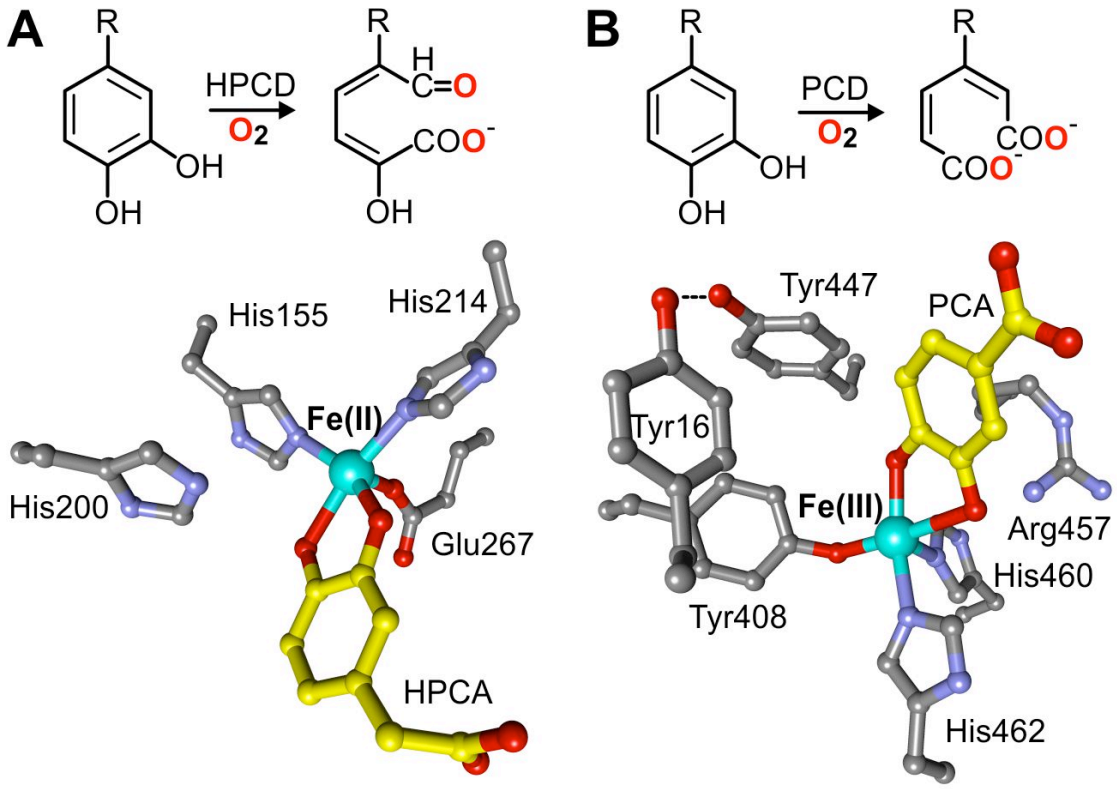

Figure 4: Reactions and the 2-His + 1-Asp/Glu Fe binding motif of representative aromatic ring cleaving dioxygenases (*28*) (*48*). (A) Reaction of 2,3-HPCD and the X-ray crystal structure of the Fe(II) 2-His-1-carboxylate ligand environment with the substrate (yellow) bound (PDBID: 1Q0C). The loss of solvent ligands from the iron as substrate binds creates a vacant site for O_2 to bind. (B) Reaction of 3,4-PCD and the X-ray crystal structure of the Fe(III) ligand environment of the substrate (yellow) complex containing one Tyr and 2 His ligands (PDBID: 3PCA). An open site is created on the Fe(III), but O_2 cannot bind without simultaneously reacting with the substrate.

displacement of the solvents. This so called 2-His + 1-Asp/Glu Fe binding motif or the 2-His-1-carboxylate facial triad is the most common iron binding motif within the mononuclear non-heme Fe(II) oxygenase family, being first recognized in the extradiol subfamily (*28, 29, 49*). This ligand set and the fact that the iron is ferrous results in a nearly colorless enzyme.

The Fe(III) of intradiol dioxygenases is bound by 2 Tyr and 2 His amino acid ligands as well as a deprotonated solvent molecule (OH^-)(Figure 4 B) (*46*). The Tyr ligands transfer charge to (but do not reduce) the Fe(III) site yielding a burgundy chromophore. In this case, the ligand set causes the redox potential to be very low so that the Fe(III) state is constant during catalysis (*45*).

Due to the different metal binding environments of Fe(II) and Fe(III) dioxygenases, the O_2 activation and ring cleaving strategies are fundamentally different. 2,3-HPCD will be used to illustrate the extradiol dioxygenase mechanism (Figure 5). The reaction cycle begins with the catecholic substrate (HPCA) binding to the Fe(II) via both of its OH groups (a chelate), only one of which deprotonates. This directly displaces two solvent ligands and indirectly displaces (or weakens) the third, allowing O_2 to bind in the newly available ligand site adjacent to the HPCA. The Fe(II) serves two functions. First, it organizes the substrates to direct the upcoming reaction. Second, it serves as a conduit to allow an electron to move from the substrate to the O_2. In this way, both the substrate and the O_2 take on radical character (*46*). Recombination of the radicals produces an alkylperoxo intermediate. This intermediate is thought to breakdown in what is termed a Criegee rearrangement in which the alkylperoxo O–O bond breaks heterolytically and one oxygen is inserted into the aromatic ring to form a lactone adduct. Finally, the lactone is hydrolyzed by the second oxygen from O_2 to yield the reaction product that can dissociate from the enzyme. In the case of the extradiol dioxygenases, the Criegee rearrangement is catalyzed by an active site His residue (His200 for HPCD) that acts as an acid catalyst, probably using the proton removed from the second OH of the HPCA

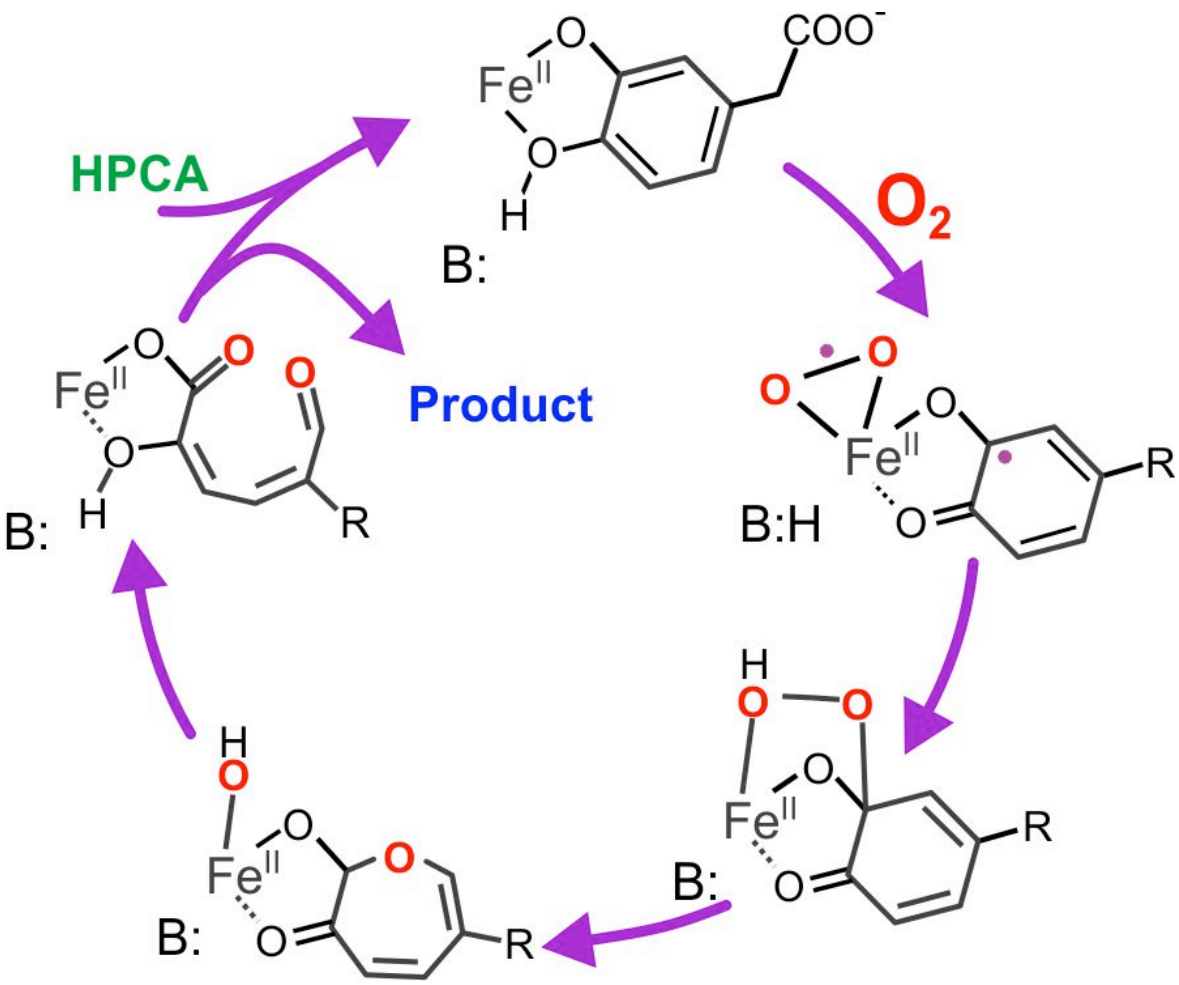

Figure 5: Proposed reaction cycle for Fe(II) extradiol dioxygenases.

The reaction cycle is illustrated for Homoprotocatechuate 2,3-Dioxygenase (*28*).

(Figure 4 A). It is important to recognize that the reaction between the iron-bound substrate and oxygen radicals is not “forbidden” and thus readily occurs. The enzyme uses iron to facilitate the generation of the radicals. The activation only occurs when both the HPCA and the O_2 are present and properly oriented, which guarantees a specific reaction. Many aspects of this mechanism have been experimentally tested, including studies that have reported electronic and three dimensional structures of proposed reaction intermediates (*50-52*).

Gentisate and salicylate dioxygenases also form a substrate-Fe(II) chelate, in this case via the carboxylate and 2-OH substituents (*46*). Structural studies have shown that there is an open Fe(II) coordination site adjacent to the substrate binding site, implying that O_2 binding and activation occurs in a similar manner to that just described for the extradiol dioxygenases (*53*). However, the iron coordination geometry contains 3 His residues rather than the usual 2-His + 1-Asp/Glu Fe binding motif suggesting that there may be subtle differences.

Protocatechuate 3,4-Dioxygenase (3,4-PCD) will be used to illustrate the O_2 activation strategy of Fe(III) dioxygenases (Figure 6). Fe(III) sites cannot bind O_2 directly and the redox potential is much too low to be reduced by catecholic substrates, so the O_2 activation strategy must take a very different course than that described for the Fe(II) extradiol class (*46*). The reaction begins by the substrate catechol (PCA) binding in a multistep process to the iron as a fully deprotonated chelate. During the binding process, the solvent OH^- and one Tyr (Tyr447 for 3,4-PCD) are dissociated and the iron coordination geometry changes (Figure 4 B). The original trigonal bipyramidal geometry (no open coordination sites) shifts to square pyramidal (one open site). This allows O_2 to bind in a unique concerted process in which bonds to the substrate and the iron are formed simultaneously to form an alkylperoxo intermediate (*45*). A Criegee rearrangement similar to that described above ensues, but this time an anhydride intermediate is formed which can be hydrolyzed by the second oxygen from O_2 to yield a muconic acid adduct as the product.

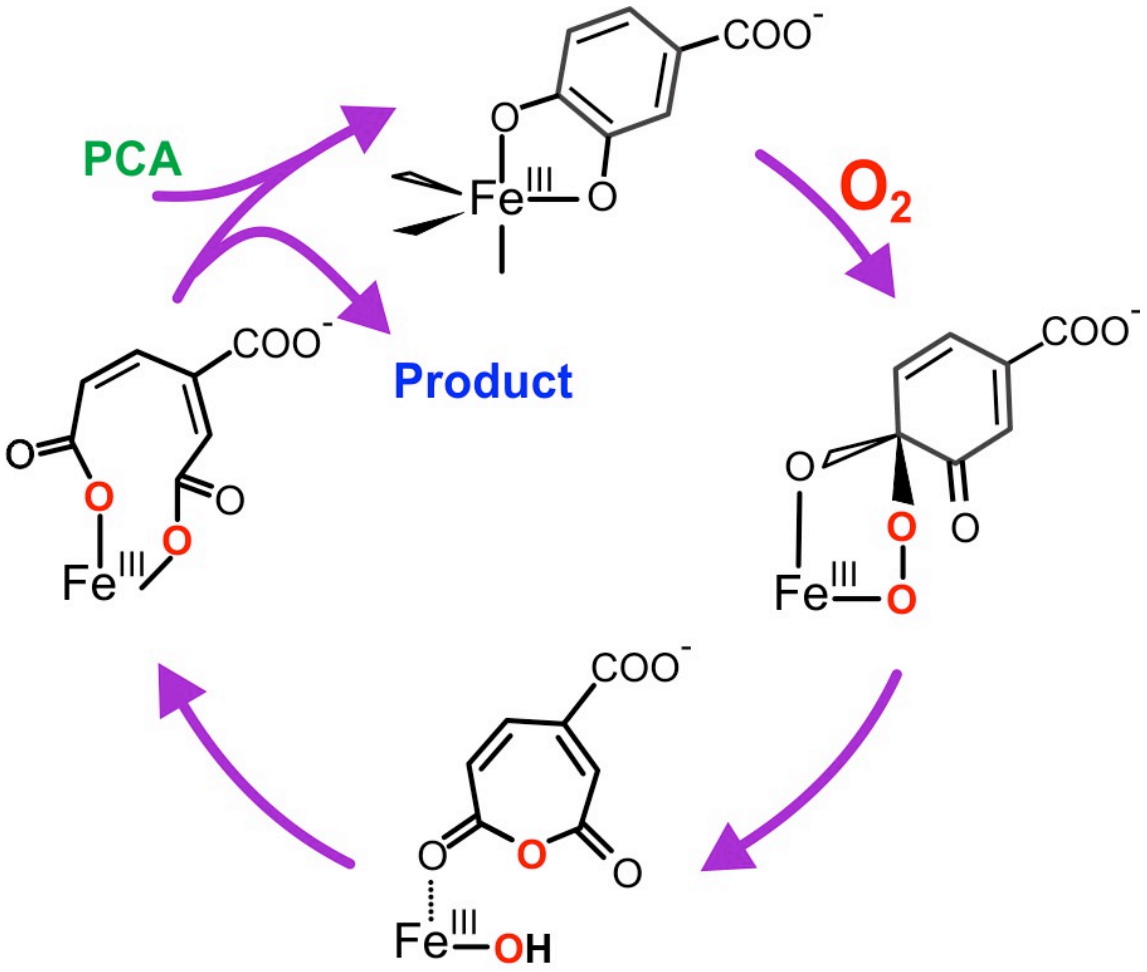

Figure 6: Proposed reaction cycle for Fe(III) intradiol dioxygenases.

The reaction cycle is illustrated for Protocatechuate 3,4-Dioxygenase (*48*).

Rieske mono- and dioxygenases.

Aromatic compounds are often encountered in the environment not as catechols or gentisates but rather as unactivated single or multi-ring species such as benzene or naphthalene. These may appear as even less reactive compounds when halo, nitro, and other deactivating substituents are present. To deal with these compounds, microorganisms often utilize Rieske mono- or dioxygenases that can introduce one or two O_2-derived hydroxyl substituents (*26, 31*). The Rieske dioxygenases introduce both atoms of oxygen from one O_2 into the same face of the aromatic ring at adjacent carbons to form a non-aromatic cis-dihydrodiol product. This product is re-aromatized by the next enzyme in the pathway to yield a catechol that can be ring cleaved by the ring-cleaving dioxygenases discussed above.

The Rieske mono- and dioxygenases have very similar structures and O_2 activation mechanisms, so the naphthalene 1,2-dioxygenase system (NDOS) will be used to illustrate the common aspects of catalysis (Figure 7). The NDOS system consists of 3 protein components. A reductase (NDR) containing an FAD flavin and a 2Fe2S iron sulfur cluster is reduced by NAD(P)H. The reduced NDR then reduces a 2Fe2S Rieske ferredoxin component (NDF) which transfers the electrons to the oxygenase component (NDO). NDO contains a Rieske type 2Fe2S cluster and a mononuclear non-heme Fe(II) bound in a 2-His + 1-Asp/Glu motif. Rieske clusters differ from the usual 2Fe2S clusters in that the two Cys residues that normally bind one of the irons are replace by His residues. The mononuclear iron of Rieske dioxygenases differs from that in ring-cleaving extradiol dioxygenases in that it is redox active and can be stabilized in either the Fe(III) or the Fe(II) state. The NDO is a trimer of dimers in which the β subunits appear to be primarily structural, and the α subunits hold both of the metal centers. The α subunit structure is such that the metal centers are far apart. However, when the enzyme assembles, the three α subunits align head to tail so that the Rieske cluster of one α subunit is only 12 Å from the mononuclear site of the adjacent α subunit. This cross-boundary pair of metals centers appears to be the active unit (*31*).

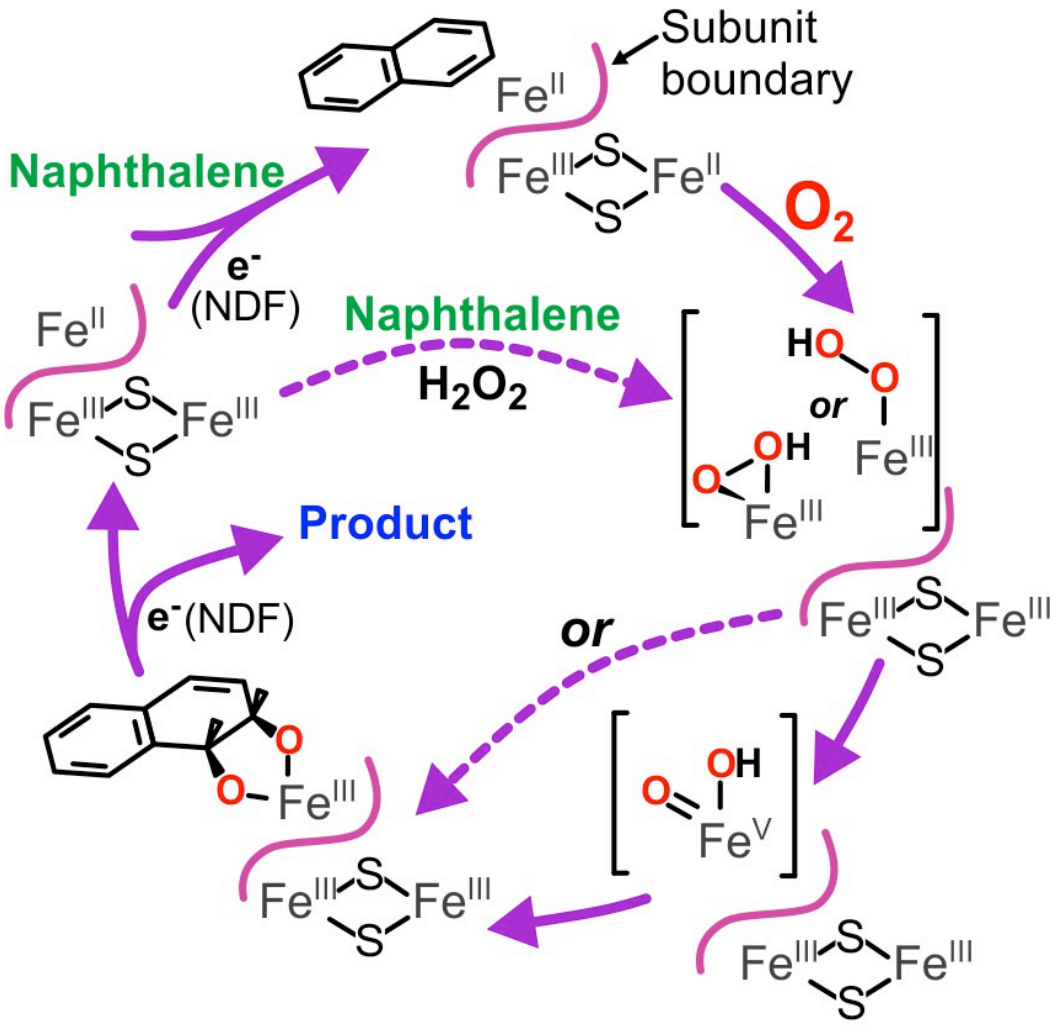

Figure 7: Proposed reaction cycle for redox-cycling Rieske oxygenases. The reaction cycle is illustrated for Naphthalene 1,2-Dioxygenase (*13*).

Catalysis is highly regulated in NDOS. The cycle begins by reduction of the enzyme by 2 electrons so that the mononuclear iron is in the Fe(II) state and the Rieske cluster holds one electron. Reduction of the mononuclear iron causes a conformational change that allows the substrate naphthalene to bind. Once the substrate and both electrons are present, O_2 is able to bind to begin the activation process. If the Rieske cluster is not reduced, O_2 will not bind even with the substrate present and the mononuclear iron reduced. This was elucidated by MCD and ENDOR studies of NDO and structural studies in the Rieske monooxygenase 2-Oxoquinoline 8-Monooxygenase (OMO)(*13*). Substrate binding near (but not to) the mononuclear Fe(II) causes the loss of one solvent ligand from the iron, opening a potential binding site for O_2, but the site is sterically blocked. Reduction of the Rieske cluster induces a series of cross-boundary structural changes initiated by protonation of one of the His ligands of the cluster. This results in the mononuclear iron being drawn away from the substrate, providing space for O_2 to bind.

The mechanism of Rieske dioxygenases remains controversial. However, two recent experimental approaches suggest that a two electron reduced form of oxygen is involved (*13*). First, 2-electron reduced NDO was shown to react with substrate and O_2 in a single turnover reaction to form product in near stoichiometric yield and leave the mononuclear iron in the Fe(III) state. Second, both NDO and a fully oxidized form of benzoate dioxygenase (BZDO) were shown to utilize H_2O_2 as a source of 2 oxygens and 2 electrons to catalyze formation of product in a single turnover. In the normal turnover reaction, it is proposed that O_2 accepts one electron from the mononuclear Fe(II) and one transferred electron from the Rieske cluster as it binds. This would result in an Fe(III)-(hydro)peroxo adduct. Accordingly, a crystal structure of an intermediate formed after adding O_2 to a single crystal with naphthalene bound shows a side-on bound Fe-(hydro)peroxo in which the O–O bond is aligned with the substrate ring C-C bond that will be dihydroxylated (*54*). Moreover, in the H_2O_2 shunt reaction with BZDO, an intermediate can be trapped from solution that has spectroscopic characteristics of an Fe(III)-(hydro)peroxo species (*13*).

Once the Fe(III)-(hydro)peroxo species is formed, the reaction with the aromatic substrate may occur directly or the species may undergo O–O bond cleavage to yield a HO-Fe(V)=O reactive intermediate. Density functional theory (DFT) computations suggest that NDO reacts via the Fe(III)-hydroperoxo species to yield a substrate epoxide that can open up to form a cation and then the cis-dihydrodiol product after reaction with the second Fe-bound oxygen (*55*). However, when NDO catalyzes monooxygenase reactions with radical clock substrates, there is clear formation of a long-lived radical intermediate which is inconsistent with attack by a peroxo species, but is the expected reaction for the HO-Fe(V)=O intermediate (*13*). Studies with model complexes and DFT calculations show that the OH-Fe(V)=O species is the most likely reactive species in the reactions of small molecule chelate complexes that catalyze cis-dihydroxylation and there is considerable experimental support for this proposal. (*56*) These complexes differ in that the iron is low spin in the precursor Fe(III)(hydro)peroxo species in contrast to the high spin Fe(III)(hydro)peroxo species of the enzymes.

Rieske monooxygenases such as OMO or oxygenating O-demethylases, such as 4-Methoxybenzoate Monooxygenase or Dicamba Monooxygenase, are likely to activate O_2 in the same manner as the Rieske dioxygenases (*57*). The true oxygenating species is unknown, although exclusive monooxygenation of the aromatic ring of 2-oxoquinoline and the above mentioned radical intermediate in the monooxygenation of radical clocks favors the HO-Fe(V)=O species.

2-Oxo acid-dependent mononuclear non-heme Fe(II) dioxygenases.

A large and diverse family of mononuclear non-heme iron oxygenases exists that utilizes 2-oxo acids as cosubstrates in reactions that result in hydroxylation of another substrate molecule (*42*). Many of these use α-ketoglutarate (αKG) as the cosubstrate and bind Fe(II) in the 2-His + 1-Asp/Glu binding motif. In the canonical reaction, the αKG chelates the iron via its carboxylate and oxo groups, resulting in release of the solvent ligands and opening an adjacent site for O_2 binding. However, the O_2 does not bind until the

substrate to be hydroxylated binds in a position near the iron, showing once again that the O_2 activation process is highly regulated.

The proposed mechanism for 2-oxo acid-dependent dioxygenases is illustrated in Figure 8 for the reaction of Taurine Dioxygenase (TauD) (*42, 58*). Oxygen binding to the Fe(II) begins the activation process. However, in contrast to the Fe(II) ring-cleaving dioxygenase substrates, αKG lacks the extended double bond character to transfer an electron to the iron, so an Fe(III)–$O_2^{\cdot -}$ rather than the Fe(II)–$O_2^{\cdot -}$ is likely to form. It is proposed that the bound $O_2^{\cdot -}$ attacks the 2-oxo carbon to generate an alkylperoxo intermediate. The role of many 2-oxo-acid dioxygenases is to hydroxylate a stable substrate, so a relatively powerful activated oxygen species must ultimately be generated. It is proposed that the O–O bond of the alkylperoxo species breaks heterolytically to yield an Fe(IV)=O reactive species while forming succinate and CO_2 from the αKG. In this case, the 2 electrons required to promote O–O bond cleavage are derived from breaking the C–C bond of αKG rather than an external source such as NADH. The Fe(IV)=O species is proposed to attack the substrate by hydrogen atom abstraction. Then rebound of $OH^{\cdot}$ and substrate radical yield the hydroxylated product and the Fe(II) resting state of the enzyme. In this enzyme family, one oxygen atom from O_2 is found in the hydroxylated product and the other in succinate, preserving the dioxygenase stoichiometry.

Support for the proposed mechanism has come through transient kinetic studies that allowed intermediates in the reaction cycle to be detected and in some cases trapped and spectroscopically characterized (*43*). The number and general kinetic properties of the intermediates are in accord with the proposed mechanism. Perhaps the most diagnostic intermediate, an Fe(IV)=O species termed J, was trapped by rapid freeze quench and characterized by Mössbauer spectroscopy (*59*). Intermediate J was shown to exhibit a large Kinetic Isotope Effect (KIE) in its reaction with substrate, as expected for the proposed hydrogen atom abstraction mechanism.

The 2-oxo-acid linked dioxygenases catalyze a remarkable number of reactions in organisms from bacteria to mammals. The types of reactions they

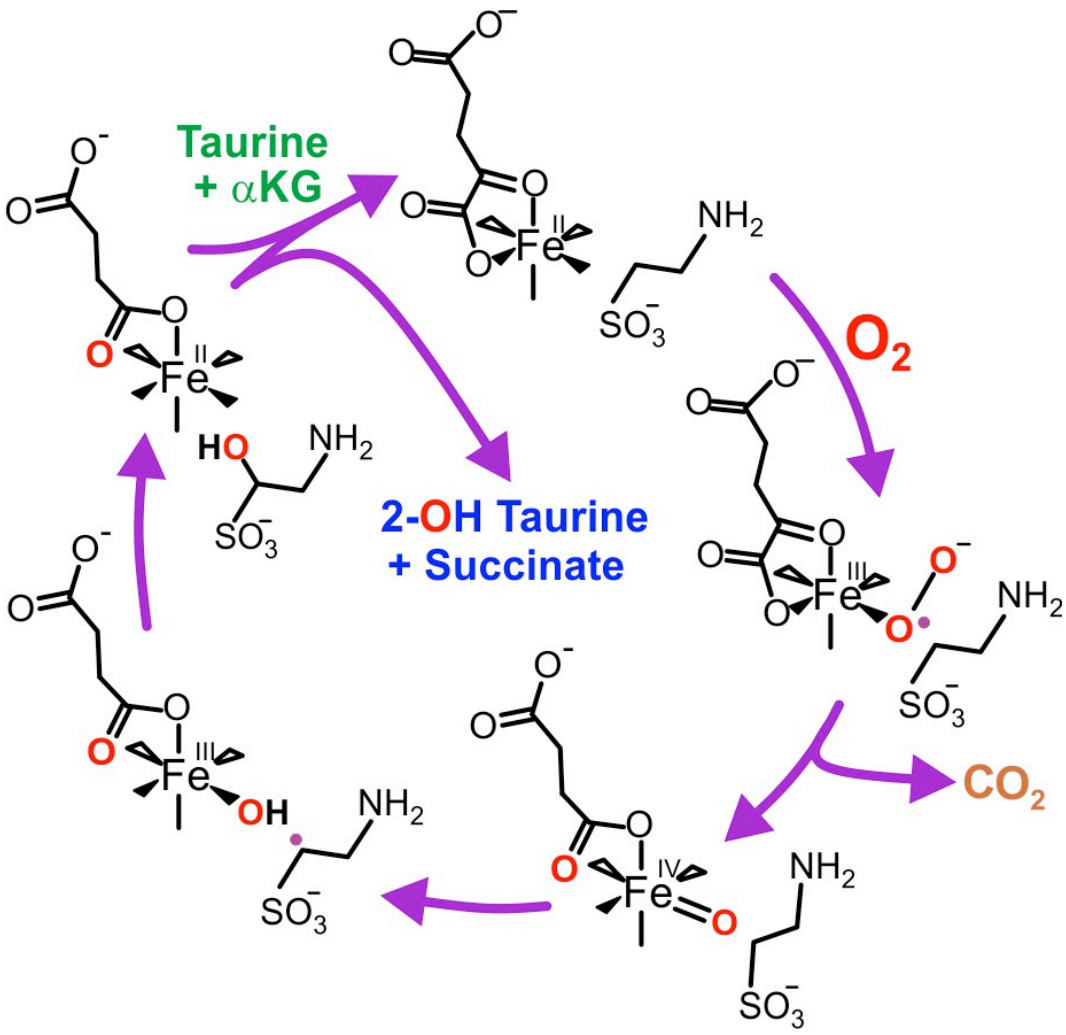

Figure 8: Proposed reaction cycle for 2-oxo acid dependent dioxygenases. The reaction cycle is illustrated for Taurine Dioxygenase (*13*) (*58*).

catalyze include hydroxylation, epoxidation, epimerization, desaturation, ring closure and expansion, and substituent migration (*42*). These reactions are characteristic of oxygenases that employ high valent iron intermediates in order to do oxidation-reduction chemistry in accord with the proposed mechanism.

While most of the enzymes use αKG or a similar separate 2-oxo acid cosubstrate, one important class incorporates the 2-oxo acid into the substrate itself. An example is the 4-Hydroxyphenylpyruvate Dioxygenase (HPPD) discussed briefly above. For HPPD, αKG is not used as a cosubstrate, instead the 2-oxo acid of the aromatic substrate side chain is key to the reaction. O_2 activation in this enzyme is thought to follow a similar course to that shown in Figure 4 except that the Fe(IV)=O intermediate may directly attack the aromatic ring to yield an arenium cation (*57*). This would allow a so called NIH shift to occur, resulting in migration of the ring substituents en route to formation of the observed homogentisate product. As such, HPPD is mechanistically related to αKG-dependent dioxygenases because the substrate-linked 2-oxo acid functions to initiated O_2 activation in order to generate the reactive Fe(IV)=O intermediate. Yet, it is distinct from αKG dependent dioxygenases in two aspects. First, only two substrates participate in catalysis (instead of three). Second, HPPD folds into the paired βαβββ structural motif that is characteristic of members in the VOC superfamily of enzymes unlike all known αKG dependent dioxygenases which fold into a double stranded β-helix fold (or jelly roll fold) (*8*).

Another recently described class of mononuclear non-heme Fe(II) dioxygenases has some similarities to the 2-oxo acid dioxygenase family in that the reactive tautomer of the substrate contains one keto- and one anionic oxygen when it is bound to the active site Fe(II). Also, the two oxygens from O_2 are found in two different products resulting from substrate cleavage. No additional cofactor is required. The only well-studied example is diketone cleaving enzyme (DEK1) which catalyzes the cleavage of acetylacetone to form methyl glyoxal and acetate (*60*). The mechanistic theory for this type of enzyme is still evolving, but it is proposed to involve attack of an initially formed Fe(III)-$O_2^{\cdot -}$ on the central carbon of the substrate α-dicarbonyl. This is similar to the first step of both the 2-

oxo acid- and the ring cleaving dioxygenase families. However, in the case of DEK1, the oxygen bound to the iron is proposed to migrate to one of the dicarbonyl oxygens to form a dioxetane, which breaks down to form the products. DEK1 is unusual in that it employs 3 His ligands to bind Fe(II) rather than the 2-His + 1-Asp/Glu facial triad. It has been proposed that the difference in net charge for these two binding motifs has a significant effect on the direction taken in the reaction chemistry (*60*).

Tetrahydropterin-dependent mononuclear non-heme Fe(II) oxygenases.

The tetrahydropterin-dependent mononuclear non-heme Fe(II) oxygenases are responsible for the biosynthesis of molecules such as DOPA, serotonin, and tyrosine in humans (*32*). Similar to the Rieske dioxygenases, these enzymes harbor both an 2-His + 1-Asp/Glu facial triad Fe(II) site and a nearby reduced cofactor. However, in this case, the tetrahydropterin cofactor can supply two rather than one election, and it can bind O_2. Structural studies show that the tetrahydropterin and the Fe(II) are aligned so that O_2 can bind to both, forming a peroxo bridge (*13, 57*). Phenylalanine Hydroxylase is used to illustrate the reaction mechanism of this subfamily in Figure 9. It is proposed that the tetrahydropterin provides two electrons to promote heterolytic O–O bond cleavage to yield 4a-hydroxypterin and an Fe(IV)=O intermediate. The latter species has recently been directly observed and trapped for spectroscopic studies (*61*). The X-ray crystal structures show that the aromatic substrate also binds near the Fe(II) site. Thus, it is proposed that the Fe(IV)=O species reacts with the aromatic ring in a one or two step reaction to yield an Fe(II)–O–substrate arenium cation (*32, 62*). This intermediate would convert to the hydroxylated product via an NIH shift and return the iron in the enzyme to the resting Fe(II) state.

The ability of the tetrahydropterin to provide 2 electrons suggests that the reactive state of this oxygenase class is one electron more reduced than the intermediate formed in the Rieske dioxygenases, making it formally a less potent reagent. Nevertheless, it is evident that the Fe(IV)=O species is often selected

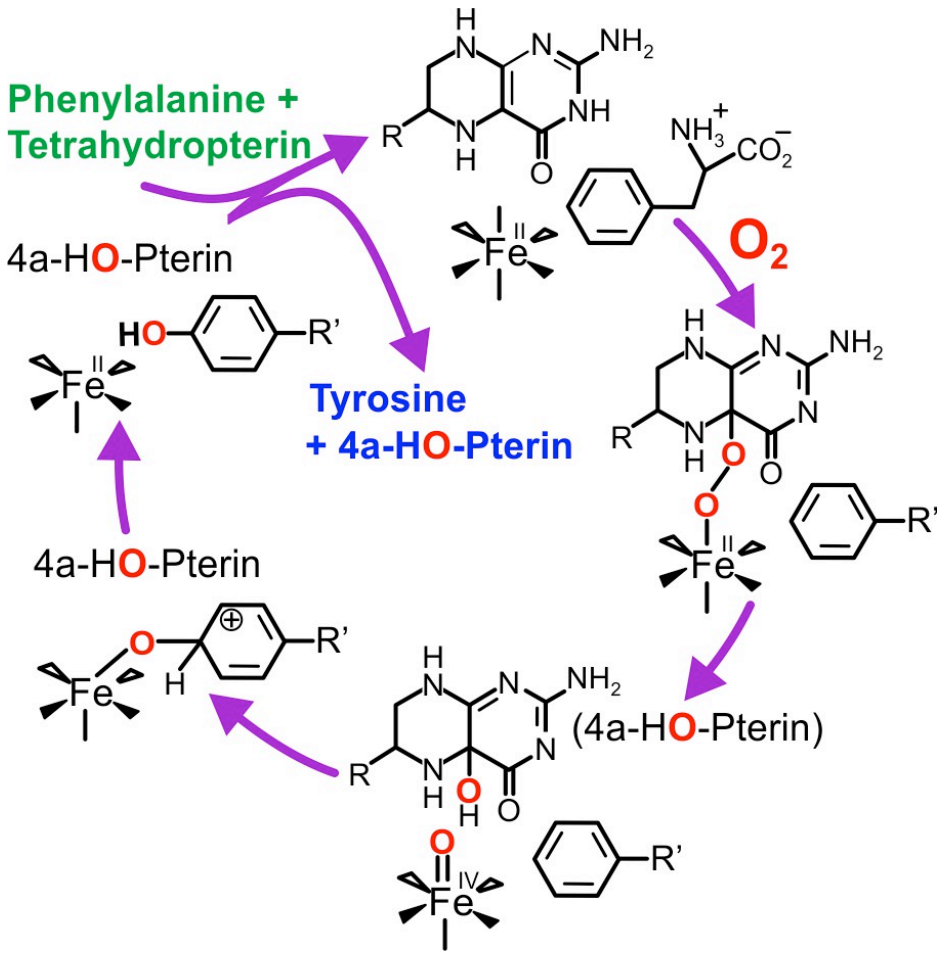

Figure 9: Proposed reaction cycle for tetrahydropterin-dependent oxygenases. The reaction cycle is illustrated for Phenylalanine Hydroxylase (*63*).

by nature as the reagent of choice to catalyze many types of difficult hydroxylation reactions (*43*). In fact, the 2-oxo acid and tetrahydropterin perform similar functions in their respective oxygenases by directly participating in the formation of an initial peroxo species and then supplying the two electrons required to ultimately form the common Fe(IV)=O reactive intermediate.

Related enzymes.

The mononuclear non-heme iron oxygenase subclasses discussed here form the majority of the general class. However there are numerous other enzymes that either employ iron to carry out oxygenase reactions using different strategies or activate O_2 for oxidase or related reactions using one of the mechanistic strategies just introduced. An example of the former class is the lipoxygenase family (*36*). The enzyme catalyzes incorporation of O_2 into polyunsaturated fatty acids in plants to generate chemicals involved in development and related processes, and into arachidonic acid in mammals to form various eicosanoids. In the resting state, these enzymes bind a non-heme Fe(II) via three His ligands, a carboxylate oxygen from a C-terminal isoleucine, a weakly associated Asn (plants) or His (mammals), and a solvent water. In contrast to the oxygenases described thus far, the O–O bond is not cleaved in the reaction. The enzyme is activated by oxidation of the resting Fe(II) to the Fe(III) state. This causes the solvent to become OH^-, which then serves to abstract a hydrogen atom from the 1,4-pentadiene moiety found in the substrates to yield a substrate radical and an Fe(II)-OH_2 complex. O_2 then directly attacks the substrate radical to form an hydroperoxy radical intermediate, which is reduced by reclaiming the hydrogen atom from the Fe(II)-OH_2 complex to regenerate the Fe(III)-OH^- state ready for another turnover.

Several non-heme Fe(II)-containing oxygenases have been identified that share the atypical 3-His Fe(II) ligation described above for DEK1 and the gentisate dioxygenases. For example, dioxygenases with this ligation have been shown to catalyze oxygen insertion reactions using cysteine, cysteamine, 4-

mercaptopropionate, acireductone and quercetin (*64, 65*). The mechanism proposed for each of these enzymes is generally similar to that of one of the major classes described above. It is clear from the initial studies that the mechanistic diversity of the 2-His + 1-Asp/Glu enzymes also applies to the new 3-His class of oxygenases.

Numerous biosynthetic or biodegradative oxidase enzymes are structurally and mechanistically more related to the non-heme oxygenase enzymes discussed here, than the familiar heme-dependent oxidases involved in bioenergetics as terminal electron acceptors. Some well studied examples of enzymes in this category are Isopenicillin N-synthase, Aminocyclopropane-1-Carboxylate Oxidase, (*S*)-2-Hydroxypropylphosphonic Acid Epoxidase, and CytC3 Halogenase (*43, 57, 66*).

Research directions.

Research in the mononuclear non-heme iron oxygenase field continues to expand rapidly due in part to the ability to recognize these enzymes in the ever-growing data base of genome sequences. Although they were initially recognized in bacteria and soon thereafter in mammals, the true extent of their pervasive and diverse roles in the metabolism of all aerobic organisms has only recently been fully appreciated. Future directions in this field will likely involve both identification of more members of this large family and in depth investigations of the molecular mechanisms of O_2 activation and insertion. To date, key aspects of the O_2-activation and insertion process remain debatable for various oxygenase enzymes (*67*) (*68*). For example, a reactive Fe(III)-O_2 radical from a native mononuclear non-heme Fe(II) oxygenase or oxidase enzyme is yet to be characterized, but this species is often invoked in corresponding reaction mechanisms (*67*). Also, the effects of protonation states and metal spin state for reactivity of Fe(III)-O_2 radical, Fe(III)-peroxo, and Fe(IV)=O intermediates from this family of enzymes and the heme counterparts are yet to be described in full detail (*43, 69*). These detailed mechanistic questions still need to be addressed. On the other hand, identification of new enzymes belonging to known

mononuclear nonheme enzyme subfamilies could lead to discovery of unrecognized metabolic roles, such as the recently described demethylation reactions of DNA (*70*) as well as new metal site environments. The search for new approaches to detect, capture, and chemically and structurally characterize intermediates is likely to allow rapid advances in mechanistic theory. Moreover, the characterization of intermediates will advance the application of correlated computational techniques to allow an understanding of the activation of O_2 at a level significantly beyond what is now possible.

Research directions for 2,3-HPCD.

In recent years, there have been major advances in mechanistic studies with extradiol dioxygenases due to new x-ray crystallography procedures (*50, 71*). The new procedures have resulted in ample evidence in support of several reaction intermediates from the proposed extradiol dioxygenase mechanism (*21*). For example, SQ-Fe(II)-O_2 radical, alkylperoxo, and gemdiol reaction intermediates have been trapped "*in-crystallo*" and their structures solved ($FeHPCD_{Int1}{}^{4NC}$, $FeHPCD_{Int2}{}^{4NC}$, and $E323L_{gem}{}^{4SC}$, respectively, Figure 10 A - C) (*50, 71*). Solving of these structures provided a major leap in mechanistic studies of extradiol dioxygenases, reinforcing key aspects of the proposed mechanism (*28*). The structure of $FeHPCD_{Int1}{}^{4NC}$ revealed a mode of O_2 and substrate binding/activation which does not require a change in the metal oxidation state (*50*). Based on the short O-O bond, long O_2 - Fe bonds, and partial sp^3 hybridization on C2 on the 4NC substrate, this reaction intermediate was proposed to be a SQ- Fe(II)-O_2 radical complex (Figure 10 A). The two radicals are positioned for a postulated radical recombination event which would result in formation of the alkyl peroxo ($FeHPCD_{Int2}{}^{4NC}$) adduct at 4NC C2 (Figure 10 B). The alkylperoxo adduct has long been proposed as a key reaction intermediate which precedes scission of the O-O bond in the written mechanism (*72*). Lastly, the structure of $E323L_{gem}{}^{4SC}$ gave experimental support

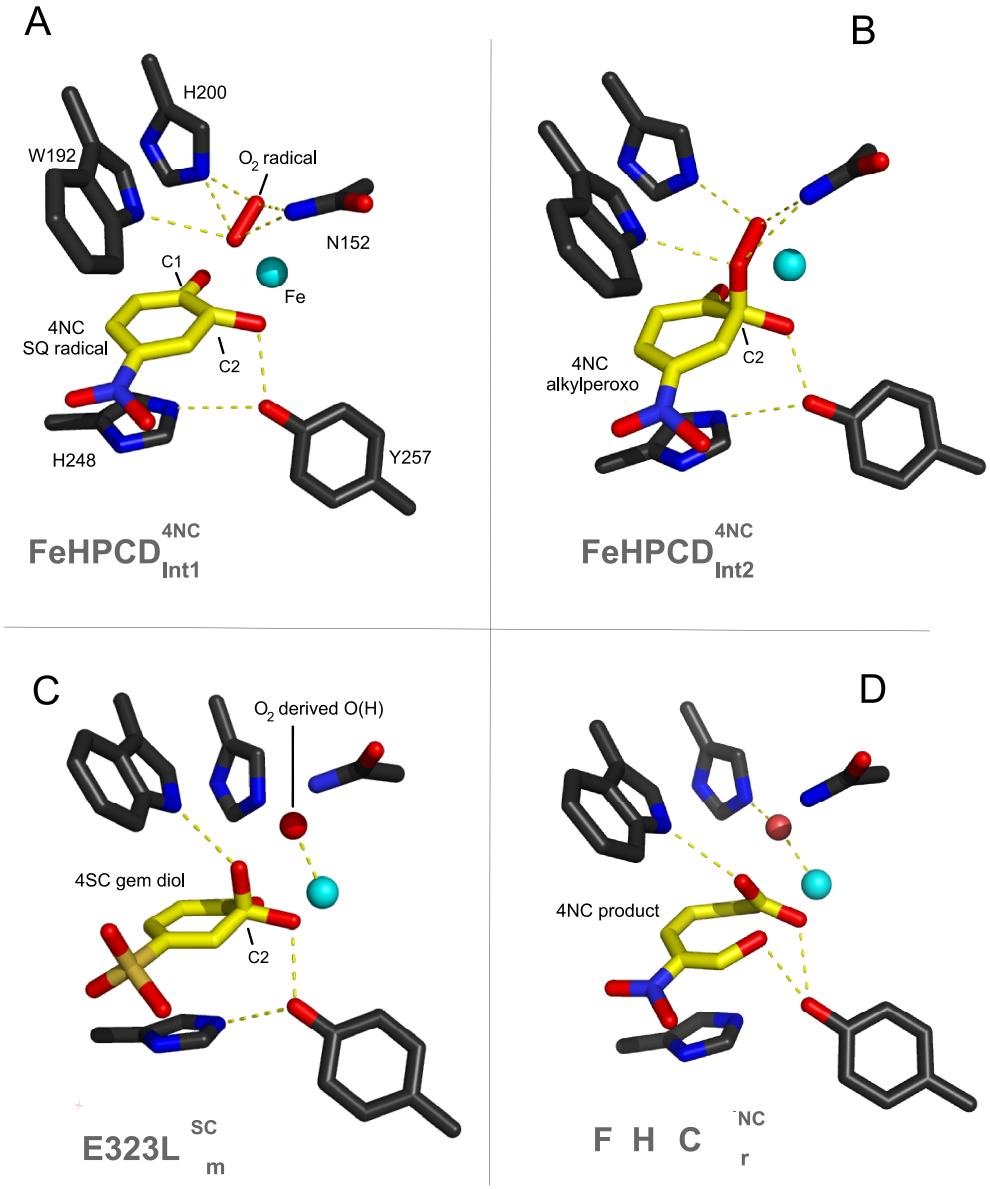

Figure 10: Intermediates observed *in-crystallo* for FeHPCD and its variants. A) $FeHPCD_{Int1}^{4NC}$, oxy complex from the FeHPCD-4NC + O_2 reaction. This reaction intermediate is proposed to have a SQ-Fe(II)-O_2 radical electronic structure. B) $FeHPCD_{Int2}^{4NC}$, the alkylperoxo reaction intermediate from the FeHPCD-4NC + O_2 reaction. C) $E323L_{gem}^{4SC}$, gemdiol reaction intermediate from the E323L-4SC + O_2 reaction. Computational studies suggest this species has unpaired spin density on the gemdiol adduct and the Fe (*73*). D) $FeHPCD_{prod}^{4NC}$, product complex from the FeHPCD-4NC + O_2 reaction.

for a gemdiol type of reaction intermediate, a species which was proposed based on DFT calculations to occur after scission of the O-O bond of the alkylperoxo (Figure 10 C) (*71*). The *in-crystallo* results have given strong evidence for the proposed mechanism up to product formation (Figure 10 A, B and D), leaving only a structure of the lactone reaction intermediate unsolved (see Figure 5 for proposed lactone reaction intermediate). Evidence for the lactone reaction intermediate comes from DFT calculations and experiments that have shown extradiol dioxygenases can hydrolyze lactones to yield the appropriate ring-cleaved product (*73, 74*). However, this intermediate is yet to be trapped and characterized directly. Also, definitive evidence for a O_2 radical or a SQ radical species during the extradiol ring-cleaving reaction of FeHPCD in solution is missing, although, in-solution precedence for a SQ radical in the extradiol ring cleaving reaction is available from radical trap experiments (*75*).

Even though key tenets of the extradiol mechanism have been established by theoretical calculations and experimental results, some aspects of the established mechanism are controversial whereas others, such as the lactone reaction intermediate, are yet to be observed. In addition, key aspects of the reaction mechanism such as protonation states of $FeHPCD_{Int1}{}^{4NC}$, $FeHPCD_{Int2}{}^{4NC}$, and $E323L_{gem}{}^{4SC}$ reaction intermediates remain unexplored and the overall electronic distribution in $FeHPCD_{Int1}{}^{4NC}$ and $E323L_{gem}{}^{4SC}$ are controversial (*76, 77*) .

Perhaps the central controversy regarding the electronic distribution of reaction intermediates revolves around the question of whether the metal ion is redox active during catalysis. It has long been suspected that various mononuclear iron dependent oxygenases and oxidases, including enzymes which utilize the 2-His + 1-Asp/Glu Fe binding motif, activate O_2 by first forming a short-lived Fe(III)-O_2 radical species (*67*). However, the proposed SQ-Fe(II)-O_2 radical electronic structure from $FeHPCD_{Int1}{}^{4NC}$ obviates the need for a reactive Fe(III)-O_2 radical species during substrate activation, ring-attack/oxygen insertion steps, leaving open the question of whether such as species can be observed during the early O_2 activation steps. For 2,3-HPCD, it has been argued that an

Fe(III)-O_2 radical intermediate seems unlikely based on insightful steady-state kinetic experiments with MnHPCD and FeHPCD (*78*). These studies revealed MnHPCD and FeHPCD to have comparable k_{cat} and $k_{cat}/K_m^{O_2}$ values for the ring-cleaving reaction with HPCA and O_2 substrates despite the presumed 0.7 V difference in Mn and Fe metal redox potentials (*78*). These results provide an indirect argument against a redox active metal center during the extradiol ring cleaving reaction because no structural support for metal redox tuning could be discerned (*28*). In the absence of redox tuning by the enzyme environment, comparable k_{cat} values for MnHPCD and FeHPCD argue against a change in the metal redox state during the rate-limiting step, whereas comparable $k_{cat}/K_m^{O_2}$ values suggest similar activation barriers up through the first irreversible step, therefore, arguing against a redox active metal during O_2 activation/insertion steps (*78*). Regardless, freeze-quench studies with MnHPCD, and most recently, CoHPCD have provided experimental evidence for transient Mn/Co(III)-O_2 superoxo intermediates as precursors for extradiol ring-cleaving chemistry (*79*) (*80*). These studies along with DFT calculations have provided arguments for a redox active metal center during the extradiol ring-cleaving reaction (*79, 80*), opening debate regarding the occurrence of a Fe(III)-O_2 radical species in the FeHPCD reaction cycle.

In an effort to address some of the controversial mechanistic aspects regarding extradiol dioxygenases, the contents of this thesis report methods to enrich ^{57}Fe into the active site of FeHPCD and also new RFQ protocols for freeze-trapping of reaction intermediates to study their electronic structure using EPR and Mössbauer spectroscopies (*81*) (*52*). In addition, methods for using $^{17}O_2$ as a probe for electronic structure of paramagnetic freeze-trapped oxy complexes are described in addition to synthetic methods for selective labeling of HPCA with the ^{17}O isotope. These efforts were largely successful, resulting in the first studies reporting detailed electronic structures of reaction intermediates from native FeHPCD and its variants.

CHAPTER 1

Trapping and spectroscopic characterization of an Fe(III)-superoxo intermediate from a non-heme mononuclear iron-containing enzyme.

Note: This chapter is reprinted (adapted) with permission from Mbughuni, M. M., Chakrabarti, M., Hayden, J. A., Bominaar, E. L., Hendrich, M. P., Münck, E., and Lipscomb, J. D. (2010) Trapping and spectroscopic characterization of an Fe(III)-superoxo intermediate from a nonheme mononuclear iron-containing enzyme, Proc Natl Acad Sci U S A 107, 16788-16793. Copyright (2010) PNAS."

Abbreviations:

FeHPCD, Fe dependent Homoprotocatechuate 2,3-Dioxygenase.

H200N, His to Asn variant of FeHPCD at position 200.

HPCA, homoprotocatechuate or 3,4 dihydroxyphenylacetate.

$H200N_{Int1}^{4NC}$, the high-spin 4NC-Fe(III)-superoxo complex of H200N.

4NC, 4-nitrocatechol; WT, wild type

$H200N_{Int2}^{4NC}$, the high-spin 4NC $SQ^{\cdot}$-Fe(III)-(hydro)peroxo complex of H200N.

ICP-OES, Inductively Coupled Plasma - Optical Emission Spectrometry.

RFQ, Rapid Freeze Quench.

MB, Mössbauer spectroscopy.

AF, Anti-ferromagnetic.

SUMMARY

Fe(III)-$O_2^{\bullet-}$ intermediates are well known in heme enzymes, but none have been characterized in the non-heme mononuclear Fe(II) enzyme family. Many steps in the O_2 activation and reaction cycle of Fe(II)-containing 2,3-HPCD are made detectable by using the alternative substrate 4NC and mutation of the active site H200N. Here, the first intermediate ($H200N_{Int1}{}^{4NC)}$ observed after adding O_2 to the H200N-4NC complex is trapped and characterized using EPR and Mössbauer (MB) spectroscopies. $H200N_{Int1}{}^{4NC}$ is a high-spin (S_1 = 5/2) Fe(III) antiferromagnetically (AF) coupled to an S_2 = ½ radical ($J \approx 6$ cm^{-1} in H = $JS_1 \bullet S_2$). It exhibits parallel-mode EPR signals at g = 8.17 from the S = 2 multiplet, and g = 8.8 and 11.6 from the S = 3 multiplet. These signals are broadened significantly by $^{17}O_2$ hyperfine interactions ($A_{17O} \approx 180$ MHz). Thus, $H200N_{Int1}{}^{4NC}$ is an AF-coupled Fe(III)-$O_2^{\bullet-}$ species. The experimental observations are supported by density functional theory calculations that show nearly complete transfer of spin density to the bound O_2. $H200N_{Int1}{}^{4NC}$ decays to form a second intermediate ($H200N_{Int2}{}^{4NC}$). MB spectra show that it is also an AF-coupled Fe(III)-radical complex. $H200N_{Int2}{}^{4NC}$ exhibits an EPR signal at g = 8.05 arising from an S = 2 state. The signal is only slightly broadened by $^{17}O_2$ (< 3% spin delocalization), suggesting that $H200N_{Int2}{}^{4NC}$ is a peroxo-Fe(III)-4NC semiquinone radical species. Our results demonstrate facile electron transfer between Fe(II), O_2, and the organic ligand, thereby supporting the proposed wildtype enzyme mechanism.

INTRODUCTION

Most mononuclear non-heme iron-containing oxidases and oxygenases are proposed to initiate their oxygen activation cycles by binding O_2 to an active site Fe(II) (see introduction) (*13, 59, 82-87*). Internal electron transfer to form an Fe(III)-superoxo species converts the kinetically inert triplet ground state of O_2 to a doublet that can participate in the many types of chemistry characteristic of this mechanistically diverse group of enzymes. The same strategy is usually employed by heme-containing oxygenases and oxidases, leading in some cases to comparatively stable Fe(III)-superoxo intermediates that have been structurally and spectroscopically characterized (*88-91*). Instability of the putative superoxo intermediate in all mononuclear non-heme iron-containing enzymes has prevented similar characterization, although a superoxide level species has been reported for the dinuclear iron site of *myo*-inositol oxygenase (*92*).

In past studies of the Fe(II)-containing 2,3-HPCD, we have shown that 3 intermediates of the catalytic cycle can be trapped in one crystal for structural analysis (*50*). One of these intermediates has been proposed to be an Fe(II)-superoxo species based on the long Fe-O bond distances and an unexpected lack of planarity of the aromatic ring of the alternative substrate 4NC, which chelates the iron in ligand sites adjacent to that of the O_2 (Figure 10 A). In accord with the mechanism postulated for this enzyme class as shown on Figure 11 (*13, 28, 34, 73, 82, 93-96*), it has been proposed that net electron transfer from 4NC through the Fe(II) to O_2 forms adjacent substrate and oxygen radicals (Figure 11 B). Recombination of the radicals would begin the ring cleavage and oxygen insertion reactions of this enzyme that eventually yield a muconic semialdehyde adduct as the product. A localized radical on the 4NC semiquinone at the insipient position of oxygen attack would account for the lack of ring planarity. While this is the only structurally characterized non-heme Fe-superoxo species, the iron oxidation state differs from all of the other postulated Fe-superoxo intermediates.

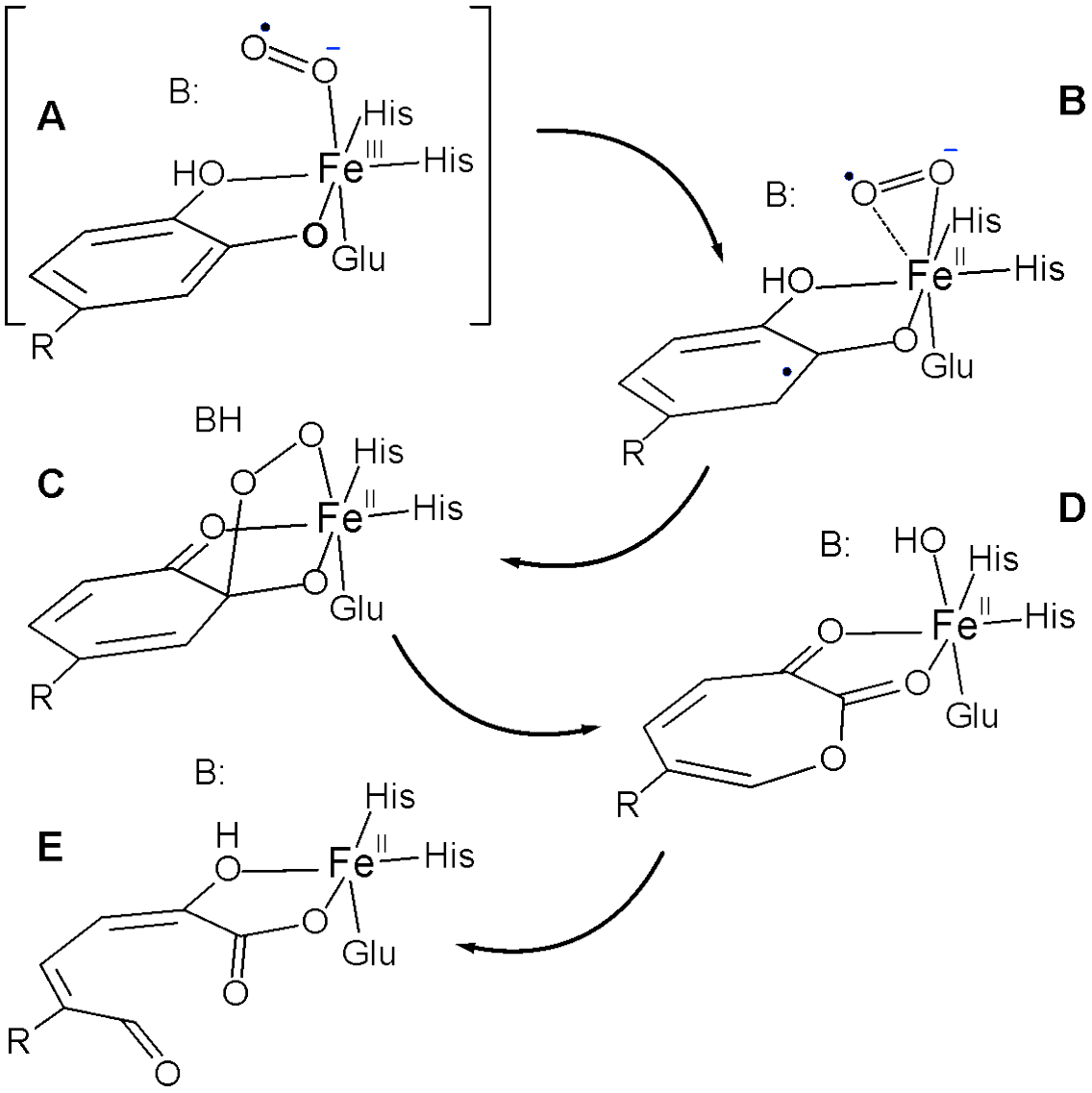

Figure 11: Proposed superoxo complex in mechanism for extradiol dioxygenases. In the case of 2,3-HPCD, R is $–CH_2COO-$ and B is His200. When R is $–NO_2$ and His200 is changed to Asn, the reaction stalls before reaching intermediate C. Peroxide is slowly released and the product is 4NC quinone.

The mechanism that emerges from the structural and kinetic studies does not require a change in metal oxidation state to form a reactive intermediate (*78*). However, studies with 2,3-HPCD in which Fe(II) is replaced with Mn(II) suggest that transient formation of an oxidized metal center may occur (*79*). The Mn(II)-replaced enzyme is fully active and has no detectible change in structure. Our studies showed that upon addition of O_2 to the enzyme complexed with the normal substrate (HPCA), an intermediate is formed with a lifetime of a few milliseconds. The EPR characteristics of this intermediate are consistent with a Mn(III)-superoxo formulation. This observation suggests that a similar intermediate might exist in the native enzyme as a transient Fe(III)-superoxo species (Figure 11 A).

RFQ studies of the WT 2,3-HPCD with HPCA as a substrate and the native Fe(II) in the active site have not revealed accumulation of an Fe(III)-superoxo species that can be detected by EPR or Mössbauer experiments (see Chapter 2). This suggests that if such a species is formed, it is very short lived, so a strategy to slow the reaction is required to detect the putative ferric-superoxo intermediate. Two methods have been described to slow the oxygen activation and substrate attack portions of the reaction cycle. The first is to use an alternative substrate with electron withdrawing substituents, such as 4NC (*95*). The second is to change the key active site acid-base catalyst and hydrogen bonding residue His200 (Figure 10) to an Asn residue (H200N) (*96*). Using either one of these strategies results in a slow reaction that gives the expected ring cleaved product at the end of the cycle. When both strategies are used simultaneously, the reaction slows further and the 4NC aromatic ring is not opened; rather, it is converted to 4NC quinone and H_2O_2 is released (*96*). Independent of whether ring cleavage (with HPCA) or ring oxidation (with 4NC) is catalyzed by H200N, oxy complexes which result from O_2 binding to the anaerobic substrate complexes are observed. The rate constants for the formation of these intermediates depend linearly on the O_2 concentration (*96*). It is shown here that this species is the initial oxy intermediate, the elusive Fe(III)-superoxo species of the mononuclear non-heme iron oxidase/oxygenase family.

The transient kinetic, EPR, and Mössbauer studies reported here will support assignment of this electronic structure.

MATERIALS AND METHODS

Reagents.

Casamino acids low in salts and iron were purchased from Benton Dickinson Inc. Yeast Extract was purchased from Biochemika Fluka. Sulfuric acid was purchased from Mallinckrodt. ^{57}Fe was purchased from Cambridge Isotopes at 95.5% purity. ^{57}Fe solution is prepared by dissolving 180 mg/ml ^{57}Fe in 9 M H_2SO_4. This solution is diluted 20x with diH_2O to a concentration of 9 mg/ml ^{57}Fe and 0.45 M H_2SO_4 for storage and use in growth media. Argon for preparing anaerobic samples was purchased from Praxair (≥ 99.99% pure, 6.0 research grade Ar). Trace contaminating O_2 was removed from the Argon gas by passage over an Agilent oxygen scrubber. 4NC was purchased from Sigma-Aldrich and re-crystallized before use as previously described (*95*). All other chemicals were purchased from Sigma-Aldrich and used with no further purification.

Over expression of the H200 variant, purification and ^{57}Fe incorporation.

The H200N variant of recombinant 2,3-HPCD from *Brevibacterium fuscum* was expressed and purified as previously described (*97, 98*). For enrichment of ^{57}Fe in 2,3-HPCD, a media composed of 24 g/L casamino acids, 8 g/L yeast extract, 9.4 g/L K_2HPO_4, and 2.2 g/L KH_2PO_4 was used. The cultures were grown at 37 ºC to an optical density of 1 at 600 nm in 1 L shaker flasks, then supplemented with 9 mg/L ^{57}Fe and induced with 280 μM IPTG for 4 h at 25 °C.

Preparation of fully reduced 2,3-HPCD.

Purified 2,3-HPCD was made anaerobic by mild stirring under argon at 4 ºC then transferred to a Coy anaerobic glovebox. The sample was reduced with 1.5 eq of $Na_2S_2O_4$ (sodium dithionite) at 25 ºC for ~30 min. Excess sodium dithionite was removed from the sample by passage through a Sephadex G-25 PD-10 column pre-equilibrated with anaerobic 200 mM MOPS buffer at pH 7.5. This procedure increased the specific activity, but the reaction cycle rate constants

were unchanged. Metals analysis of the sodium dithionite reduced enzyme revealed the reduced 2,3-HPCD picks up ~ 45 eq of sodium/enzyme. Binding of Na^+ from $Na_2S_2O_4$ is consistent with 2,3-HPCD being negatively charged and eluting from DEAE resin at ~ 250mM NaCl. Also, when 2,3-HPCD is incubated with > 2 eq of sodium dithionite for longer than 60 min, a “black band” of an iron precipitate was left behind after the enzyme is passed through a Sephadex G-25 PD-10 column. This black precipitate is most likely a dithionite Fe chelate. As such, it is very important to limit how long the enzyme incubates with excess $Na_2S_2O_4$, because the Na^+ will bind to the surface of the enzyme, leaving dithionite in solution. Since dithionite is a known Fe(II)/Fe(III) chelator, it is not surprising that a black Fe precipitate is observed following desalting of the reduced enzyme via a PD-10 column (observed only when the enzyme is incubated anaerobically for >60 min with >1.5 eq sodium dithionite).

Rapid freeze quench (RFQ) methods.

H200N-4NC anaerobic complex was prepared in the glovebox by mixing 1 eq of H200N with 1 or 2 eq of 4NC, as specified. RFQ syringes were loaded inside the anaerobic glovebox and then transferred to an Update Instrument model 1019 RFQ apparatus and allowed to equilibrate for 30 min at 4 °C. After rapid mixing and passage through a calibrated delay line, samples were collected by rapid freezing on counter-rotating aluminum wheels at Liq N_2 temperature. For samples at times >6 s, the mixed sample was collected directly in an EPR tube or Mössbauer cup and frozen in a dry ice/methanol bath (EPR) or Liq N_2 (Mössbauer) after the appropriate incubation time. For anaerobic aging of Mössbauer samples <100s, the sample was dispensed into a Mössbauer cup inside of an anaerobic vial pre-equilibrated at 4 °C. The vial and sample were then frozen in Liq N_2 at the appropriate time.

Enzyme and metal quantification.

Protein concentration was determined using absorbance at 280 nm (1.2 mg/ml/cm^{-1}) as previously described (*98*). Metal quantification was determined by Inductively Coupled Plasma – Optical Emission Spectroscopy (ICP-OES) using a Thermo Scientific iCAP 6500 dual view ICP-OES. ^{57}Fe concentrations were estimated via Mössbauer spectroscopy. ICP-OES samples are prepared by release of the iron with 18 % nitric acid following removal of the precipitated enzyme by centrifugation. 2,3-HPCD was routinely purified with iron occupancy of 85-95 %; the main contaminant is Mn at <7% occupancy. ^{57}Fe occupancy was determined to be 80-95 % by comparing protein concentrations to Mössbauer quantifications for the total iron in ^{57}Fe-enriched 2,3-HPCD from several different 2,3-HPCD preparations.

Spectroscopy.

EPR spectra were collected using a Bruker Elexsys E-500 or Bruker ESP 300 spectrometers equipped with Bruker dual mode cavities and Oxford ESR 910 liquid helium cryostats. Spectra were analyzed using the software package SpinCount (M.P. Hendrich, Carnegie Mellon University). Signal quantification was relative to a Cu(II) EDTA or Fe(III) EDTA spin standard using SpinCount. Absorption spectra were collected using an Applied Photophysics model SX.18.MV stopped-flow spectrometer fitted with a diode array detector or a Hewlett-Packard 8453 diode array spectrophotometer. Mössbauer spectroscopy was performed as previously described (*99*). Spectra were analyzed using the software WMOSS (SEE Co, Edina, MN, USA).

DFT calculation.

The DFT calculations were performed with Gaussian '03 [Revision E.01] (S4) using the hybrid functional B3LYP and basis set 6-311G. The computational structure includes the iron and its ligands (dioxygen, 4NC, Glu267, His155, and His214) and second coordination sphere residues (Asn157, Trp192, Asn200, and Tyr257). The atom positions of the dioxygen and the 4NC were

optimized; the remaining atoms were positioned on the basis of the wild type 2,3-HPCD-4NC structure (PDB code 2IGA subunit C). Residue His200 was changed to Asn and optimized using COOT (S5). A planar 4NC aromatic ring and end-on bound dioxygen were modeled as the starting point for computations.

RESULTS

Absorption spectra show that an intermediate precedes substrate oxidation.

The stoichiometric H200N-4NC complex exhibits an absorption spectrum characteristic of the dianionic form of 4NC at 518 nm. Mixing this complex with 1 eq of O_2 causes a shift to 506 nm within 25 ms at 4 °C showing that an intermediate ($H200N_{Int1}^{4NC}$) is formed (Figure 12) (*95, 96*). The small magnitude of the shift suggests that 4NC is still in the aromatic, dianion form. $H200N_{Int1}^{4NC}$ decays over a period of > 200 s, to form an intermediate with an absorption spectrum maximizing at 405 nm ($H200N_{Int2}^{4NC}$) (Figure 12). This spectrum is characteristic of bound 4NC quinone product complex (*96*). 4NC quinone is more tightly bound than the ring-cleaved product derived from the reaction of 4NC with the WT enzyme such that complete dissociation to form the resting enzyme requires hours. The released quinone product has a λ_{max} at 380 nm, suggesting that an alternative form of the quinone is bound in $H200N_{Int2}^{4NC}$.

$H200N_{Int1}^{4NC}$ and $H200N_{Int2}^{4NC}$ exhibit EPR signals from S_1 = 5/2 Fe(III) that is antiferromagnetically coupled to S_2 = 1/2 species.

The anaerobic Fe(II) H200N-4NC complex shows EPR signals from minor *S* = 5/2 contaminants of Fe(III) and Mn(II) with *g*-values near 4.27 (0.05 spins/subunit) and 2 (< 0.07 spins/subunit), respectively (Figure 13 A). Figure 13 D and 14 A and B show EPR spectra recorded in parallel mode for a sample frozen 10 s after the anaerobic H200N-4NC complex was rapidly mixed with 1 eq of O_2 at 4 °C. This sample exhibits a pronounced new spectrum ($H200N_{Int1}^{4NC}$) with integer-spin resonances at *g* = 8.17, 8.8, and 11.6, which are observed in maximum yield in RFQ experiments at the earliest time point collected (32 ms) (Figure 15). $H200N_{Int1}^{4NC}$ decays very slowly (k = 0.015 s^{-1}, Figure 15, inset) to yield a long lived intermediate ($H200N_{Int2}^{4NC}$), which exhibits, also in parallel mode, a new EPR signal at *g* = 8.05 (Figure 13 F and 14 D).

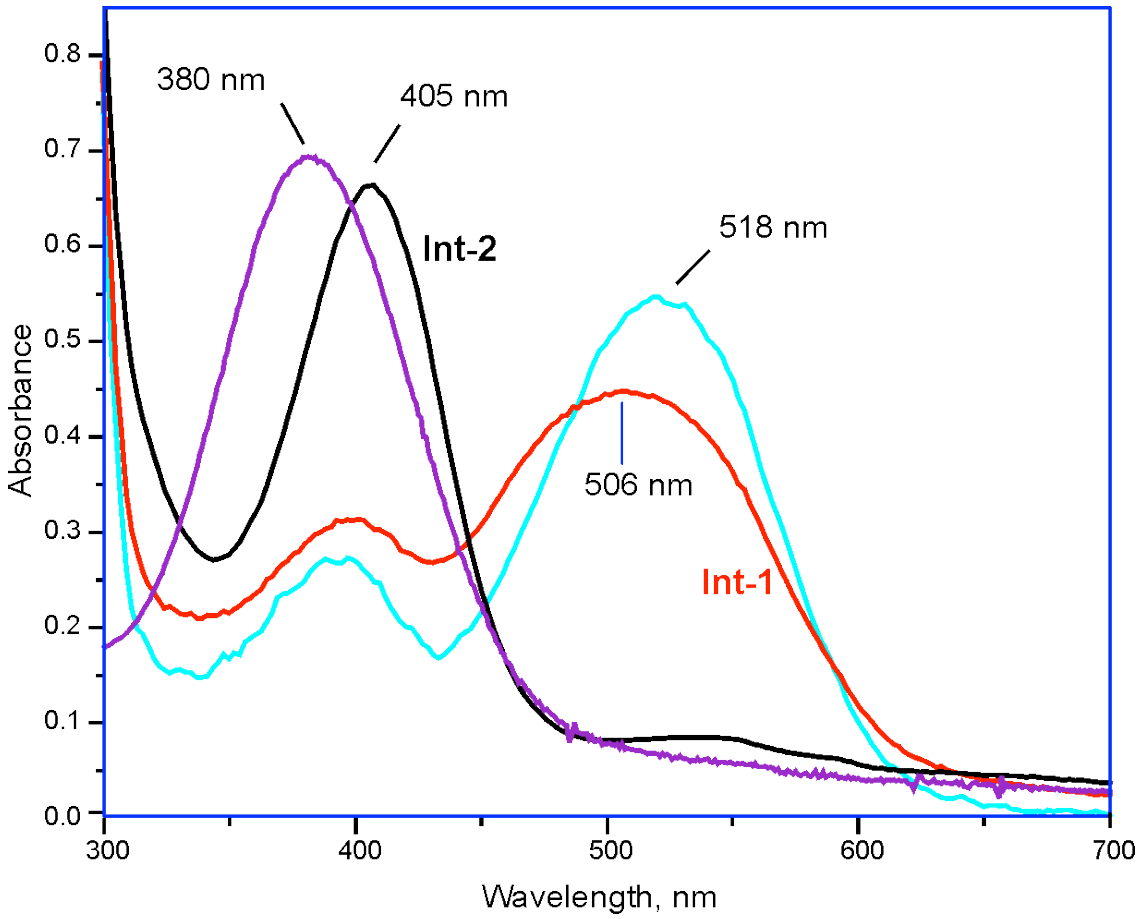

Figure 12: Absorption spectra (path length 0.2 cm). Blue: The anaerobic H200N-4NC complex. Red: $H200N_{Int1}{}^{4NC}$ 10 s after mixing H200N-4NC complex with O_2 saturated buffer at 4 °C. Black: $H200N_{Int2}{}^{4NC}$, 10 min after mixing. Maroon: Released product purified from the end complex. The product was isolated using a G25 PD10 column after denaturing the enzyme with 7 M Urea. The relative absorbance of the isolated product is approximate on this figure. Reaction conditions prior to mixing: 400 μM H200N-4NC, 200 mM MOPS buffer, pH 7.5. Abbreviations: Int-1 = $H200N_{Int1}{}^{4NC}$ and Int-2 = $H200N_{Int1}{}^{4NC}$.

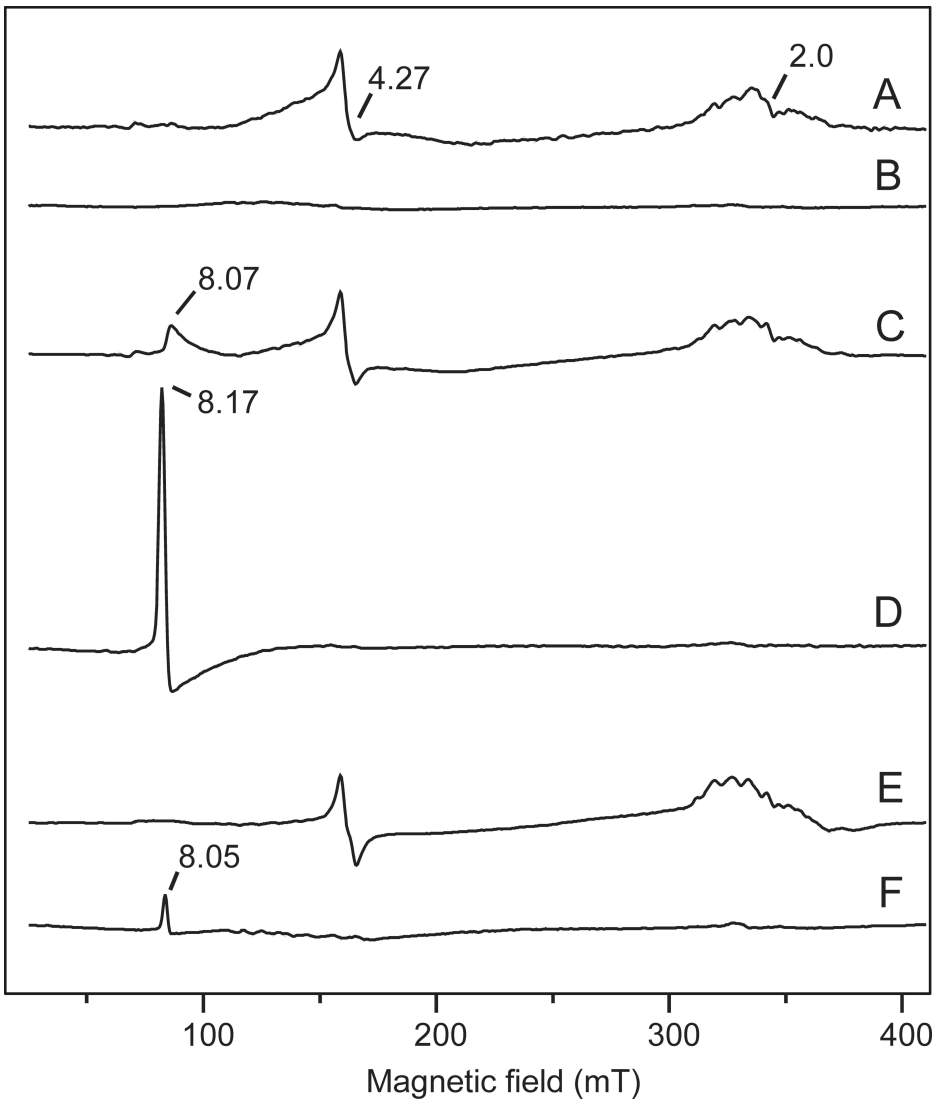

Figure 13: EPR spectra of reaction intermediates from H200N-4NC + O_2 reaction. Anaerobic H200N-4NC complex, (A) perpendicular mode spectrum and (B) parallel mode spectrum; 10 s after mixing H200N-4NC complex with O_2 at 4 °C, (C) perpendicular mode spectrum and (D) parallel mode spectrum; End complex, (E) perpendicular mode spectra and (F) parallel mode spectra. Conditions prior to mixing: 1.64 mM H200N-4NC, 200 mM MOPS buffer pH 7.5. EPR measurement conditions: Frequency = 9.65 GHz (A, C, E) or 9.35 GHz (all others), microwave power = 4 mW, Temp = 2 K, modulation amplitude = 10 G. The *g*-values of resonances are marked on the figure.

The EPR spectra of $H200N_{Int1}{}^{4NC}$ over a range of temperatures (spectra at 2K and 9K are shown in Fig. 14 A and B) show that the g = 8.17 resonance originates from a ground doublet, and the g = 8.8 and 11.6 resonances from excited states. The Mössbauer spectra, shown below (Figure 18), reveal that the iron in both $H200N_{Int1}{}^{4NC}$ and $H200N_{Int2}{}^{4NC}$ is high-spin (S_1=5/2) Fe(III). Figure 14 B shows a simulation of the $H200N_{Int1}{}^{4NC}$ spectrum for an S_1 = 5/2 center antiferromagnetically (AF) coupled to an S_2 = ½ center, using the spin Hamiltonian of Equation (Eq.) 1 for the parameters given in the caption and Table 1.

$$\mathcal{H}_e = J\mathbf{S_1}\bullet\mathbf{S_2} + D_1[S^2_{1z} - 35/12 + (E/D)_1\,(S^2_{1x} - S^2_{1y})] \qquad [1]$$

$$+ \beta(\mathbf{S_1}\bullet\mathbf{g_1} + \mathbf{S_2}\bullet\mathbf{g_2})\bullet\mathbf{B}$$

$$+ [\mu_0\beta/(4\pi r^3)][(\mathbf{g_1}\bullet\mathbf{S_1})\cdot(\mathbf{g_2}\bullet\mathbf{S_2})$$

$$+ 3(\mathbf{g_1}\bullet\mathbf{S_1}\bullet\mathbf{r})(\mathbf{g_2}\bullet\mathbf{S_2}\bullet\mathbf{r})/(r^2)]$$

The exchange, zero-field splitting, Zeeman, and dipole-dipole terms have their common definitions. The simulation is quantitative, i. e. the signal intensities are correctly predicted by simulation for the protein concentration. The agreement unambiguously established the spin centers of $H200N_{Int1}{}^{4NC}$ as S_1 = 5/2 and S_2 = ½, and determines J = +6 cm^{-1}. The energy of the exchange interaction is larger than the zero-field splitting energy, and consequently the spin system approximates isolated S = 2 and 3 multiplets (see energy diagram Figure 16). The EPR resonances are from the transitions indicated in the diagram. Subtle shifts from the expected positions of these transitions (g = 8 and 12) require the introduction of dipole-dipole interaction between the two spin centers with a distance of ≈ 0.3 nm.

The parallel mode EPR spectrum of $H200N_{Int2}{}^{4NC}$ is distinctly different from that of $H200N_{Int1}{}^{4NC}$. Specifically, the g = 11.6 and 8.8 features are not present,

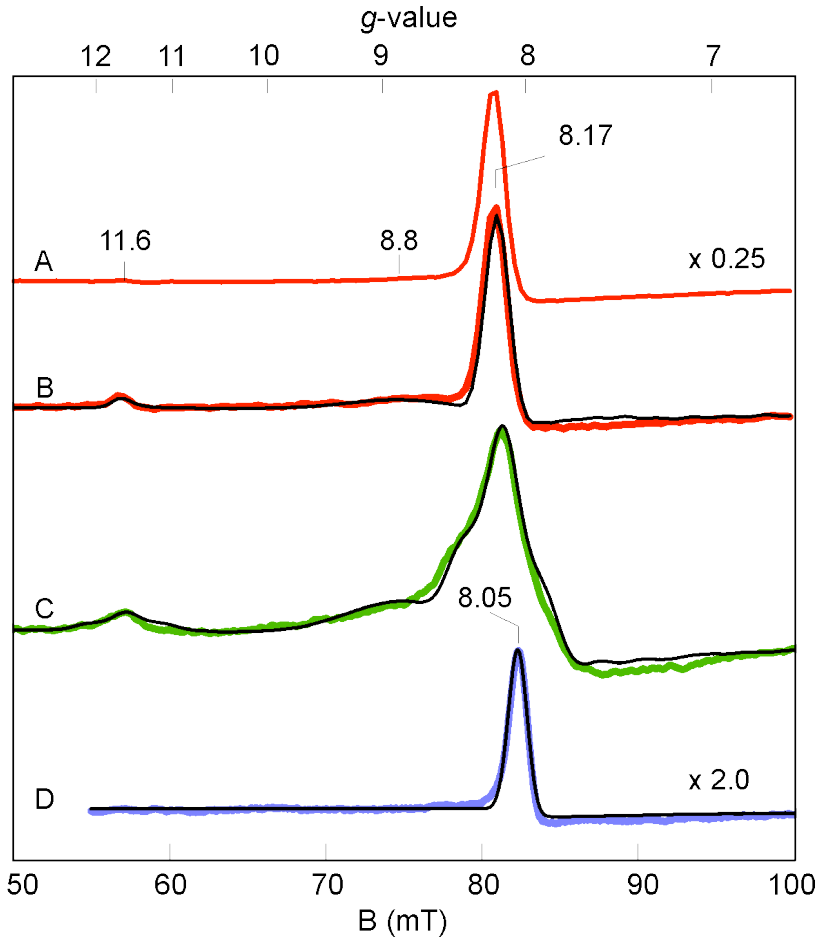

Figure 14: Parallel-mode EPR spectra of $H200N_{Int1}{}^{4NC}$ and $H200N_{Int2}{}^{4NC}$ (colored lines) and simulations (thin black lines). (A) 2 K spectrum 10 s after mixing H200N-4NC complex with O_2 saturated buffer at 4 °C. (B) Sample of A at 9 K. (C) Spectrum at 10 K for a sample prepared as in A but with 70% enriched $^{17}O_2$. (D) Sample from A at 9 K after 10 min incubation at 4 °C. Conditions prior to mixing: 1.64 mM H200N-4NC, 200 mM MOPS buffer pH 7.5. Simulation parameters: B: S_1=5/2, S_2= ½, J = +6 cm^{-1}, D_1 = -0.48 cm^{-1}, E/D_1 = 0.20, g_1 = 2.01, g_2 = (2.02, 1.98, 2.04), r = 0.29 nm, r_θ=90° , r_φ= 55°. C: same as B but with $A17_O$ = 180 MHz (I = 5/2). D: S_1=5/2, S_2= ½, J = +40 cm^{-1}, D_1 = +0.5 cm^{-1}, E/D_1 = 0.13, g_1 = 2.01, g_2 = 2.00. EPR conditions: frequency, 9.24 GHz, power, 20 mW, modulation amplitude, 10 G.

Table 1: Electronic and nuclear parameters of $H200N_{Int1}^{4NC}$ and $H200N_{Int1}^{4NC}$ obtained from EPR (italics) and Mössbauer spectroscopy.

Species	J (cm^{-1})	D_1 (cm^{-1})	$(E/D)_1$	$g_n\beta_n$ (T)	ΔE_Q (mm/s)	η	δ (mm/s)
Int-1	*+6(2)**	-0.59 *-0.48*	0.20 *0.20*	-21.4(2)	-0.33(2)	-3	0.50(1)
Int-2	*+40(10)*	+0.67 *+0.50*	0.11 *0.13*	-21.5(2)	0.87(2)	-7.2	0.49(1)

*Numbers in parentheses give estimate of uncertainty. **Abbreviations:** Int-1 = $H200N_{Int1}^{4N}$ and Int-2 = $H200N_{Int1}^{4N}$.

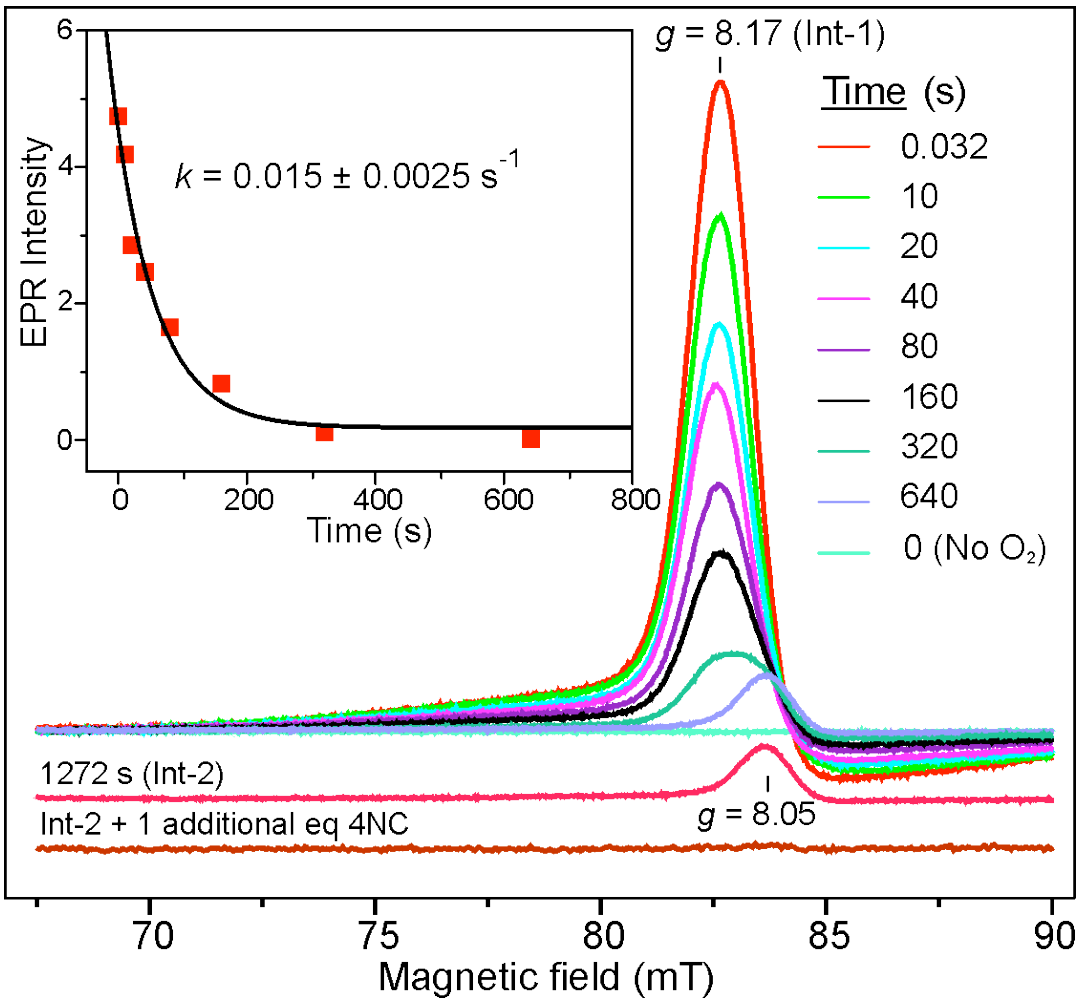

Figure 15: Time dependence of $H200N_{Int1}^{4NC}$ EPR signal decay. Parallel mode EPR spectra of the *g* = 8 region for samples frozen at the indicated times after mixing anaerobic 1.7 mM stoichiometric H200N-4NC complex with buffer containing 1 eq of O_2 at 4 °C in MOPS buffer pH 7.5. The bottom trace is the result of including 2 eq of 4NC and incubating anaerobically for 1.5 h at 25 °C. Inset: Exponential fit to the decay of the EPR signal. EPR conditions: frequency 9.35 GHz microwave power, 1 mW, modulation amplitude, 10 G, temperature 2 K.

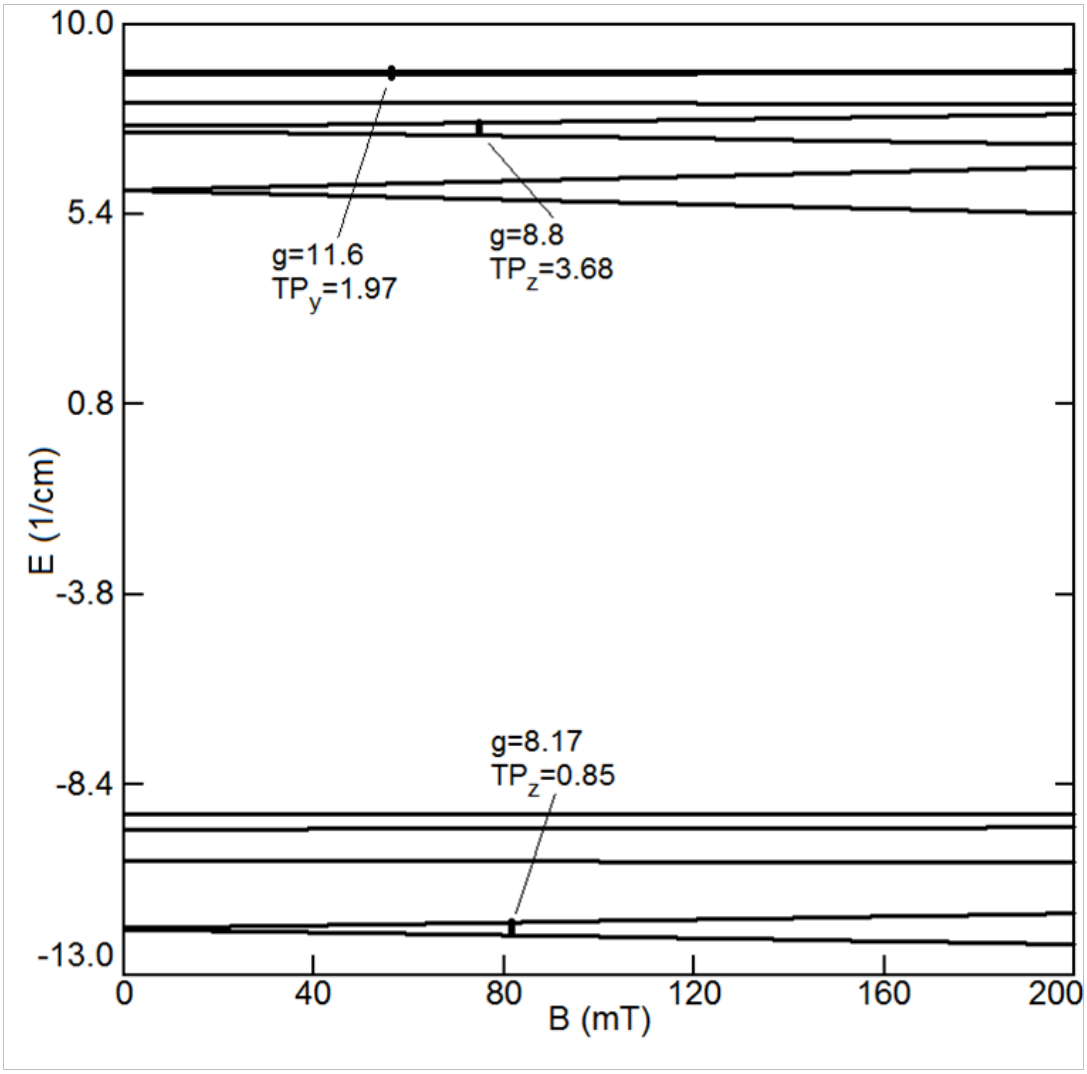

Figure 16: Energy level diagram for the spin system of H200N$_{Int1}$^{4NC}. Approximate *S* = 2 ground and S = 3 excited multiplets. The parameters used are the same as those cited in Figure 13. Energy splittings are shown as a function of the applied magnetic field, B. The *g* = 8.17 and 8.8 transitions are observed with B along z, while the *g* = 11.6 resonance is observed along y. Relative transition probabilities (TP) are given.

the main signal is shifted to g = 8.05, and its temperature dependence indicates that it arises from an excited doublet (Figure 17 A). The simulation displayed in Figure 14 D is for an S_1 = 5/2 center AF coupled to an S_2 = ½ center with parameters given in the figure caption. From the temperature dependence of the signal, we obtained $J \approx +40$ cm^{-1}. The simulation is also quantitative, showing that the spin concentration approximately matches the concentration of the protein.

Mössbauer spectroscopy shows that the iron of H200N$_{Int1}^{4NC}$ is an S_1 = 5/2 Fe(III) AF coupled to an S_2 = 1/2 species.

Mössbauer spectra of resting H200N recorded at 4.2 K in zero applied field (B = 0) exhibit a doublet with quadrupole splitting ΔE_Q = 3.01 mm/s and isomer shift δ = 1.24 mm/s, consistent with 6-coordinate high-spin Fe(II) with N/O coordination (*100, 101*) (also see chapter 2, Figure 28 A). The crystal structure of 2,3-HPCD has shown that substrate binding converts the Fe(II) site from a 6-coordinate octahedral geometry to a 5-coordinate square pyramidal geometry through release of solvent (*102*). Accordingly, after anaerobic addition of 1 eq of 4NC to H200N, the parameters of the Fe(II) site changed to ΔE_Q = 3.57 mm/s and δ = 1.12 mm/s (Figure 18 A). The decreased δ is consistent with conversion of the metal site to 5-coordinate, or a 6-coordinate site with one loosely bound solvent (*59, 100*).

Figure 18 B and C shows spectra of samples from the single turnover reaction in which pre-formed H200N-4NC complex was mixed rapidly with 1 eq of O_2 at 4 °C. The sample of Figure 18 B, frozen 10 s after mixing, exhibits at 4.2 K a doublet (representing 80% of Fe) with ΔE_Q = 0.33 mm/s and δ = 0.50 mm/s assigned to H200N$_{Int1}^{4NC}$; the remainder of the Fe belongs to H200N$_{Int2}^{4NC}$. The observation of a quadrupole doublet for B = 0, rather than a magnetically split spectrum, implies a species with integer (or zero) electronic spin. A δ value of 0.50 mm/s, on the other hand, unambiguously shows that the iron of H200N$_{Int1}^{4NC}$ is high-spin Fe(III), rather than Fe(II).

The spectra recorded in strong applied magnetic fields (between 0.6 and 8 T), see Figure 19 A and B, have features typical of high-spin Fe(III) sites. We have analyzed these spectra with the spin Hamiltonian $\mathcal{H} = \mathcal{H}_e + \mathcal{H}_{hf}$ (omitting the dipole-dipole term in $\mathcal{H}_e$) where $\mathcal{H}_{hf}$ describes the ^{57}Fe hyperfine interactions.

$$\mathcal{H}_{hf} = A_0\mathbf{S}_1\bullet\mathbf{I}_1 + (eQV_{zz}/12)[3I^2_{1z} - 15/4 + \eta(I^2_{1x} - I^2_{1y})] - g_n\beta_n\mathrm{B}\bullet\mathbf{I} \qquad [2]$$

In Eq. 2 all symbols have their conventional meanings. The high-field Mössbauer spectra are associated with the lowest spin doublet (roughly the $M_S = \pm 2$ doublet); the g = 8.17 EPR feature originates from this doublet. The observed magnetic hyperfine field is along z, which is also the direction for which the g = 8.17 feature is observed. For the ^{57}Fe magnetic hyperfine coupling constant of the ferric ion, we obtained $A_0/g_n\beta_n$ = -21.4(2) T, which compares well with A_0 values reported for sites with octahedral Fe(III) with N/O coordination (*103*). The parameters obtained from the Mössbauer analysis are listed in Table 1; the D and E/D values obtained from EPR and Mössbauer spectroscopy agree within the uncertainties.

^{17}O-Hyperfine coupling shows that an oxygen radical is present in H200N$_{Int1}^{4NC}$.

Figure 14 C shows parallel mode EPR spectra for a sample of H200N$_{Int1}^{4NC}$ prepared with 70% enriched $^{17}O_2$ (I = 5/2). It is evident that ^{17}O broadens the spectrum considerably. Figure 14 C also shows a simulation of the spectrum of the ^{17}O-enriched sample using the same set of electronic parameters as that shown in Figure 14 B, with the inclusion of a term for the hyperfine interaction with ^{17}O. For the 70% enrichment of this sample, the fit to the data gives $A_{17O} \approx 180$ MHz. The simulations show that at least one ^{17}O A-

tensor component for $H200N_{Int1}^{4NC}$ must be as large as 180 MHz. This large hyperfine constant is therefore indicative of >80% radical electron density on the oxygen, identifying $H200N_{Int1}^{4NC}$ as an Fe(III)-$O_2^{\bullet-}$ radical species.

$H200N_{Int2}^{4NC}$ may contain a bound peroxo and a product radical.

The zero field Mössbauer spectrum of $H200N_{Int2}^{4NC}$, shown in Figure 18 C consists of a doublet with ΔE_Q = 0.83 mm/s and δ = 0.50 mm/s. As for $H200N_{Int1}^{4NC}$, the system reflects a high-spin Fe(III) ion that is exchange coupled to some S = ½ radical. Analysis of the Mössbauer spectra recorded in strong applied fields (a 1.0 T spectrum is shown in Figure 19 C), demonstrates AF coupling with a $J > 6$ cm^{-1}.

In contrast to $H200N_{Int1}^{4NC}$, formation of $H200N_{Int2}^{4NC}$ using 70% enriched $^{17}O_2$ resulted in only a slight hyperfine broadening of the EPR signal in the g = 8 region (Figure 17 B). Simulations for $H200N_{4NC}^{Int2}$ indicate $A_{17O} \approx 5$ MHz. This small A-value indicates little spin density (<3%) on the oxygen, showing that the quantitative radical must be localized elsewhere. Because the absorption spectra show that the quinone product of the reaction is present in the active site of $H200N_{Int2}^{4NC}$, it is possible that this is the site of the radical. This was indirectly tested by displacing the quinone product with 4NC. The reaction was started with 1 eq of O_2 and 2 eq of 4NC relative to the active site Fe(II). The samples from the reaction time course were aged and frozen anaerobically in order to limit O_2 to 1 eq. The samples progressed normally through $H200N_{Int1}^{4NC}$ (Figure 20 A) and $H200N_{Int2}^{4NC}$, but at 80 s (Figure 20 B), the spectrum of the Fe(II) H200N-4NC substrate complex began to reappear, representing 20% of the total iron. This suggests slow replacement of the quinone product by the excess 4NC. After 30 min (anaerobically) at room temp (Figure 20 D and Figure 20 C), the reaction mixture contained 20% $H200N_{Int2}^{4NC}$ while 80% of the sample was the Fe(II) H200N-4NC complex. It is notable that in this complete cycle, the active site iron returns to the Fe(II) state without the introduction of external reducing equivalents. This suggests $H200N_{Int2}^{4NC}$ is formally a peroxo- Fe(II)-4NC quinone complex but internal electron transfer forms the quasi-stable peroxo- Fe(II)-4NC

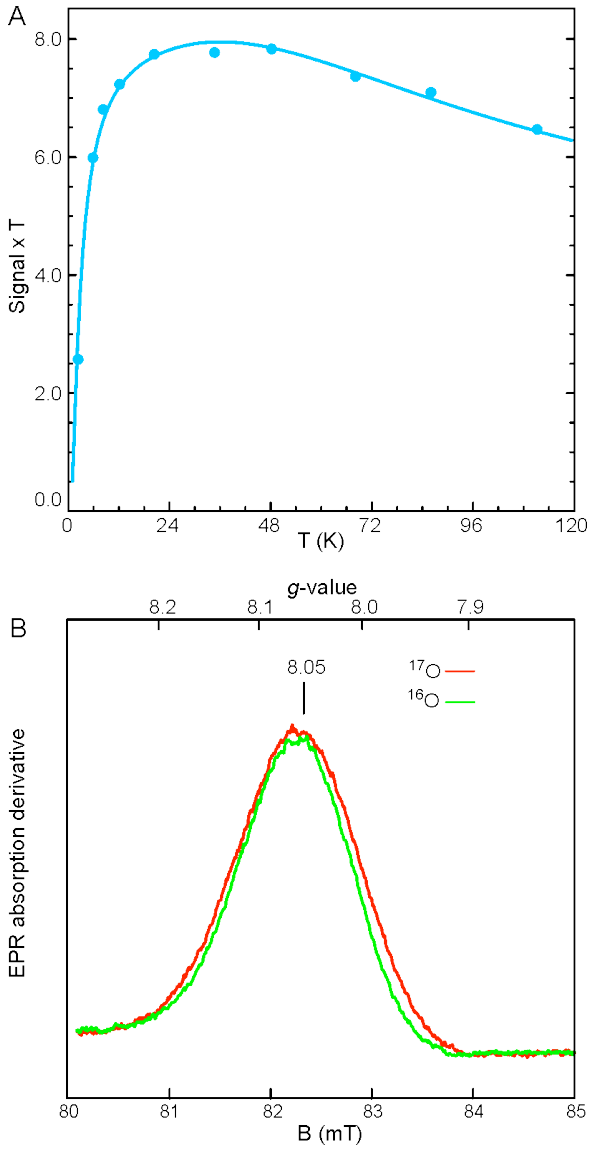

Figure 17: Detailed H200N$_{Int2}^{4NC}$ EPR result. (A) Signal x temperature versus temperature of the *g* = 8.05 parallel mode EPR signal of H200N$_{Int2}^{4NC}$ (dots) recorded with non-saturating microwave powers. The fit (line) uses the parameters given in Table 1. (B) ^{17}O-Hyperfine broadening of H200N$_{Int2}^{4NC}$. Parallel mode EPR spectra of the *g* = 8 region for samples frozen 10 min after mixing with ~ 1 eq of $^{16}O_2$ or 70% $^{17}O_2$. Conditions before mixing with O_2 saturated buffer at 4 °C: 1.7 mM H200N-4NC, 200 mM MOPS pH 7.5. EPR conditions: frequency, 9.28 GHz; power 20, mW; modulation, 10 G; temperature, 5 K.

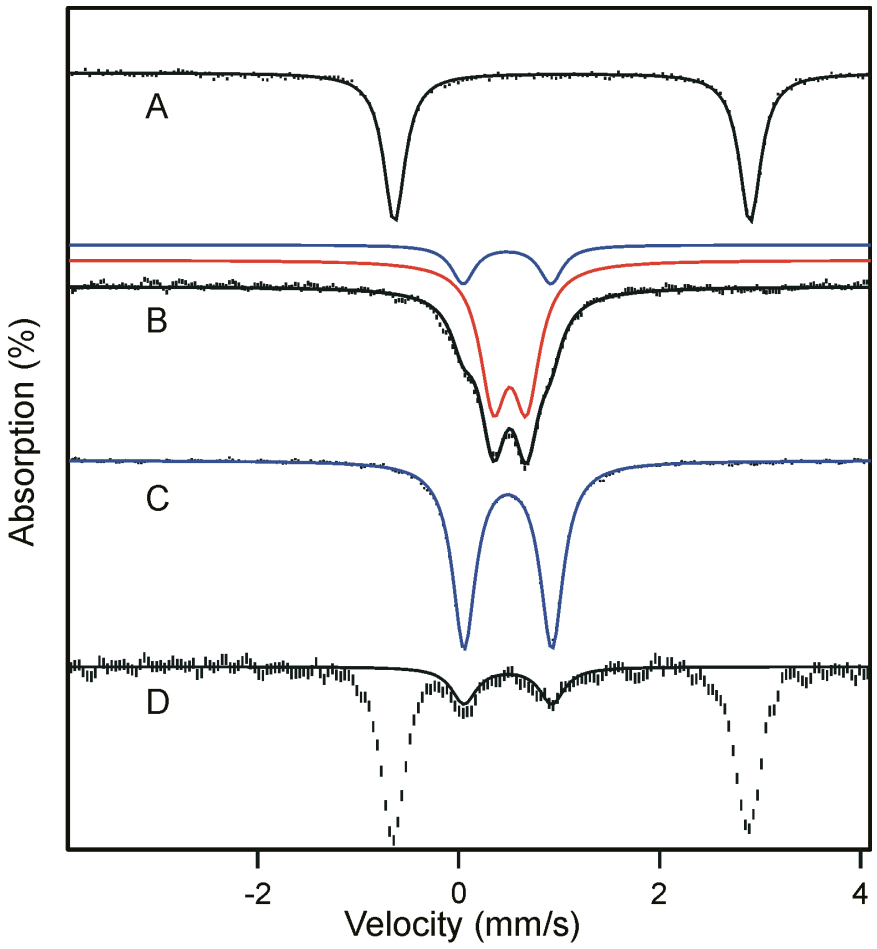

Figure 18: 4.2 K Mössbauer spectra of H200N variants recorded for B = 0. (A) Anaerobic H200N-4NC complex. (B) $H200N_{Int1}{}^{4NC}$ prepared by freezing the sample from (A) 10 s after mixing with 1 equivalent of O_2. The sample contains a small amount of $H200N_{Int2}{}^{4NC}$ (blue, ~20% of Fe). (C) Sample of $H200N_{Int2}{}^{4NC}$ frozen 10 min after mixing with O_2. (D) Endpoint complex in the presence of 1 additional equivalent of 4NC but stoichiometric O_2. This sample was prepared as described in Materials and Methods. The black, red or blue lines are fits using parameters of Table 1. Concentrations before mixing: 1.62 mM H200N-4NC (except in D, where an additional eq of 4NC is added), 50 mM MOPS pH 7.5 at 4 °C. The ^{57}Fe enrichment of H200N was approximately 95 %.

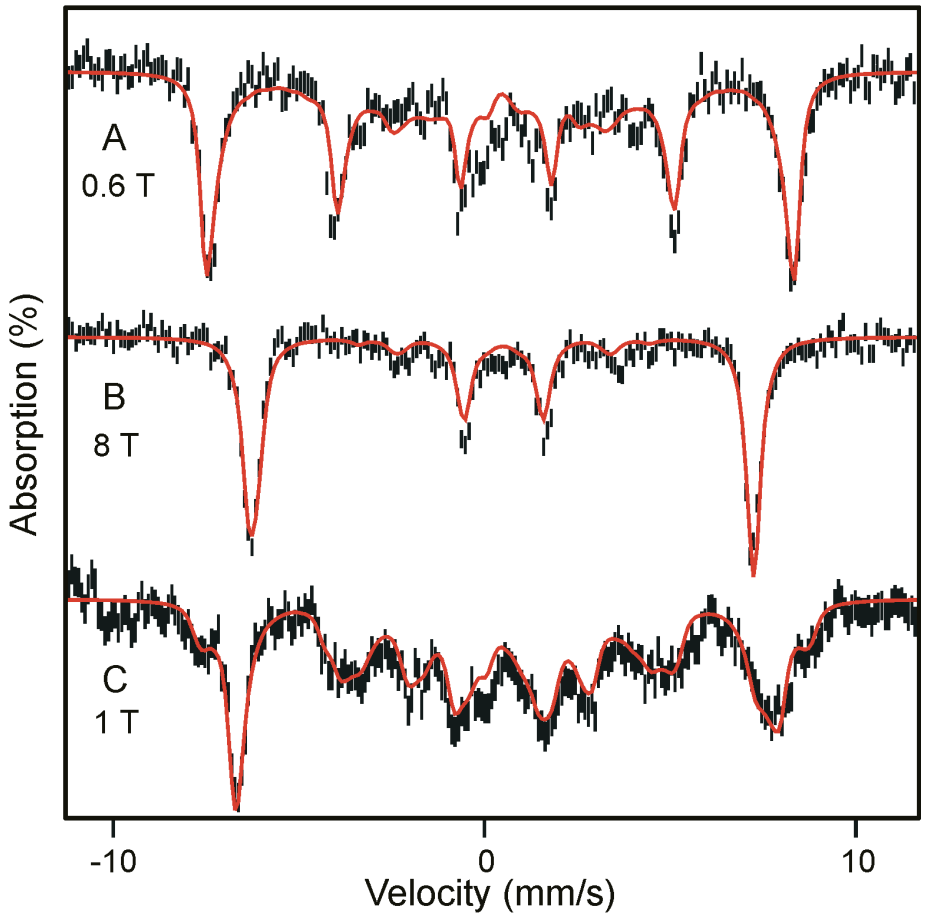

Figure 19: 4.2 K Mössbauer spectra in parallel applied magnetic fields, $H200N_{Int1}^{4NC}$ and $H200N_{Int2}^{4NC}$. (A, B) Spectrum of $H200N_{Int1}^{4NC}$. The 20% contribution of $H200N_{Int2}^{4NC}$ has been subtracted from the spectra. Red solid lines are simulations based on eqs 1 and 2 using the parameters listed in Table 1. (C) Spectrum of $H200N_{Int2}^{4NC}$. Red line is a spectral simulation using the parameters of Table 1.

quinone radical species actually observed. The presence of the peroxo would account for the slight broadening of the EPR spectrum due to ^{17}O. As the peroxide and quinone dissociate, the electron from the quinone radical is retained by the iron to restore the resting Fe(II) state (Figure 20 D) ready for another turnover cycle.

$H200N_{Int1}{}^{4NC}$ structure from DFT calculations.

The DFT optimizations were performed for states with spins S = 2 and S = 3. The calculation for the S = 3 state resulted in a Fe(III)-$O_2^{\bullet-}$ state in which the spin of the Fe(III) (S_{Fe} = 5/2) is parallel to the spin of the $O_2^{\bullet-}$ (S_{sox} = 1/2) moiety. (Note that this calculation did *not* converge to the plausible alternative state, namely, the Fe(II)-O_2 state in which the spins of Fe(II) (S_{Fe} = 2) and O_2 (S_{ox} = 1) are parallel and yield total spin S = 3.) Based on the ferromagnetic solution we prepared a guess state to initiate the calculation for the broken symmetry state that mimics the spin 2 state obtained by coupling the spin of the $O_2^{\bullet-}$ (S_{sox} = 1/2) antiparallel to the spin of Fe(III) (S_{Fe} = 5/2). The difference between the energies for the ferromagnetic state and the broken-symmetry state implies a ferromagnetic coupling constant J of -5.8 cm^{-1} ($J\mathbf{S}_{Fe}\cdot\mathbf{S}_{sox}$ convention). This value and those for selected hyperfine parameters are listed in Table 2 together with the corresponding experimental values.

The structure for the broken-symmetry state, which closely matches the structure for the ferromagnetic state, is shown in Figure 21 A. Using the perspective of Figure 21 A, Figure 21 B depicts the spin density profile for the broken-symmetry state. The shape of the π^* orbital containing the radical electron is clearly recognizable from the contour plot. Table 3 lists the spin populations for iron and the oxygen atoms of the superoxo ligand in the broken-symmetry state and the ferromagnetic state. The spin populations indicate that the superoxo bond is somewhat polarized by the iron. Using the averages over the two spin states we obtain different spin populations for oxygens: (0.29 + 0.48)/2 = 0.385 for the proximal oxygen and (0.59 + 0.64)/2 = 0.615 for the distal oxygen (the difference can be seen from the spin density plot in Figure 21 B).

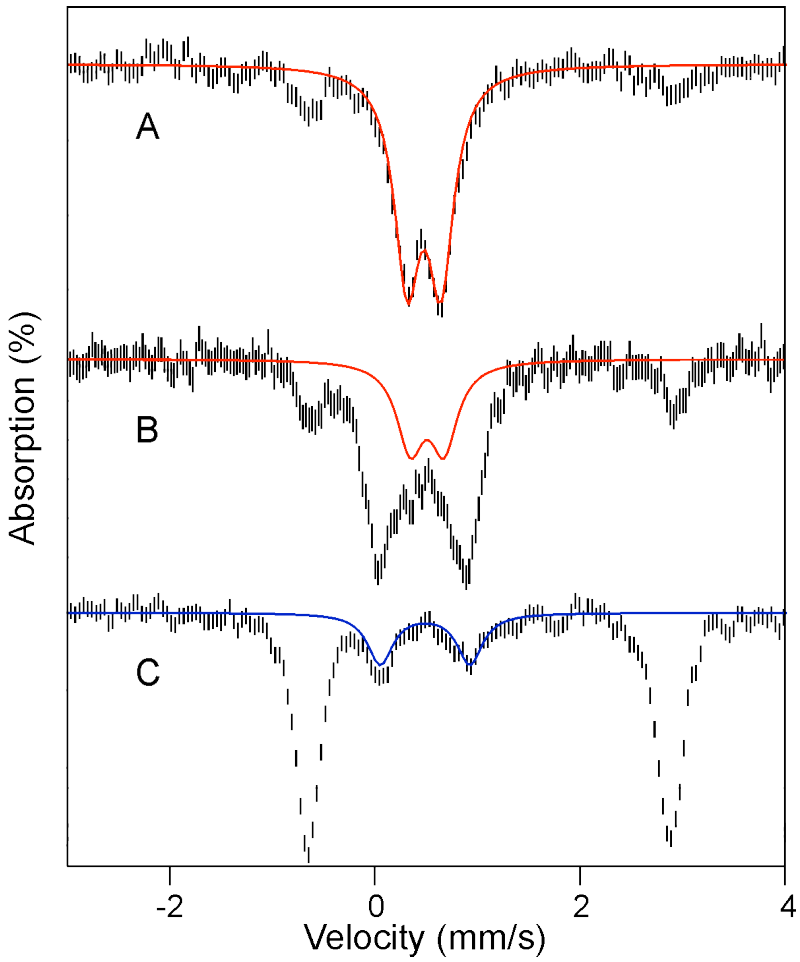

Figure 20: 4.2 K Mössbauer spectra of the single turnover time course in the presence of 2 X 4NC at 4 °C. (A) 24 ms after mixing 1 eq-H200N-2 eq 4NC complex with 1 eq of O_2. The sample at this time point is prepare by freezing the reaction mixture on counter-rotating aluminum wheels at Liq N_2 temperatures. The red line is a fit to the data using the parameters from Table 1. (B) 80 s after mixing with O_2. This sample is prepared by shooting the reaction mixture into an anaerobic vial for aging before freezing the sample in Liq N_2. The red line shows the contribution of $H200N_{Int1}{}^{4NC}$ to the spectrum. (C) The end complex. This sample is a RFQ powder frozen in Liq N_2, transferred into the anaerobic glovebox, then thawed for 20 min at 25 °C. The blue line shows the contribution of $H200N_{Int2}{}^{4NC}$ to the spectrum. Concentrations before mixing: 1.62 mM H200N-4NC (plus one additional eq of 4NC), 200 mM MOPS pH 7.5.

Table 2: Hyperfine parameters and exchange coupling constants for $H200N_{Int1}{}^{4NC}$.

	^{57}Fe			^{17}O superoxo	
	d (mm/s)	ΔE_Q (mm/s)	J (cm^{-1})	$A_{proximal}$ (MHz)	A_{distal} (MHz)
Experiment	0.50	–0.33	6	- †	180‡,- †,- †
DFT	0.56	–0.66	–5.8	–123, +74, +128 §	–226, +59, +81 §
Ref (*104*)				–214, +20, +23§	

† Not measured.

‡ Experimental 180 MHz splitting is assumed to be associated with the distal oxygen atom.

§ Values for $A_{x'}$, $A_{y'}$, and $A_{z'}$. z' is along O-O bond, x' in plane of π^* orbital.

The averaged spin populations for the two oxygens add up to a total of 1.000, representing the radical electron. The spin population of the iron is smaller than the number of 5 for a free high-spin Fe(III), indicating some degree of spin density transfer to the ligands. The spin populations for the oxygen atoms in Table 3 can be decomposed as −0.385 + 0.095 = −0.29 (O_{prox}) and −0.615 + 0.025 = −0.59 (O_{dist}) for the broken-symmetry state and 0.385 + 0.095 = 0.48 (O_{prox}) and 0.615 + 0.025 = 0.64 (O_{dist}) for the ferromagnetic state. The quantities +0.095 and +0.025 are the contributions to the spin populations arising from spin 2 polarization of the superoxo by the high-spin Fe(III) site, which are positive in both the ferromagnetic and broken-symmetry states and yield a total of spin transfer 0.12 from iron to superoxo. The differences in the spin densities for the proximal and distal oxygen are reflected in the magnetic hyperfine parameters listed in Table 2.

Table 3: Mulliken spin populations**.**

	Broken Symmetry State	Ferromagnetic State
Fe	4.25	4.24
$O_{proximal}$	–0.29	0.48
O_{distal}	–0.59	0.64

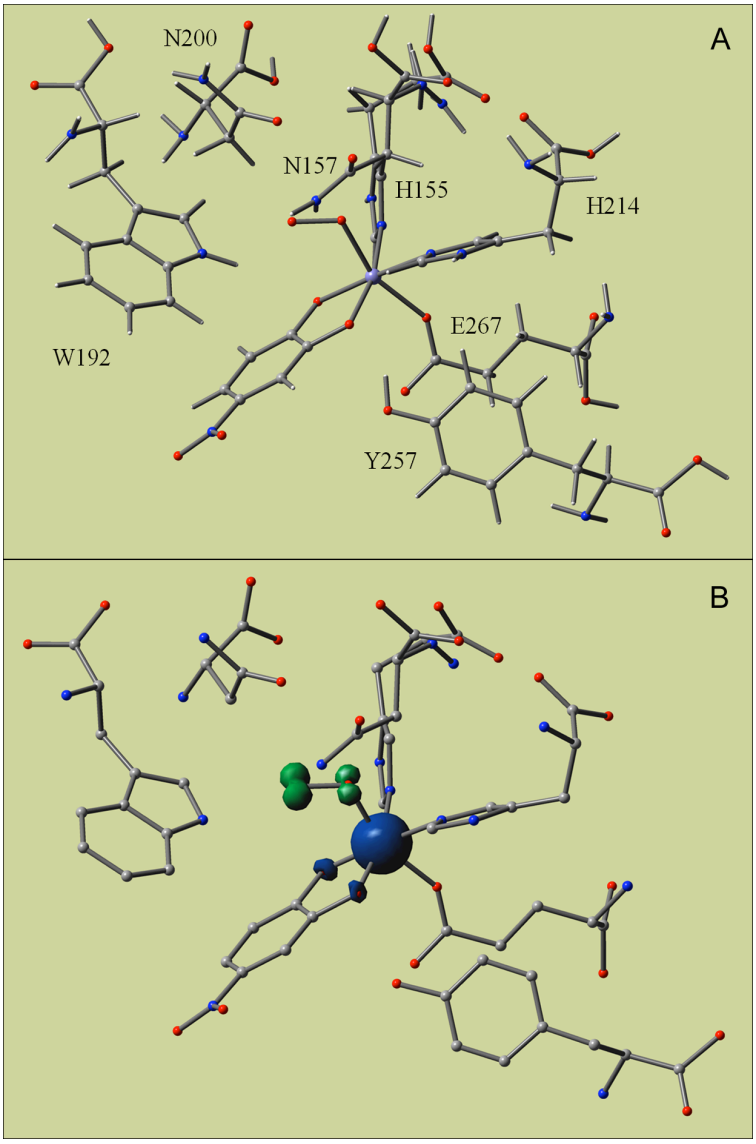

Figure 21: DFT result for $H200N_{Int1}^{4NC}$. (A) Structure of the truncated model for $H200N_{Int1}^{4NC}$ adopted in DFT calculations. (B) Spin density contour plot for broken symmetry state of $H200N_{Int1}^{4NC}$ obtained with DFT. Majority spin (centered at iron) is in blue and minority spin (at superoxo) is in green.

DISCUSSION

Past studies from our laboratories and several others have shown that O_2 activation at non-heme iron centers in oxidases and oxygenases is usually a highly regulated process designed to produce a reactive form of oxygen only when it can react rapidly with a substrate (*13, 34, 59, 82, 92, 105-107*). This promotes regiospecificity and prevents adventitious reactions with other biological components, but often leads to fleeting intermediates that can be detected only after the development of strategies to slow the reaction (*21, 108*). The study described here employs both mutagenesis of a key active site acid/base catalyst and the use of a slow substrate to kinetically resolve the half reactions of what we believe are very fast processes in the catalytic cycle of the WT enzyme. The first intermediate in this process is an active site Fe(III)-$O_2^{\bullet-}$, the first such species to be stabilized in the large non-heme mononuclear iron oxygenase enzyme class. Below, the characteristics of this species and its relevance to catalysis are discussed.

Electronic Structure of H200N$_{Int1}^{4NC}$.

The above spectroscopic data clearly indicate that H200N$_{Int1}^{4NC}$ is well described as a high-spin Fe(III) ion exchanged coupled to a superoxo radical (Fe^{III}–$O_2^{\bullet-}$). The ^{57}Fe hyperfine interaction ($A_0/g_n\beta_n$ = -21.4 T) compares well with that of the mononuclear Fe(III) site (-21.2 T) of protocatechuate 3,4 dioxygenase from *Brevibacterium fuscum* (*103*), and the isomer shift (δ = 0.50 mm/s) falls squarely into the range of high-spin Fe(III) (*101*). The ^{17}O hyperfine interaction of the superoxide radical is large (A_{17O} = 180 MHz) as in superoxide adsorbed onto various surfaces (*104, 109*) and oxycobaltomyoglobin (*110*).

The electronic structure of H200N$_{Int1}^{4NC}$ developed from spectroscopy is supported by DFT calculations for a truncated system, consisting of the Fe, its

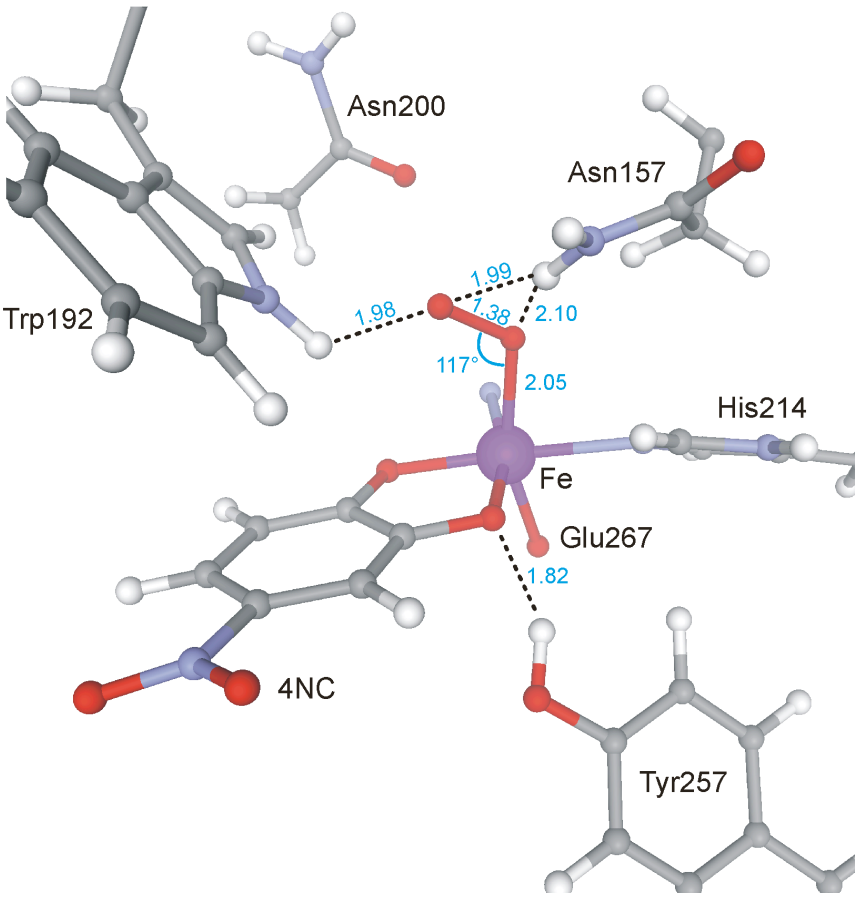

Figure 22: DFT geometry optimization of $H200N_{Int1}{}^{4NC}$. Dashed lines indicate hydrogen bonds. Blue numbers indicate distance in Angstroms or angle in degrees. All possible orientation of Asn200 are beyond hydrogen bonding range to the O_2.

coordinated ligands, and residues of the second coordination sphere in 2,3-HPCD (Figure 21 A). The calculations yield an Fe(III)-$O_2^{\bullet-}$ ground state with a superoxo radical bound end-on to a high-spin Fe(III) (Fe-O-O = 117°) (Figure 22). The calculated values for δ and ΔE_Q are typical for high-spin Fe(III) and agree well with the experiment (Table 2). The calculated *A*-values for the distal ^{17}O, $A_{1,2,3}$ = (-226, +59, +81) MHz, are quite similar to those observed in matrix-isolated $O_2^{\bullet-}$ (*104, 109*), with the largest component perpendicular to the O–O axis in the plane of the π^* orbital containing the unpaired electron. Since the largest ^{17}O splitting is observed along the z axis of Eq 1, it follows that this axis is in the plane of the π^* orbital and perpendicular to O–O bond. The calculated O–O bond length (1.38 Å) is close to that calculated for $O_2^{\bullet-}$ (1.41 Å), and quite different from that for O_2 (1.26 Å). The computations show nearly complete transfer of the electron to the dioxygen with some polarization such that the distal oxygen has a higher spin population (Table 1). This oxygen points towards the catechol carbon *para* to the nitro group (Figure 22), whereas structural studies show that the side-on bound Fe(II)-superoxo species of the WT 2,3-HPCD-4NC complex points the adjacent hydroxyl bearing carbon (*50*). The calculated *J* value is small (J = -5 cm^{-1}), as observed experimentally (J = +6 cm^{-1}), but ferromagnetic. Preliminary calculations suggest that the orientation of the radical-containing π^* orbital (Figure 21 B) and the exchange-coupling constant are sensitive to hydrogen bonding interactions between $O_2^{\bullet-}$ and the protein residues, and that minor changes in protein conformation may change the *J*-value by as much as 100 cm^{-1}. The nature of these correlations is currently under investigation.

Comparison of $H200N_{Int1}^{4NC}$ with Fe(III)-$O_2^{\bullet-}$ species from heme-containing enzymes.

As in the case of the non-heme iron-containing oxidases and oxygenases, the reaction of O_2 with heme-containing systems usually involves a reaction with iron in a 5-coordinate S = 2 state. An electron is transferred to O_2 in both the heme and non-heme systems. However, the reactions diverge at this point

because the iron in the heme system generally becomes a low-spin Fe(III) - $O_2^{\bullet-}$ system, with a DFT-calculated singlet – triplet gap of ≈1200 cm^{-1} for P-450 (*11*). The Fe(III)-$O_2^{\bullet-}$ species of hemes is rarely proposed as a reactive species in oxygenase reactions unless the substrate is highly activated as, for example, in the final step of the nitric oxide synthase cycle (*111*). It is generally thought that the heme Fe(III)-$O_2^{\bullet-}$ state is first converted to a peroxo, hydroperoxo, or high-valent oxo intermediate. While similar conversions are postulated for many non-heme systems, others are thought to use the superoxo state directly as described below.

Significance for nonheme mononuclear iron-containing enzymes.

Fe(III)-$O_2^{\bullet-}$ intermediates have been proposed to serve important roles in the reaction cycles of non-heme mononuclear iron-containing enzymes. For example, it has been proposed that this type of intermediate abstracts a hydrogen atom from the beta carbon of iron-bound cysteinyl moiety of the tripeptide δ-(Lδα-aminoadipoyl)-L-cysteinyl-D-valine during the isopenicillin N-synthase catalyzed formation of the β-lactam ring of penicillin N (*112*). In the reaction cycle of the myriad of α-ketoglutarate linked dioxygenases, an Fe(III)-$O_2^{\bullet-}$ intermediate is proposed to attack the alpha carbon of the iron-bound α-keto glutarate to form an alkylperoxo intermediate prior to the release CO_2 and the formation of a high valent intermediate that ultimately hydroxylates the substrate (*59*). In these and all other examples, the putative iron-superoxo species has not been directly detected. $H200N_{Int1}^{4NC}$, on the other hand, is detectable at 4 °C for several minutes and is shown here to contain oxygen from O_2, presenting an opportunity to characterize a non-heme Fe(III)-$O_2^{\bullet-}$ for the first time.

Electronic structure of $H200N_{Int2}^{4NC}$.

Based on the small hyperfine interaction from ^{17}O, the loss of the g = 8.05 EPR signal upon displacement of the quinone product, and observation of an Fe(III) by Mössbauer spectroscopy, it seems likely that $H200N_{Int2}^{4NC}$ is a peroxo-Fe(III)-4NC semiquinone complex. Small molecule transition metal ligand

complexes with quinones are well studied (*113, 114*). It has been shown that charge distribution between a transition metal and the non-innocent quinone ligand depends largely on relative energy levels between the quinone frontier and metal orbitals (*113*). This has been used to explain the rich redox chemistry commonly observed when a quinone interacts with a divalent metal ion such as Fe(II), Mn(II), and Co(II) (*115*). In most cases, these complexes exhibit a resultant spin state consistent with electron transfer from the metal to the quinone, with AF coupling between the metal and the quinone radical as we propose for $H200N_{Int2}^{4NC}$.

Implications for the mechanism of extradiol dioxygenases.

We show here that the turnover of 4NC by H200N leads initially to generation of an Fe(III)-$O_2^{\bullet-}$ complex that cannot rapidly attack the substrate. This raises the question of whether $H200N_{4NC}^{Int1}$ is relevant to normal ring-cleaving catalysis. It should be noted that the transient absorption feature at 610 nm that we associate with $H200N_{Int1}^{4NC}$ is observed when H200N catalyzes either ring cleavage of HPCA or quinone formation from 4NC. In the mechanistic model we have proposed (Figure 11), the reaction becomes committed to ring cleavage by superoxo radical attack on the substrate semiquinone to form the structurally characterized alkylperoxo intermediate (*50*). It is likely that the highly electron withdrawing nitro substituent of 4NC greatly decreases the rate of electron transfer to the Fe(III)-$O_2^{\bullet-}$, especially in the absence of an acid-base catalyst and orienting residue at position 200. Consequently, the ability to see a long-lived $H200N_{Int1}^{4NC}$ in H200N with 4NC may reflect a decrease in driving force for electron transfer from the substrate rather than the formation of a unique species in this enzyme variant.

CONCLUSION

Most heme-containing oxidases and oxygenases that catalyze reactions involving cleavage of strong bonds of unactivated substrates generate Fe(III)-hydroperoxo or Fe(IV)-oxo π cation radical reactive species. These are formed by first transferring two electrons in rapid succession to O_2. In contrast, the non-heme Fe(II) aromatic ring cleaving dioxygenases appear to follow a different strategy involving a one-electron transfer to oxygen. The studies reported here and our previous studies suggest that this process proceeds by initial formation of a short-lived Fe(III)-$O_2^{\bullet-}$. We propose that this species is very rapidly converted in normal catalysis to a substrate radical-Fe(II)-$O_2^{\bullet-}$ intermediate, which is the true reactive species from which oxygen attack on the substrate occurs. The initial formation of Fe(III)-$O_2^{\bullet-}$ is likely to be a common theme throughout the remarkably diverse mononuclear nonheme Fe(II) containing superfamily, most members of which share the 2-His + 1-Asp/Glu Fe(II) binding motif (*116*). After formation of the Fe(III)-$O_2^{\bullet-}$ intermediate, the proposed reaction mechanisms diverge such that in some cases the Fe(III)-$O_2^{\bullet-}$ is the reactive species, while in other cases further activation steps are required. Thus, the Fe(III)-$O_2^{\bullet-}$ species described here is likely to be the intermediate from which emerges an exceptionally rich range of enzyme chemistry.

Chapter 1 contributions.

This work is supported by the NIH grant GM 24689 (John. D. Lipscomb.), grant EB-001475 (Eckard Münck.), grant GM77387 (Michael P. Hendrich) and graduate traineeship GM08700 (Michael. M. Mbughuni). This research was supported in part by the N.S.F. grant TG-CHE070073 through Teragrid. I would like to thank Elena G. Kovaleva for assistance in analyzing structural data used for DFT computations. The DFT calculation is the work of Mrinmoy Chakrabarti, Emile L. Bominaar and Eckard Münck. The result from the calculation is incorporated into this thesis because it greatly complements the RFQ/Spectroscopic analysis of H200N_{Int1}^{4NC}. Mössbauer analyses were done by

Eckard Münck and Mrinmoy Chakrabarti. EPR simulations were done by Michael P. Hendrich and Joshua A. Hayden. All these contributions have made this work possible.

CHAPTER 2

Oxy-intermediates of Homoprotocatechuate 2,3-Dioxygenase: Facile electron transfer between substrates.

Note: This chapter is reprinted (adapted) with permission from Mbughuni, M. M., Chakrabarti, M., Hayden, J. A., Meier, K. K., Dalluge, J. J., Hendrich, M. P., Münck, E., and Lipscomb, J. D. (2011) Oxy-intermediates of homoprotocatechuate 2,3-dioxygenase: Facile electron transfer between substrates, *Biochemistry 50*. Copyright (2011) American Chemical Society."

Abbreviations:

$H200N_{Int1}^{HPCA}$ and $H200N_{Int2}^{HPCA}$, intermediates observed in the H200N-HPCA + O_2 reaction.

$FeHPCD_{Int1}^{HPCA}$, intermediate observed in the FeHPCD-HPCA + O_2 reaction.

$H200N_{ES1}^{HPCA}$, $H200N_{ES2}^{HPCA}$, $FeHPCD_{ES1}^{HPCA}$, and $FeHPCD_{ES2}^{HPCA}$, substrate complexes of H200N or FeHPCD with the substrate HPCA.

LC-MS, Liquid chromatography /electrospray ionization-tandem mass Spectrometry

SUMMARY

In the proposed ring cleaving mechanisms of 2,3-HPCD, substrates HPCA and O_2 bind to the Fe(II) of 2,3-HPCD in adjacent Fe(II) coordination sites. Transfer of an electron(s) from HPCA to O_2 via the iron is proposed to activate the substrates for reaction with each other to initiate aromatic ring cleavage. Here, rapid-freeze-quench methods are used to trap and spectroscopically characterize ring-cleaving intermediates in the reactions of the HPCA complexes of FeHPCD and the H200N variant (FeHPCD-HPCA and H200N-HPCA) with O_2. A blue intermediate forms within 20 ms after mixing O_2 with H200N-HPCA ($H200N_{Int1}^{HPCA}$). Parallel mode EPR and Mössbauer spectroscopies show that this intermediate contains high-spin Fe(III)(S = 5/2) antiferromagnetically coupled to a radical (S_R=1/2) to yield an S = 2 state. Together, optical and Mössbauer spectra of the intermediate support assignment of the radical as an HPCA semiquinone, implying that oxygen is bound as a (hydro)peroxo ligand. $H200N_{Int1}^{HPCA}$ decays over the next 2 s, possibly through an Fe(II) intermediate ($H200N_{Int2}^{HPCA}$), to yield product and the resting Fe(II) enzyme. Reaction of FeHPCD-HPCA with O_2 results in rapid formation of a colorless Fe(II) intermediate ($FeHPCD_{Int1}^{HPCA}$). This species decays within 1 s to yield the product and the resting enzyme. The absence of a chromophore from a semiquinone or evidence for a spin-coupled specie in $FeHPCD_{Int1}^{HPCA}$ suggests it is an intermediate occurring after O_2 activation and attack. The similarity of the Mössbauer parameters for $FeHPCD_{Int1}^{HPCA}$ and $H200N_{Int2}^{HPCA}$ suggest these are similar intermediates. The results show that electron transfer from the substrate to O_2 via the iron does occur leading to aromatic ring cleavage.

INTRODUCTION

As discussed in the Introduction and Chapter 1, the ring-cleaving reaction of extradiol dioxygenases allows a host of aerobic microorganisms to channel carbon from naturally occurring and man-made aromatic compounds into the TCA cycle, facilitating biodegradation (Figure 1) (*6, 34, 46, 94*). As such, the ring-cleaving extradiol dioxygenases play a role in human health and maintenance of the global carbon cycle. This chapter will focus on the electronic structure of catechol ring cleaving reaction intermediates from the WT and H200N variant.

For the extradiol dioxygenases, it has been shown the catecholic substrate and O_2 bind to the metal in adjacent coordination sites (Figure 4 A, Figure 10 A and Chapter 1) (*50*). It has also been proposed that electron transfer from the substrate to dioxygen via the metal gives radical character to both the substrate and the oxygen, (Figure 23 D) (*46, 50, 75, 82, 93*). Recombination of the radicals would initiate ring attack and oxygen insertion to form a metal-bound alkylperoxo intermediate (Figure 23 E), leading to extradiol catechol ring cleavage.

An oxygen activation mechanism of this type does not require a formal change in oxidation state of the metal between the initial enzyme-aromatic substrate complex and postulated diradical reactive state. However, it is shown in Chapter 1 that when His200 is replaced by Asn (H200N), and 4NC is used as the substrate, O_2 binds to form a long-lived, antiferromagnetically coupled Fe(III)-$O_2^{\cdot -}$ species, allowing a study of its electronic structure in solution ($H200N_{Int1}{}^{4NC}$, Figure 23 B). This species decayed during the following 100 s to another intermediate ($H200N_{Int2}{}^{4NC}$) postulated to be a 4NC $SQ^{\cdot}$- Fe(III)-peroxo species. Rather than undergo ring cleavage, this intermediate decayed to release 4NC quinone and H_2O_2 and restore the Fe(II) center of the enzyme. This study shows that a change in the iron redox state can occur as O_2 binds, but the downstream chemistry deviates from normal catalysis, suggesting that the H200N mutation and/or the use of a substrate with an electron withdrawing substituent can uncouple O_2 activation from ring cleaving chemistry.

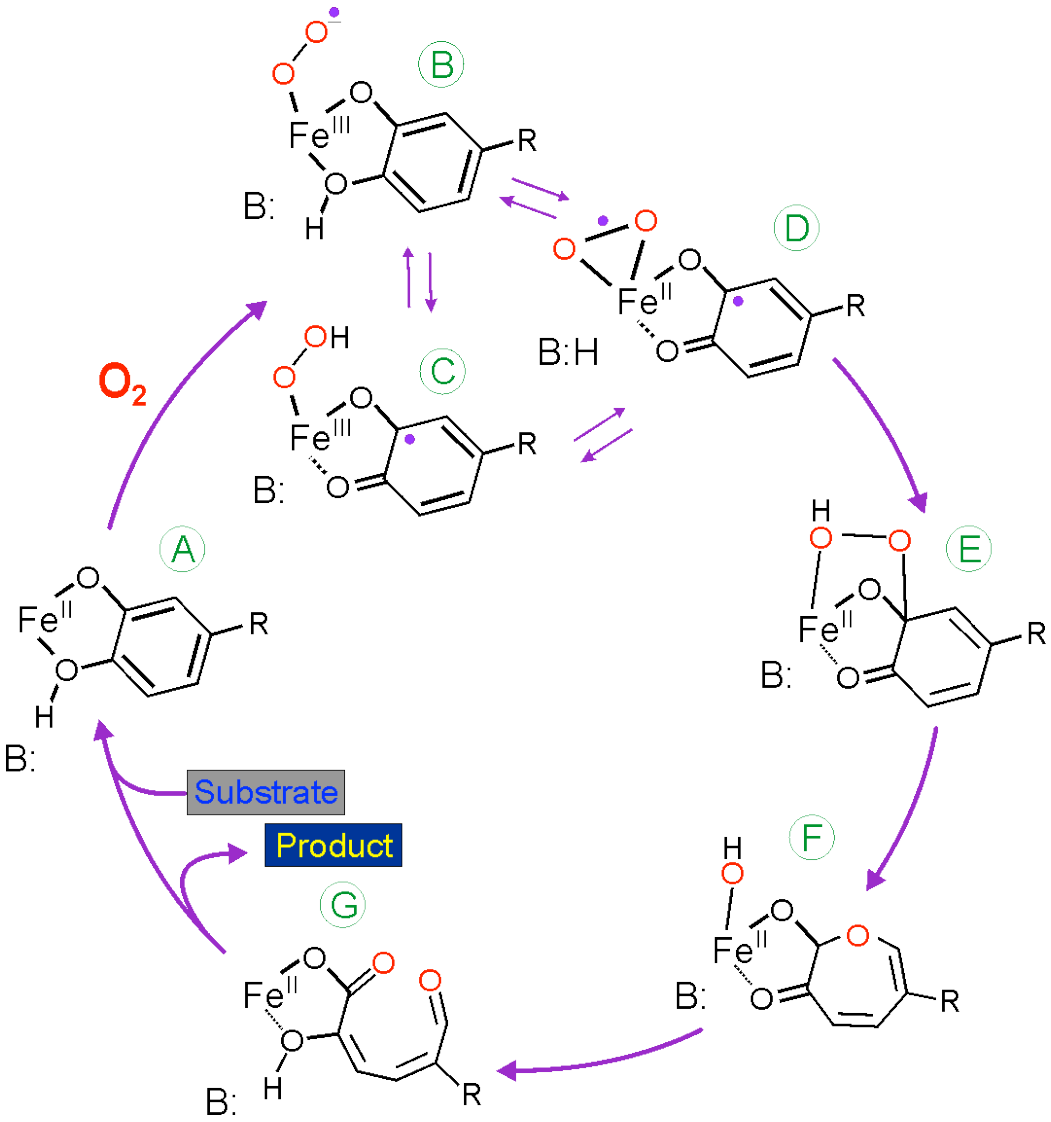

Figure 23: Proposed O_2 activation by extradiol dioxygenases. For the studies described here, R is either $-CH_2COO^-$ (HPCA) or $-NO_2$ (4NC). In the case of 4NC, the substrate is fully deprotonated, so the proton required for catalysis must derive from solvent.

Transient kinetic studies of extradiol dioxygenase reactions that yield the correct ring-cleaved products have been carried out using HPCA as the substrate for FeHPCD and H200N (*95, 96*). These studies revealed at least four intermediates following addition of O_2 with a pre-formed enzyme-substrate complex. In the case of H200N, the O_2 binding step itself could be monitored because a visible absorption band associated with the complex was observed near 610 nm. In this chapter, rapid-freeze-quench (RFQ) methods are used to trap and spectroscopically characterize the intermediates from the reaction of FeHPCD- and H200N-HPCA complexes with O_2. The earliest trapped intermediates differ markedly from that identified in the H200N-4NC reaction with O_2 (*51*). Together, they support a mechanism in which facile electron transfer between bound HPCA and O_2 via the Fe(II) forms the basis for O_2 activation and insertion chemistry (Figure 23 B - E).

EXPERIMENTAL PROCEDURES

Reagents and enzymes.

All chemicals were purchased from Sigma-Aldrich and were used without purification except for HPCA which was recrystallized from water at 4 °C to remove minor contaminants. Anaerobic conditions were achieved by repeated cycling of solutions between argon gas and vacuum. Trace contaminating O_2 was removed from the Ar gas by passage through an Agilent GC-1 POP O_2 scrubbing cartridge, then through an Agilent GC-4 POP O_2 indicating cartridge. Formate dehydrogenase (FDH) was prepared as previously described (*117*). The C_1 and C_2 *p*-hydroxyphenylacetate hydroxylase system from *Acinetobacter baumannii* was the generous gift of David P. Ballou. Recombinant *Brevibacterium fuscum* FeHPCD and the H200N variant were expressed and purified as previously described (*96, 98*). ^{57}Fe-enriched enzyme was prepared for RFQ/ Mössbauer experiments as previously described (*51*). Mushroom Tyrosinase was purchased from Sigma.

Stopped-flow and spectroscopy.

All stopped-flow experiments were performed using an Applied Photophysics model SX.18MV stopped flow device at 4 °C. The reaction procedures were as previously described (*95*). The kinetic data were analyzed to extract reciprocal relaxation times using the Applied Photophysics Pro-Data Viewer version 4.0.17. EPR spectra were collected using a Bruker Elexsys E-500 or Bruker ESP 300 spectrometer each equipped with a Bruker dual mode cavity and an Oxford ESR 910 liquid helium cryostat. Mössbauer spectroscopy was performed as previously described (*51, 101*). Spectra were analyzed using the software WMOSS (SEE Co, Edina, MN, USA).

RFQ methods.

Anaerobic substrate complexes were prepared in a Coy glovebox as described in chapter 1 (*51*). RFQ syringes were loaded inside the anaerobic

glovebox before transferring to the Update RFQ Instrument (Model 1019 RFQ) where they were equilibrated at 4 °C for 30 min using an ice bath. After rapid mixing and passage through a calibrated delay line, samples were collected by rapid freezing on counter-rotating aluminum wheels at Liq N_2 temperature. A programmed delay was used for time points > 0.4 s. For samples at times >1.5 s, the mixed sample was collected directly in an EPR tube or Mössbauer cup and frozen by rapid emersion in a dry ice/methanol bath (EPR) or Liq N_2 (Mössbauer) after the appropriate incubation time. We have observed that freezing on the counter-rotating wheels introduces a small splash artifact that becomes more prominent at the highest ram drive speeds. The splashed material falls into the Liq N_2 bath directly and freezes more slowly than the material on the wheel, causing the appearance of the spectrum of the product complex in early samples. The rate of product formation for the reactions investigated here is well known from stopped flow experiments (*95*), and no product-complex is expected in the earliest RFQ samples collected.

Synthesis of HPCA enriched with ^{17}O at the C3 hydroxyl functional group.

3- ^{17}OH-HPCA was prepared from p-hydroxyphenylacetate (HPA). The C_1 and C_2 hydroxylase from *Acinetobacter baumannii* (*118*) was used to catalyze conversion of HPA to 3-(^{17}OH),4-(^{16}OH)-dihydroxyphenylacetic using 70% enriched $^{17}O_2$ (Cambridge Isotopes). A 2 mL reaction mixture was prepared in a 5 mL pear shaped flask fitted with a 3-way valve in the anaerobic glovebox. Concentrations of the reactants were10 μM C_1, 20 μM C_2, 20 μM FDH, 100 μM NADH, 15 mM formate, and 10 mM HPA. The flask mouth was capped with a SUBA seal septa crimped with copper wire and the valve closed prior to removal from the glovebox. The 3-way valve was connected to a vacuum/argon line and to a tank of 70% enriched $^{17}O_2$ and the lines were evacuated and exchanged with argon several times. The system was opened to vacuum and the head space of the pear shape flask evacuated for ~ 1 s. The vacuum line was closed and the flask was filled with 1-2 psi of 70% enriched $^{17}O_2$ to initiate the reaction. The reaction was allowed to proceed for 2 h at room temperature to reach

completion, and then it was quenched with 3% H_2SO_4. The quenched reaction was centrifuged at 39,000 × g for 40 min to remove insoluble materials. The supernatant from centrifugation was assayed for HPCA using the catalytic activity of FeHPCD which converts HPCA to the α-hydroxy δ-carboxymethyl *cis*-muconic semialdehyde, which has an extinction coefficient at 380 nm of 38,000 M^{-1} cm^{-1}. (*95*) The assay revealed nearly stoichiometric conversion of HPA to HPCA. The reaction supernatant containing 3-^{17}OH-HPCA was lyophilized and then dissolved in 50 mM MOPS buffer pH 7.5 and stored at -80 °C until used in RFQ experiments. LC/MS/MS analysis of the synthesized HPCA is described below and shows nearly 68% enrichment of one atom of ^{17}O per HPCA molecule.

Liquid chromatography electrospray ionization-tandem mass spectrometry of ^{17}OH-C3-HPCA.

LC/MS/MS determinations of 3-^{17}OH-HPCA were performed using a Waters Acquity HPLC coupled to a Waters TQD mass spectrometer. Separation was achieved with a Waters Acquity HPLC HSS T3 column (100 mm x 2.1 mm, 1.8 μm) C_{18} column heated to 35 °C employing a flow rate of 0.4 mL/min and mobile phase A and B, 0.1% aqueous formic acid and 0.1% formic acid in acetonitrile, respectively, and with the following gradient: 3% B, 0 to 2 min, 3% B to 97% B, 2 to 6 min, 97% B, 6 to 8 min, 97% B to 3% B, 8 to 9 min. Total run time was 12 min. Electrospray ionization tandem mass spectrometric methods (ESI-MS–MS) were created for the 3-^{17}OH-HPCA using selected reaction monitoring (SRM) optimized by direct infusion. Parameters of the ESI-MS–MS system were selected based on in-source generation of the deprotonated ions of each reactant and product (monoisotopic and isotopically labeled) as well as production of compound-specific fragment ions. The following negative ionization mode parameters were used for determination of these compounds: capillary, 3.20 kV; cone, 21 V; extractor, 3 V; rf lens, 0.3 V; source temperature, 150 ºC; desolvation temperature, 350 ºC; desolvation gas flow, 800 L/h; cone gas flow, 20 L/h; low-mass resolution (Q1), 12 V; high-mass resolution (Q1), 12 V; ion energy (Q1), 0.3 V; entrance, -5 V; collision energy, 8 V; exit, 1 V; low-mass

resolution (Q2), 15 V; high-mass resolution (Q2), 15 V; ion energy (Q2), 3.5 V; gain, 1.0. SRM transitions monitored for each analyte were as follows: HPCA: 167.2>123.1; HPCA first isotope (for calculation of natural first isotope abundance, accounted for in calculation of percent enrichment ^{17}O in corresponding products): 168.2>124.1; Product: 199.2>155.1 (loss of CO_2); $^{17}O_1$ Product: 200.2>155.1 (loss of $^{17}O_1$-CO_2); 200.2>156.1 (loss of CO_2); $^{17}O_2$ Product: 201.2 >156.1 loss of $^{17}O_1$-CO_2); 201.2>157.1 (loss of CO_2). The mass spec results are summarized in Table 4.

Preparation of HPCA quinone.

HPCA was oxidized using mushroom tyrosinase (Sigma) in 100 mM MES buffer pH 5.6 and 4 °C. The reaction was initiated and monitored using the stopped-flow spectrometer with diode-array detection. A solution of 2 mM HPCA was mixed with 10 mg/ml mushroom tyrosinase. The quinone product formed during the first 5 min of the reaction and then slowly decayed to an unidentified secondary species.

Table 4: Mass spec Analysis of ^{17}O-C3-HPCA.

Compound	SRM Transition (MS/MS)	Intensity	%	corrected %
HPCA	167.2 > 123.1	22902	92.8	
HPCA	168.2 > 124.1	1801	7.2	
^{17}O(C3)-HPCA	167.2 > 123.1	6372	30.3	32.6
^{17}O(C3)-HPCA	168.2 > 124.1	14648	69.7	67.3

RESULTS

Single-turnover studies of the H200N-HPCA + O_2 reaction reveal a transient intermediate.

Previous stopped-flow studies revealed the accumulation of at least four reaction cycle intermediates after the pre-formed H200N-HPCA complex reacts with O_2 in a single-turnover reaction (*96*). Improvements in the stopped-flow instrumentation and procedures (*51*) allow the first of these intermediates to accumulate in higher yield so that it can be studied in detail.

As shown in Figure 24 A, for the reaction of a stoichiometric (per active site) H200N-HPCA complex with a slight excess of O_2 at pH 7.5, the previously described 610 nm transient intermediate ($H200N_{Int1}^{HPCA}$, $\varepsilon_{610\ nm} \sim 1100\ M^{-1}\ cm^{-1}$) rapidly accumulates and then more slowly decays to give the ring-cleaved product ($\varepsilon_{380\ nm} \sim 38{,}000\ M^{-1}\ cm^{-1}$). The absorption maximum for product is shifted to 325 nm ($\varepsilon_{325\ nm} \sim 23{,}600\ M^{-1}\ cm^{-1}$) when the reaction is conducted at pH 5.5, allowing a second maximum in the spectrum of $H200N_{Int1}^{HPCA}$ to be observed near 395 nm ($\varepsilon_{395\ nm} \sim 3200\ M^{-1}\ cm^{-1}$) (Figure 24 B). These same features plus an additional feature at 310 nm are revealed by subtracting the 3 ms spectrum from the 32 ms spectrum for the reaction at pH 7.5 (Figure 24 A, inset). When the reaction is conducted at pseudo first-order concentrations of O_2 at pH 7.5 (Figure 25), the time course can be fit well by a two-summed exponential equation with reciprocal relaxation times of $1/\tau_1 = 230 \pm 20\ s^{-1}$ and $1/\tau_2 = 1.60 \pm 0.15\ s^{-1}$, showing that the reaction consists of at least two steps. The spectroscopic data reported below shows that the intermediate builds to nearly stoichiometric yield. The observed value of $1/\tau_1$ is linearly dependent on O_2 concentration with a zero intercept, (*96*) suggesting that the reaction involves irreversible O_2 binding with a $1/\tau_1 = k_{form} = k_1$. The formation of the alkylperoxo intermediate and the ring-cleaving reaction are also likely to be irreversible so that $1/\tau_2 = k_{decay} = k_2$ for $H200N_{Int1}^{HPCA}$. At pH 5.5, the reaction is slightly slower due to a decrease in k_2 ($k_1 = 235 \pm 20\ s^{-1}$ and $k_2 = 1.1 \pm 0.1\ s^{-1}$).

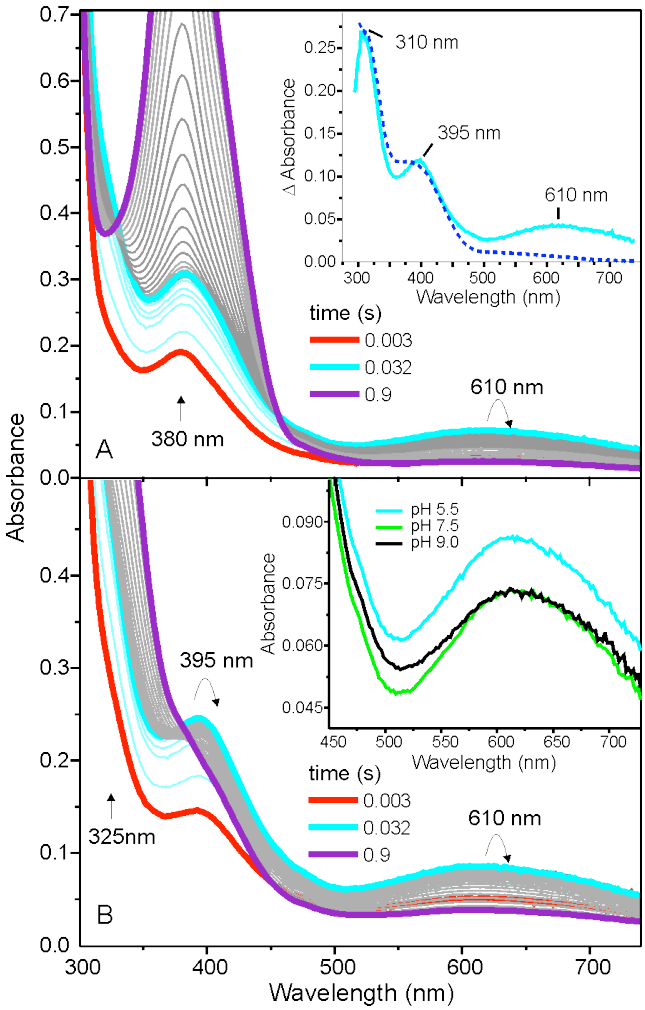

Figure 24: H200N-HPCA + O_2 reaction monitored by stopped-flow.
Panel A shows diode array spectra recorded between 3 ms and 2 s after mixing stoichiometric 640 μM (sites) H200N-HPCA anaerobic complex with O_2-saturated buffer (~ 1.8 mM) (1:1) at 4 °C in 200 mM MOPS pH 7.5 (2 mm pathlength). The thick line spectra are for the specific times shown. Thin line cyan, 3 – 32 ms; gray, 32 ms – 2 s. The inset shows spectrum that results from subtracting the spectrum at 3 ms from that at 32 ms (cyan) and the spectrum of HPCA quinone produced by treatment of HPCA with mushroom tyrosinase (blue, dashed). Panel B shows the time course of the same reaction as in Panel A, but in 200 mM MES buffer pH 5.5. *Inset*: Comparison of the spectra of the 610 nm feature formed at pH 5.5, 7.5, and 9.0.

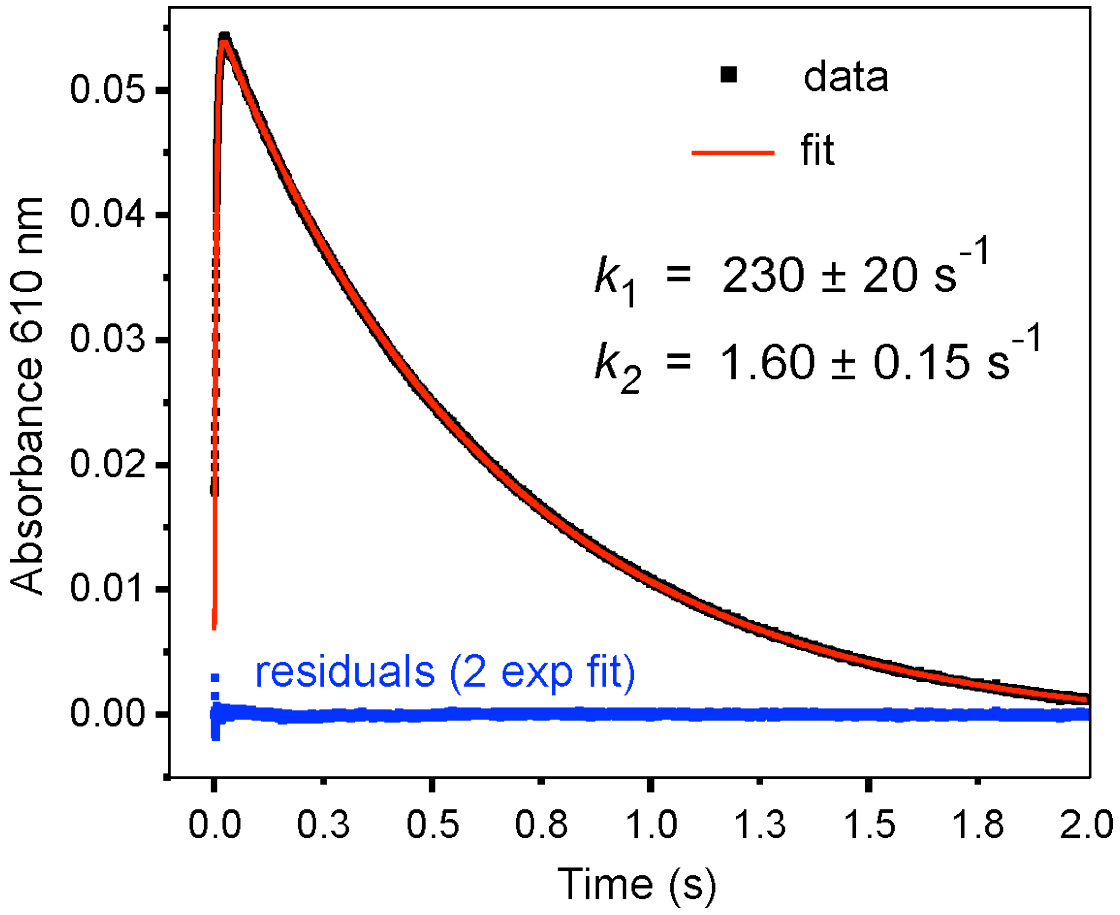

Figure 25: The time course of the reaction of H200N-HPCA + O_2 monitored at 610 nm. After mixing 100 μM total concentration of H200N-HPCA. Anaerobic stoichiometric (sites) H200N-HPCA is mixed 1:1 with 600 μM O_2-containing 200 mM MOPS buffer at pH 7.5 (1 cm pathlength) (black line). The 610 nm data can be fit to a sum of two exponentials (red line).

The two reciprocal relaxation times derived from the fits of the time course at this pH are found to be independent of wavelength when monitored at 310, 395, or 610 nm, suggesting that all features result from $H200N_{Int1}^{HPCA}$. The spectra of the intermediate change very little in the range between pH 5.5 and 9 (Figure 24 B, inset). The reaction could not be monitored at pH values significantly above pH 9 due to structural alterations of the enzyme.

RFQ EPR and Mössbauer studies show that $H200N_{Int1}^{HPCA}$ has an S_1=5/2 Fe(III) site coupled to an S_R =½ radical.

The anaerobic H200N-HPCA complexes (see below) contain a high-spin Fe(II) that is EPR-silent in both perpendicular (not shown) and parallel modes (Figure 26, top). The parallel mode EPR spectra of RFQ samples frozen at times between 20 ms and 2 s during the time course of the reaction of this complex with O_2 are shown in Figure 26. At 20 ms, an EPR resonance near g = 8.2 is observed in parallel mode (Figure 26). This feature maximizes at approximately 40 ms and then decays over the course of 2 s.

A superposition of the fit of the 610 nm stopped-flow data from Figure 25 and the g = 8.2 EPR time course is shown in Figure 26, inset. The congruence of these data indicates that the g = 8.2 EPR feature originates from $H200N_{Int1}^{HPCA}$. Furthermore, the observation of this signal in parallel mode and its absence in perpendicular mode demonstrates that it belongs to a species with integer electronic spin.

The EPR spectrum of $H200N_{Int1}^{HPCA}$ quenched at 40 ms is shown in more detail in Figure 27. The spectrum has contributions from two species, namely, $H200N_{Int1}^{HPCA}$ (g = 8.2) and a broader resonance from an Fe(II) species. At 2 K, the g = 8.2 signal intensity is small relative to that of the Fe(II) species. The g = 8.2 feature is significantly larger at 10 K, indicating that it originates from an *excited* spin doublet. The Mössbauer spectra discussed below (Figure 28) reveal that the iron of $H200N_{Int1}^{HPCA}$ is high-spin (S_1 = 5/2) Fe(III) that resides in a complex with integer spin. The Mössbauer and EPR data are readily reconciled by assuming that $H200N_{Int1}^{HPCA}$ has an S_1 = 5/2 site that is antiferromagnetically

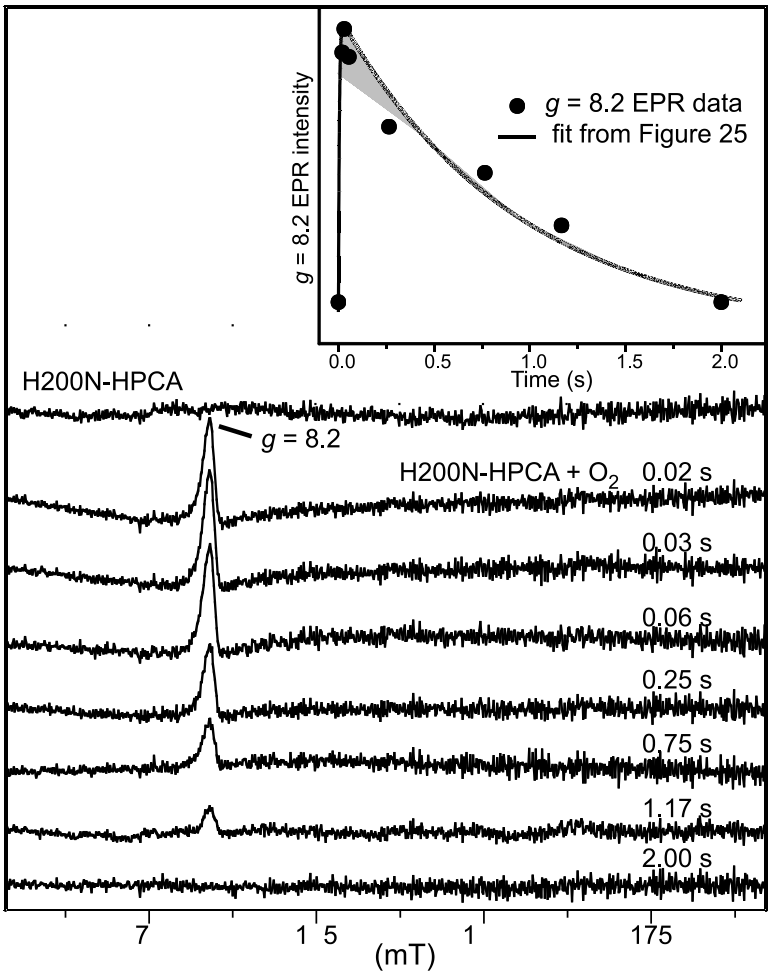

Figure 26: Time dependent parallel mode EPR spectra from the H200N-HPCA + O_2 reaction. Parallel mode EPR spectra in the *g* = 8 region of RFQ samples frozen between 0 (top, unreacted) and 2 s after mixing 1.65 mM anaerobic H200N-HPCA complex with O_2-saturated buffer (1:1) at 4 °C in 200 mM MOPS buffer, pH 7.5 are shown. EPR conditions: Frequency 9.35 GHz; microwave power, 50.4 mW; modulation amplitude, 1 mT, and temperature 50 K. *Inset:* Time course of the *g* = 8.2 signal intensity (•). The solid line is the fit to the *optically* monitored time course at 610 nm from Figure 24.

(AF, $J > 0$) coupled to an S_R = ½ radical. The exchange coupling separates the electric levels into a ground multiplet with S = 2 and an excited state with S = 3. The g = 8.2 signal originates from the M_S = ± 2 doublet, at energy $E \approx 5.4$ cm^{-1}, of the S = 2 multiplet; this doublet is indicated in the energy level diagram in Figure 27. The electronic levels of the system can be described by the spin Hamiltonian (this is the uncoupled representation):

$$\mathcal{H}_e = J\mathbf{S_1}\bullet\mathbf{S_R} + D_1[S^2_{1z} - 35/12 + (E/D)_1 (S^2_{1x} - S^2_{1y})] + \beta(\mathbf{S_1}\bullet\mathbf{g_1} + \mathbf{S_R}\bullet\mathbf{g_R})\bullet\mathbf{B} \qquad [3]$$

where the subscripts 1 and R refer to the Fe(III) and the radical, respectively. The exchange coupling (J), the zero-field splitting (D, E) of the ferric ion, and electronic Zeeman terms have their common definitions. Throughout this manuscript we will use isotropic g_1 = 2.015 and g_R = 2.00 (the data is sensitive only to the z-component of the tensors). For describing the broadening of the g = 8.2 resonance for ^{17}O enriched samples is advisable (reason given below) to use the S = 2 Hamiltonian (the coupled representation).

$$\mathcal{H}_{S=2} = D\,[S^2_z - 2 + (E/D)\,(S^2_x - S^2_y)] + \beta B_z g_z S_z + S_z A_z^{O,c} I_z^O \qquad [4]$$

The parameters of Eq. 4 are related to those of Eq. 3 by: $D = (4/3)D_1$, $E/D = (E/D)_1$ and $g_z = (7/6)g_{1z} - (1/6)g_{Rz} \approx 2.00$. The third term in Eq. 4 describes the hyperfine interaction of the ^{17}O nucleus with its electronic environment, where $A_z^{O,c}$ is expressed in the coupled representation. For the $^{17}O_2$ enriched sample, depending on the bonding, there could be one or two ^{17}O nuclei contributing to the broadening. The spectra are only broadened by the nuclear interaction and do not show resolved splittings, thus the derived value of $A_z^{O,c}$ assumes one ^{17}O interaction and is an upper limit (two equivalent ^{17}O nuclei would reduce $A_z^{O,c}$ by 25%). The temperature dependence of the g = 8.2 $H200N_{Int1}^{HPCA}$ signal in Figure 27 is plotted as signal times temperature versus temperature. Signal times temperature is proportional to the population of the EPR active doublet, and a fit

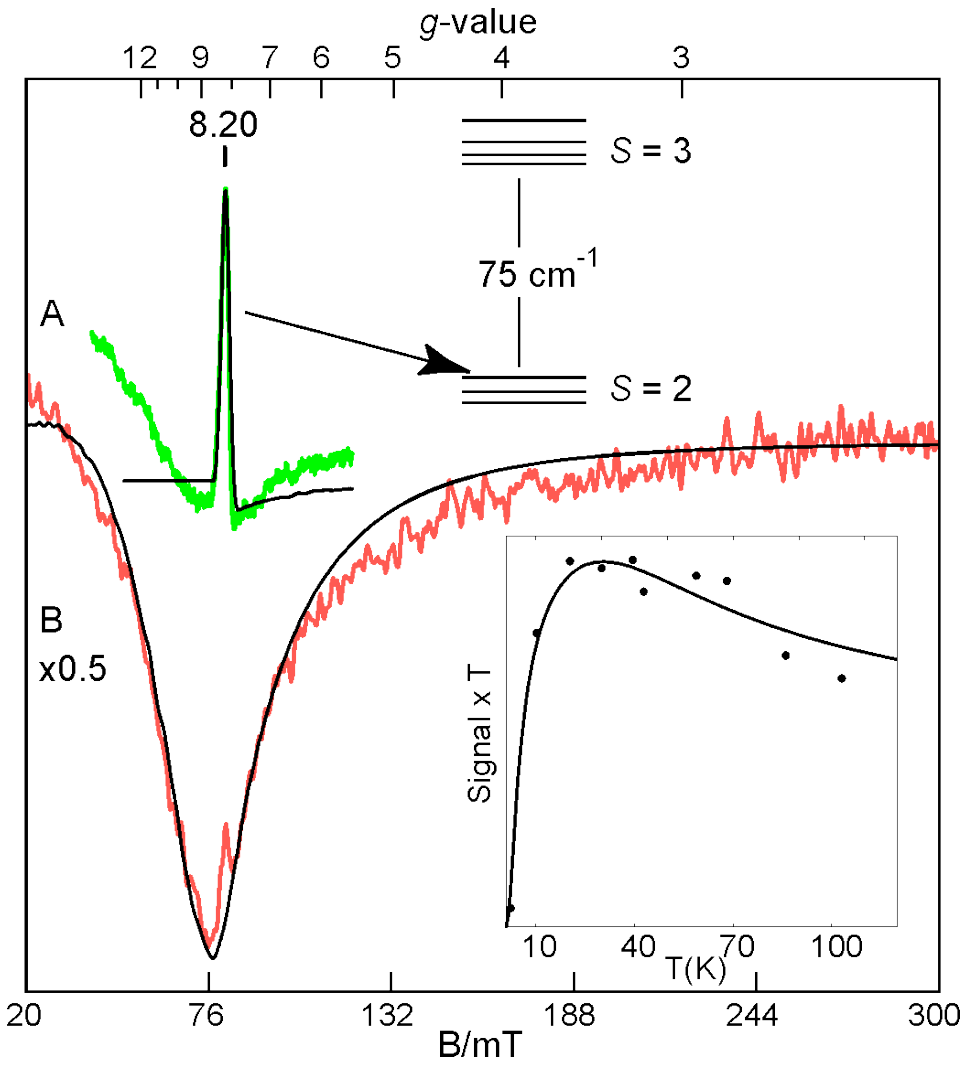

Figure 27: Parallel-mode EPR spectra (colored) and simulations (black) for H200N-HPCA frozen 40 ms after reaction with O_2. (A) 10 K and (B) 2 K. Prior to mixing with O_2-saturated buffer: 1.5 mM H200N-HPCA, 200 mM MOPS buffer pH 7.5. Simulation parameters: A: S_1 = 5/2, S_R=1/2, J = +25 cm^{-1}, D_1 = 1 cm^{-1}, E/D_1 = 0.12, g_{1z} = 2.015, g_{Rz} = 2.00. B: S = 2, D = -4 cm^{-1}, E/D = 0.15, g_z = 2.00. EPR conditions: microwaves, 20 mW (A), 0.2 mW (B) at 9.29 GHz; modulation, 1.0 mT. The intensity of B has been reduced by a factor of 2. The *inset* shows a plot of signal times temperature for the g = 8.2 feature and a theoretical fit to this intensity.

to the points based on Eq. 3 gives the exchange coupling constant J = +25 cm^{-1}. The rise of the signal at low temperature is due to the increasing population of the M_S = ± 2 level within the S = 2 multiplet, whereas its decline at higher temperature reflects population of the S = 3 multiplet. The solid line in Figure 27 A shows a SpinCount simulation of the $H200N_{Int1}^{HPCA}$ spectrum using the parameters given in the caption and in Table 5. For $J/D_1 \approx 25$, the system is in the strong coupling limit and consists of two well separated S = 2 and S = 3 multiplets. The intensity of the EPR signal (accounting for ≈ 80 % of the iron in the sample) is in approximate agreement with the concentration of the sample; however, due to somewhat variable packing density of the RFQ sample, this concentration has a 10 % uncertainty. Figure 27 B shows a simulation of the Fe(II) species with parameters given in the figure caption. This species accounts for ≈ 20 % of the iron in the sample, and it is not present in the starting Fe(II) enzyme prior to mixing with substrate and oxygen. Further details of this species are given below.

Figures 28 A-D show selected Mössbauer spectra from the time course of the H200N-HPCA reaction with O_2; these spectra were collected at 4.2 K in the absence of an applied magnetic field (B = 0). As reported previously, the iron site of H200N exhibits *one* doublet with quadrupole splitting ΔE_Q = 3.01 mm/s and isomer shift δ = 1.24 mm/s; these parameters are typical of high-spin Fe(II) with octahedral O/N coordination (*51*). The anaerobically prepared, stoichiometric H200N-HPCA sample of Figures 28 A exhibits two high-spin ferrous species, namely $H200N_{ES1}^{HPCA}$ (green, 60% of Fe) with ΔE_Q = 3.45 mm/s, δ = 1.16 mm/s and $H200N_{ES2}^{HPCA}$ (blue, 40%) with ΔE_Q = 2.32 mm/s, δ = 1.20 mm/s (see also Table 5). Samples prepared with a 2-fold excess of substrate or at pH 6 displayed the same species in the same ratio[b]. Within 20 ms after mixing the H200N-HPCA complex(es) with stoichiometric amounts of O_2, both doublets have disappeared. The 20 ms spectrum is dominated by a new

[b] The origin of the two enzyme-substrate species remains unknown. Crystal structures of enzyme-substrate complexes show that the small molecule ligand site of the iron has variable solvent occupancy, offering a possible source of the heterogeneity.

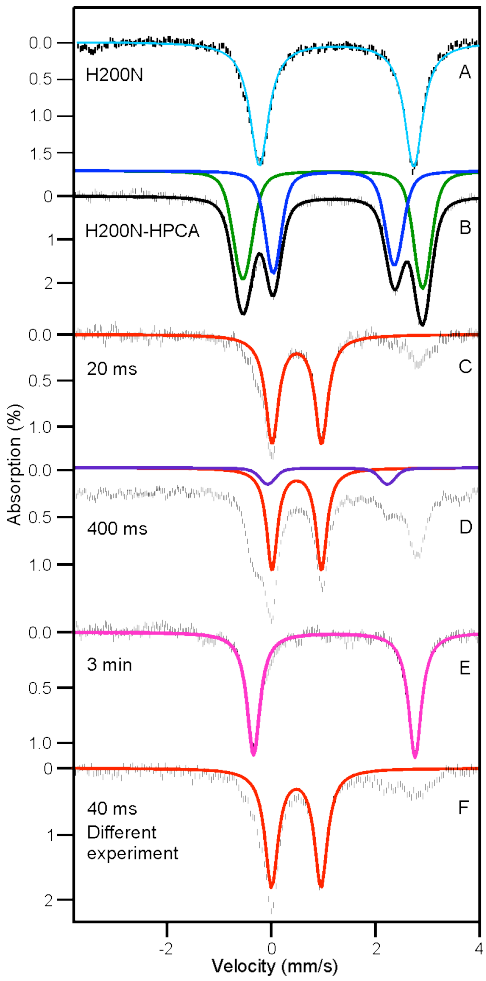

Figure 28: 4.2 K, zero field Mössbauer spectra of H200N-HPCA complexes. (A) H200N, 0.9 mM at pH 7.5 in 200 mM MOPS buffer. The colored line is a simulation. (B) Stoichiometric (sites) H200N-HPCA complex, 1.54 mM, at pH 7.5 in 200 mM MOPS buffer. Simulations of the doublets of the two enzyme-substrate complexes, $H200N_{ES1}{}^{HPCA}$ (green) and $H200N_{ES2}{}^{HPCA}$ (blue), are depicted by the colored lines. The black line represents the sum of the two species. (C-E) Reaction of 1.48 mM H200N-HPCA with O_2-saturated buffer (1:1). For the RFQ samples quenched at (C) 20 ms and (D) 400 ms, we have outlined in red the spectrum of the intermediate, $H200N_{Int1}{}^{HPCA}$. (E) Sample frozen (not by RFQ) at 3 min representing the end of the reaction. The colored line is a simulation of the spectrum. (F) B = 0 spectrum of the RFQ sample of Figure 28 prepared in a different experiment under the same conditions.

Table 5: Spin-Hamiltonian parameters for exchange coupled intermediates from EPR (italics) and Mössbauer spectroscopy.

Species	δ (mm/s)	ΔE_Q (mm/s)	η	J (cm^{-1})	D_1 (cm^{-1})	$(E/D)_1$	$A_0/g_n\beta_n$ (T)	A ° ((MHz)	
								$^{17}O_2$	[^{17}O] -HPCA
$H200N_{Int1}^{4NC}$	0.5	-0.33	-3[a]	*+6(2)*[a]	-0.59 *-0.48*	0.20 *0.20*	-21.4(2)	*180*	N/A
$H200N_{Int2}^{4NC}$	0.49	0.87	-7.2	*+40(10)*	+0.67 *+0.50*	0.11 *0.13*	-21.5(2)	*<5*	N/A
$H200N_{Int1}^{HPCA}$	0.48(1)	0.95(2)	+3[a]	*+25(5)*	+1.1[b] *+1.1*	0.12 *0.12*	-21.5(2)		
$H200N_{int1}^{HPCA}$ S = 2 Hamiltonian[b]	0.48	0.95	+3		1.5	0.12	-25.1	*17*	*17*

[a] η = +3 and -3 imply that the EFG is axial around the x and y axis, respectively.

[b] The last row lists the parameters as evaluated for S = 2 multiplet of the coupled system. The full Hamiltonian is given in Eq. 4. This representation must be used for analysis of the ^{17}O data (an explanation is given in the text). If the radical were on the O_2 moiety, the coupling in the uncoupled representation would be 6×17=102 MHz which can be compared with the 180 MHz reported for $H200N_{Int1}^{4NC}$.

species (representing ~ 75% of the Fe) with ΔE_Q = 0.95 mm/s and δ = 0.48 mm/s. This species, called $H200N_{Int1}^{HPCA}$, has a δ value typical of high-spin Fe(III) (S_1 = 5/2). The observation of a quadrupole doublet at 4.2 K in zero field, rather than a spectrum exhibiting paramagnetic hyperfine structure, as is usual for isolated Fe(III), suggests that $H200N_{Int1}^{HPCA}$ has an overall zero or integer spin. This is consistent with the formulation of $H200N_{Int1}^{HPCA}$ that emerged from our EPR studies. About 20-25% of the iron in 20 ms the sample belongs to an Fe(II) species, perhaps multiple species, with $\Delta E_Q \approx 3.10$ mm/s and $\delta \approx 1.20$ mm/s (this species may give rise to the broad integer spin EPR spectrum of Figure 27 B). As pointed out in Methods, at high mixing speeds some of the material bounces off the aluminum wheel of the quencher and cools more slowly, leading to the appearance of later species in earlier time point samples. Our kinetic data indicates the reaction has not progressed appreciably beyond $H200N_{Int1}^{HPCA}$ at 40 ms under the experimental conditions (Figure 29), suggesting that the ferrous species in the 20 ms sample, which differ(s) from the substrate complexes, arises from this "splashed" material. A spectrum recorded for a sample quenched at 40 ms (not shown) was identical to the one obtained at 20 ms, showing that the amount of material attributed to splash is constant, as expected. At 400 ms, the fraction of iron in $H200N_{Int1}^{HPCA}$ has decreased to 50% of the Fe in the sample (Figure 28 D). In this sample, approximately 10% of the Fe belongs to a doublet with $\Delta E_Q \approx 2.30$ mm/s and $\delta \approx 1.10$ mm/s (blue line in Figure 28 D); this ferrous species is possibly another intermediate (tentative $H200N_{Int2}^{HPCA}$, Table 5). Figure 28 E shows a spectrum of a sample frozen (not by RFQ) at 180 s, a time where solution kinetics predict product will have formed and dissociated (Figure 29). However, the parameters of the observed doublet are ΔE_Q = 3.10 mm/s and δ =1.20 mm/s (> 90% of Fe), which are slightly different from those of the substrate-free enzyme. It is possible that the high concentration of product present in the Mössbauer sample prevents net product dissociation or leads to a mixture of product bound and free enzyme in this sample. Accordingly, this species is also present in the 400 ms sample (representing roughly 20% of Fe over and above the splashed material), a time

at which approximately 25 % of the enzyme is expected to be present in the product complex (Figure 29). The product proved to be insufficiently stable to make an enzyme-product complex by adding purified product to resting enzyme.

Figure 28 E shows a zero field spectrum from a different set of experiments for a sample quenched at 40 ms. The sample contains about 70 % of the Fe in $H200N_{Int1}^{HPCA}$ (red line). Figure 30 shows spectra of this sample taken in parallel applied fields of 4.0 T and 8.0 T. The features observed are typical of high-spin Fe(III) sites (the middle section of the spectra is contaminated by the unknown spectral features of the "splashed" ferrous species). We have analyzed the spectra of $H200N_{Int1}^{HPCA}$ with the spin Hamiltonian $\mathcal{H} = \mathcal{H}_e + \mathcal{H}_{hf}$ (omitting the dipole-dipole term in $\mathcal{H}_e$ of Eq. 3) where $\mathcal{H}_{hf}$ describes the ^{57}Fe hyperfine interactions.

$$\mathcal{H}_{hf} = A_0\mathbf{S}_1\bullet\mathbf{I}_1 + (eQV_{zz}/12)[3I^2_{1z} - 15/4 + \eta(I^2_{1x} - I^2_{1y})] - g_n\beta_n\mathbf{B}\bullet\mathbf{I}_1 \qquad [5]$$

In Eq. 5 all symbols have their conventional meanings. For the ^{57}Fe magnetic hyperfine coupling constant of the ferric ion, we obtained $A_0/g_n\beta_n$ = -21.5 ±0.2 T, which compares well with A_0 values reported for octahedral Fe(III) sites with N/O coordination (*103*). This observation, together with the observation that the δ value of $H200N_{Int1}^{HPCA}$ falls squarely into the center of high-spin ferric δ values, indicates that the iron is Fe(III) with little delocalization between the radical and the ferric ion. From the field dependence of the Mössbauer spectra, we were able to constrain the zero field splitting parameter, D_1, as follows. The observation of the resonance at g = 8.2 implies that the EPR active doublet is split in zero field by $\Delta = (4/3)\ 3D_1(E_1/D_1)^2 \approx 0.065\ cm^{-1}$; (4/3 is a spin projection factor that enters through consideration of exchange coupling when the EPR data are described by Eq. 4). The high field Mössbauer spectra then constrain D_1 and $(E/D)_1$ to the reasonably narrow ranges $1.1\ cm^{-1} \le D_1 <\le 1.4\ cm^{-1}$ and $0.12 \le (E/D)_1 \le 0.14$. The red lines in Figure 30 are spectral simulations of $H200N_{Int1}^{HPCA}$ using the parameters listed in Table 5.

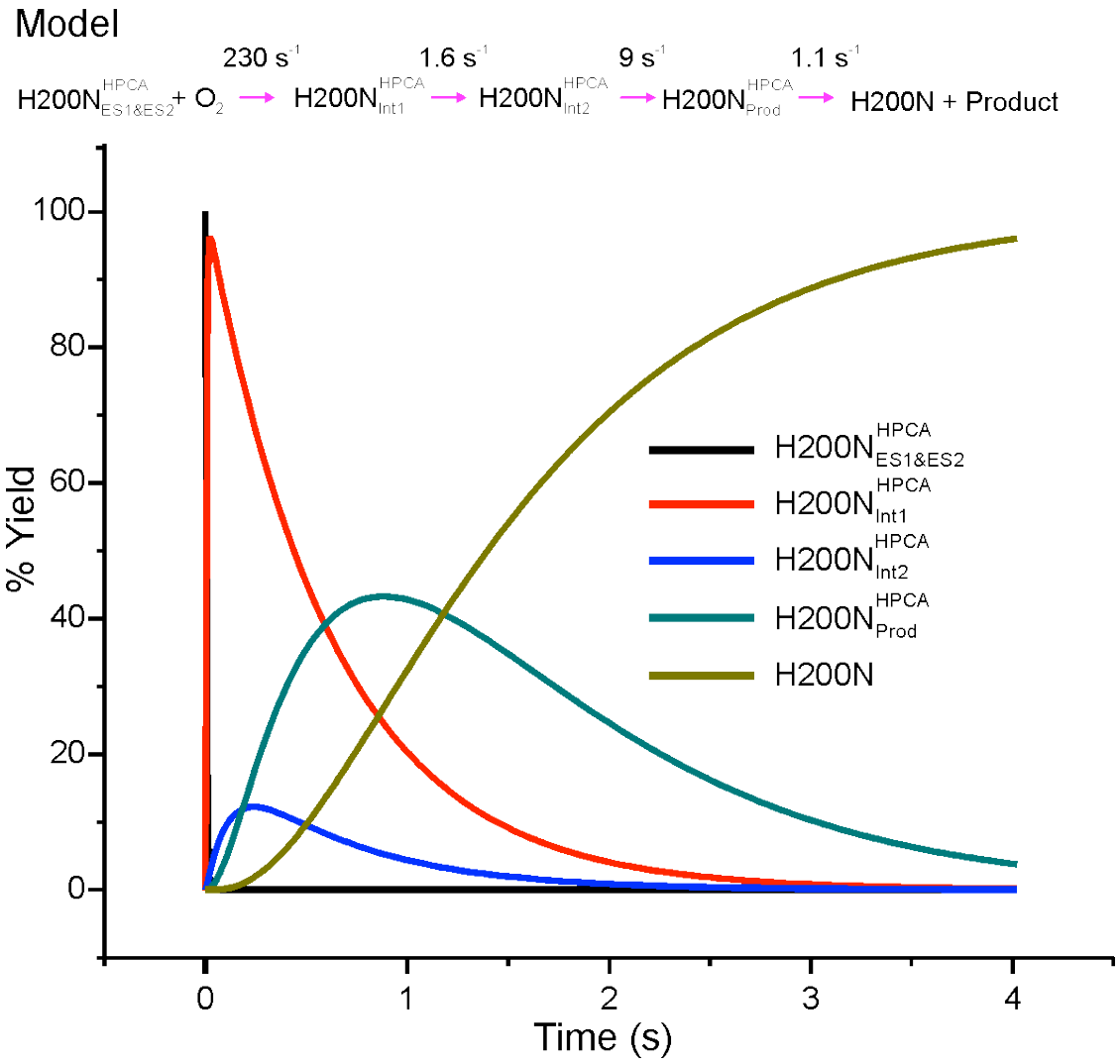

Figure 29: Numerical integration simulation of the time course of the H200N-HPCA + O_2 reaction.

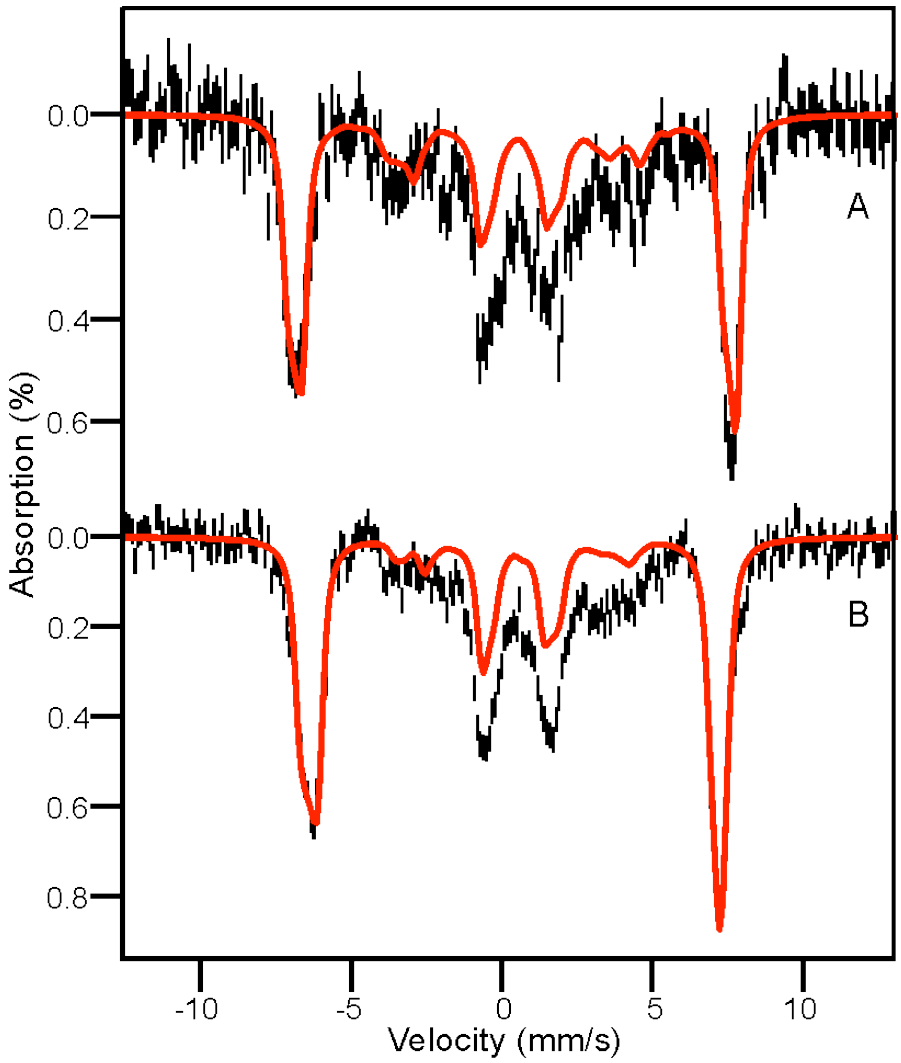

Figure 30: 4.2 K Mössbauer spectra of H200N_{Int1}^{HPCA} recorded in parallel applied magnetic field. (A) 4.0 T, and (B) 8.0 T. The central features of the spectra have unresolved contributions from the "splashed" ferrous contaminant. The red lines, drawn to represent 70 % of total Fe, are WMOSS spectral simulations based on Eq. 3 using the parameters listed in Table 5. This is the sample from Figure 27 F.

^{17}O-Hyperfine coupling suggests that H200N$_{Int1}^{HPCA}$ contains an Fe-peroxo and a substrate radical moiety.

To further probe the nature of the S_R = 1/2 species in H200N$_{Int1}^{HPCA}$, we have prepared samples enriched with ^{17}O in either $^{17}O_2$ or in ^{17}O-C3-HPCA (^{17}O, I_{17O} = 5/2). Parallel-mode EPR spectra of H200N$_{Int1}^{HPCA}$ prepared with $^{16}O_2$ (red), 70% enriched $^{17}O_2$ (blue), and 68% enriched ^{17}O-C3-HPCA (green) are shown in Figure 31. The g = 8.2 resonance of both enriched samples is broadened relative to its ^{16}O counterpart. For the two samples, the broadening is the same within the experimental uncertainty.

For our analysis of the ^{17}O broadenings, we used the S = 2 Hamiltonian of Eq. 4. As will emerge shortly, the uncoupled representation of Eq. 3 is less suitable for this analysis. Using Eq. 4, SpinCount analysis yielded $|A_z^{O,c}|$ = 17 MHz for both the $^{17}O_2$ and ^{17}O-C3-HPCA enriched samples. As mentioned above, the $^{17}O_2$ analysis assumes that only one ^{17}O nucleus contributes to the signal. The g = 8.2 resonance is observed when the applied field, B, is along the molecular z-direction defined by the zero-field splitting term of Eq. 4. Therefore, the spectra are only sensitive to A_z^O. We have considered whether the ^{17}O is part of the radical moiety (such as a superoxo radical) or whether it is part of a non-radical bearing ligand coordinated to the iron. In the former case, the ^{17}O A-tensor of the coupled representation is related to the intrinsic (uncoupled) hyperfine tensor by $A^{O,c}$ = (-1/6)A^O, which yields A_z^O = 102 MHz. In Chapter 1, we have characterized a related intermediate species from the same mutant HPCD using 4NC as a substrate, identified as an Fe(III)-$O_2^{\bullet-}$ species (*51*). The superoxo-based radical had a substantially larger A_z^O = 180 MHz, resulting in a profound broadening of the EPR signal, and different values of J, D_1 and $(E/D)_1$ (see Table 5). One might suspect that the reduced A_z^O reflects a superoxo radical that has donated significant negative spin density to the iron. However, if this were the case, we would have observed a larger Mössbauer isomer shift and the ^{57}Fe A-tensor would exhibit substantial anisotropy due to a spin-dipolar term that would reflect the ferrous admixture to the site. This consideration is in

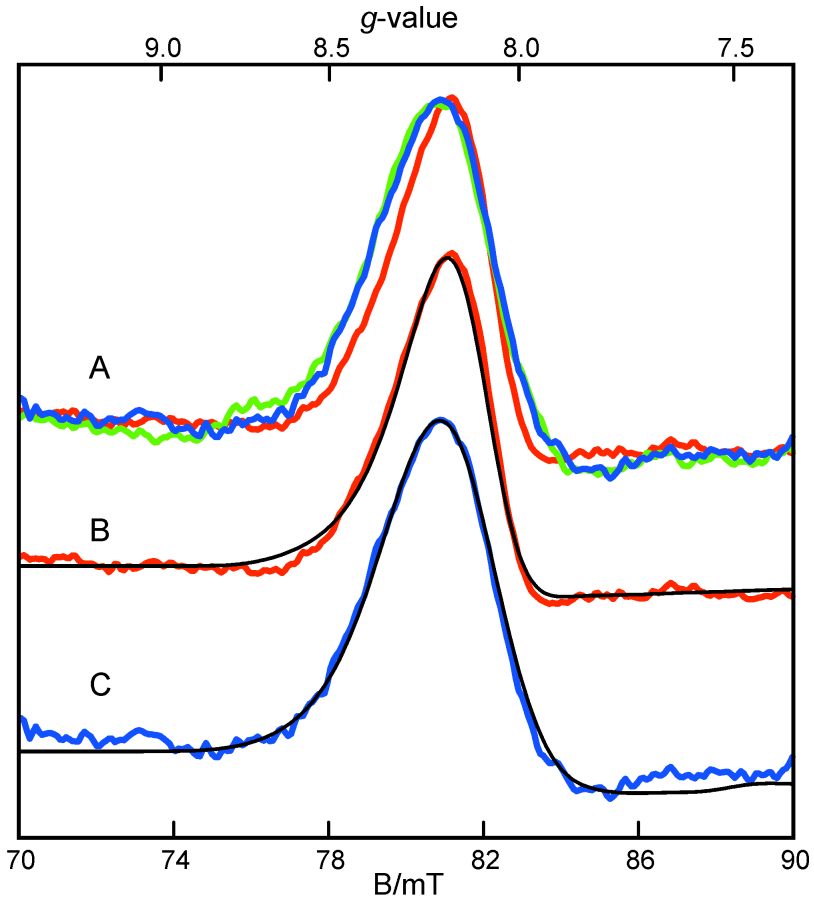

Figure 31: EPR spectra of isotopically enriched $H200N_{Int1}^{HPCA}$.
(A) Prepared with (red) natural abundance isotopes, (blue) 70% enriched $^{17}O_2$, (green) HPCA enriched to 68% with ^{17}O at the C3 OH functional group. Samples were prepared as described in Figure 25. Conditions before mixing: 1.65 mM H200N-HPCA complex, saturated O_2-containing buffer, 200 mM MOPS pH 7.5 and 4 °C. EPR conditions: Frequency 9.29 GHz; microwave power, 20 mW; modulation, 1.0 mT, temperature, 10 K. The simulations of natural abundance (B) and 70% enriched $^{17}O_2$ (C) samples are for S = 2, D = 1.3 cm^{-1}, E/D = 0.12, with $A_z^{O,c}$ of 0 (B) or 17 MHz (C).

in marked contrast to what is observed here. We thus conclude that $H200N_{Int1}{}^{HPCA}$ does not contain a superoxo radical, but instead contains a radical which resides on the HPCA moiety, presumably as an aromatic radical. Indeed, none of the other iron ligands are likely radical sites. The broadening from $^{17}O_2$ enrichment is therefore likely due to a peroxo species bound to the iron in a HPCA$^{\bullet}$- Fe(III)-(hydro)peroxo complex. If the radical is located on the HPCA, the observed ^{17}O hyperfine coupling would be due to covalent spin polarization delocalization of the peroxo moiety by the ferric ion. In this case, the ^{17}O *A*-tensor in the coupled representation is related to the intrinsic (uncoupled) hyperfine tensor by $A^{O,c} = (7/6)A^{O}$, from which we obtain $|A_z{}^{O}| = 15$ MHz.

The labeling of the ^{17}O-C3-HPCA results in a broadening of the spectrum comparable to that of the $^{17}O_2$ sample. The interpretation of the broadening for ^{17}O-C3-HPCA is significantly more complex, because the C3 oxygen may have spin density contributions not only from coordination to the Fe(III) but also from the HPCA radical. A covalent spin polarization contribution to the ^{17}O hyperfine interaction induced by the Fe(III) has a favorable spin projection factor (+7/6), compared to the (-1/6) factor for the case in which the radical resides on the HPCA moiety (N.B. The use of Eq. 3, rather than Eq. 4, would bias the primary analysis of the EPR spectra.). Thus, for comparable spin density contributions to the labeled O (Fe *vs*. HPCA•) the *A*-value would be dominated by the contribution from the Fe(III). In the absence of quantitative insight about the source of the spin density at the C3 oxygen by quantum chemical calculations it seems prudent to reserve judgment as to the precise origin of the broadening by ^{17}O-C3-HPCA[c].

[c] Very little EPR linewidth change was observed when uniformly enriched ^{13}C-HPCA was used (data not shown). Since the ^{13}C would be part of the radical moiety, the spin projection factor (-1/6) would strongly suppress the broadening. Ongoing DFT computations showed that the ^{13}C enrichment would not broaden the $g = 8.2$ resonance to any significant extent even if the radical would be centered on labeled carbon.

Stopped-flow spectroscopy of the FeHPCA + O_2 reaction reveals no evidence for an intermediate similar to $H200N_{Int1}^{HPCA}$.

Figure 32 shows diode array spectra from the single-turnover reaction in which pre-formed, anaerobic, stoichiometric FeHPCD-HPCA substrate complex is rapidly mixed with O_2-containing buffer at 4 °C. The spectra show only formation of the ring-cleaved product with λ_{max} near 380 nm with no detectable chromophore in the lower energy region from 500 - 700 nm; reaction of a 1 mM FeHPCD-HPCA sample also failed to show a long wavelength band. However, kinetic analysis of product formation using a single wavelength trace at 380 nm has previously revealed that product formation proceeds in several phases, including a fast phase that decays with k_1 ~ 38 s^{-1} and a slower phase with k_2 ~ 3.8 s^{-1} (*95*).

In our current preparations, both rates are slightly faster (k_1 = 59 ± 4 s^{-1} and with k_2 = 6.0 ± 0.5 s^{-1}). The fast phase is associated with a lag in product formation as shown in Figure 32, *inset*, and precedes formation of the product chromophore. Consequently, while there are discrete intermediates in the oxygen activation and insertion processes, none of the detectible intermediates have optical features like $H200N_{Int1}^{HPCA}$. Following mixing of the FeHPCD-HPCA complex with O_2, single wavelength data at 380 nm (Figure 32, *inset*) show that the lag phase persists to ~ 30 ms, providing an opportunity to use the RFQ approach for trapping reaction intermediates that precede product formation in the FeHPCD + O_2 reaction.

RFQ samples from the FeHPCD + O_2 reaction reveal an Fe(II) reaction intermediate.

Because both the H200N-4NC + O_2 and H200N-HPCA + O_2 reactions have revealed high yields of oxygenated intermediates at times < 1 s (Figure 24 - 31 (*51*)), we have prepared RFQ samples from the wild type FeHPCD-HPCA + O_2 reaction in order to look for reaction intermediates associated with the lag phase in the kinetic time course before product formation.

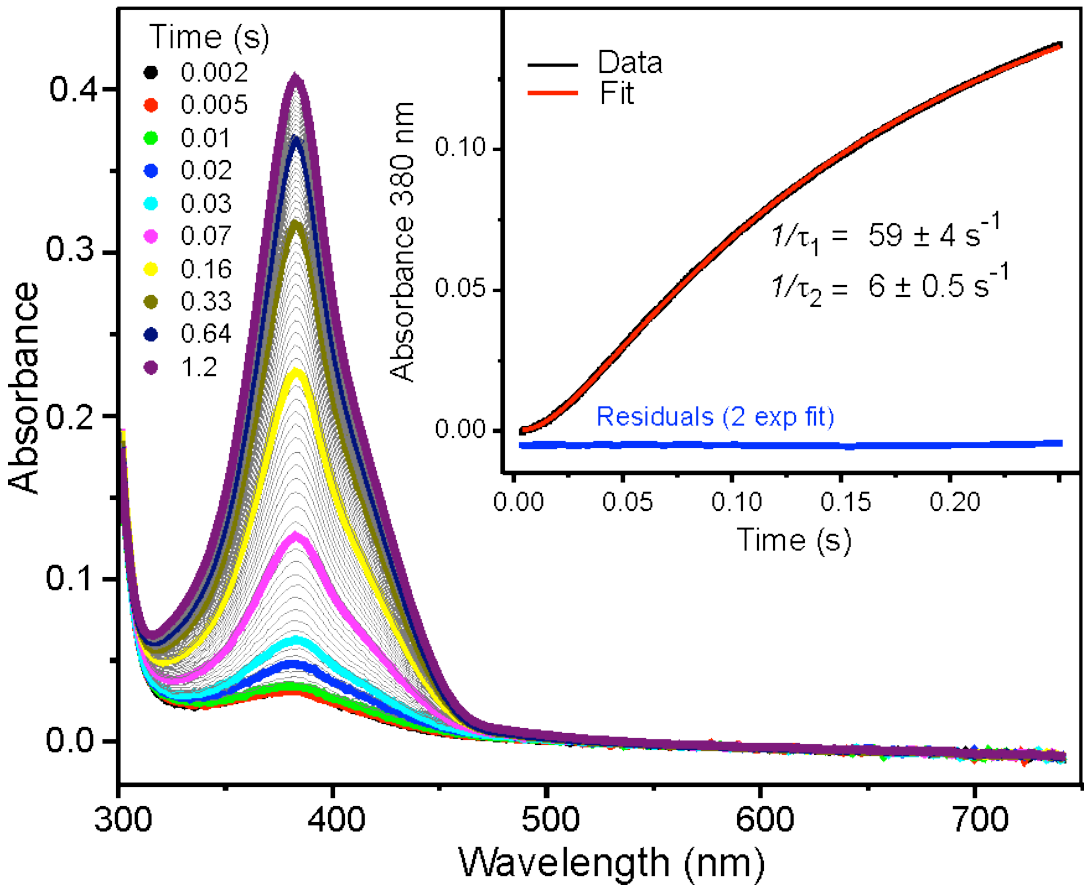

Figure 32: FeHPCD-HPCA + O_2 reaction monitored by stopped-flow. Diode array spectra recorded between 4 ms and 2 s after mixing 100 μM (based on active sites) stoichiometric, anaerobic FeHPCD-HPCA complex with O_2 saturated buffer (~1.8 mM) at 4 °C in 200 mM MOPS pH 7.5 (2 mm path length). Inset: Reaction monitored by single wavelength stopped-flow spectroscopy at 380 nm. In the time range shown, the data (black line) can be fit to a sum of two exponential terms (red line) with the reciprocal relaxation times shown.

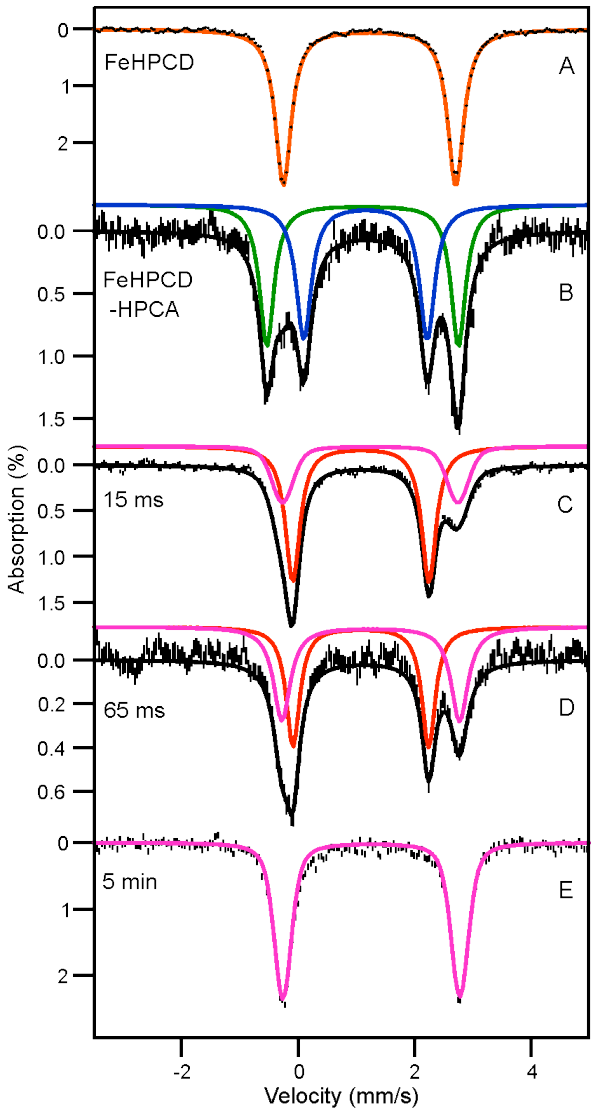

Figure 33: Mössbauer spectra from the FeHPCD-HPCA + O_2 reaction at 4.2K for B = 0. (A): FeHPCD, (B): The anaerobic FeHPCD-HPCA complex, (C): FeHPCD-HPCA + O_2 at 15 ms after mixing with O_2, (D): FeHPCD-HPCA + O_2 at 65 ms after mixing with O_2, (E): 5 min after mixing. Conditions before mixing: ~ 1.8 mM enzyme-substrate complex, 200 mM MOPS, pH 7.5, and 4 °C all reactions. For (A) the sample concentration was ~ 0.9 mM.

The Mössbauer spectrum of the resting state WT enzyme consists of one doublet with ΔE_Q = 2.97 mm/s and δ = 1.23 mm/s, consistent with a 6-coordinate high-spin Fe(II) species (Figure 33 A) (*100, 101*). Anaerobic addition of HPCA to the resting state WT enzyme yields a Mössbauer spectrum consisting of two ferrous doublets (Figure 33 B). One doublet accounts for 55% of the iron with parameters ΔE_Q = 3.29 mm/s and δ = 1.14 mm/s ($FeHPCD_{ES1}^{HPCA}$, Table 6) while the other species has 45% of the iron giving a doublet with parameters ΔE_Q = 2.18 mm/s and δ = 1.18 mm/s ($FeHPCD_{ES2}^{HPCA}$, Table 6) [d]. The spectrum of a sample frozen at 15 ms, which is within the lag phase of the FeHPCD-HPCA + O_2 reaction, is shown in Figure 33 C. It reveals two new species exhibiting quadrupole doublets from ferrous ions. One doublet has ΔE_Q = 2.33 mm/s, δ = 1.08 mm/s ($FeHPCD_{Int1}^{HPCA}$, Table 6) and accounts for ~ 70% of the iron. This species appears to decay to the second species which has parameters similar to those of the resting state enzyme (ΔE_Q = 3.03 mm/s, δ = 1.24 mm/s) which amounts to ~95% of the signal shown at the end of the reaction (Figure 32 E). It is not clear whether this is the product-free resting enzyme or enzyme with product still bound due to its relatively high concentration in the Mössbauer sample. Its presence in the 15 ms sample may again be due to splash from the freezing wheels at high ram velocity. Our combined stopped-flow and RFQ/Mössbauer data suggest that $FeHPCD_{Int1}^{HPCA}$ is a ferrous reaction intermediate which accumulates to nearly quantitative yields in the reaction cycle of the wildtype enzyme.

[d] Note that these parameters differ from those observed for the H200N-HPCA complex. .

Table 6: Comparison of quadrupole splitting and isomer shift parameters for the Mössbauer spectra of FeHPCD and its variants and complexes.

Species	ΔE_Q (mm/s)	δ (mm/s)	% present in sample at maximum
FeHPCD	2.97(3)	1.23(2)	>90
H200N	3.01(3)	1.24(2)	>90
H200N-4NC[1]	3.57	1.12	>90
$FeHPCD_{ES1}^{HPCA}$ $FeHPCD_{ES2}^{HPCA}$	3.29(3) 2.18(3)	1.14(2) 1.18(2)	55 45
$H200N_{ES1}^{HPCA}$ $H200N_{ES2}^{HPCA}$	3.45(3) 2.32(3)	1.16(2) 1.20(2)	60 40
$FeHPCD_{Int1}^{HPCA}$	2.33(3)	1.08(2)	~ 95[2]
$H200N_{Int1}^{HPCA}$	0.95(2)	0.48(1)	~ 95[2]
$H200N_{Int2}^{HPCA}$	≈2.30	≈1.10	~ 10

[1] From Ref (*51*).

[2] After correction for material splashed from the rapid freezing surface at high ram velocities.

DISCUSSION

The isolation and characterization of the intermediates that follow binding of O_2 in the reaction cycle of Fe(II)-containing catechol dioxygenases such as FeHPCD has been an elusive goal. Our recent characterization of the relatively long-lived intermediates in the reaction of H200N-4NC with O_2 was informative; however, the reaction leads to ring oxidation rather than ring cleavage (*51, 96*). The short lifetimes of intermediates in the reaction cycles of WT and mutant enzymes catalyzing ring cleavage reactions present a greater challenge. Here, the intermediates formed after oxygen binding in the H200N- and FeHPCD-catalyzed ring cleavage of HPCA have been trapped for spectroscopic characterization and comparison. The results show that the first intermediates trapped after O_2 addition in each of these systems differ fundamentally from each other as well as from the 4NC-Fe(III)-superoxo intermediate trapped in the non-ring cleaving H200N-4NC + O_2 system. The structural insights gained from the evaluation of the spectra of these intermediates and the relevance to the mechanism of O_2 activation for aromatic ring cleavage are discussed here.

Identity of $H200N_{Int1}^{HPCA}$.

The studies described here show that $H200N_{Int1}^{HPCA}$ contains a high-spin Fe(III) (S_1 = 5/2) site that is antiferromagnetically coupled to a radical (S_R = 1/2) to yield a ground multiplet with S = 2. The ^{57}Fe magnetic hyperfine coupling of $H200N_{Int1}^{HPCA}$ ($A_0/g_n\beta_n$ = -21.5 T) compares well to those observed for mononuclear Fe(III) sites and the isomer shift, δ = 0.48 mm/s, is characteristic of octahedral high-spin Fe(III) sites with N/O ligands (Table 6) (*51, 100, 101, 119*). As judged by the values of A_0 and δ, one electron has been transferred from the Fe(II). A radical species that couples to the resulting Fe(III) must have been formed either directly or indirectly as a result of this transfer.

The most likely candidates for the S_R = 1/2 species bound to the Fe(III) are suggested by the two intermediates discovered during our previous study of the H200N-4NC + O_2 reaction; namely, $H200N_{Int1}^{4NC}$ formulated as 4NC-Fe(III)-

$O_{2^{\cdot-}}$ and $H200N_{Int2}^{4NC}$ formulated as 4NC$^{\cdot}$-Fe(III)- (hydro)peroxo. The spectroscopic data for $H200N_{Int1}^{HPCA}$ are overall quite similar to those of the latter, $H200N_{Int2}^{4NC}$, and differ significantly from the former. Specific similarities include: Mössbauer parameters, EPR spectra, substantially positive *J* values (antiferromagnetic) with $D_1 > 0$, and small ^{17}O hyperfine constants. In contrast, the 4NC-Fe(III)- $O_{2^{\cdot-}}$ complex has a much smaller *J* value (6 cm^{-1}) , $D_1 < 0$, and its EPR signal is significantly more broadened when $^{17}O_2$ is used. Thus, we propose that $H200N_{Int1}^{HPCA}$ is formulated as HPCA$^{\cdot}$-Fe(III)-(hydro)peroxo [b].

The HPCA-SQ$^{\cdot}$ as the site of the radical is in accord with the crystallographic structure of the oxy-intermediate formed in the reaction of FeHPCD-4NC with O_2, which revealed substantial ring deformation at the carbon, where oxygen subsequently attacks to form the alkylperoxo intermediate. This suggests that a localized radical forms at this carbon of the ring (*50*). However, the 2.4 Å bond lengths of the metal ligands to the bound dioxygen species which we see in this intermediate, suggest that the iron is in the Fe(II) state. This would mean that the bound oxygen is likely to be superoxo rather than peroxo.

The UV-vis spectrum of $H200N_{Int1}^{HPCA}$ shows three main features; namely, a high energy shoulder at ~310 nm ($\varepsilon_{310\ nm}$ ~ 7000 M^{-1} cm^{-1}), a maximum at 395 nm ($\varepsilon_{395\ nm}$ ~ 3200 M^{-1} cm^{-1}) and a lower energy feature near 610 nm ($\varepsilon_{610\ nm}$ ~ 1100 M^{-1} cm^{-1}). This spectrum is inconsistent with HPCA bound in the catecholic form (*20, 120, 121*). The two higher energy features are similar to those observed for unbound catechol quinones and semiquinones, which themselves have similar spectra (Table 7) (*122, 123*). Indeed, the spectrum of $H200N_{Int1}^{HPCA}$ in the 300-500 nm region is very similar to that of HPCA quinone (Figure 24 A, *inset*, blue dashed spectrum). Binding of these molecules to oxidized metals causes little change in the band positions or intensities. However, the semiquinone complexes can give rise to additional charge transfer bands in the 600 - 800 nm region with widely ranging extinction coefficients (300 - 3000 M^{-1} cm^{-1}) (Table 7) (*124, 125*). Very few ligand-Fe(III)-SQ$^{\cdot}$ model complexes with $S = 2$ have been spectroscopically characterized, but those available show similar optical characteristics (Table 7) (*115, 125, 126*). When considered in light of the

EPR and Mössbauer analysis, the optical spectrum of $H200N_{Int1}^{HPCA}$ is most consistent with a HPCA-$SQ^{\cdot}$ radical and peroxo ligands bound to Fe(III).

While the 610 nm chromophore may derive from an HPCA $SQ^{\cdot}$-Fe(III) interaction, another possibility is a (hydro)peroxo-to-Fe(III) LMCT band, given the structure of $H200N_{Int1}^{HPCA}$ proposed here. A band in this region might also arise from a Fe(III)-OOR complex, but in the current case, this would be the alkylperoxo intermediate of the reaction cycle which is expected to contain Fe^{II} based on computational studies (*73, 127*). Many end-on Fe(III)-OOH and side-on bound Fe(III)-O_2^{2-} complexes from non-heme mononuclear model complexes have been characterized (Table 7) (*128, 129*). The Fe(III)-OOH complexes are often low-spin when the iron is coordinated by nitrogen ligands, but incorporation of at least one carboxylate ligand can result in a high spin Fe^{III}-OOH complex as would pertain to the intermediates of FeHPCD. In comparison to the 610 nm species observed here, the high spin Fe^{III}-OOH model complexes generally have a UV-vis transition with comparable intensity (ε = 450 - 2000 M^{-1} cm^{-1}) but shorter λ_{max} (440 - 570 nm) (Table 7) (*128, 129*).

In model compounds, it has been shown that the Fe(III)-OOH complexes can be deprotonated to form the conjugate base side-on bound Fe(III)-O_2^{2-} complex for pH > 10 (*128, 129*). In such a case, the resultant complex is often high spin, exhibiting a λ_{max} shift into the range of the 610 nm species (λ_{max} ~ 525 – 750 nm), but the ε values (ε = 450 - 600 M^{-1} cm^{-1}) are lower. Many of these side-on peroxo species have an EPR spectrum originating from an excited state like $H200N_{Int1}^{HPCA}$, but the Mössbauer isomer shift is somewhat larger (0.66 mm/s vs 0.48 mm/s). A third possibility is suggested by the high spin Fe(III)-(hydro)peroxo intermediate in benzoate 1,2-dioxygenase, which we know from the crystal structure of the equivalent intermediate found in naphthalene 1,2-dioxygenase to be a side-on bound Fe(III) species (*54*). Our spectroscopic analysis of the species from benzoate 1,2 dioxygenase shows that the

Table 7: Electronic parameters for quinone, semiquinone and peroxo model complexes.

Complex	λ_{max} nm (ε_M)	Ref
Fe(III)-η^1-OOR		
[Fe(6-MeTPA)H_2O(OO*t*-Bu)]	598 (2000[a])	(*130*)
[Fe(6-Me_2TPA)H_2O(OO*t*-Bu)]	552 (2000 [a])	(*130*)
[Fe(6-Me_3TPA)H_2O(OO*t*-Bu)]	562 (2000[a])	(*130*),(*131*)
[Fe(6-Me_3TPA)OBz(OO*t*-Bu)]	510 (2300[b])	(*132*)
[Fe(6-Me_3TPA)OBz(OOcumyl)]	506 (2300[b])	(*132*)
[Fe(BBPA)(OO*t*-Bu)]	613 (2000[a])	(*133*)
[Fe(BBPA)(OOcumyl)]	585 (2200[a])	(*133*)
[Fe(Me_4(15)aneN_4)SPh(OO*t*-Bu)]	630 (2300[b])	(*134*)
[Fe(Me_4(15)aneN_4)OTf(OO*t*-Bu)]	600 (1080[b])	(*134*)
[Fe(L_3Py_2)OTf(OO*t*-Bu)]	580 (2500[b])	(*135*)
[Fe(L_3Py_2)OBz(OO*t*-Bu)]	545(2700[b])	(*135*)
[Fe(L_3Py_2)SAr(OO*t*-Bu)]	510(2200[b])	(*135*)
[Fe(L_3Py_2)pyO (OO*t*-Bu)]	510(2450[b])	(*135*)
[Fe(L_4)(OO*t*-Bu)]	550 (700[c])	(*136*)
SLO-1 + 13-HPDO	590 (1400)[e]	(*137*)
15-RLO + 13-HPDO	580 (2400)[e]	(*138*)
Fe(III)-η^1-OOH		
[(TMC)Fe(η^1-OOH)]	500 (450)[a]	(*139*)
[Fe(H_2bppa)(OOH)]	568 (1200[d])	(*140*)
Fe(III)-η^2-OO^{2-}		
[(EDTA)Fe(η^2-O_2)]	520 (520)	(*141*)
[(TrispicMeen)Fe(η^2-O_2)]	740 (500[f])	(*142, 143*)
[(Ettpen)Fe(η^2-O_2)]	747 (500[f])	(*144*)
[(Bztpen)Fe(η^2-O_2)]	748 (500[f])	(*145*)
[(N4Py)Fe (η^2-O_2)]	685 (520[f])	(*129*)
[(Rtpen)Fe((η^2-O_2)]	716-771 (NA)	(*146*)
[(OEP)Fe(η^2-O_2)]-		(*147*)
[(Me-tpen)Fe((η^2-O_2)]	780 (>350[f])	(*148*)
[(N4Py-tpen)Fe(η^2-O_2)]	721 (521[f])	(*148*)
SOR-E47A-η^2-OO^{2-}	560 (400)	(*149*)
[(CYDTA)Fe(η^2-O_2)]	545	(*150*),(*151*)

Table 7 cont.	**Fe(III)-SQ**	
[L_1-Fe-DBSQ]	560 (6000)[h] 350 (8500)[h] 290 (20000)[h]	(*125*)
L_2-Fe-NPSQ	463 (NR)[g] 430 (NR)[g] 298 (NR)[g]	(*115*)
L_2-Fe-PheSQ	463 (NR)[g] 402 (NR)[g] 299 (NR)[g]	(*115*)
L_2-Fe-DBSQ	613 (NR)[g] 489 (NR)[g] 452 (NR)[g] 425 (NR)[g] 357 (NR)[g] 302 (NR)[g]	(*115*)
Semiquinone		
3,5-Di-tert-Butyl-o-Benzosemiquinone	~ 650 (~500)[i] 350-400 (~ 2900)[i] ~ 300 (~8000)[i]	(*152*)
Norepinephrine SQ	~ 310 (~5500)[e] ~ 350 (~ 2100)[e]	(*153*)
D L β-3,4-Dihydroxyphenylalanine SQ	~ 310 (~6000) ~ 350 (~ 2100)	(*153*)
2,5-dihydroxyphenylacetate SQ	~ 310 (~11000) ~ 350 - 425 (~ 6000)	(*153*)
6-hydroxydopamine SQ	~ 350 (~8000) ~ 450 (~ 3900)	(*153*)
Quinone		
4-Nitro-catechol Q	380 (8500)[e]	(*154*)
3, 4-Dihydroxyphenylalanine Q	305 (9332)[e] 475 (3467)[e]	(*155*)
Rubreserin	300 (9332)[e] 480 (2754)[e]	(*156*)
Adrenochrome	300 (NR)[e] 480 (NR)[e]	(*156*)
3,5-Di-Tert-Butylquinone	~ 400 (~ 1900)[l]	(*122*)
Catechol Q	300 (NR)[e] 390 (1834)[e] 420 (2040)[e]	(*155*), (*154*)
4-Thiocyanato-Catechol Q	395 (1330)[e]	(*154*)

Table 7 cont. 4-Acetyl Catechol Q	410 (1090)[e]	(*154*)
4-Methyl Catechol Q	300 (NR)[e] 400 (NR)[e]	(*157*)
4-Formyl-catechol Q	410 (1470)[e]	(*154*)
4-*tert*-butylcatechol Q	420 (NR)	(*158*)
Dopa quinone	278 (NR) 395 (1250)[e]	(*158*)
Dopamine quinone	303 (NR) 394 (NR)	(*158*)
Norepinephrine Q	296 (NR) 384 (NR)	(*158*)
Epinephrine	302 (NR) 387 (NR)	(*158*)
N-Acetyldopamine	392 (NR)	(*158*)

Abbreviations for Table 7: Solvent are denoted by the superscript: a = acetonitrile, b = dichloromethane, c = diethylether, d = acetone, e = aqueous, f = methanol, g = benzene, h = THF, i = dimethylformamide. NR = not reported, L_1 = N,N'-bis(4-methyl-6-tert-butyl-2-methyl-phenolato)-N,N'-bismethyl- 1,2 diaminoethane, L_2 = N,N'-ethylenebis(salicylidenimine), L_3 = N,N'-bis(2-pyridylmethyl)-1,5-diazacyclooctane, L_4 = hydrotris(3-tert-butyl-5-isopropyl-1-pyrazolyl)borate. TPA = tris(2-pyridylmethyl)amine, BPPA = bis(6-pivalamido-2-pyridylmethyl)(2-pyridylmethyl)amine, $Me_4(15)aneN_4$ = 1,4,8,12-tetraazacyclopentadecane 1,4,8,12-Tetramethyl-1,4,8,12-tetraazocyclopentadecane, OTf = ortho-triflated, OBz = ortho-Benzoate, SAr = 4-methylbenzenethiolate, pyO = pyridine N-oxide.

Mössbauer isomer shift is 0.5 mm/s, as found for $H200N_{Int1}^{HPCA}$. We have proposed that this is due to protonation of the side-on bound peroxo moiety (*159*). If this is the case, a pH dependence might be expected for the low energy band of the $H200N_{Int1}^{HPCA}$ spectrum, but none is observed in the range between pH 5.5 and 9.0 (Figure 24 B, *inset*). One possible explanation for this is that the pK_a for this type of species is relatively high, as observed for the end-on hydroperoxo complexes, such that it remains protonated throughout the range of stability for the enzyme. Based on this analysis, it is not currently possible to definitively assign the origin of the 610 nm species, and it could, in fact, result from the sum of both Fe(III)-HPCA $SQ^{\cdot}$ and Fe(III)-(hydro)peroxo interactions. Resonance Raman data may provide an assignment, but attempts to obtain spectra to date have been unsuccessful due to experimental difficulties arising from the ice lattice of frozen RFQ samples.

Identity of $H200N_{Int2}^{HPCA}$.

Analysis of transient kinetic data from the time course of the 610 nm intermediate as well as product formation in the H200N-HPCA + O_2 reaction (values from the current preparation are shown in Figure 25, 29 and Scheme 1) (*96*) suggests that $H200N_{Int1}^{HPCA}$ accumulates to near stoichiometric yield.

$$\text{H200N-HPCA} \xrightarrow[O_2]{7 \times 10^5\ M^{-1}\ s^{-1}} H200N_{Int1}^{HPCA} \xrightarrow{1.6\ s^{-1}} H200N_{Int2}^{HPCA} \xrightarrow{9\ s^{-1}} \text{H200N-Product}$$

Scheme 1. Kinetic model from stopped-flow studies of the H200N-HPCA + O_2 reaction.

This is in accord with the Mössbauer and EPR spectra of this reaction intermediate shown here. On the other hand, the kinetic model predicts $H200N_{Int2}^{HPCA}$ would accumulate to only ~12 % at 400 ms due to the rapid decay

of the species (Figure 29). Analysis of the Mössbauer reaction time-course does show that $H200N_{Int2}^{HPCA}$ accumulates to only ~10 % at 400 ms (Figure 30 C). Due to low yields of $H200N_{Int2}^{HPCA}$, we were unable to obtain precise Mössbauer parameters of this species. However, it is clear that $H200N_{Int2}^{HPCA}$ is ferrous with $\Delta E_Q \approx 2.33$ mm/s and $\delta \approx 1.1$-1.2 mm/s. It is possible that this species is either the predicted (Figure 23 D) HPCA$^{\cdot}$-Fe(II)-$O_2^{\cdot-}$, or perhaps more likely, the Fe(II)-alkylperoxo or lactone intermediates, which derive from $H200N_{Int1}^{HPCA}$ prior to formation of the yellow ring cleaved product.

Identity of $FeHPCD_{Int1}^{HPCA}$.

The Mössbauer parameters for $FeHPCD_{Int1}^{HPCA}$ show that this reaction intermediate contains a high-spin Fe(II) site, in sharp contrast to the Fe(III) containing initial intermediates described here and in our earlier study (*51*). Unlike $H200N_{Int1}^{HPCA}$, no optical spectrum of this intermediate could be detected even in the first few milliseconds of the reaction. Consequently, our stopped-flow studies of the FeHPCD-HPCA + O_2 reaction were limited to monitoring product formation, which is clearly at least a two-step process (*95*). The largest reciprocal relaxation time from this process makes the largest contribution to the observed lag phase and shows no O_2 concentration dependence. Thus, it is dominated by the rate constants for a step separated from the initial O_2 binding by at least one irreversible step. $FeHPCD_{Int1}^{HPCA}$ is temporally associated with this initial lag in product formation, suggesting that it occurs after the effectively irreversible step in the reaction. The lack of an optical spectrum from a semiquinone or quinone for $FeHPCD_{Int1}^{HPCA}$ is consistent with this hypothesis and also argues against a HPCA SQ$^{\cdot}$-Fe(II)-$O_2^{\cdot-}$ or HPCA quinone-Fe(II)-(hydro)peroxo structure. $FeHPCD_{Int1}^{HPCA}$ cannot be a product complex, which would be intensely yellow even before dissociation from the enzyme; the true product complex builds on a much longer time scale. Taken together, these observations suggest $FeHPCD_{Int1}^{HPCA}$ is one of the intermediates that results after oxygen attacks the substrate, but before ring cleavage, such as the alkylperoxo or lactone intermediates of the proposed reaction cycle. Accordingly,

the Mössbauer parameters for this species are very similar to those of $H200N_{Int2}^{HPCA}$ which is postulated above to be such a species.

Mechanistic implications of the observed intermediates.

Our studies of the intermediates of the O_2 activation and insertion portion of the extradiol dioxygenase reaction cycle have shown that the nature and reactivity of the intermediates are functions of both the electronic characteristics of the substrate and the amino acid residues present in the second sphere of the active site. Figure 33 illustrates the intermediates that have been trapped and characterized by various means. Studies thus far have focused on substrates with progressively more electron withdrawing *para*-substituents and mutation of the key acid/base catalyst, His200. It is found that when a shorter Asn residue is substituted for His200, two types of intermediates can rapidly form in nearly 100% yield, both of which contain Fe(III) spin-coupled to a radical. More specifically, an end-on bound Fe(III)-$O_2^{\cdot-}$ adduct is formed when the substrate has a strongly electron withdrawing *p*-nitro substituent (Figure 34 B) (*51*), whereas a substrate $SQ^{\cdot}$-Fe(III)-(hydro)peroxo species (peroxo orientation or protonation state is not definitively determined) is formed when HPCA with its electron donating substituent is used (Figure 34 C). These two intermediates differ substantially not only in their respective lifetimes, but also in the eventual outcomes of catalysis.

The 4NC-Fe(III)-$O_2^{\cdot-}$ intermediate persists for many minutes and eventually yields 4NC-quinone and H_2O_2, whereas the HPCA $SQ^{\cdot}$-Fe(III)-(hydro)peroxo intermediate disappears in 2 s at 4 °C and yields the normal ring cleaved product. The ability of O_2 to bind to the enzyme is also affected by the *para*-substituent of the substrate in the H200 mutant such that the binding rate constant is 4-fold slower and the binding event becomes reversible when 4NC is bound in place of HPCA (*96*). These observations suggest that the effects of

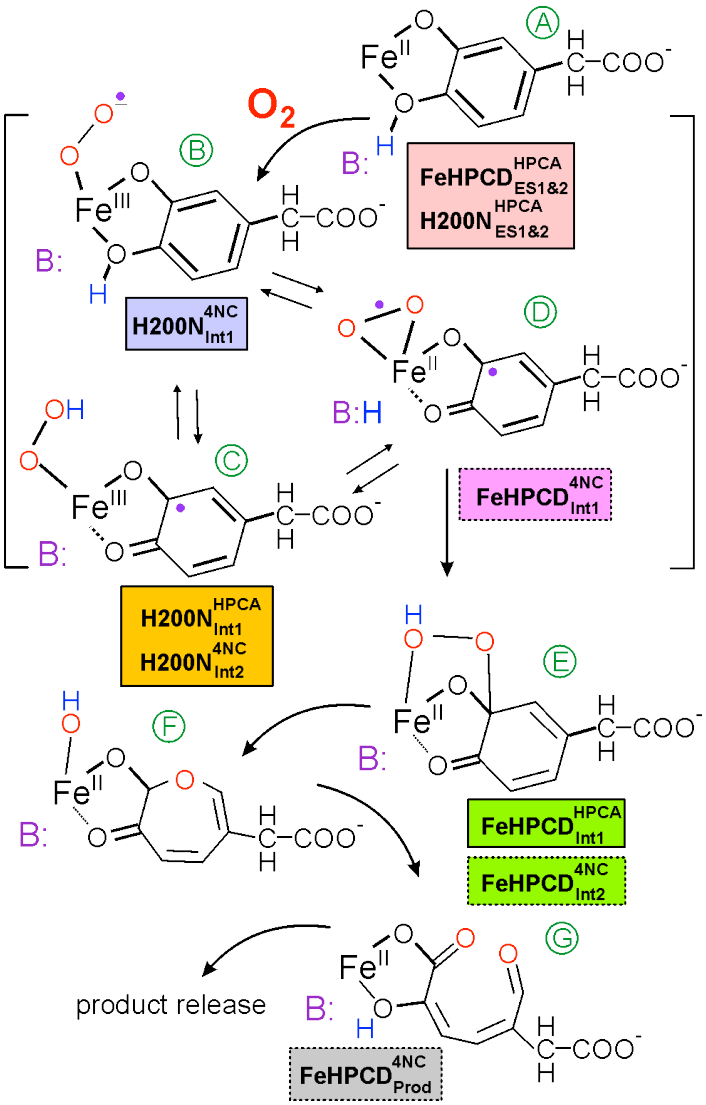

Figure 34: Intermediates from the FeHPCD and H200N turnover cycles. The intermediates shown are those proposed for the FeHPCD reaction with HPCA as the substrate. The colored boxes identify trapped intermediates that either correlate exactly with or are similar to these intermediates. The boxes with solid borders identify intermediates from solution RFQ studies reported here and in a previous study (*51*), while those with dashed borders are from crystal structures reported previously. (*50*)

either electron withdrawal or donation in the substrate ring are transmitted through the iron to affect its ability to share electrons with O_2 during binding. We have proposed that this transmission of electron density from the substrate through the iron to the bound O_2 is a fundamental aspect of oxygen activation in this enzyme family (*50, 82, 93*).

The reaction of the native enzyme with 4NC and HPCA reveals other aspects of the mechanism. When His200 is present, substrates with either electron withdrawing or donating substituents are converted into ring-cleaved products, albeit at 25-fold different rates. The crystallographically characterized intermediate in the reaction of FeHPCD-4NC with O_2 ($FeHPCD_{Int1}^{4NC}$) (Figure 34 D) (*50*) and the spectroscopically characterized $FeHPCD_{Int1}^{HPCA}$ intermediate (Figure 34 E) described here both have Fe(II) in the active site rather than Fe(III). However, the former appears to be a species with radical character on both the substrate and the bound O_2, while it is argued above that the latter is likely to be a state after oxygen attack on the substrate. If this is the case, then the formation and reaction of the reactive oxygen intermediate(s) must be very fast such that there is no evidence for any of the types of spin-coupled Fe(III) intermediates described here or in our previous study. This may mean that an Fe(III) species of some sort forms, but its lifetime is too short to be detected even on the millisecond time scale. Alternatively, the iron may serve purely as a conduit for electron density that does not change oxidation state as an electron is transferred from the catechol to O_2. The final alternative, namely that there is no transfer of electron density between the substrates is unlikely because the reaction of unactivated oxygen with catechols is slow and does not result in ring cleavage.

CONCLUSION

The oxy-intermediates that have been trapped thus far using FeHPCD and its variants with HPCA and alternative substrates show that a radical species can reside on either the substrate or the oxygen and that an electron can be transferred from the iron, the substrate, or both to the oxygen. Based on the *in crystallo* studies published previously (*50*), it is possible for an electron to be transferred in either a stepwise or a concerted fashion from the iron to the oxygen and from the substrate to the iron to yield a diradical pair. All of these observations support the most fundamental aspect of catalysis established for this enzyme class which envisions oxygen activation by coordinating oxygen reduction with substrate oxidation to form a reactive pair. The results reported in our previous study show that simple formation of an Fe(III)- $O_2^{\cdot-}$ species alone is not sufficient for high reactivity or ring cleaving chemistry. The current study suggests that, following electron transfer from the substrate, either a substrate $SQ^{\cdot}$-Fe(II)-$O_2^{\cdot-}$ or a substrate $SQ^{\cdot}$-Fe(III)-peroxo intermediate might serve as the reactive species. However, the high reactivity of the enzyme containing Fe(II), Mn(II), or Co(II) (*78, 160*) favors the substrate $SQ^{\cdot}$-Fe(II)-$O_2^{\cdot-}$ species, for which there is no net change in oxidation state between the enzyme-substrate complex and the reactive species. Although the current study suggests for the first time that a substrate $SQ^{\cdot}$-Fe(III)-peroxo intermediate can lead to ring cleavage, its low rate of reaction suggests that it is not the species that carries out this reaction in the reaction cycle of the WT enzyme. It is notable that the maximal rates of O_2 activation and reaction is achieved only when His200 is present . This is consistent with previous proposals that this residue plays many roles over and above its role as acid/base catalyst. These may include charge stabilization that promotes formation of the $SQ^{\cdot}$-Fe(II)-$O_2^{\cdot-}$ species as well as hydrogen bonding and steric interactions that properly orient the superoxo species for reaction with the activated substrate.

Chapter 2 contributions.

This work is supported by the NIH grant GM 24689 (to John. D. Lipscomb.), grant EB-001475 (Eckard Münck.), grant GM77387 (to Michael P. Hendrich) and graduate traineeship GM08700 (to Michael. M. Mbughuni). Mössbauer analyses were done by Eckard Münck, Mrinmoy Chakrabarti and Katlyn K. Meier. EPR simulations were done by Michael P. Hendrich and Joshua A. Hayden. Joseph J. Dalluge developed LC-MS methods for analysis of labeled HPCA. Also, many thank to Dr. David P. Ballou for the generous gift of the C_1 and C_2 enzymes used for synthesis of ^{17}O-labeled HPCA. All these contributions have made this work possible.

CHAPTER 3

Detection of novel ring-cleaving oxygenated intermediates from a tyrosine 257 mutant of 2,3-HPCD.

Abbreviations:

Y257F, Tyr to Phe variant of 2,3-HPCD at position 257.

Q, quinone of HPCA.

SQ, semiquinone radical.

H-bonding, hydrogen bonding interaction.

$Y257F_{Int1}^{HPCA}$ and $Y257F_{Int2}^{HPCA}$, novel intermediates observed in the Y257F-HPCA + O_2 reaction.

$Y257F_{ES}^{HPCA}$, substrate complex of Y257F with the substrate HPCA.

SUMMARY

Chapter 2 focused on RFQ and stopped-flow studies with the WT 2,3-HPCD and H200N mutant enzymes. These studies showed that 2,3-HPCD reacts with HPCA and O_2 to give the ring-cleaved product through a colorless Fe(II) reaction intermediate termed $FeHPCD_{Int1}^{HPCA}$. The corresponding reaction with the H200N mutant goes through a SQ-Fe(III)-(hydro)peroxo ($H200N_{Int1}^{HPCA}$) intermediate before forming an Fe(II) species ($H200N_{Int2}^{HPCA}$), which is most likely the species initiating oxygen insertion into the substrate to achieve the observed ring-cleaving chemistry. Chapter 3 will focus on studies with yet another mutant, the Y257F mutant of 2,3-HPCD. It is shown here that the Y257F-HPCA + O_2 reaction accumulates at least two reaction intermediates prior to formation of the ring-cleaved product, namely $Y257F_{Int1}^{HPCA}$ and $Y257F_{Int2}^{HPCA}$. The former accumulates as a consequence of an O_2 binding event and is marked by a distinct, yet short-lived lag-phase of the Y257F-HPCA + O_2 reaction time course. The latter is most likely a Q-Fe(II)-(H)peroxo (or possibly a SQ-Fe(II)-superoxo), exhibiting a distinct and intense chromophore at 425 nm which develops after the O_2-binding event. Steady-state and transient kinetic analysis shows that the k_{cat} for Y257F turnover of HPCA is about 20% of that of WT enzyme at pH 7.5 and 22 °C. Clearly, steps throughout the catalytic cycle are significantly slowed. The rate-limiting step appears to be one of the steps which lead to formation of a competent enzyme-substrate complex. This differs from the case for WT enzyme where the ring-opening appear to be rate limiting. The K_d for HPCA binding is similar to that observed for WT enzyme (< 5 μM), but K_m is increased by 10-fold, showing the effect of decreased rate constants in the catalytic cycle. The rate constant for O_2 binding is decreased at least 100-fold over that found for the WT enzyme and the binding becomes fully reversible at pH 7.5 (K_d = 400 μM). The O_2 binding rate is similar at pH 5.5, but the reaction is effectively irreversible. These effects on the rate of catalysis are discussed in the context of interactions between the second sphere Tyr257 and the bound HPCA substrate.

INTRODUCTION

X-ray crystallographic structures of oxygenated reaction cycle intermediates from 2,3-HPCD have revealed H200 as a residue which is uniquely positioned to interact with both the oxy complex and the C1-O^- from the bound 4NC substrate (Figures 43A, (*50*)). Even though H200 is not the only second sphere residue observed to interact with the oxy ligand, it is the only one capable of stabilizing the oxy ligand and also promote conversion of reaction intermediates to product through acid/base chemistry (*28*). This role for H200 as an acid/base catalyst is in accord with the H-bonding interactions observed for this residue in $FeHPCD_{Int1}{}^{4NC}$ (Figure 43A). The proposed roles for H200 have also been supported by solution studies of H200 mutants, which are reported in Chapter 1-2 and references (*95, 96*). Other residues observed within H-bonding distance from the oxy ligand include W192 and N157 (Figure 43A). However, these residues are not capable of acid/base chemistry and their roles in catalysis may be limited to stabilization of reaction intermediates through H-bonding interactions.

Another potentially important active site residue is Y257, which appears to play a key role by forming H-bonding interactions with the C3-O^- of the HPCA substrate and H248 (Figure 43B). In the structurally characterized SQ-Fe^{II}-$O_2{}^{\cdot-}$ and alkylperoxo intermediates, a homologous H-bond to the 4NC substrate is observed to increased in strength by out-of-plane displacement of the C2-O^- substituent of 4NC (Figure 46). We postulate that it promotes ring attack/cleaving chemistry in several ways related to favoring a tetrahedral geometry at the site of ring attack. In the SQ-Fe^{II}-$O_2{}^{\cdot-}$ complex, the 4NC ring is seen to become non-planar, forcing this deprotonated hydroxyl (C2-O^- in this case) below the plane of the ring (Figures 43A and 46). This, in turn, strengthens the hydrogen bond with Tyr257 and promotes formation of the intermediate. Similarly, further strengthening of the hydrogen bond would occur during formation of the alkylperoxo intermediate as the C2 carbon of 4NC becomes fully sp^3 hybridized, thereby pulling the reaction toward the intermediate.

Here we explore the roles of Tyr257 in catalysis by mutating it to a Phe (Y257F), which preserves the spatial characteristics of Tyr, but not the ability to hydrogen bond. It is found that, in accord with the postulated role for Y257, the Y257F-HPCA + O_2 reaction forms ring-cleaved product with kinetics that are slow in comparison to those of the wild-type reaction. The slow internal steps of the Y257F reaction cycle allow new intermediates to be detected, trapped, and characterized. The new intermediates support the proposed requirement for electron transfer to the oxygen from the substrate without a net change in metal oxidation state prior to O_2 attack.

MATERIALS AND METHODS

Y257F mutant.

Y257F mutant of 2,3-HPCD was prepared using the Stratagene QuickChange kit. The following mutagenesis primer was used along with its reverse complement:

Mutagenesis primer - GCGTCTCCAACGCGTTCTACCTG**TTC**ATCC.

The mutant codon is shown in bold highlight. The mutation was confirmed via sequencing at the University of Minnesota MicroChemical Facility using a sequencing primer that binds ~ 100 codons upstream of the mutagenesis site:

Sequencing primer - GCACATGCGCTACGACCTGTACTC .

Recombinant WT 2,3-HPCD and Y257F were purified as previously described (*98*) with a few modifications to the purification protocol. No cysteine or Fe was added to the purification buffers, but all buffers used in the purification were continually sparged with ~ 1-5 psi of N_2 to remove O_2. After loading 2,3-HPCD onto the DEAE sepharose column, the column was gravity washed with 10 column volumes of wash buffer (50 mM MOPS pH 6.8 + 190 mM NaCl). The wash buffer was sparged with 1-5 psi of N_2 during this process. After the wash, a salt gradient totaling 10 column volumes was run from 190 - 350 mM NaCl using a gravity dependent gradient maker sparged with 1-5 psi N_2 in the mixing chamber (chamber with low salt buffer). The pooled fractions from the DEAE sepharose column were found to be sufficiently pure for kinetic and spectroscopic studies. Mössbauer analysis of the purified Y257F mutant has revealed ~1 eq of ^{57}Fe(II)/site enrichment as previously described for the wild type enzyme and the H200N mutant (*52*). Purified Y257F retained ~ 21% of the

wild-type activity and yielded the correct ring cleaved product from HPCA. Y257F shows limited solubility at low pH and in the presence of excess Na^+. At pH 5.5, Y257F precipitates from solution when concentrated to >1 mM in the presence of excess Na^+ (>200 eq). Dilute solutions of Y257F are soluble as low as pH 5.5 even in the presence of excess Na^+. This phenomenon appears to be reversible, the precipitate observed in concentrated Y257F solutions becomes soluble with retention of activity upon dilution at pH 5.5 or when pH is increased to ~7.5. Wild-type 2,3-HPCD and the H200N are more soluble than Y257F under the conditions described above.

Iron quantification using ICP-OES.

The ICP-OES samples are digested in 20% nitric acid at 37°C for at least 24 hrs. Insoluble materials are removed by centrifugation at 10,000xg at 4°C. The supernatant was analyzed for transitional metals using ICP-OES at the Aqueous Geochemistry Lab (University of Minnesota, Department of Earth Science).

Steady-state kinetic experiments.

Steady-state kinetic parameters for the ring-cleaving reaction of WT 2,3-HPCD and Y257F mutant were monitored using UV-vis detection. The initial velocity of product formation was measuring at 380 nm using a stopped-flow device. The product absorbance was monitored over a 10 s interval using constant pressure shots. The linear portion of the trace is fit using the Pro Data Viewer software package. After mixing, the enzyme concentration was kept at < 1 μM for WT 2,3- HPCD and < 6 μM for Y257F with varying HPCA substrate concentrations. Typical experiments were done at either 4 °C or 22 °C in 200 mM MES or MOPS buffer at pH 5.5 or pH 7.5, respectively, in air saturated buffer. Initial velocities were fit as a hyperbolic function of substrate concentration to determine K_m and V_{max} using the data analysis software in Origin.

Estimation of K_d for HPCA binding to Y257F and WT enzymes.

The dissociation constants for HPCA binding to Y257F and WT were estimated using UV-vis detection. Since the anaerobic Y257F-HPCA complex has no unique UV-vis features, the affinity for HPCA was estimated based on the ability of HPCA to compete with 4NC binding to Y257F and WT. The experiment was done in 200 mM MOPS pH 7.5 inside a Coy anaerobic glove box. The samples were sealed in a 0.6 ml UV-vis cuvette with a septum sealed screw cap. The UV-vis spectra were collected using a Hewlett Packard 8453 UV-vis spectrometer.

Transient kinetic experiments.

All stopped-flow experiments were conducted at 4 °C in 50 mM MOPS buffer at pH 7.5 or 50 mM MES buffer at pH 5.5, as previously described (*52*). Solutions varying in O_2 concentrations used for stopped-flow experiments of the Y257F-HPCA + O_2 reaction were prepared by diluting a stock O_2 buffer solution with anaerobic buffer in a gas-tight 5 ml Hamilton syringe equilibrated on ice. The stock buffered (50 mM MES pH 5.5) O_2 solution was prepared by bubbling O_2 through 150 ml bottle with a septa-sealed crimp-capped mouth. The O_2 was supplied at ~5 psi, and the buffered O_2 solution was kept on ice with bubbling gas and stirring. The gas pressure was released through a needle-valve which punctured the septa seal. After 30 min, the pressure outlet was closed and the solution left under ~5 psi of O_2 and stirring for at least 30 minutes before sampling. The solution of anaerobic 50 mM MES pH 5.5 buffer was made in an identical container/volume. It was made anaerobic by bubbling argon gas through the buffer with stirring at room temperature. After 1 hour, the solution pressure outlet was closed and the solution was stirred for at least 1 hr on ice in order to allow equilibration under ~5 psi of argon gas. After equilibration on ice, the buffers were left under 5 psi of O_2/Ar and the pressure was released only during sampling of the O_2/Ar saturated buffers. Mixtures of O_2/Ar saturated buffers were

prepared by first sampling the Ar buffer and then sampling the O_2 buffer at different ratios to achieve a total volume of 4 or 5 ml. The container pressure outlet was opened during sampling of O_2/Ar saturated buffers so that the 5 ml gas-tight syringe did not fill up with O_2/Ar positive pressure while sampling the buffer.

Rapid freeze quench (RFQ) methods.

1.6 mM Y257F-HPCA anaerobic complex was prepared in the glove box by mixing 1 eq of Y257F with 1 eq of HPCA. RFQ syringes were loaded inside the anaerobic glove box and then transferred to an Update Instrument model 1019 RFQ apparatus and allowed to equilibrate for 30 min at 4 °C using a Neslab Endocal LT-50 low temperature circulator. The RFQ samples were mixed with O_2 buffer as previously described (*52*). Previously, we observed a splash artifact when the shortest time reaction mixtures were frozen on the counter-rotating aluminum wheels maintained at Liq N_2 temperature (*52*). To avoid this artifact, the Pittman Ametek VDC motor (Model 14204S005) used to rotate the wheels was operated at higher velocity (60 V applied voltage) so that the wheels rotated much faster. This allowed the reaction mixture to always contact the metal surface rather than frozen solution. Also, plastic scrapers in contact with the wheels were used to remove the frozen reaction mixture from the wheels into a Liq N_2 buffer as the wheels rotated. Samples at times >1 s were frozen as previously described (*52*) .

Preparation of HPCA semiquinone and HPCA quinone.

HPCA was oxidized to a quinone using mushroom tyrosinase (Sigma) in 100 mM MOPS buffer pH 7.5 and 4 °C. The reaction was initiated and monitored using the stopped-flow spectrometer with diode-array detection (2 mm path). A solution of 2 mM HPCA was mixed with 10 mg/ml mushroom tyrosinase. The quinone is photo-labile and formed during the first 4 min of the reaction and then slowly decayed to an unidentified secondary species. HPCA was oxidized to a transient semiquinone by oxidation with 3,4,5,6-Tetrachloro-1,2-benzoquinone or

O-Chloranil (Sigma) in ethanol and 20 °C. The reaction was initiated and monitored using the stopped-flow spectrometer with diode-array detection (2 mm path). A solution of 2 mM HPCA was mixed with 2 mM of O-Chloranil. The semiquinone formed during the first 150 s of the reaction and then slowly decayed to an unidentified species.

RESULTS.

The Y257F mutation causes a significant decrease in the rate of HPCA turnover.

The steady-state parameters for Y257F with the HPCA substrate were determined at 4 and 22 °C and at pH 7.5 and pH 5.5 by monitoring the initial velocity of product formation using stopped-flow spectroscopy as summarized in Table 8. An example of the Michaelis-Menten plot for various HPCA concentrations at pH 7.5 and 4 °C is shown in Figure 35. The results show that the k_{cat} value decreases to about 21% of that of the WT enzyme at pH 7.5, 22 °C. The K_m^{HPCA} is increased by about 16 fold by the mutation.

Substrate binds tightly to Y257F.

Alteration of a residue in close proximity to the substrate binding site might cause a decrease in substrate affinity which could, in turn, account for the observed increase in K_m^{HPCA} versus that observed for the WT enzyme. Direct determination of the substrate K_d is complicated by the lack of a visible or fluorescence change upon binding. However, the K_d can be approximated by comparison to 4NC binding. The K_d for 4NC for WT enzyme has been previously determined to be 5 μM based on the spectroscopic change that occurs as monoanionic 4NC in solution converts to the dianionic form bound to the enzyme. The fraction of 4NC bound during a titration of Y257F is the same as that observed for the WT enzyme showing that the K_d does not change significantly (Figure 36). Spectra of anaerobic 40 μM Y257F in the presence or absence of 80 μM HPCA after the addition of 80 μM 4NC at pH 7.5 are shown in Figure 36. The results show no 4NC binding to Y257F or WT in the presence of an equimolar concentration of HPCA. This is not the case when a weak binding substrate 4-chlorocatechol (4CC) is added. Consequently, the K_d for HPCA is much less than 5 μM for Y257F as observed for HPCA binding to the WT enzyme, and the high K_m^{HPCA} value must be attributed to other steps in the

Table 8: Steady state parameters for 2,3-HPCD-HPCA and Y257F-HPCA reaction with O_2.[a]

Kinetic parameter	Wild type 22 °C pH 7.5	Y257F 22 °C pH 7.5	Y257F 4 °C pH 7.5	Y257F 22 °C pH 5.5
k_{cat} (s^{-1})	10 ±1.5	2.7 ±0.13	0.38 ±0.07	0.7 ±0.1
K_m^{HPCA} (mM)	0.016[b]	0.26 ±0.05	0.25 ±0.05	0.13 ±0.02
k_{cat}/ K_m^{HPCA} ($mM^{-1}s^{-1}$)	625	10.4	1.5	3.1
K_m^{O2} (mM)	0.015 ±0.007	0.08 ±0.03	0.02 ±0.008	0.01 ±0.003
k_{cat}/ K_m^{O2} ($mM^{-1}s^{-1}$)	667	34	19	40

[a] Reactions were conducted in 200 mM MES or MOPS at pH 5.5 or 7.5, respectively. The buffer is air saturated at either 4 °C or 22 °C. At this O_2 concentration, the reaction is saturated.

[b] From (92).

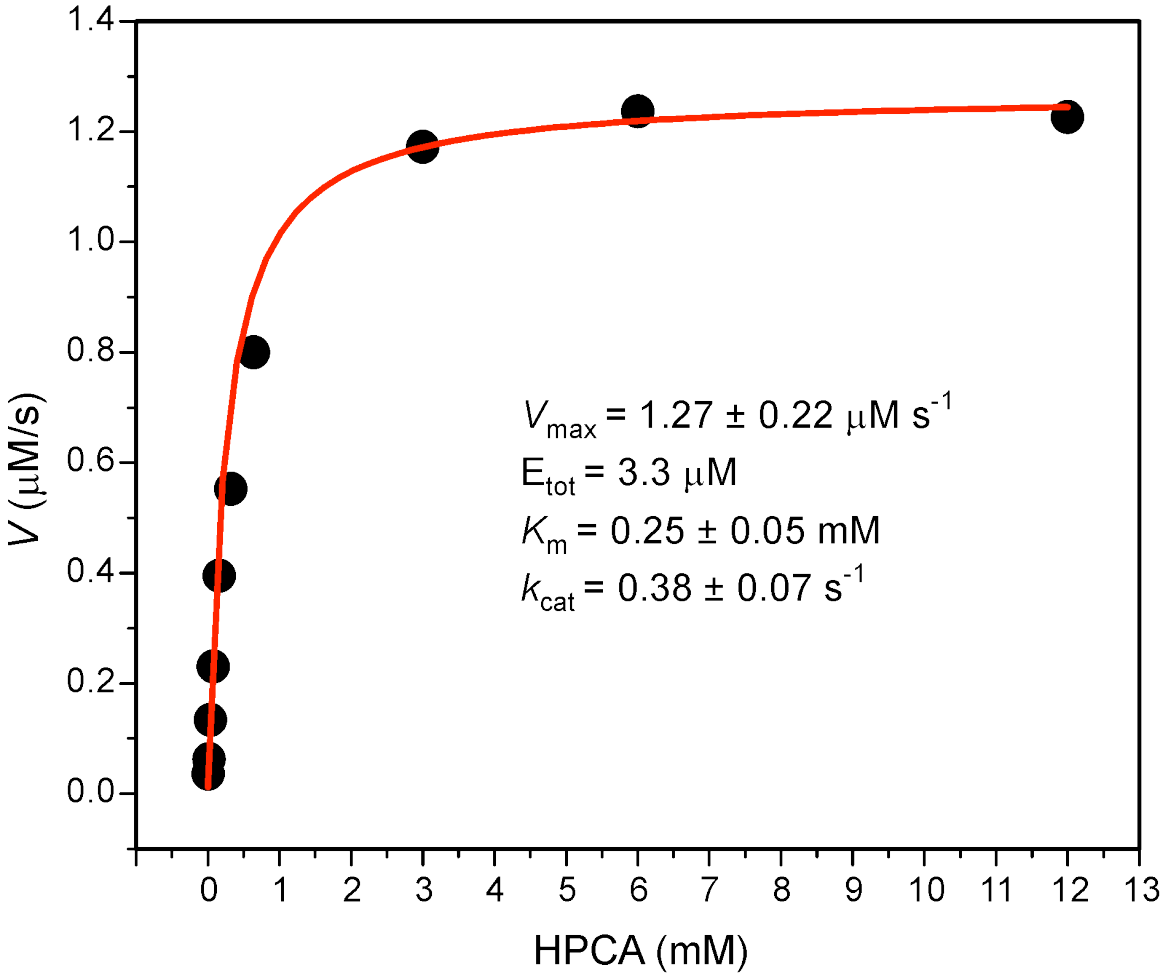

Figure 35: Michaelis-Menten plot from the reaction of Y257F with HPCA and O_2 saturated buffer at 4 °C**.** Reaction is conducted in 200 mM MOPS buffer pH 7.5 in air saturated buffer. Initial velocities are measured by stopped-flow spectroscopy as described in Materials and Methods.

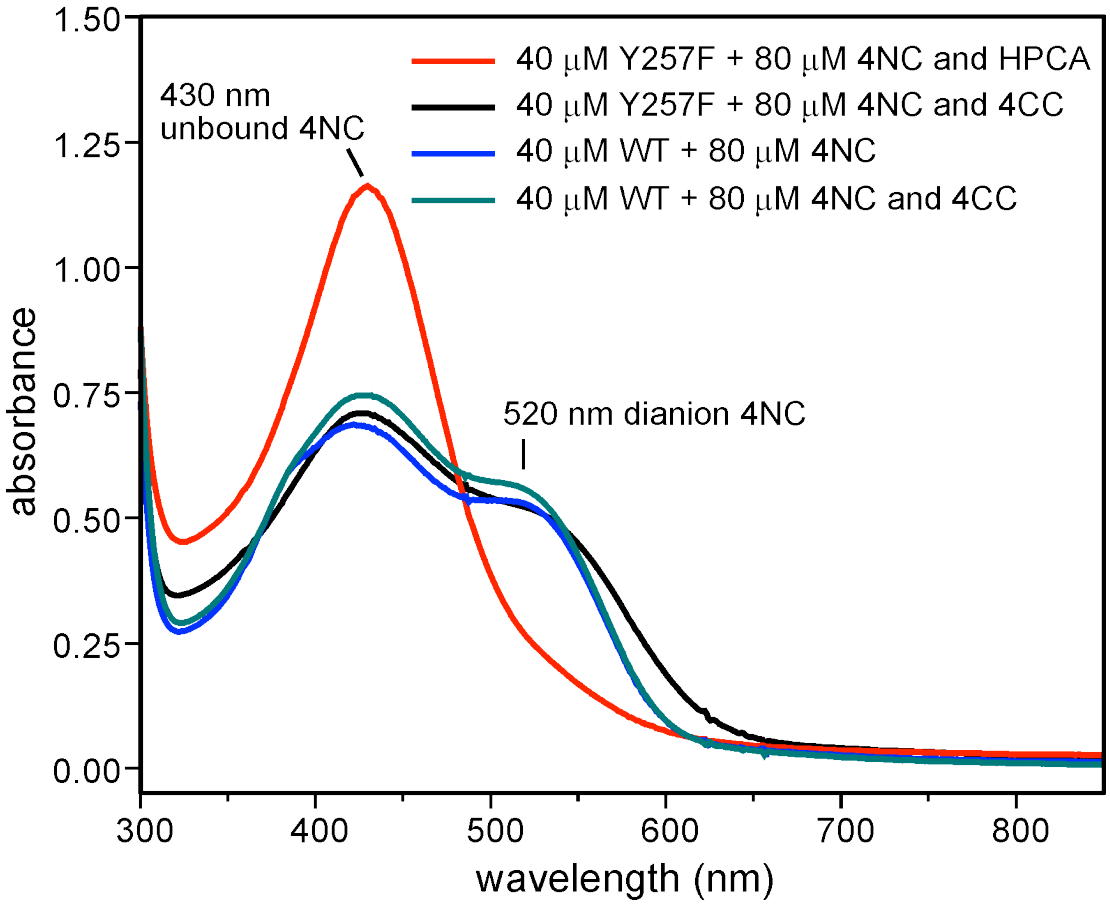

Figure 36: Estimation of K_d for HPCA binding to Y257F. The anaerobic substrate complexes were prepared in 200 mM MOPS buffer pH 7.5. The samples were prepared in the anaerobic glove box in anaerobic 200 mM MOPS buffer pH 7.5. 4CC is a weak binding catechol, 4-chlorocatechol.

reaction cycle. The low K_d value facilitates transient kinetic experiments as described below.

Single-turnover studies of the Y257F-HPCA + O_2 reaction reveal two reaction intermediates.

The diode-array stopped-flow spectra from an experiment wherein anaerobic, stoichiometric Y257F-HPCA complex reacts with a large excess O_2 at 4 °C at pH 7.5 or pH 5.5 are shown on Figure 37 A and B, respectively. There is little change in the spectra in the first 30 ms at either pH value. Indeed, single wavelength data at 450 nm from pH 7.5 and pH 5.5 diode-array time courses clearly reveal a lag-phase during this period (Figure 37 A and B insets, respectively). This suggests that there is at least one colorless intermediate formed at the outset of the reaction before formation of a chromophoric species.

At slightly longer times, a transient species with a chromophore in the 400 - 470 nm range is observed. At pH 7.5, the chromophore begins to appear after 30 ms and maximizes at ~ 250 ms before it decays over the course of several seconds to yield the extradiol ring-cleaved product (λ_{max} = 380 nm). The spectrum of the transient species has an isosbestic point with that of the ring-cleaved product, so it is most likely to be a direct precursor of product formation in the reaction cycle. However, it is possible that other short-lived intermediates may intervene.

It was previously shown that λ_{max} for the ring-cleaved product shifts to shorter wavelength at low pH (*52*). Accordingly, when the Y257F-HPCA + O_2 reaction is conducted at pH 5.5, λ_{max} for the ring-cleaved product shifts to 325 nm, revealing the chromophore associated with the new intermediate at 425 nm (Figure 37 B). The pH 5.5 data shows that the new intermediate maximizes at ~ 700 ms, suggesting one or both rate constants for formation and decay of this species have changed at low pH. We will designate the first and second new intermediates $Y257F_{Int1}^{HPCA}$ and $Y257F_{Int2}^{HPCA}$, respectively.

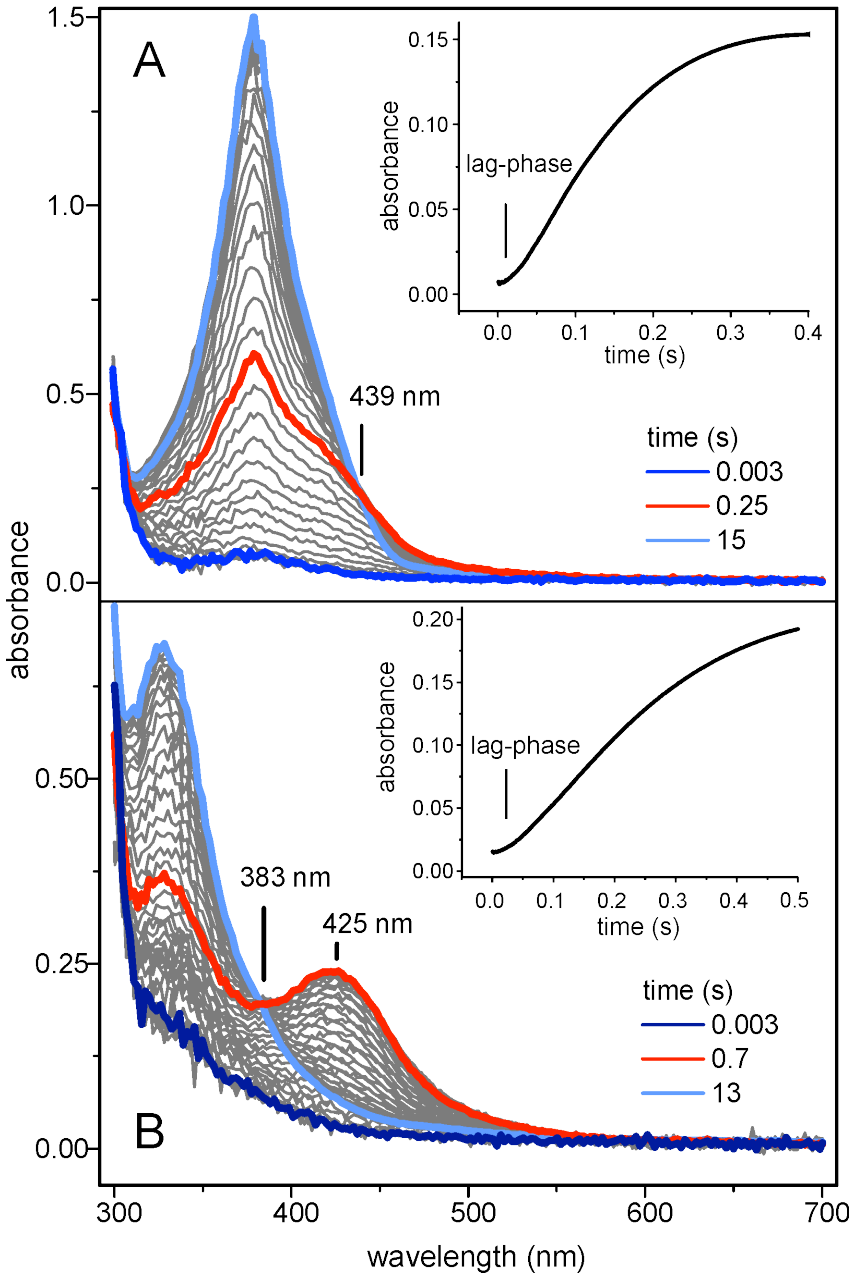

Figure 37: The Y257F-HPCA + O_2 reaction time-course followed using diode-array detection. Approximately 80 μM Y257F-HPCA complex is mixed with ~ 500 μM O_2 at 4 °C and pH 7.5 (A) and pH 5.5 (B) (1 cm pathlength). *Inset*: The reaction time course is monitored with single-wavelength detection at 450 nm.

Photochemical conversion of the enzyme-product complex.

When the reaction is followed over a longer time period using diode-array detection at pH 7.5 and 4 °C, the time course reveals a slow change in the UV-vis spectrum of the product, resulting in a decrease of absorption near 380 nm and an increase at 470 nm (Figure 38 A). The slow product transformation can also be observed for reactions catalyzed by the WT enzyme (Figure 37 B) and H200N mutant (data not shown). However, it occurs faster with the Y257F mutant. The reaction is also much faster for enzyme that has been reduced anaerobically with dithionite before removal of excess reductant and byproducts by gel filtration. The reaction rate is dependent on the intensity of the white light source, and thus, it appears to involve photochemistry of the product. Surprisingly, it is not observed in the absence of enzyme, suggesting that it occurs in the enzyme-product complex. The 470 nm chromophore can be separated from the enzyme (Figure 38 C) by gel filtration, showing that it is not a modified form of the enzyme. The photochemical reaction occurs when enzyme is added stoichiometrically to isolated product, suggesting that product may rebind to the enzyme at high concentrations to allow the reaction. The rate of this product transformation under all conditions is much less than k_{cat} for enzyme turnover. Consequently, it is unlikely to be relevant to normal enzyme catalysis.

Rate constants for the formation and decay of the intermediates.

Single-wavelength kinetic time courses were analyzed using regression methods to obtain reciprocal relaxation times associated with the reaction. Figure 39 shows the single wavelength time course monitored under pseudo first order conditions at 450 nm or 350 nm for the first 15 s of the Y257F-HPCA + O_2 reaction at pH 7.5 or 5.5 (4 °C). Each of the time courses requires four summed exponential phases to achieve a satisfactory fit (summarized in Table 9). The slowest, phase in each case has a low amplitude and a $1/\tau$ value much less than k_{cat} measured at the same pH and temperature (Table 8), and thus, it is not kinetically relevant. This phase arises from the photochemical side reaction described above.

Observation of at least three competent phases in product formation at pH 5.5 and pH 7.5 shows that the Y257F-HPCA + O_2 single turnover reaction entails at least three distinct steps under both low and high pH conditions (Table 9). For a given pH, pairs of reciprocal relaxation times are similar at the two wavelengths in all cases, suggesting that three phases are sufficient to describe the product formation time courses. The reciprocal relaxation times all decrease with decreasing pH, albeit not proportionally, consistent with the slower formation and longer lifetime observed for the chromophoric intermediate $Y257F_{Int2}^{HPCA}$ at pH 5.5 (Figure 37 A and B).

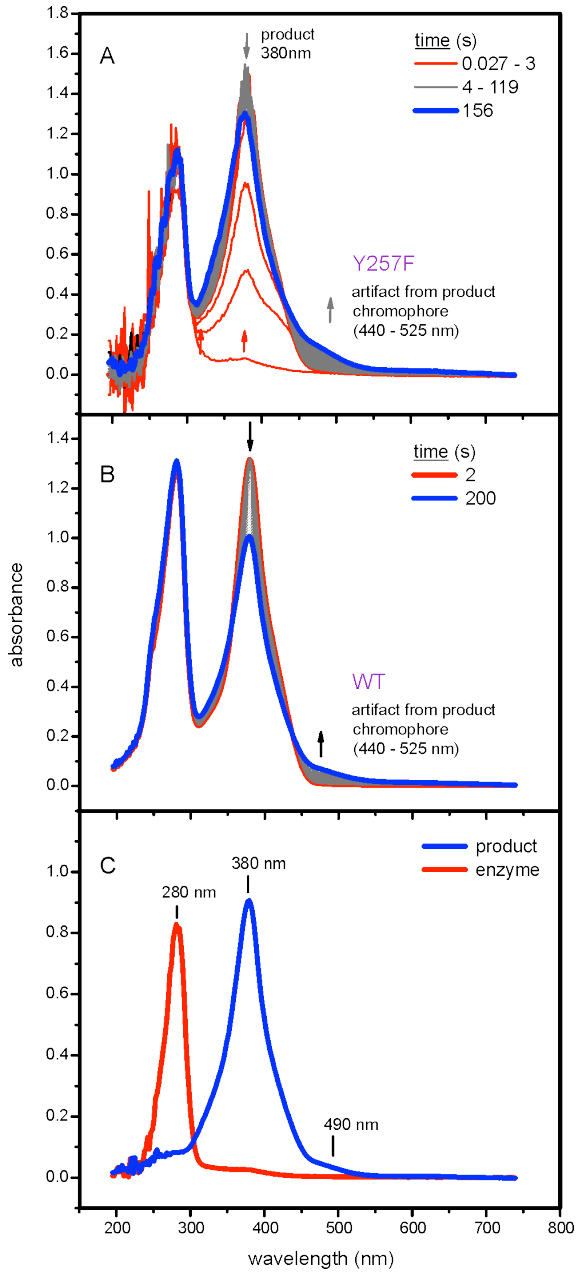

Figure 38: Photochemistry of the ring-cleavage product. A) ~ 80 μM Y257F-HPCA complex is mixed with ~ 500 μM O_2 at 4 °C and pH 7.5, (1 cm pathlength, 2 mm slit width). B) Approximately 80 μM WT-HPCA complex is mixed with ~ 500 μM O_2 at 4 °C and pH 7.5 (1 cm pathlength, 10 mm slit width). C) UV-vis spectrum of 2,3-HPCD and ring-cleaved product separated using a Sephadex PD10 column following a single turnover reaction.

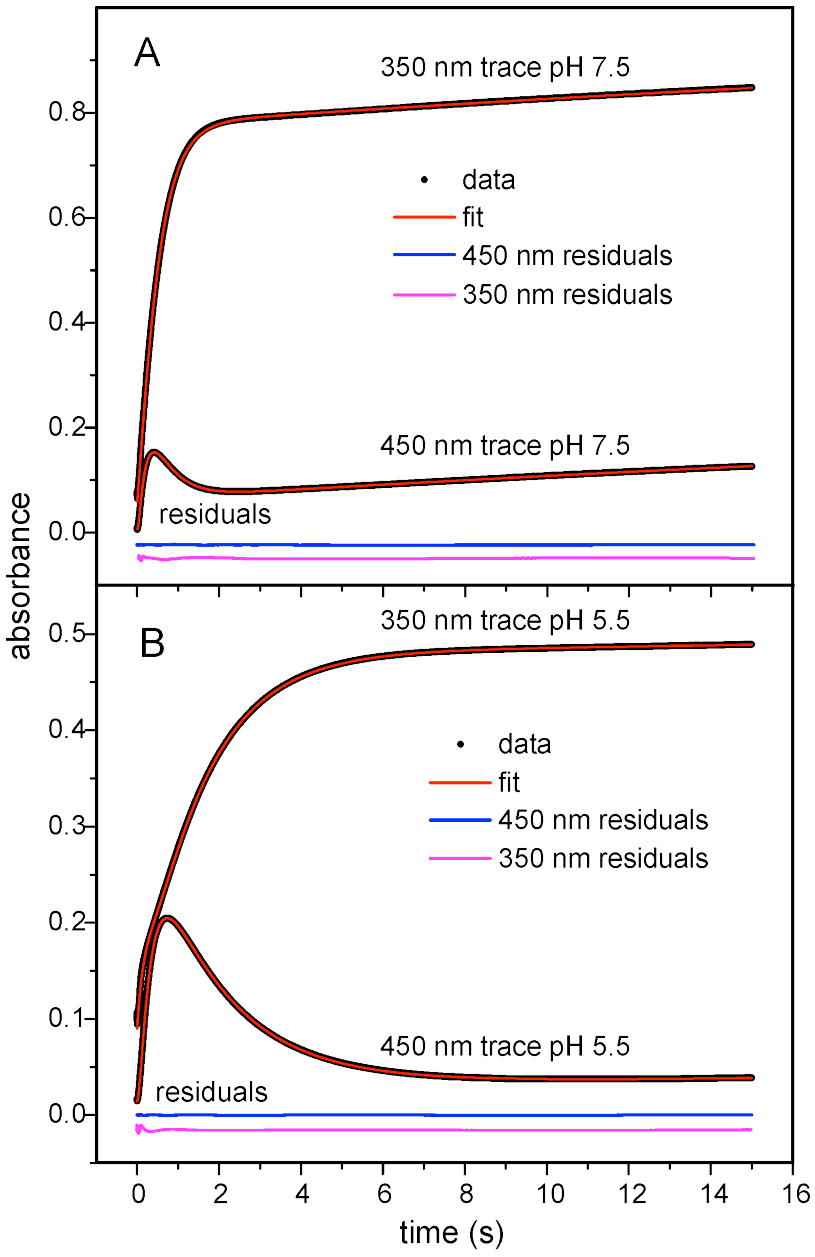

Figure 39: The Y257F-HPCA + O_2 reaction time course followed using single-wavelength detection at 450 nm and 350 nm. Approximately 80 μM Y257F-HPCA complex is mixed with ~ 500 μM O_2 at 4 °C and (A) pH 7.5 or (B) pH 5.5 (1 cm pathlength).

Table 9: Reciprocal relaxation times and amplitudes obtained from fitting single wavelength data from the Y257F-HPCA + O_2 reaction at 4 °C and either pH 7.5 or 5.5. [a]

Reciprocal relaxation time number	450 nm pH 7.5 s^{-1} (amp)	350 nm pH 7.5 s^{-1} (amp)	450 nm pH 5.5 s^{-1} (amp)	350 nm pH 5.5 s^{-1} (amp)
1	23[b] (0.07)[c]	23 (0.017)	13 (0.09)	8 (-0.1)
2	5.5 (-0.40)	5.0 (0.18)	3.0 (-0.41)	3.0 (0.12)
3	1.8 (0.27)	2.2 (-0.91)	0.74 (0.30)	0.65 (-0.41)
4	0.03 (-0.18)	0.03 (-0.25)	0.002 (-0.08)	0.002 (-0.08)

[a] Fitting to a 4 summed exponential equation by nonlinear regression using Pro Data viewer software available with SX series stopped-flow. Reactant concentrations after mixing were as described in Figure 38.

[b] The fitting error for all data in a single experimental run with at least 5 repeated trials is less than ±3 %. For the experiment repeated using different enzyme batches over multiple days, the error is approximately ±10%.

[c] The sign of an amplitude from exponential fitting is the opposite of the observed direction of change.

The reciprocal relaxation times for the reaction monitored at 425 nm are plotted vs the O_2 concentration in Figure 40. For the reaction at pH 5.5, it is seen that only $1/\tau_1$ is dependent on O_2 concentration and that the dependence is linear passing through zero (Figure 40 A). The linear dependence suggests that $1/\tau_1$ is at least dominated by the rate constant for O_2 binding step and the zero intercept suggests that this step is effectively irreversible. If the binding reaction occurs first in the reaction sequence and is irreversible then $1/\tau_1 = k_1 = 4.03 \pm 0.03 \times 10^4$ M^{-1} s^{-1}.

At pH 7.5, the fastest reciprocal relaxation time is again linearly dependent on O_2 concentration, but the intercept of the plot is not zero (Figure 40 D). This is the expected result if the O_2 binding reaction occurs first and is reversible at this pH value. The forward and reverse rate constants are given by the slope and intercept of the plot respectively ($k_1 = 2.7 \pm 0.01 \times 10^4$ M^{-1} s^{-1}, $k_{-1} = 11$ $s^{-1} \pm 0.6$, $K_d^{O2} = k_{-1}/k_1 = 400$ μM). The consequence of a fast reversible first step in the reaction is expected to be a hyperbolic plot for another of the $1/\tau$ vs O_2 plots, as observed in Figure 40 E. The y-intercept of this plot is the reverse rate constant k_{-2} for the step following O_2 binding (zero in this case). The plot asymptotically approaches the sum of $k_2 + k_{-2}$, while the K for the plot is the K_d for the O_2 binding reaction (non-linear fitting gives $k_2 = 15$ $s^{-1} \pm 0.8$ and $K_d^{O2} = 500$ μM). The irreversible nature of this step would uncouple the third reciprocal relaxation time from the others, so that it would be expected to be independent of O_2 concentration and equal to the sum of the forward and reverse rate constants for the third step in the reaction as observed ($k_3 + k_{-3} = 2$ $s^{-1} \pm 0.22$) (Figure 40 F). The amplitude for this uncoupled third phase monitored at 350 nm is much larger than that of the others, suggesting that the third step in the reaction is ring-cleavage. If this is the case then the reaction is irreversible and $k_{-3} = 0$. The irreversible steps following O_2 association are presumably the explanation for the low observed K_m value for O_2 (~10 μM, pH 7.5, 22 °C) despite that rather high K_d^{O2} value for complex formation.

Returning to the pH 5.5 data, the occurrence of an initial irreversible O_2 binding step would uncouple $1/\tau_2$ and $1/\tau_3$ from O_2 concentration

dependence, as observed Figure 40 B and C). This does not indicate *a priori* that $1/\tau_2$ and $1/\tau_3$ are uncoupled from each other, and they may not be if the second reaction step is reversible. However, our previous studies of intermediates in extradiol dioxygenase cycles have shown that they are generally well described as irreversible; attack of an activated oxygen intermediate on substrate to form a covalent alkylperoxo species or subsequent breaking of the O-O bond are unlikely to be reversible processes. Thus, it is likely that $1/\tau_2$ and $1/\tau_3$ are equal to rate constants of unique steps. This analysis does not indicate which rate constant is associated with which step, although it is likely that the order established by the pH 7.5 data is maintained (k_2 = 3 s^{-1} ± 0.21 and k_3 = 0.74 s^{-1} ± 0.01. The assignment can be directly probed by analysis of the extinction coefficient of the chromophoric intermediate (see Discussion) or by directly trapping the intermediate for quantification using a technique such as Mössbauer spectroscopy.

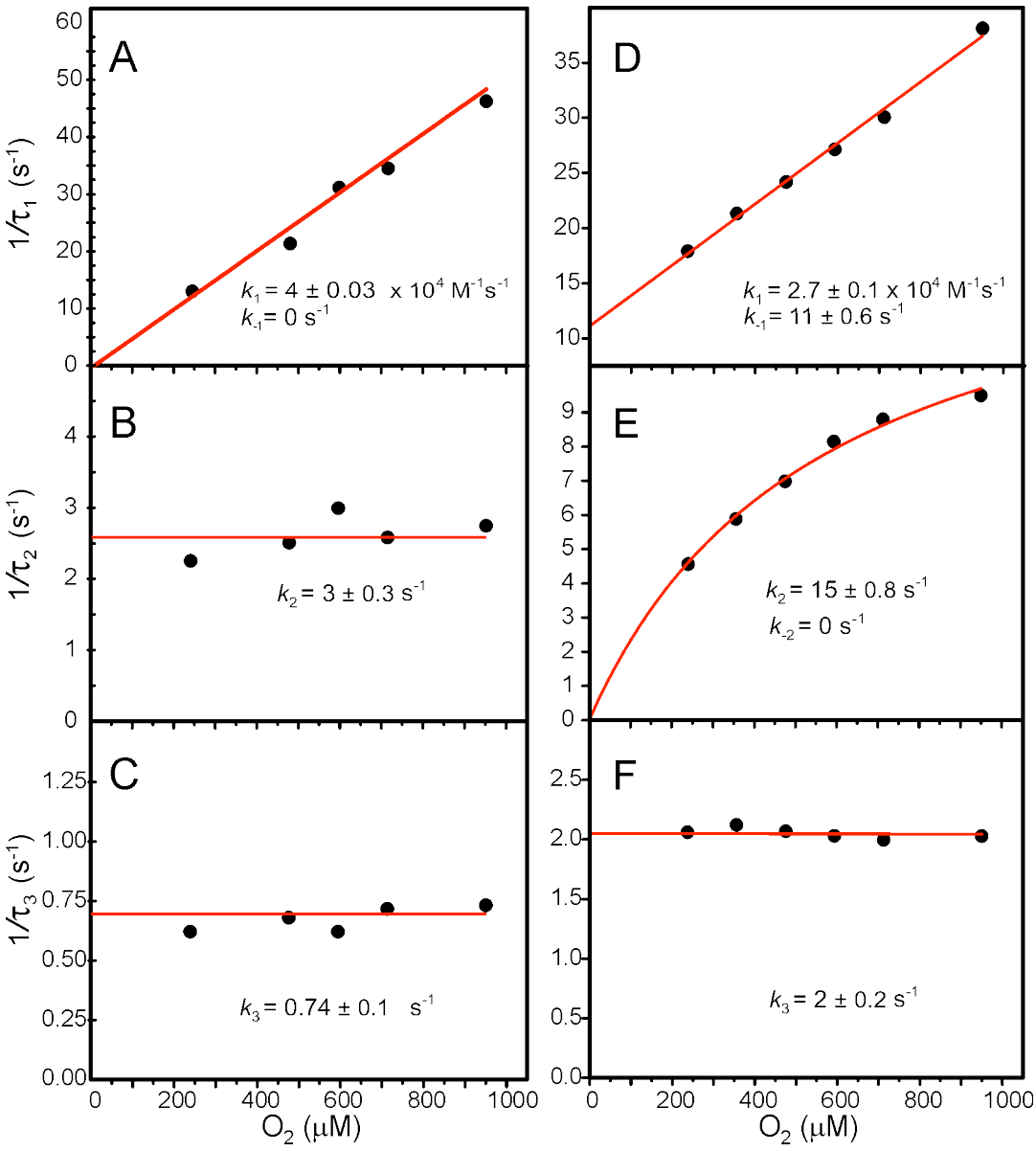

Figure 40: O_2 dependence of the three kinetically competent reciprocal relaxation times from the Y257F-HPCA + O_2 reaction. The data were collected using single wavelength detection at 425 nm following the reaction of ~ 60 - 80 μM Y257F-HPCA complex with varying amounts of O_2 at 4 °C and pH 5.5 (left) or pH 7.5 (right).

Mössbauer reveals $Y257F_{Int1}^{HPCA}$ and $Y257F_{Int2}^{HPCA}$ both contain Fe(II).

The Mössbauer spectra from the Y257F-HPCA + O_2 reaction at pH 7.5 and 4 °C are shown in Figure 41. The Y257F-HPCA anaerobic substrate complex reveals a ferrous doublet at 94% yield with parameters δ = 1.13 mm/s and ΔE_Q = 3.16 mm/s ($Y257F_{ES}^{HPCA}$, Figure 41 A). Observation of a single species in the substrate complex differs from the two quadrupole doublet spectra observed for the HPCA complexes with H200N and 2,3-HPCD (*52*). However, $Y257F_{ES}^{HPCA}$ has Mössbauer parameters similar to those reported for one of the two doublets in each case, specifically, $H200N_{ES1}^{HPCA}$ and $FeHPCD_{ES1}^{HPCA}$ (*52*).

Figure 41 B shows a sample rapid-freeze quenched at ~12 ms after mixing with ~ 1 eq of O_2 at pH 7.5 and 4°C. This sample reveals two species, Site 1 (60% yield) and 2 (30% yield) with parameters, δ = 1.15 mm/s, ΔE_Q = 3.16 mm/s and δ = 1.15 mm/s, ΔE_Q = 2.75 mm/s, respectively. Site 1 has the parameters of the anaerobic substrate complex, whereas site 2 is a new Fe(II) species which has formed after the substrate complex was combined with O_2. The kinetic analysis described above predicts that $Y257F_{Int1}^{HPCA}$ would be formed in the observed yield at this point in the time course. Rapid freeze-quench EPR samples at this time point show no spectrum that can be associated with the new intermediate.

Preliminary Mössbauer spectra of a sample frozen at the time $Y257F_{Int2}^{HPCA}$ is expected to show that all species present contain Fe(II). The mixture of species at this time point (~250 ms) complicates the analysis, but it is unlikely that this intermediate contains ferric ion.

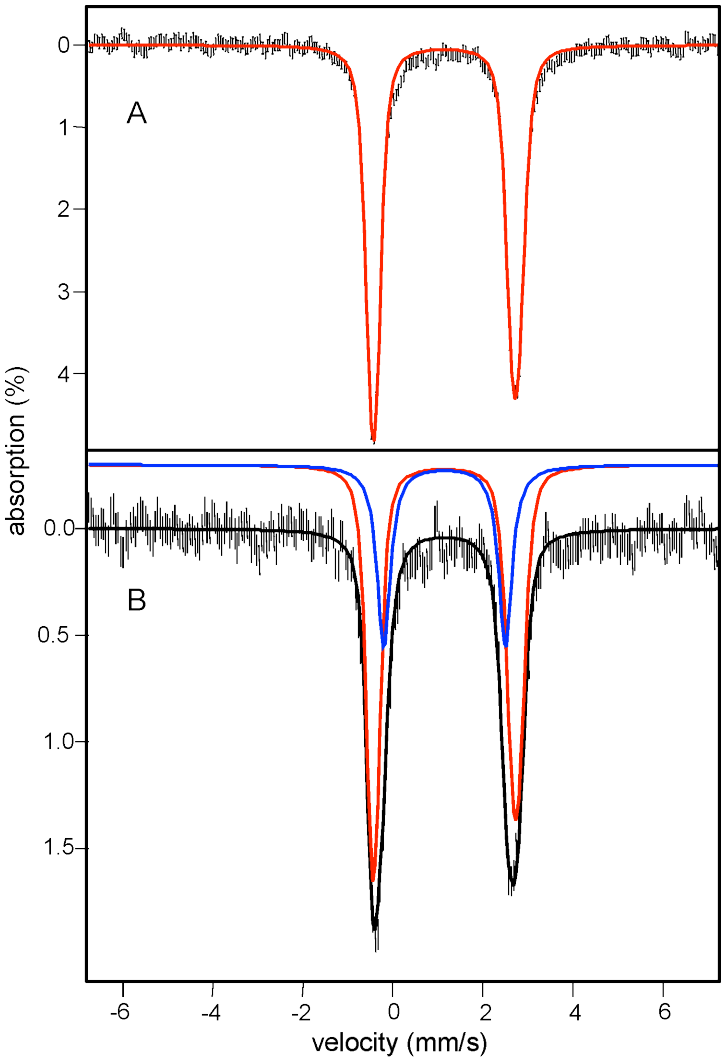

Figure 41: Mössbauer spectra from the Y257F-HPCA + O_2 reaction series at pH 7.5 and 4 °C (B = 0 and T = 4.2K). (A) Anaerobic Y257F-HPCA complex at 1.6 mM (B) RFQ sample from the Y257F-HPCA + O_2 reaction frozen at 12 ms after mixing with O_2. The RFQ experiment was done using 200 mM MOPS, pH 7.5. The red line represents a fit of the Mössbauer spectra for $Y257F_{ES}^{HPCA}$ using parameters and % yields mentioned in the main text for the anaerobic Y2578F-HPCA complex (A) and the sample frozen 12 ms after reaction with O_2 (B). The blue line represents a fit of the Mössbauer spectra for $Y2577_{Int1}^{HPCA}$ using parameters and % yields mentioned in the text for t the sample frozen at 12 ms after reaction with O_2.

Rate-limiting step.

The rate constants for the reaction cycle steps that can be directly observed are all significantly greater than the k_{cat} value at both pH 7.5 and 5.5. These steps apparently encompass O_2 binding through formation of the product. It is unclear from this analysis whether product formation in the active site is followed by rapid product release or whether product release is rate-limiting overall in the cycle. If it is not rate-limiting, then a step in substrate binding must be rate-limiting. This was examined by mixing 100 μM Y257F with 16 equivalents of HPCA and excess O_2 as shown in Figure 42 (black curve). The time course exhibits a distinct lag due to the steps prior to product formation. The time course for the reaction shown below was simulated by numerical integration using the rate constants determined here and establishing either product release, initial second-order substrate binding, or a first-order step in the substrate binding process as rate-limiting. The assumption is made that the enzyme-product complex exhibits a chromophore similar to that of free product. The precedent for multiple steps in the substrate binding process was established using 4NC as a probe and 2,3-HPCD mutants at position 200 (*95*).

Scheme 2. Model for the Y257F-HPCA + O_2 reaction**.**

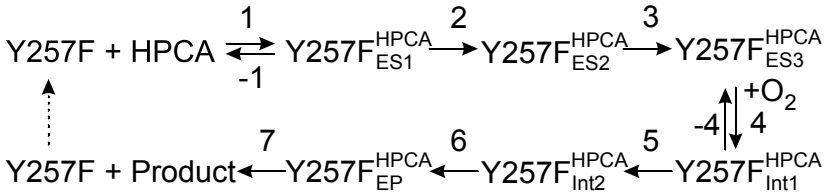

The observed time course is fit well only in the case of a rate-limiting step in the substrate binding process (step 3 in Scheme 2). A rate-limiting product release step would produce the burst kinetics shown in the blue trace. If second order product association were rate-limiting, the time course would become nonlinear at long times as the substrate is depleted (purple trace). Also, the steady state rate would be substrate concentration dependent even at high concentrations, which is not the case (Figure 35).

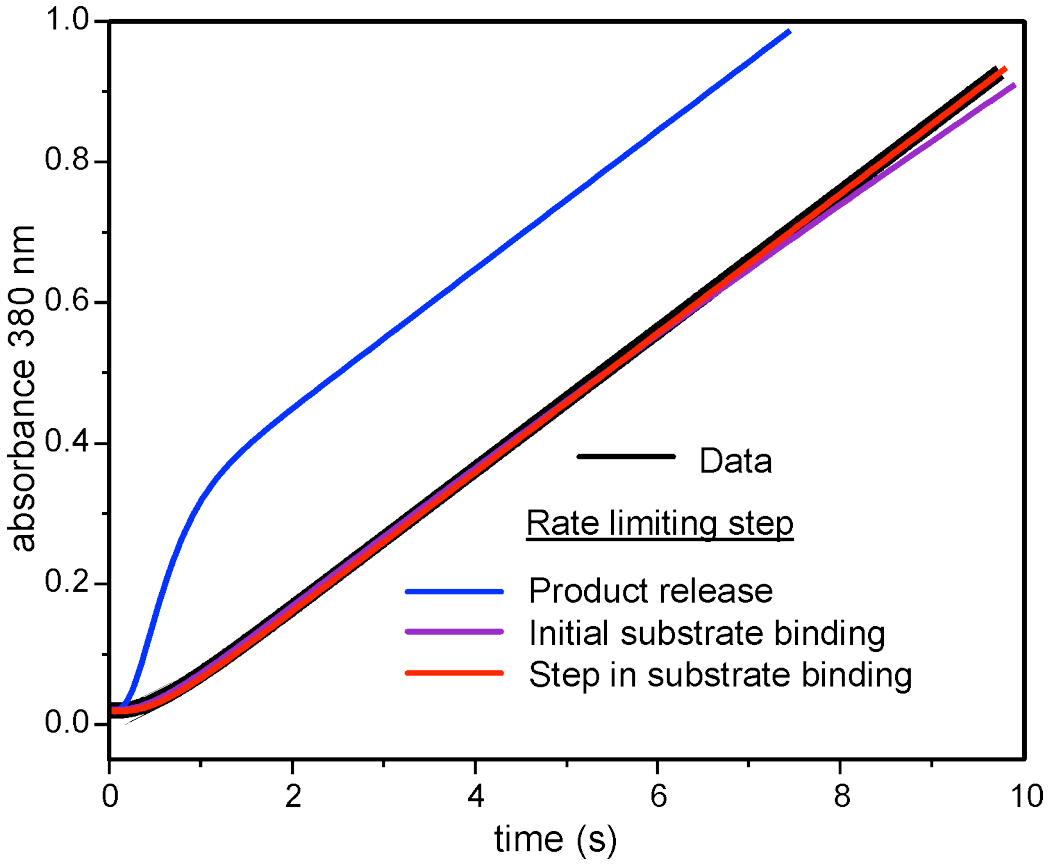

Figure 42: Simulations for the reaction time course based on Scheme 2. Black line: Actual time course for 100 μM Y257F + ~ 1700 μM O_2 was mixed with 16 equivalents of HPCA + ~ 1700 μM O_2 at 4 °C, pH 7.5. The rate limiting step was changed as shown on the figure while maintaining the same reactant concentrations and rate constants for the steps established in this study. Fixed rate constants were: Step 4, $k_{forward}$ = 2.7 x 10^4 M^{-1} s^{-1}, $k_{reverse}$ = 11 s^{-1}; Step 5, k = 15 s^{-1}; Step 6, k = 2.0 s^{-1}. Steps 1, 3, or 7 were assigned successively to first order or pseudo first order rate constants equal to the observed k_{cat} of 0.38 s^{-1} for the simulations shown. When not assigned as the rate limiting step, these steps were arbitrarily assigned non-rate limiting first order or pseudo first order rate constants of 20 s^{-1} (the computed time course is not affected by the value selected). Irreversible step 2 is included based on previous studies of 4NC binding to 2,3-HPCD and H200N. It is arbitrarily set to a non-rate limiting 20 s^{-1}.

DISCUSSION

The results described in this chapter show that Tyr257 plays an important role in efficient catalysis at several points in the catalytic cycle of 2,3-HPCD. This residue is located adjacent to the bound substrate, and structural studies indicate that it forms a hydrogen bond to the deprotonated substrate C3-O^- in the anaerobic 2,3-HPCD-HPCA complex and in $FeHPCD_{Int1}^{4NC}$ (Figure 43 B). This work complements the studies described in Chapters 1 and 2 where the roles of His200 and the nature of its interaction with the second iron-bound substrate, O_2, were examined. These studies support the hypothesis that the two substrates are connected electronically through the iron and that the loss of electron density from the catecholic substrate to O_2 is the basis for oxygen activation in this system. The studies described in this thesis show that the second sphere residues of the iron, specifically His200 and Tyr257, must also work in concert to make the O_2 activation process efficient and specific. Newly recognized aspects of this complex collaboration for catalysis are discussed here.

Kinetic model for catalysis.

The kinetic model presented above in Scheme 2 accounts well for steady state turnover rate and the lag observed during the first turnover (Figure 42). The rate constants for the non-rate limiting internal steps of the cycle are determined from the analyses of data such as that presented in Figures 39 and 40. As described above, the rate constant for the O_2 binding reaction to form $Y257F_{Int1}^{HPCA}$ can be unequivocally assigned (k_1 at pH 7.5 and 5.5). At pH 7.5, k_1 corresponds to reversible O_2 binding, but at pH 5.5, this step is irreversible. At pH 7.5, k_2 shows hyperbolic O_2 dependence as expected for a step which would follow the reversible O_2 binding event. As such, at pH 7.5, k_2 corresponds to decay of $Y257F_{Int1}^{HPCA}$ and formation of $Y257F_{Int2}^{HPCA}$ and k_3 must therefore correspond to decay of $Y257F_{Int2}^{HPCA}$ to yield the product complex (Scheme 3, Model 1). It is argued above that this order of steps is most likely to stay the same for the three reciprocal relaxation times observed for the single turnover reaction at pH 5.5 (Scheme 3, Model 2).

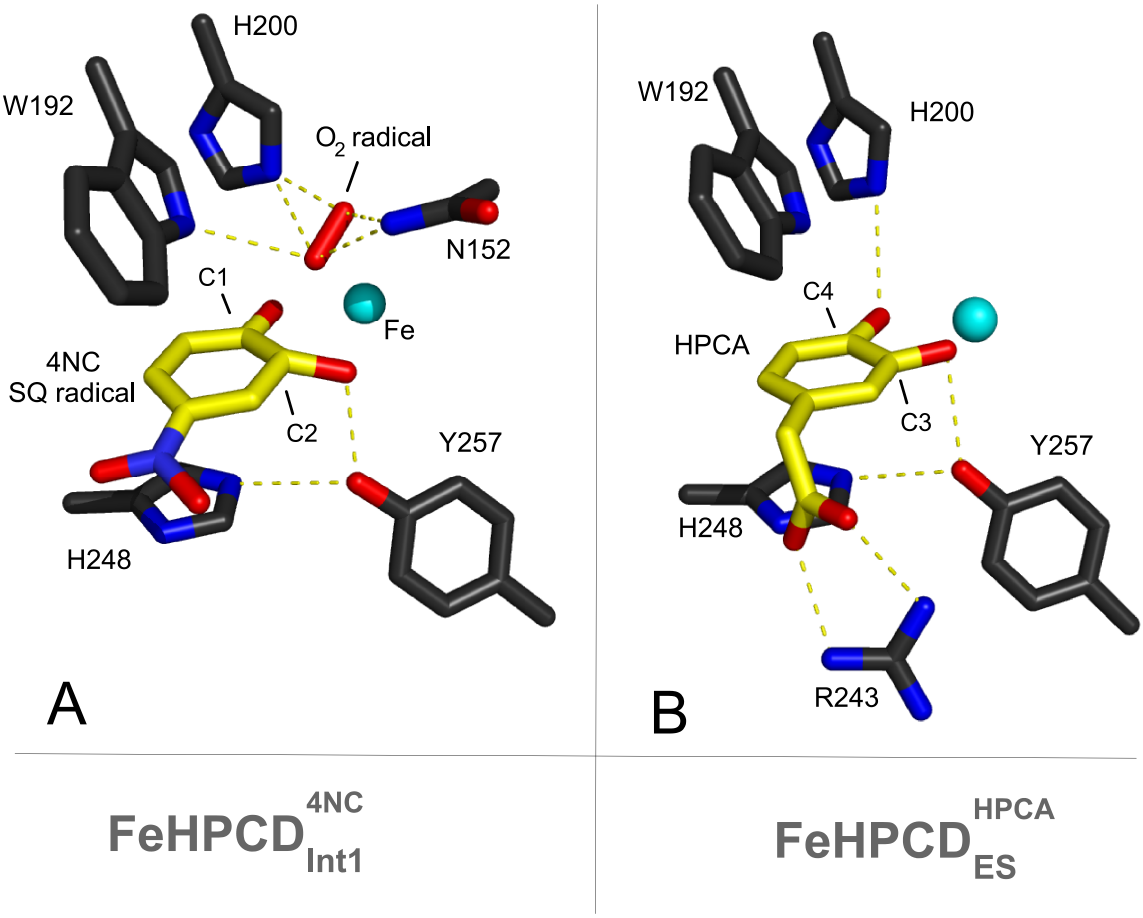

Figure 43: Second sphere residues which are proposed to participate in catalysis. A) $FeHPCD_{Int1}^{4NC}$, structure of the oxy complex from the FeHPCD-4NC + O_2 reaction (*50*). This reaction intermediate is proposed to have a SQ-Fe(II)-O_2 radical electronic structure. B) $FeHPCD_{ES}^{HPCA}$, structure of the anaerobic 2,3-HPCD-HPCA substrate complex (*102*).

Figure 44 shows numerical integration simulations of the single turnover reaction of Y257F-HPCA + O_2 at pH 7.5 and 5.5 for the assignment of rate constants where both k_2 and k_3 belong to irreversible steps. At pH 7.5, the kinetic model predicts an accumulation of $Y257F_{Int1}^{HPCA}$ of ~ 30% at 50 ms while that of $Y257F_{Int2}^{HPCA}$ is calculated to be ~ 55% at 250-350 ms (Figure 44). At pH 5.5, $Y257F_{Int1}^{HPCA}$ will accumulate to ~64% at 90 ms, and $Y257F_{Int2}^{HPCA}$ will build to ~ 63% at 700-800 ms (Figure 44).

Given the known total enzyme concentration and absorbance at the maximum, extinction coefficients for $Y257F_{Int2}^{HPCA}$ of ε_{425} =10,000 M^{-1} s^{-1} is predicted. This value, is in accord with extinction coefficients of known quinone or semiquinone forms of related catecholic substrates. In addition, Model 1 correctly predicts $Y257F_{Int1}^{HPCA}$ yields observed in RFQ/MB samples from a reaction time course at pH 7.5 (Figure 41).

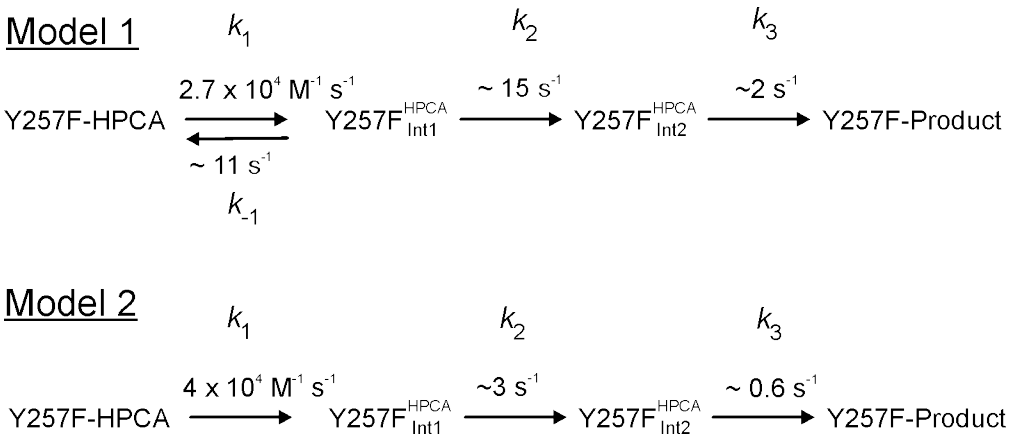

Scheme 3: Kinetic models for species occurring in the Y257F-HPCA + O_2 single-turnover reaction. Rate constants are as determined from kinetic analysis of the Y257F-HPCA + O_2 reaction at pH 7.5 (Model 1) and pH 5.5 (Model 2).

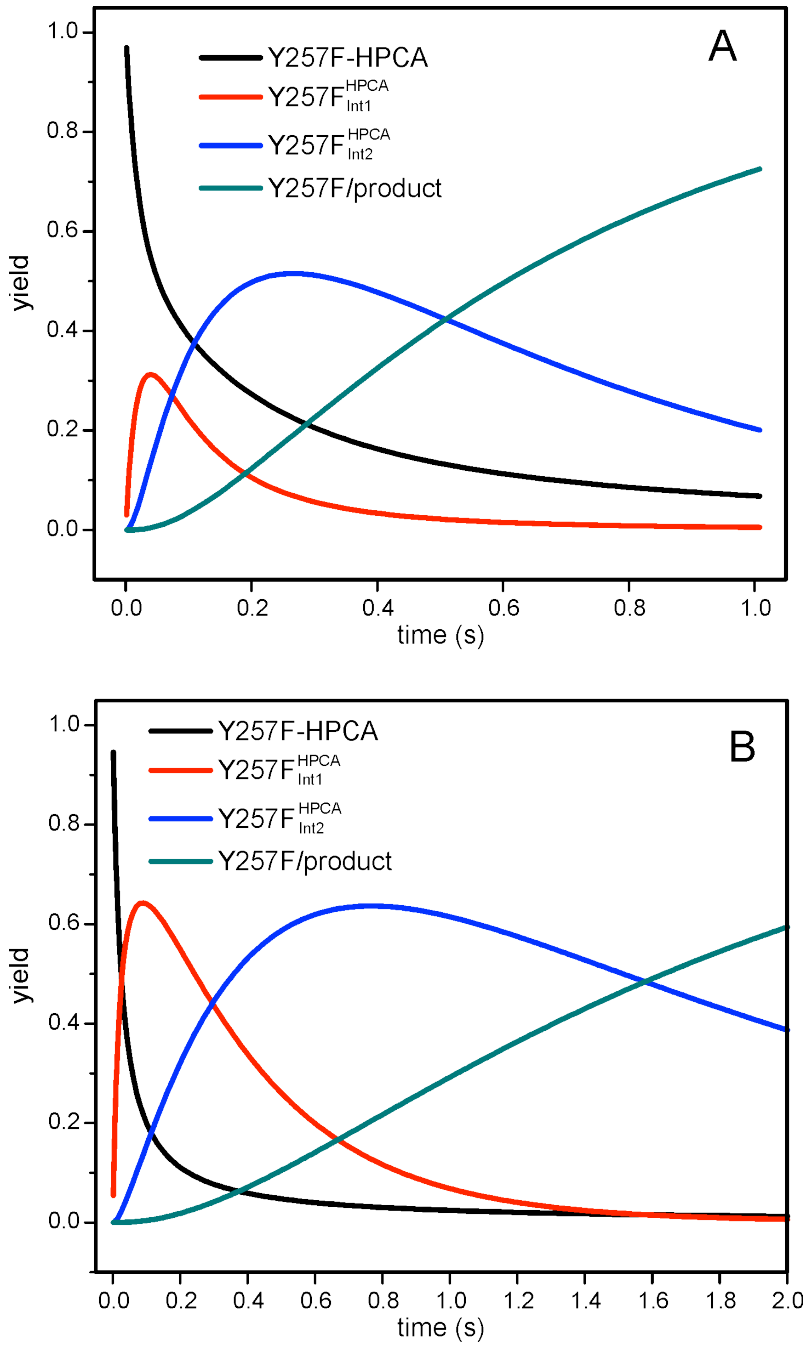

Figure 44: Simulation of expected time-dependent yields for reaction intermediates from the Y257F-HPCA + O_2 reaction.(A) Simulation for Model 1 in Scheme 3. (B) Simulation for Model 2 in Scheme 3. The simulation assumes the presence of only one Y257F-HPCA species at pH 7.5 and 5.5.

Chemical nature of $Y257F_{Int1}^{HPCA}$.

$Y257F_{Int1}^{HPCA}$ forms in a second order reaction between Y257F-HPCA and O_2, so it is an oxygen complex of some sort. However, it differs from each of the oxygen complexes found thus far for 2,3-HPCD and its variants. $Y257F_{Int1}^{HPCA}$ forms in a reversible reaction at pH 7.5, exhibits no chromophore or EPR spectrum, and contains only Fe(II). By contrast, $H200N_{Int1}^{4NC}$ also forms reversibly upon O_2 binding to H200N-4NC, but it contains an Fe(III) spin coupled to bound superoxide anion and exhibits an integer spin EPR spectrum. $H200N_{Int1}^{HPCA}$ binds O_2 irreversibly, has a distinctive chromophore at 310, 395, and 610 nm, and exhibits an integer spin EPR spectrum from Fe(III) spin coupled to a radical on the substrate. It has been assigned as a substrate semiquinone-Fe(III)-(H)peroxo species. Finally, $FeHPCA_{Int1}^{HPCA}$ contains Fe(II) and has no chromophore or EPR spectrum like $Y257F_{Int1}^{HPCA}$, but it differs in that it exhibits no O_2 concentration dependence for its formation, suggesting that it is a species well into the reaction cycle, perhaps the alkylperoxo intermediate. $Y257F_{Int1}^{HPCA}$ could in principle be the SQ-Fe(II)-$O_2^{\cdot -}$ postulated to be the reactive oxygen-activated species and observed *in crystallo* when a crystal of 2,3-HPCD -4NC is exposed to O_2. It is illustrated below that the electronic transitions which give rise to the SQ chromophore are not significantly perturbed when the SQ ligand is spin coupled to a high-spin Fe(III)-(H)peroxo site. This could also be the case for a SQ ligand spin-coupled to a Fe(II)-O_2 radical site, but there is no precedent in solution for this state to the best of our knowledge. Assuming the SQ will exhibit a chromophore independent of the oxidation state of the iron or the bound O_2, then the lack of a strong chromophore from $Y257F_{Int1}^{HPCA}$ suggests that this intermediate does not contain a semiquinone or quinone form of the substrate. Since MB data shows that $Y257F_{Int1}^{HPCA}$ contains Fe(II), the lack of a bound SQ suggests that the bound oxygen must remain close to the O_2 oxidation state. This would not be expected to be a strong bond, which is in accord with the weak affinity observed here for the complex at pH 7.5. It is also possible that O_2 is bound in the active site, but not to the iron. This type of complex appears to be an intermediate in the O_2 binding process in 2,3-HPCD and other dioxygenases

based on previous transient kinetic studies (*95, 161, 162*). However, this is made less likely by the significant perturbation observed in the Mössbauer spectrum. Therefore, we propose that $Y257F_{Int2}^{HPCA}$ is most likely to be an HPCA-Fe(II)-O_2 complex with minor electron transfer or spin delocalization to the oxygen.

Chemical nature of $Y257F_{Int2}^{HPCA}$.

In contrast to $Y257F_{Int1}^{HPCA}$, $Y257F_{Int2}^{HPCA}$ exhibits a relatively intense chromophore at 425 nm and possibly a weak feature near 325 nm [e]. The λ_{max} and intensity of this chromophore are fully consistent with the spectra observed in the UV-vis region from unbound quinones or semiquinones (Table 7). Incubation of HPCA in the absence of 2,3-HPCD with a high potential quinone results in a unbound HPCA-SQ which exhibits a very similar long wavelength spectrum to that observed for $H200N_{Int1}^{HPCA}$ (Figure 45, λ_{max} near 610 nm for $H200N_{Int1}^{HPCA}$ and 645 nm for HPCA-SQ), suggesting that the electronic transitions which give rise to the SQ chromophore are retained when the SQ ligand is spin coupled to a high-spin Fe(III)-(H)peroxo site. It is not known whether this will also be true when the SQ ligand is spin coupled to a Fe(II)-O_2 radical site, but it is likely to be the case, since the origin of the band is evidently not charge transfer.

The UV-vis spectrum of $Y257F_{Int2}^{HPCA}$ is missing the low energy feature associated with the HPCA-SQ, but it does have a feature is similar to that observed for the unbound HPCA-Q (Figure 45, λ_{max} near 425 nm for $Y257F_{Int2}^{HPCA}$ and 395 nm for unbound HPCA-Q). Based on this spectrum, $Y257F_{Int2}^{HPCA}$ is unlikely to contain a HPCA SQ, Thus far, preliminary Mössbauer spectra from a sample expected to contain >50% $Y257F_{Int2}^{HPCA}$ has revealed only Fe(II) species, although the spectral resolution at present is not sufficient to make specific assignments. The absence of Fe(III) species, the lack of a low-

[e] This region of the spectra is obscure with the presence of significant amounts of product at the times when there are high yields of $Y257F_{Int2}^{HPCA}$.

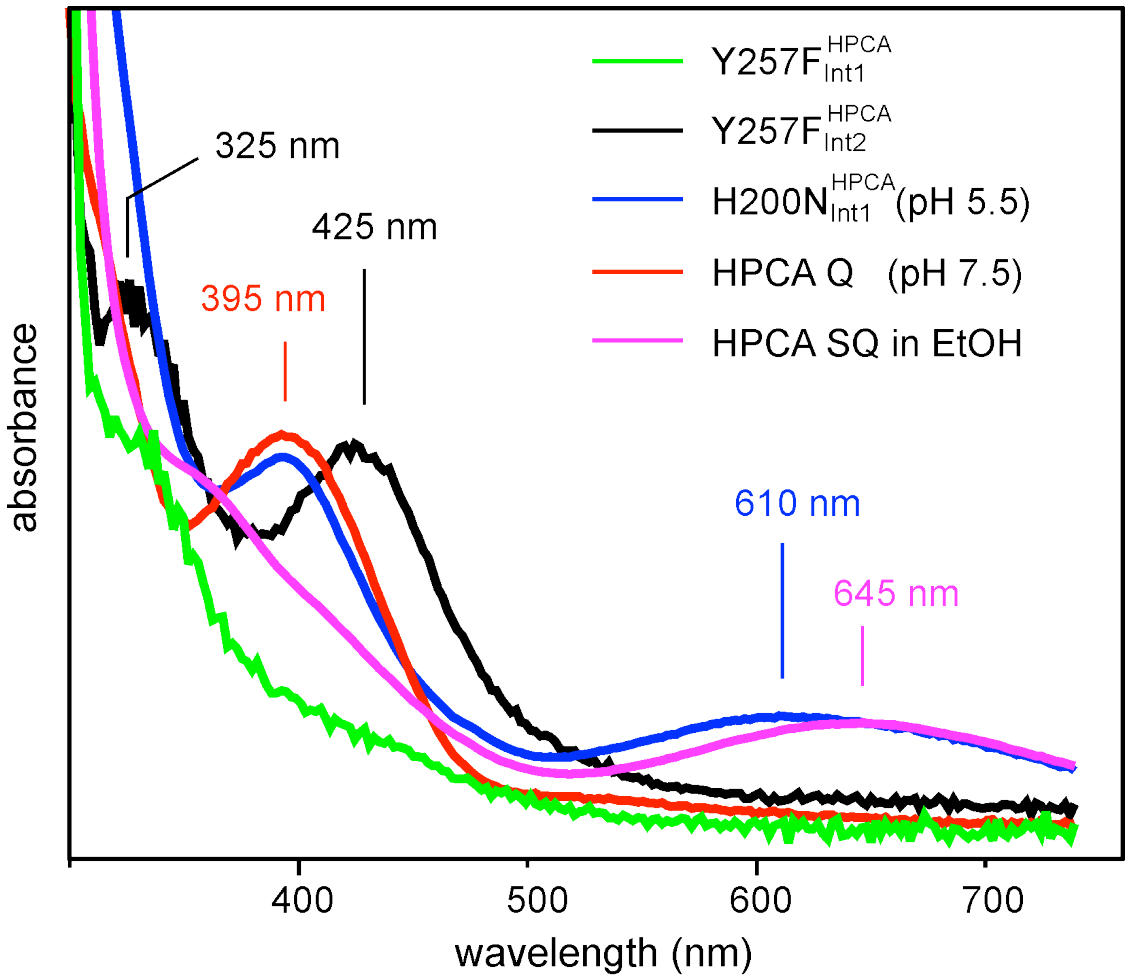

Figure 45: Comparison of UV-vis spectra of unbound HPCA quinone and HPCA semiquinone to those of $Y257F_{Int1}^{HPCA}$. $Y257F_{Int2}^{HPCA}$ and $H200N_{Int1}^{HPCA}$. The spectrum of $Y257F_{Int1}^{HPCA}$ and $Y257F_{Int2}^{HPCA}$ come from the time course on Figure 37 (100 ms spectra for $Y257F_{Int1}^{HPCA}$ and 500 ms for $Y257F_{Int2}^{HPCA}$). HPCA quinone and HPCA semiquinone are synthesized as described in Materials and Methods. The spectra are scaled arbitrarily to facilitate comparison of UV-vis features.

energy band, and the presences of the intense feature near 425 nm suggest that $Y257F_{Int2}^{HPCA}$ is most likely a HPCA Q-Fe(II)-(H)peroxo complex.

Basis for slow substrate binding in the rate limiting step while retaining high affinity.

2,3-HPCD binds HPCA rapidly and with high affinity at the start of the reaction cycle, and the rate limiting step occurs during the ring-cleaving process immediately before fast product release. In contrast, Y257F binds HPCA in the rate limiting step of the cycle, albeit still with high affinity. The binding process appears to be multistep with the true rate-limiting step occurring after initial binding of HPCA in the active site. An analogous multistep binding process occurs in the case of 4NC binding to both 2,3-HPCD and H200N. Although it is not rate limiting, the slowest step in 4NC binding to both enzymes is much slower than HPCA binding. This must be the case because the respective turnover numbers for the reaction of 2,3-HPCD or H200N with HPCA and O_2 are larger than the slowest step for 4NC binding to 2,3-HPCD or H200N. As such, the observation that the Y257F mutant has an overall rate-limiting step associated with HPCA binding suggests that Tyr257 plays a key role in rapid formation of a competent enzyme-substrate complex.

The crystal structures of 2,3-HPCD-HPCA and 2,3-HPCD-4NC show that a hydrogen bond from Tyr257 to the HPCA C3-O^- could facilitate deprotonation of this group during binding and also stabilize its displacement from the plane of the aromatic ring as the HPCA C3 carbon moves from sp^2 to sp^3 hybridization during the proposed reaction cycle. Substitution of Phe at position 257 would eliminate the stabilization of the deprotonated substrate, and thus decrease the rate of substrate deprotonation, perhaps accounting for the shift in the rate limiting step. We have observed that 4NC also binds very slowly to Y257F despite the fact that it binds as a dianionic rather than monoanionic catechol. When 4NC enters the active site at pH 7.5, it is in the monoanionic form with the C1-hydroxyl deprotonated. This means that the same C2-hydroxyl is deprotonated for both 4NC and the equivalent C3-hydroxyl of HPCA is

deprotonated during the binding process even though they finish in different deprotonation states in the respective enzyme-substrate complexes. Again, the absence of Tyr257 would remove an important stabilization for the deprotonated 4NC, potentially slowing its binding.

Despite the slow rate of binding, the affinity of the final complex is high and comparable to that found for the WT enzyme. One possible explanation for this is that Tyr257 cannot act as an active site base to facilitate deprotonation, and thus the actual active site base is still in place in the Y257F variant. One candidate for the active site base is His248, which is hydrogen bonded to Tyr257 (3 Å) and out of hydrogen bonding range from the HPCA C3-hydroxyl (4 Å). Thus, His248 may still function to accept the proton from substrate as it binds, but the process may not be fast in the absence of the intervening Tyr257. The final substrate complex would then have the same state of substrate protonation as found for the WT enzyme. Indeed, 4NC is bound in the same dianionic state in Y257F as it is in the WT enzyme. A second possible explanation for the high affinity of HPCA in Y257F stems from the distortion from aromatic ring planarity that appears to be facilitated by Tyr257 as part of the oxygen activation process. In the absence of Tyr257, this distortion may not occur. The substrate loses a hydrogen bond to Y257, but the ring geometry and charge are optimized for binding to the iron, which may allow a stronger final complex to form.

Origin of rate constant decreases in reaction cycle steps – mechanistic significance.

The rate constants for intermediate conversion in the catalytic cycle are affected in similar ways by the Y257F mutation as by the use of 4NC as the substrate. We have proposed that 4NC slows the reaction because the electron withdrawing nitro substituent makes electron transfer through the Fe(II) to the O_2 less favorable. This is dramatically observed in the H200N-4NC reaction with O_2 where the 4NC-Fe(III) superoxo species persists for hundreds of seconds without attacking the 4NC. In the case of HPCA, the electron donating inductive effects of the para substituent will make it much more favorable to donate an electron

through the iron to the O_2, leading to rapid, irreversible binding. The effect of this putative electron transfer will be to give the substrate semiquinone character that would facilitate subsequent attack by the superoxo species formed in the process. However, a radical semiquinone will normally form by delocalizing the unpaired spin on the ring which would cause the ring to remain essentially planar and also not provide a specific position for attack by superoxide. Stabilization of the HPCA C3-O^- below the plane of the ring by hydrogen bonding to Tyr257 (< 2.4 Å) would serve to not only promote the formation of the semiquinone, and thus electron transfer, but also to localize the radical on C3 of HPCA. This would direct the position of superoxide attack, which is completely specific in the case of 2,3-HPCD. It is possible that without this additional stabilization, electron transfer between the substrates does not readily occur, leading to slow kinetics for the same reasons just described for the 4NC reaction.

The natures of $Y257F_{Int1}{}^{HPCA}$ and $Y257F_{Int2}{}^{HPCA}$ appear to support the proposal that the rate of electron transfer between substrates is slowed. The discussion above suggests that no electron has transferred from the substrate in $Y257F_{Int1}{}^{HPCA}$ while in $Y257F_{Int2}{}^{HPCA}$ most likely two electrons have transferred without immediate attack of the resulting activated oxygen species on the substrate as occurs in the reaction cycle of the WT enzyme. It may be that without the localized radical and ring distortion caused by Tyr257, attack on the ring is much less favorable.

Basis for pH effects on O_2 binding.

The binding of O_2 to the iron of 2,3-HPCD is a complex process that is carefully regulated to assure specificity. The current and several past studies show that substrate must bind first to provide the electrons needed to stabilize the Fe-O_2 bond and perhaps to facilitate the release of solvent that blocks the O_2 binding site in the resting enzyme. In the absence of Tyr257, we hypothesize that the supply of electrons to stabilize the Fe-O_2 bond will be compromised, causing the binding process to be slow and reversible. One way the enzyme can counter the reversibility is to protonate His200 which is in hydrogen bonding and

charge interaction range of the bound O_2 (Figure 10 and 43). In particular, the new positive charge gained by protonating His200 at low pH would stabilize $O_2^{\cdot -}$ character as O_2 binds to the iron. This would not necessarily make the binding process more rapid (as observed), but it might serve to slow oxygen release.

CONCLUSION

Mechanistic studies with 2,3-HPCD in solution have focused on unmasking oxygen activation steps through the use of slow substrates and or mutation of the postulated acid-base catalyst His200. Here, mechanistic consequences of mutating Tyr257 are revealed with kinetic and spectroscopic studies of the Y257F mutant. Tyr257 interacts strongly with the C-O^- group associated with the site of ring attack, and this interaction was postulated to effect out of plane distortion of this functional group, thereby facilitating electron transfer from the substrate to the oxygen and helping to designate the eventual site of oxygen attack. Consistent with the loss of this key interaction, single turnover studies of the Y257F reaction with HPCA and O_2 have shown significant decreases in the rate constants of several steps in the reaction cycle and revealed discrete oxygenated reaction intermediates. First, a labile oxygenated complex termed $Y257F_{Int1}{}^{HPCA}$ is formed upon O_2 binding to the anaerobic substrate complex. Mössbauer reveals $Y257F_{Int1}{}^{HPCA}$ contains Fe(II) and with no major change in the optical or EPR spectrum from resting enzyme-substrate complex. As such, this species most likely corresponds to a labile HPCA-Fe(II)-O_2 complex. The reversible nature of the O_2 binding event is consistent with this idea and also suggests that dioxygen is not reduced.

As the Y257-HPCA + O_2 reaction proceeds, $Y257F_{Int1}{}^{HPCA}$ decays to form $Y257F_{Int2}{}^{HPCA}$, a novel reaction intermediate with an intense and prominent chromophore (ε_{425nm} = 10,500 M^{-1} cm^{-1}). The chromophore associated with $Y257F_{Int2}{}^{HPCA}$ resembles the main feature observed from a HPCA-Q synthesized in the absence of 2,3-HPCD. Based on this comparison and the lack of evidence for an Fe(III) site from preliminary analysis of MB samples containing $Y257F_{Int2}{}^{HPCA}$ (data now shown), this reaction intermediate most likely corresponds to a HPCA Q-Fe(II)-(H)peroxo, which proceeds with slow ring-cleaving chemistry. The ability to observe $Y257F_{Int1}{}^{HPCA}$ and $Y257F_{Int2}{}^{HPCA}$ in the normally very fast oxygen activation and insertion phase of the reaction cycle

suggests that Tyr257 plays a key role in aiding the ring attack/oxygen insertion steps. However, it is also observed that the Y257F mutant has an overall rate limiting step in the multistep HPCA binding process. This observation implies Tyr257 plays a second key role during formation of the monoanionic enzyme-substrate complex.

Chapter 3 contributions.

This work is supported by the NIH grant GM 24689 (to John. D. Lipscomb), grant EB-001475 (Eckard Münck), and graduate traineeship GM08700 (to Michael. M. Mbughuni). Mössbauer analyses were done by Eckard Münck and Katlyn K. Meier. Also, many thanks to Dr. Stephanie Groce who originally made the Y257F mutation

PERSPECTIVE

The mechanistic proposal for extradiol dioxygenases put forth initially by our laboratory and supported by theory and experiments from many other laboratories is based on the premise that the enzyme facilitates migration of electron density from the aromatic substrate to O_2 (*28*). This would establish an intermediate in which reaction between the substrates could occur in a spin allowed process. Our proposal has been that simultaneous binding of the two substrates to the iron serves to connect the substrates so that this transfer can occur while also orienting the substrates to promote specificity of attack and ring cleavage.

Several variations on this core theme have been proposed or seem feasible based on the known chemistry of metalloenzymes and oxygenases. For example, the electron transfer might involve either one or two electrons to yield either a diradical pair or a quinone-(hydro)peroxo pair bound to Fe(II). Both of these possible intermediates would be likely to react to yield an alkylperoxo intermediate as seen for intermediates trapped *in-crystallo* (*50*). Alternatively, the electron transfer might involve only the iron and O_2 to yield an Fe(III)-superoxo species while the substrate remains fully aromatic (*51*). This type of intermediate is likely to be less reactive than the former two, but it has been proposed as the reactive species in other oxygenases and oxidases.

The advent of crystal structures of 2,3-HPCD and other extradiol dioxygenases brought to light the potential importance of a final piece in the mechanistic picture, namely, the involvement of second sphere amino acids *(49*). As in other aspects of the mechanism, many different residues have been proposed and many roles for these residues have been advanced (*34*)(*28*). Mutagenesis studies by our laboratory and others have highlighted the importance and many potential roles of the conserved histidine at the position equivalent to H200 in 2,3-HPCD (*94*)(*96*). However, the strong hydrogen bonding interactions with the substrates suggest that other residues such as the Tyr at the equivalent of position 257 in 2,3-HPCD are likely to also be important

(*102*). We have emphasized that the roles of the second sphere amino acids may, in many cases, relate to the core theme of substrate activation by electron transfer described above.

The studies described in this thesis have been designed to test the core electron transfer hypothesis and to investigate the influence of the second sphere amino acids on this process. Prior to the start of this work several intermediates for the WT and H200 reactions with 4NC had been reported by our laboratory based on stopped flow studies, but none had been trapped for analysis of their chemical nature (*94*)(*96*). Parallel studies of intermediates trapped *in crystallo* had been conducted, but connections to the core electron transfer process in these species was tentative (*50*). Based on the current studies, six different types of intermediates have now been described and their chemical nature determined from spectroscopic studies. These intermediates are summarized in Table 10. One type of intermediate, the Fe(II)-alkylperoxo was found in two different contexts bringing the number of new intermediates described to a total of seven.

It is clear from these intermediates that our core proposal that electrons can be transferred from the aromatic substrate to the oxygen while both are bound to the active site iron is valid. They also show that there is a profound influence of the second sphere amino acids at positions 200 and 257 on the distribution of electron density in the system, and in some cases, on the efficacy of the ring cleaving reaction itself. Not shown in the table, but amply demonstrated in the Chapters, is the extremely large difference in rate constants for the reactions of the intermediates engendered by mutation of these residues (~ 6 orders of magnitude span). Similar effects are seen to derive from the chemical nature of the substrate, especially the inductive effects of the substituent on the opposite side of the aromatic ring from the vicinal hydroxyl functions.

Several general findings derive from this study. First, in all cases except $Y257F_{Int1}{}^{HPCA}$, the oxygen becomes reduce, but both superoxo and (hydro)peroxo states are observed. The one case where superoxo can be

directly identified, $H200N_{Int1}^{4NC}$, stabilizes an Fe(III) and exhibits very slow decay to yield a quinone product. The 4NC substrate in the $H200N_{Int1}^{4NC}$ intermediate remains fully aromatic. These results suggest that the typical Fe(III)-superoxo species found in many types of metalloenzymes is not the reactive species in extradiol dioxygenases. With the exception of the effectively dead end product complex $H200N_{Int2}^{4NC}$, the Fe(II) and Fe(III) peroxo complexes ($Y257F_{Int2}^{HPCA}$ and $H200N_{Int1}^{HPCA}$, respectively) are much more reactive and lead to the correct ring cleaved product. It is possible that one of these represents the chemical nature of the reactive species in the wild type system, although their reaction rate constants are still at least one order of magnitude slower than that for formation of the native product complex after O_2 is added to the enzyme-HPCA complex.

A second general finding is that an intermediate Fe(III) species is never observed when histidine is at position 200. This may mean that an Fe(III) intermediate is formed and then is very rapidly reduced, but no evidence for such an intermediate is observed. Moreover, the reaction of the Y257F mutant is slow enough that steps in the O_2 binding and activation process can be easily observed, but still there is no evidence for an Fe(III) intermediate. These observations support the role of the iron as a “wire” connecting the two substrates. It is consistent with ongoing studies which show that iron, manganese, and cobalt can function very effectively in the active site of 2,3-HPCD, despite a 1.3 V span in redox potential, arguing against a sustained change in redox state during catalysis (*78*). It seems likely that His200 serves many functions including acting as an acid base catalyst, stabilizing the buildup of charge density on the bound O_2 as it is activated and perhaps stabilizing the oxygen in the side-on binding orientation through steric interactions. Additional insight into the proposed roles for H200 and Y257 can come from pH studies of the intermediates described here, also, the chemical and spectroscopic

Table 10: Intermediates formed by 2,3-HPCD and its variants with HPCA and alternative substrates.

Intermediate	Fe ox state (Mössbauer)	Optical spectrum	EPR signal	Reversible O_2 binding	Assignment ref
$FeHPCD_{Int1}^{HPCA}$	Fe(II)	No	No	No	Fe(II)-alkylperoxo (*52*)
$H200N_{Int1}^{HPCA}$	Fe(III) Spin-coupled	Yes HPCA-SQ $\varepsilon_{395} \cong 3200$ $\varepsilon_{610} \cong 1100$	Yes $S = 2$ ES	No	HPCA SQ-Fe(III)-(H)peroxo (*52*)
$H200N_{Int2}^{HPCA}$	Fe(II)	No	No	No	Fe(II)-alkylperoxo
$H200N_{Int1}^{4NC}$	Fe(III) Spin-coupled	Yes 4NC $\varepsilon_{506} \cong 10,000$ $\varepsilon_{630} \cong 1,200$	Yes $S = 2$ GS	Yes	4NC-Fe(III)-$O_2^{\cdot -}$ (*51*)
$H200N_{Int2}^{4NC}$	Fe(III) Spin-coupled	Yes 4NC-SQ $\varepsilon_{405} \cong 15,000$ $\varepsilon_{675} \cong 1,000$	Yes $S = 2$ ES	N/A	4NC SQ-Fe(III)-(H)peroxo (*51*)
$Y257F_{Int1}^{HPCA}$	Fe(II)	No	No	Yes	HPCA-Fe(II)-O_2 Chapter 3
$Y257F_{Int2}^{HPCA}$	Fe(II)	Yes $\varepsilon_{425} \cong 10,500$	No	N/A	HPCA Q-Fe(II)-(H)peroxo Chapter 3

Abbreviations: GS = ground state and ES = exited state.

characterization of these intermediates is likely to be useful in interpreting ongoing experiments designed to trap oxy intermediates in crystals of the H200 and Y257 mutants as they react with substrates.

A third general finding is that electron transfer from the substrate in the first observable step as well as reaction of an activated oxygen species with substrate to form the alkylperoxo intermediate are greatly accelerated in the presence of Y257. Our model for the reaction mechanism predicts steps in the activation of both O_2 and the catecholic subtrate would be accelerated by stabilizing sp^3 hybridization of the substrate ring carbon that is attacked by oxygen (*50*). The initial formation of a semiquinone is promoted by stabilization of a buckled ring and localization of the radical at a specific carbon would promote attack at this carbon by an activated oxygen radical. The hydrogen bonding interaction between Tyr257 and the HPCA C3-O^- detected in the crystal structure of the anaerobic 2,3-HPCD-HPCA complex would provide this stabilization as a driving force toward sp^3 hybridization of this carbon. Conversely, crystal structures of quinone adducts of catechols bound in the active site of 2,3-HPCD show that the ring is planar, as opposed to buckled, as expected (Communication from Dr. Elena Kovaleva). Thus, one effect of mutating Y257 to Phe might be to stabilize a quinone-Fe(II)-(H)peroxo intermediate like $Y257F_{Int2}^{HPCA}$, but the slow rate of product formation for this intermediate argues against a quinone-Fe(II)-(H)peroxo intermediate being the reactive species in the wild type system.

A final general finding is that the substrate plays a central role in determining both the type of intermediate formed and its rate of reaction. An electron donating substituent greatly accelerates the formation and decay of the types of intermediates found here. This is in accord with the core hypothesis that electron transfer from the substrate to the O_2 is key to catalysis. A second aspect to this may also be that the substrate is the most likely source of the proton needed to promote O-O bond cleavage. The use of Fe(II) in this enzyme class and the presence of an Asp ligand to the iron means that a single deprotonation of the catechol is favored during substrate binding to maintain a

charge neutral metal center. This means upon substrate binding, a proton is present in the active site that can be removed during the reaction cycle and used to protonate the proximal oxygen to the iron as the O-O bond of the alkylperoxo is cleaved. Substrates like 4NC have lower pKa's and are fully deprotonated when bound to the Fe(II) due to the electron withdrawing nitro substituent. This suggests that during catalysis, the necessary proton must be transported from solution, leading to a decrease in the rate of the reaction. The intermediates studied here illustrate how much the reaction is slowed when either 4NC is used or when H200 is missing. This is in accord with the proposed role of His200 as an acid base catalyst (*28*). In the absence of the acid base catalyst His200, the transfer of a proton from the substrate is slow even for substrates that bring a proton into the active site for this purpose (e.g HPCA substrate).

In conclusion, the reaction intermediates described in this thesis illustrate that the 2-His + 1-Asp/Glu Fe binding motif is a versatile and robust catalytic platform for O_2 activation chemistry in biology. Also, this study reveals the extent to which nature has used the second coordination sphere to fine tune 2,3-HPCD as a catalyst for extradiol ring-cleaving chemistry. The various intermediates described here suggest the electron donating capacity of HPCA and guidance from His200 and Y257 allow native 2,3-HPCD to orchestrate productive O_2 and HPCA activation within the dead time of the stopped-flow and RFQ instruments. Slower steps of the O_2 dependent reaction cycle must therefore correspond to conversion of reaction cycle intermediates that occur late in the cycle (Figure 46). During O_2 binding, His200 must impose a productive side-on O_2 binding mode through H-bonding and/or steric interactions. His200 can also take on a positive charge in order to pull electron density from the substrate to O_2 and stabilize the resultant superoxo anion. The side-on O_2 binding mode is advantageous because it would minimize reorganization of the oxy complex in order to form the alkylperoxo adduct. As O_2 binds, Y257 can activate the substrate for regio-specific ring attack by pulling the C3-O^- functional group of HPCA below the plane of the ring, favoring

formation of the sp^3 hybridized alkylperoxo adduct at C3 of the native HPCA substrate (C2 for 4NC). In the native reaction cycle, His200 and Y257 would work in concert, minimizing the lifetime of the initial oxy complex and committing the reaction to ring-cleaving oxygenase chemistry by forming the alkylperoxo or lactone reaction intermediates in the first few milliseconds of the wild-type reaction cycle.

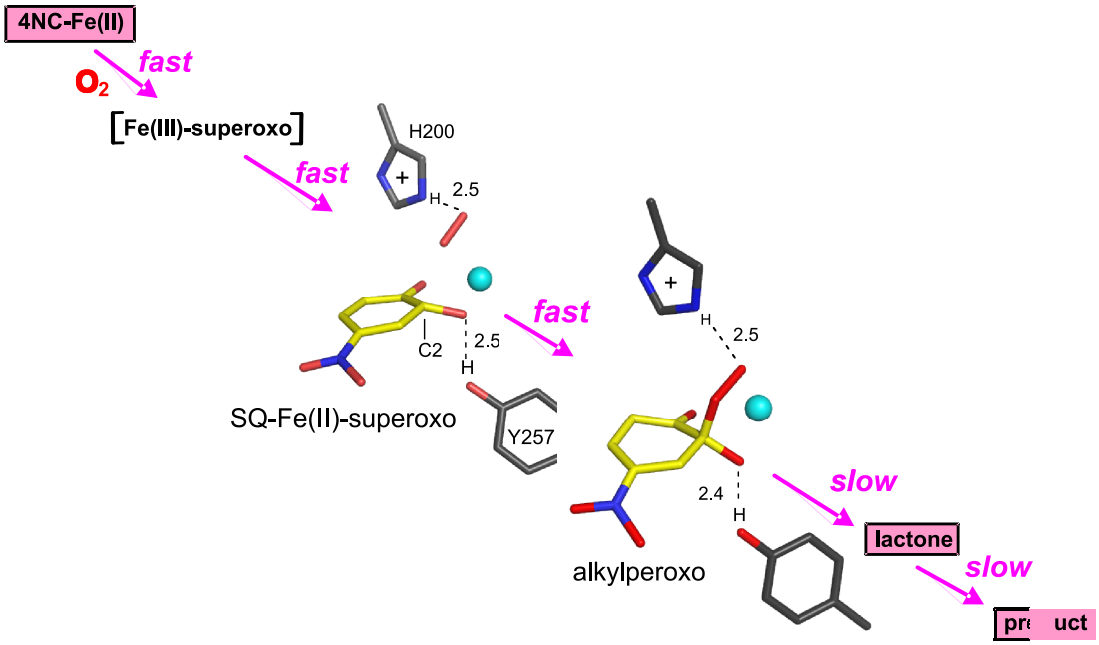

Figure 46: Proposed reaction intermediates in the native 2,3-HPCD reaction cycle. 4NC substrate is used for the illustration instead of HPCA because the structure of $FeHPCD_{Int1}^{4NC}$ and $FeHPCD_{Int2}^{4NC}$ are used to illustrate the SQ-Fe(II)-superoxo and alkylperoxo reaction intermediates . The values on the dashed lines correspond to distances for H-bonding interactions in Å (as measured from the crystal structures of $FeHPCD_{Int1}^{4NC}$ and $FeHPCD_{Int2}^{4NC}$).

REFERENCES

1. Martinez-Espinosa, R. M., Cole, J. A., Richardson, D. J., and Watmough, N. J. (2011) Enzymology and ecology of the nitrogen cycle, *Biochem. Soc. Trans*. *39*, 175-178.
2. Kerr, R. A. (2005) Earth science. The story of O_2, *Science 308*, 1730-1732.
3. Falkowski, P. G., and Isozaki, Y. (2008) Geology. The story of O_2, *Science 322*, 540-542.
4. Dagley, S. (1976) Microbial catabolism and the carbon cycle, *Biochem. Soc. Trans. 4*, 455-458.
5. Gibson, D. T. (1988) Microbial metabolism of aromatic hydrocarbons and the carbon cycle, in *Microbial metabolism and the carbon cycle* (Hagedorn, S. R., Hanson, R. S., and Kunz, D. A., Eds.), pp 33-58, Harwood Academic Publishers, Chur, Switzerland.
6. Dagley, S. (1978) Microbial catabolism, the carbon cycle and environmental pollution, *Die Naturwissenschaften 65*, 85-95.
7. Wackett, L. P., and Hershberger, D. (2001) *Biocatalysis and Biodegradation: Microbiol transformation of organic compounds.*, ASM press., Washington, DC.
8. Loenarz, C., and Schofield, C. J. (2008) Expanding chemical biology of 2-oxoglutarate oxygenases, *Nat Chem Biol 4*, 152-156.
9. McDonough, M. A., Loenarz, C., Chowdhury, R., Clifton, I. J., and Schofield, C. J. (2010) Structural studies on human 2-oxoglutarate dependent oxygenases, *Curr. Opin. Struct. Biol. 20*, 659-672.
10. Bugg, T. D. H., Ahmad, M., Hardiman, E. M., and Singh, R. (2011) The emerging role for bacteria in lignin degradation and bio-product formation, *Curr. Opin. Biotechnol. 22*, 394-400.
11. Shaik, S., Cohen, S., Wang, Y., Chen, H., Kumar, D., and Thiel, W. (2010) P450 enzymes: Their structure, reactivity, and selectivities modeled by QM/MM calculations, *Chem. Rev. 110*, 949-1017.
12. Chen, P., Bell, J., Eipper, B. A., and Solomon, E. I. (2004) Oxygen activation by the noncoupled binuclear copper site in peptidylglycine α-hydroxylating monooxygenase. Spectroscopic Definition of the Resting Sites and the Putative CuIIM-OOH Intermediate, *Biochemistry 43*, 5735-5747.
13. Kovaleva, E. G., and Lipscomb, J. D. (2008) Versatility of biological non-heme Fe(II) centers in oxygen activation reactions, *Nat. Chem. Biol. 4*, 186-193.
14. Bugg, T. D. H. (2001) Oxygenases: mechanisms and structural motifs for O_2 activation, *Curr. Opin. Chem. Biol. 5*, 550-555.
15. Renger, G. (2011) Light induced oxidative water splitting in photosynthesis: energetics, kinetics and mechanism, *J. Photochem. Photobiol B. 104*, 35-43.

16. Abe, S., Ueno, T., Watanabe, Y., and Ward, T. (2009) Artificial Metalloproteins Exploiting Vacant Space: Preparation, Structures, and Functions Bio-inspired Catalysts, pp 25-43, Topics in Organometallic Chemistry, Springer Berlin / Heidelberg.
17. El Albani, A., Bengtson, S., Canfield, D. E., Bekker, A., Macchiarelli, R., Mazurier, A., Hammarlund, E. U., Boulvais, P., Dupuy, J. J., Fontaine, C., Fursich, F. T., Gauthier-Lafaye, F., Janvier, P., Javaux, E., Ossa, F. O., Pierson-Wickmann, A. C., Riboulleau, A., Sardini, P., Vachard, D., Whitehouse, M., and Meunier, A. (2010) Large colonial organisms with coordinated growth in oxygenated environments 2.1 Gyr ago, *Nature 466*, 100-104.
18. Hamilton, G. A. (1974) *Molecular Mechanisms of Oxygen Activation*, Academic Press, London.
19. Solomon, E. I., Decker, A., and Lehnert, N. (2003) Non-heme iron enzymes: contrasts to heme catalysis, *Proc. Natl. Acad. Sci. U.S.A. 100*, 3589-3594.
20. Costas, M., Mehn, M. P., Jensen, M. P., and Que, L., Jr. (2004) Dioxygen activation at mononuclear nonheme iron active sites: enzymes, models, and intermediates, *Chem. Rev. 104*, 939-986.
21. Kovaleva, E. G., Neibergall, M. B., Chakrabarty, S., and Lipscomb, J. D. (2007) Finding intermediates in the O_2 activation pathways of non-heme iron oxygenases, *Acc. Chem. Res. 40*, 475-483.
22. Hamilton, G. A. (1974) Chemical Models and Mechanisms for Oxygenases, in *Molecular Mechanisms of Oxygen Activation* (Hayaishi, O., Ed.), pp 405 - 451, Academic Press, New York.
23. Wackett, L. P. (2011) Microbes and the carbon cycle: an annotated selection of World Wide Web sites relevant to the topics in Environmental Microbiology, *Environ Microbiol 13*, 1380-1381.
24. Wackett, L. P. (2004) Evolution of new enzymes and pathways: Soil microbes adapt to s-triazine herbicides, *ACS Symp. Ser. 863*, 37-48.
25. Gibson, D. T., and Subramanian, V. (1984) Microbial degradation of aromatic hydrocarbons, in *Microbial degradation of organic compounds* (Gibson, D. T., Ed.), pp 181-252, Marcel Dekker, Inc., New York, New York.
26. Gibson, D. T., and Parales, R. E. (2000) Aromatic hydrocarbon dioxygenases in environmental biotechnology, *Curr. Opin. Biotechnol. 11*, 236-243.
27. Solomon, B. D. (2010) Biofuels and sustainability, *Ann N Y Acad Sci 1185*, 119-134.
28. Lipscomb, J. D. (2008) Mechanism of extradiol aromatic ring-cleaving dioxygenases, *Curr. Opin. Struct. Biol. 18*, 644-649.
29. Koehntop, K. D., Emerson, J. P., and Que, L., Jr. (2005) The 2-His-1-carboxylate facial triad: a versatile platform for dioxygen activation by mononuclear non-heme iron(II) enzymes, *J. Biol. Inorg. Chem. 10*, 87-93.
30. Armstrong, R. N. (2000) Mechanistic diversity in a metalloenzyme superfamily, *Biochemistry 39*, 13625-13632.

31. Ferraro, D. J., Gakhar, L., and Ramaswamy, S. (2005) Rieske business: Structure-function of Rieske non-heme oxygenases, *Biochem. Biophys. Res. Commun. 338*, 175-190.
32. Fitzpatrick, P. F. (1999) Tetrahydropterin-dependent amino acid hydroxylases, *Annu. Rev. Biochem. 68*, 355-381.
33. Purpero, V., and Moran, G. R. (2007) The diverse and pervasive chemistries of the alpha-keto acid dependent enzymes, *J Biol Inorg Chem 12*, 587-601.
34. Vaillancourt, F. H., Bolin, J. T., and Eltis, L. D. (2006) The ins and outs of ring-cleaving dioxygenases, *Crit. Rev. Biochem. Mol. Biol. 41*, 241-267.
35. He, P., and Moran, G. R. (2011) Structural and mechanistic comparisons of the metal-binding members of the vicinal oxygen chelate (VOC) superfamily, *J Inorg Biochem 105*, 1259-1272.
36. Klinman, J. P. (2007) How do enzymes activate oxygen without inactivating themselves?, *Acc. Chem. Res. 40*, 325-333.
37. Bugg, T. D. H. (2003) Dioxygenase enzymes: catalytic mechanisms and chemical models, *Tetrahedron 59*, 7075-7101.
38. Valentine, J. S., and Nam, W. (2007) Dioxygen activation by metalloenzymes and models, *Acc. Chem. Res. 40*, 465-634.
39. Hayaishi, O. (2005) IUB(MB) 50th Anniversary, *IUBMB Life 57*, 213-214.
40. Hayaishi, O. (2005) An odyssey with oxygen, *Biochem. Biophys. Res. Commun. 338*, 2-6.
41. Bugg, T. D. H. (2011) Non-heme iron-dependent dioxygenases: Mechanism and structure, in *Iron-containing enzymes: Versatile catalysts of hydroxylation reactions in nature* (de Visser, S. P., and Kumar, D., Eds.), pp 42-66, The Royal Society of Chemistry, Cambridge, UK.
42. Hausinger, R. P. (2004) Fe(II)/α-ketoglutarate-dependent hydroxylases and related enzymes, *Crit. Rev. Biochem. Mol. Biol. 39*, 21-68.
43. Krebs, C., Fujimori, D. G., Walsh, C. T., and Bollinger, J. M., Jr. (2007) Non-heme Fe(IV)-oxo intermediates, *Acc. Chem. Res. 40*, 484-492.
44. Boyd, D. R., Sharma, N. D., Bowers, N. I., Boyle, R., Harrison, J. S., Lee, K., Bugg, T. D. H., and Gibson, D. T. (2003) Stereochemical and mechanistic aspects of dioxygenase-catalyzed benzylic hydroxylation of indene and chroman substrates, *Org. Biomol. Chem. 1*, 1298-1307.
45. Pau, M. Y. M., Lipscomb, J. D., and Solomon, E. I. (2007) Substrate activation for O_2 reactions by oxidized metal centers in biology, *Proc. Natl. Acad. Sci. U. S. A. 104*, 18355-18362.
46. Lipscomb, J. D., and Orville, A. M. (1992) Mechanistic aspects of dihydroxybenzoate dioxygenases, *Metal Ions Biol. Syst. 28*, 243-298.
47. Harpel, M. R., and Lipscomb, J. D. (1990) Gentisate 1,2-dioxygenase from Pseudomonas. Substrate coordination to active site iron(2+) and mechanism of turnover, *J. Biol. Chem. 265*, 22187-22196.
48. Pau, M. Y. M., Lipscomb, J. D., and Solomon, E. I. (2008) Substrate activation for O_2 reactions by oxidized metal centers in biology. [Erratum to document cited in CA148:138097], *Proc. Natl. Acad. Sci. U. S. A. 105*, 1098.

49. Han, S., Eltis, L. D., Timmis, K. N., Muchmore, S. W., and Bolin, J. T. (1995) Crystal structure of the biphenyl-cleaving extradiol dioxygenase from a PCB-degrading pseudomonad, *Science 270*, 976-980.
50. Kovaleva, E. G., and Lipscomb, J. D. (2007) Crystal structures of Fe^{2+} dioxygenase superoxo, alkylperoxo, and bound product intermediates, *Science 316*, 453-457.
51. Mbughuni, M. M., Chakrabarti, M., Hayden, J. A., Bominaar, E. L., Hendrich, M. P., Münck, E., and Lipscomb, J. D. (2010) Trapping and spectroscopic characterization of an FeIII-superoxo intermediate from a nonheme mononuclear iron-containing enzyme, *Proc Natl Acad Sci U S A 107*, 16788-16793.
52. Mbughuni, M. M., Chakrabarti, M., Hayden, J. A., Meier, K. K., Dalluge, J. J., Hendrich, M. P., Münck, E., and Lipscomb, J. D. (2011) Oxy-intermediates of homoprotocatechuate 2,3-dioxygenase: Facile electron transfer between substrates, *Biochemistry 50*.
53. Chen, J., Li, W., Wang, M., Zhu, G., Liu, D., Sun, F., Hao, N., Li, X., Rao, Z., and Zhang, X. C. (2008) Crystal structure and mutagenic analysis of GDOsp, a gentisate 1,2-dioxygenase from *Silicibacter pomeroyi*, *Protein Sci 17*, 1362-1373.
54. Karlsson, A., Parales, J. V., Parales, R. E., Gibson, D. T., Eklund, H., and Ramaswamy, S. (2003) Crystal structure of naphthalene dioxygenase: Side-on binding of dioxygen to iron, *Science 299*, 1039-1042.
55. Bassan, A., Blomberg, M. R. A., and Siegbahn, P. E. M. (2004) A theoretical study of the *cis*-dihydroxylation mechanism in naphthalene 1,2-dioxygenase, *J. Biol. Inorg. Chem. 9*, 439-452.
56. Prat, I., Mathieson, J. S., Guell, M., Ribas, X., Luis, J. M., Cronin, L., and Costas, M. (2011) Observation of Fe(V)=O using variable-temperature mass spectrometry and its enzyme-like C-H and C=C oxidation reactions, *Nat Chem 3*, 788-793.
57. Bruijnincx, P. C. A., van Koten, G., and Klein Gebbink, R. J. M. (2008) Mononuclear non-heme iron enzymes with the 2-His-1-carboxylate facial triad: Recent developments in enzymology and modeling studies, *Chem. Soc. Rev. 37*, 2716-2744.
58. Bollinger, J. M., Jr., Price, J. C., Hoffart, L. M., Barr, E. W., and Krebs, C. (2005) Mechanism of taurine: alpha-ketoglutarate dioxygenase (TauD) from *Escherichia coli*, *Eur. J. Inorg. Chem. 2005*, 4245-4254.
59. Price, J. C., Barr, E. W., Tirupati, B., Bollinger, J. M., Jr., and Krebs, C. (2003) The first direct characterization of a high-valent iron intermediate in the reaction of an a-ketoglutarate-dependent dioxygenase: A high-spin Fe(IV) complex in taurine alpha-ketoglutarate dioxygenase (TauD) from *Escherichia coli*, *Biochemistry 42*, 7497-7508.
60. Diebold, A. R., Straganz, G. D., and Solomon, E. I. (2011) Spectroscopic and computational studies of α-keto acid binding to Dke1: Understanding the role of the facial triad and the reactivity of β-diketones, *J. Am. Chem. Soc. 133*, 15979-15991.

61. Eser, B. E., Barr, E. W., Frantom, P. A., Saleh, L., Bollinger, J. M., Jr., Krebs, C., and Fitzpatrick, P. F. (2007) Direct spectroscopic evidence for a high-spin Fe(IV) intermediate in tyrosine hydroxylase, *J. Am. Chem. Soc. 129*, 11334-11335.
62. Bassan, A., Blomberg, M. R. A., and Siegbahn, P. E. M. (2003) Mechanism of aromatic hydroxylation by an activated FeIV=O core in tetrahydrobiopterin-dependent hydroxylases, *Chem.- Eur. J. 9*, 4055-4067.
63. Pavon, J. A., and Fitzpatrick, P. F. (2006) Insights into the catalytic mechanisms of phenylalanine and tryptophan hydroxylase from kinetic isotope effects on aromatic hydroxylation, *Biochemistry 45*, 11030-11037.
64. de Visser, S. P., and Straganz, G. D. (2009) Why do cysteine dioxygenase enzymes contain a 3-His ligand motif rather than a 2His/1Asp motif like most nonheme dioxygenases?, *J Phys Chem A 113*, 1835-1846.
65. Schaab, M. R., Barney, B. M., and Francisco, W. A. (2006) Kinetic and spectroscopic studies on the quercetin 2,3-dioxygenase from *Bacillus subtilis*, *Biochemistry 45*, 1009-1016.
66. Clifton, I. J., McDonough, M. A., Ehrismann, D., Kershaw, N. J., Granatino, N., and Schofield, C. J. (2006) Structural studies on 2-oxoglutarate oxygenases and related double-stranded β -helix fold proteins, *J. Inorg. Biochem. 100*, 644-669.
67. Bollinger, J. M., and Krebs, C. (2007) Enzymatic C-H activation by metal-superoxo intermediates, *Curr. Opin. Chem. Biol. 11*, 151-158.
68. Que, L., Jr., and Tolman, W. B. (2008) Biologically inspired oxidation catalysis, *Nature. 455*, 333-340.
69. Que, L., Jr. (2007) The road to non-heme oxoferryls and beyond, *Acc Chem Res 40*, 493-500.
70. Yi, C., Jia, G., Hou, G., Dai, Q., Zhang, W., Zheng, G., Jian, X., Yang, C.-G., Cui, Q., and He, C. (2010) Iron-catalysed oxidation intermediates captured in a DNA repair dioxygenase, *Nature 468*, 330-333.
71. Kovaleva, E. G., and Lipscomb, J. D. (2008) Intermediate in the O-O bond cleavage reaction of an extradiol dioxygenase, *Biochemistry 47*, 11168-11170.
72. Lipscomb, J. D., Whittaker, J. W., and Arciero, D. M. (1982) Comparative studies of intra- and extradiol protocatechuate dioxygenases, in *Oxygenases and Oxygen Metabolism* (Nozaki, M., Ed.), pp 27-38, Academic Press, New York.
73. Siegbahn, P. E. M., and Haeffner, F. (2004) Mechanism for catechol ring-cleavage by non-heme iron extradiol dioxygenases, *J. Am. Chem. Soc. 126*, 8919-8932.
74. Sanvoisin, J., Langley, G. J., and Bugg, T. D. H. (1995) Mechanism of extradiol catechol dioxygenases: Evidence for a lactone intermediate in the 2,3-dihydroxyphenylpropionate 1,2-dioxygenase reaction, *J. Am. Chem. Soc. 117*, 7836-7837.

75. Spence, E. L., Langley, G. J., and Bugg, T. D. H. (1996) Cis-trans isomerization of a cyclopropyl radical trap catalyzed by extradiol catechol dioxygenases: Evidence for a semiquinone intermediate, *J. Am. Chem. Soc. 118*, 8336-8343.
76. Christian, G. J., Ye, S., and Neese, F. (2012) Oxygen activation in extradiol catecholate dioxygenases - a density function study, *Chemical Science. 3*, 1600 - 1611.
77. Borowski, T., Georgiev, V., and Siegbahn, P. E. M. (2010) On the observation of a gem diol intermediate after O-O bond cleavage by extradiol dioxygenases. a hybrid DFT study, *J. Molec. Mod.16*, 1673-1677.
78. Emerson, J. P., Kovaleva, E. G., Farquhar, E. R., Lipscomb, J. D., and Que, L., Jr. (2008) Swapping metals in Fe- and Mn-dependent dioxygenases: Evidence for oxygen activation without a change in metal redox state, *Proc. Natl. Acad. Sci. U. S. A. 105*, 7347-7352.
79. Gunderson, W. A., Zatsman, A. I., Emerson, J. P., Farquhar, E. R., Que, L., Lipscomb, J. D., and Hendrich, M. P. (2008) Electron paramagnetic resonance detection of intermediates in the enzymatic cycle of an extradiol dioxygenase, *J. Am. Chem. Soc. 130*, 14465-14467.
80. Fielding, A. J., Lipscomb, J. D., and Que, L., Jr. (2012) Characterization of an O_2 adduct of an active cobalt-substituted extradiol-cleaving catechol dioxygenase, *J Am Chem Soc 134*, 796-799.
81. Mbughuni, M., M., Chakrabarti, M., Hayden, J., A., Bominaar, E., L., Hendrich, M., P., Münck, E., and Lipscomb, J., D. (2010) Trapping and spectroscopic characterization of an Fe^{III}-superoxo intermediate from a nonheme mononuclear iron-containing enzyme, *Proc. Natl. Acad. Sci. U. S. A. 107*, 16788-16793.
82. Arciero, D. M., and Lipscomb, J. D. (1986) Binding of ^{17}O-labeled substrate and inhibitors to protocatechuate 4,5-dioxygenase-nitrosyl complex. Evidence for direct substrate binding to the active site Fe^{2+} of extradiol dioxygenases, *J. Biol. Chem. 261*, 2170-2178.
83. Baldwin, J. E., and Bradley, M. (1990) Isopenicillin N synthase: Mechanistic studies, *Chem. Rev. 90*, 1079-1088.
84. Chen, V. J., Orville, A. M., Harpel, M. R., Frolik, C. A., Surerus, K. K., Münck, E., and Lipscomb, J. D. (1989) Spectroscopic studies of isopenicillin N synthase. A mononuclear nonheme Fe^{2+} oxidase with metal coordination sites for small molecules and substrate, *J. Biol. Chem. 264*, 21677-21681.
85. Rocklin, A. M., Kato, K., Liu, H.-w., Que, L., and Lipscomb, J. D. (2004) Mechanistic studies of 1-aminocyclopropane-1-carboxylic acid oxidase: single turnover reaction, *J. Biol. Inorg. Chem. 9*, 171-182.
86. Proshlyakov, D. A., Henshaw, T. F., Monterosso, G. R., Ryle, M. J., and Hausinger, R. P. (2004) Direct detection of oxygen intermediates in the non-heme Fe enzyme taurine/α-ketoglutarate dioxygenase, *J. Am. Chem. Soc. 126*, 1022-1023.

87. Mukherjee, A., Cranswick, M. A., Chakrabarti, M., Paine, T. K., Fujisawa, K., Munck, E., and Que, L., Jr. (2010) Oxygen activation at mononuclear nonheme iron centers: A superoxo perspective, *Inorg. Chem. 49*, 3618-3628.
88. Weiss, J. J. (1964) Nature of the iron-oxygen bond in oxyhaemoglobin, *Nature 202*, 83-84.
89. Sharrock, M., Debrunner, P. G., Schulz, C., D., L. J., Marshall, V., and Gunsalus, I. C. (1976) Cytochrome $P450_{cam}$ and its complexes. Mössbauer parameters of the heme iron., *Biochim. Biophys. Acta 420*, 8-26.
90. Schlichting, I., Berendzen, J., Chu, K., Stock, A. M., Maves, S. A., Benson, D. E., Sweet, B. M., Ringe, D., Petsko, G. A., and Sligar, S. G. (2000) The catalytic pathway of cytochrome $P450_{cam}$ at atomic resolution, *Science 287*, 1615-1622.
91. Davydov, R., Makris, T. M., Kofman, V., Werst, D. E., Sligar, S. G., and Hoffman, B. M. (2001) Hydroxylation of camphor by reduced oxy-cytochrome P450cam: Mechanistic implications of EPR and ENDOR studies of catalytic intermediates in native and mutant enzymes, *J. Am. Chem. Soc. 123*, 1403-1415.
92. Xing, G., Diao, Y., Hoffart, L. M., Barr, E. W., Prabhu, K. S., Arner, R. J., Reddy, C. C., Krebs, C., and Bollinger, J. M., Jr. (2006) Evidence for C-H cleavage by an iron-superoxide complex in the glycol cleavage reaction catalyzed by myo-inositol oxygenase, *Proc. Natl. Acad. Sci. U. S. A. 103*, 6130-6135.
93. Shu, L., Chiou, Y. M., Orville, A. M., Miller, M. A., Lipscomb, J. D., and Que, L., Jr. (1995) X-ray absorption spectroscopic studies of the Fe(II) active site of catechol 2,3-dioxygenase. Implications for the extradiol cleavage mechanism, *Biochemistry 34*, 6649-6659.
94. Bugg, T. D. H., and Winfield, C. J. (1998) Enzymic cleavage of aromatic rings: mechanistic aspects of the catechol dioxygenases and later enzymes of bacterial oxidative cleavage pathways, *Nat. Prod. Rep. 15*, 513-530.
95. Groce, S. L., Miller-Rodeberg, M. A., and Lipscomb, J. D. (2004) Single-turnover kinetics of homoprotocatechuate 2,3-dioxygenase, *Biochemistry 43*, 15141-15153.
96. Groce, S. L., and Lipscomb, J. D. (2005) Aromatic ring cleavage by homoprotocatechuate 2,3-dioxygenase: Role of His200 in the kinetics of interconversion of reaction cycle intermediates, *Biochemistry 44*, 7175-7188.
97. Wang, Y. Z., and Lipscomb, J. D. (1997) Cloning, overexpression, and mutagenesis of the gene for homoprotocatechuate 2,3-dioxygenase from *Brevibacterium fuscum*, *Protein Exp. Purif. 10*, 1-9.
98. Miller, M. A., and Lipscomb, J. D. (1996) Homoprotocatechuate 2,3-dioxygenase from *Brevibacterium fuscum* - A dioxygenase with catalase activity, *J. Biol. Chem. 271*, 5524-5535.

99. Fox, B. G., Shanklin, J., Somerville, C., and Münck, E. (1993) Stearoyl-acyl carrier protein Δ^9 desaturase from *Ricinus communis* is a diiron-oxo protein, *Proc. Natl. Acad. Sci. U. S. A. 90*, 2486-2490.
100. Arciero, D. M., Lipscomb, J. D., Huynh, B. H., Kent, T. A., and Münck, E. (1983) EPR and Mössbauer studies of protocatechuate 4,5-dioxygenase. Characterization of a new Fe^{2+} environment, *J. Biol. Chem. 258*, 14981-14991.
101. Münck, E. (2000) Aspects of ^{57}Fe Mössbauer spectroscopy, in *Physical Methods in Bioinorganic Chemistry* (Que, L., Jr, Ed.), pp 287-319, University Science Books, Sausalito, CA.
102. Vetting, M. W., Wackett, L. P., Que, L., Jr., Lipscomb, J. D., and Ohlendorf, D. H. (2004) Crystallographic comparison of manganese- and iron-dependent homoprotocatechuate 2,3-dioxygenases, *J. Bacteriol. 186*, 1945-1958.
103. Whittaker, J. W., Lipscomb, J. D., Kent, T. A., and Münck, E. (1984) *Brevibacterium fuscum* protocatechuate 3,4-dioxygenase. Purification, crystallization, and characterization, *J. Biol. Chem. 259*, 4466-4475.
104. Chiesa, M., Giamello, E., Paganini, M. C., Sojka, Z., and Murphy, D. M. (2002) Continuous wave electron paramagnetic resonance investigation of the hyperfine structure of $^{17}O_2$- adsorbed on the MgO surface, *J. Chem. Phys. 116*, 4266-4274.
105. Zhou, J., Gunsior, M., Bachmann, B. O., Townsend, C. A., and Solomon, E. I. (1998) Substrate binding to the alpha-ketoglutarate-dependent non-heme iron enzyme clavaminate synthase 2: coupling mechanism of oxidative decarboxylation and hydroxylation, *J. Am. Chem. Soc. 120*, 13539-13540.
106. Wolfe, M. D., Parales, J. V., Gibson, D. T., and Lipscomb, J. D. (2001) Single turnover chemistry and regulation of O_2 activation by the oxygenase component of naphthalene 1,2-dioxygenase, *J. Biol. Chem. 276*, 1945-1953.
107. Price, J. C., Barr, E. W., Hoffart, L. M., Krebs, C., and Bollinger, J. M., Jr. (2005) Kinetic dissection of the catalytic mechanism of taurine:alpha-ketoglutarate dioxygenase (TauD) from *Escherichia coli*, *Biochemistry 44*, 8138-8147.
108. Bollinger, J. M., and Krebs, C. (2006) Stalking intermediates in oxygen activation by iron enzymes: Motivation and method, *J. Inorg. Biochem. 100*, 586-605.
109. Che, M., Tench, A. J., and Naccache, C. (1974) Electron spin resonance studies of isotopically labeled oxygen species adsorbed on supported molybdenum, *J. Chem. Soc., Faraday Trans. 1 70*, 263-272.
110. Dickinson, L. C., and Chien, J. C. W. (1980) Electron paramagnetic resonance crystallography of oxygen^{17}-enriched oxycobaltomyoglobin: Stereoelectronic structure of the cobalt dioxygen system, *Proc. Natl. Acad. Sci. U. S. A. 77*, 1235-1239.
111. Jousserandot, A., Boucher, J.-L., Henry, Y., Niklaus, B., Clement, B., and Mansuy, D. (1998) Microsomal cytochrome P450 dependent oxidation of

N-hydroxyguanidines, amidoximes, and ketoximes: Mechanism of the oxidative cleavage of their C:N(OH) bond with formation of nitrogen oxides, *Biochemistry 37*, 17179-17191.
112. Brown, C. D., Neidig, M. L., Neibergall, M. B., Lipscomb, J. D., and Solomon, E. I. (2007) VTVH-MCD and DFT studies of thiolate bonding to $\{FeNO\}^7/\{FeO_2\}^8$ complexes of isopenicillin N synthase: substrate determination of oxidase versus oxygenase activity in nonheme Fe enzymes, *J. Am. Chem. Soc. 129*, 7427-7438.
113. Pierpont, C. G., and Lange, C. W. (1994) The chemistry of transition metal complexes containing catechol and semiquinone ligands, in *Prog. Inorg. Chem.* (Karlin, K. D., Ed.), pp 331-442.
114. Pierpont, C. G., and Buchanan, R. M. (1981) Transition metal complexes of o-benzoquinone, o-semiquinone, and catecholate ligands, *Coord. Chem. Rev. 38*, 45-87.
115. Kessel, S. L., Emberson, R. M., Debrunner, P. G., and Hendrickson, D. N. (1980) Iron(III), manganese(III), and cobalt(III) complexes with single chelating o-semiquinone ligands, *Inorg. Chem. 19*, 1170-1178.
116. Hegg, E. L., and Que, L. (1997) The 2-His-1-carboxylate facial triad: An emerging structural motif in mononuclear non-heme iron(II) enzymes, *Eur. J. Biochem. 250*, 625-629.
117. Jollie, D. R., and Lipscomb, J. D. (1990) Formate dehydrogenase from *Methylosinus trichosporium* OB3b, *Methods Enzymol. 188*, 331-334.
118. Sucharitakul, J., Chaiyen, P., Entsch, B., and Ballou, D. P. (2005) The reductase of p-hydroxyphenylacetate 3-hydroxylase from *Acinetobacter baumannii* requires p-hydroxyphenylacetate for effective catalysis, *Biochemistry 44*, 10434-10442.
119. Wolgel, S. A., Dege, J. E., Perkins-Olson, P. E., Jaurez-Garcia, C. H., Crawford, R. L., Münck, E., and Lipscomb, J. D. (1993) Purification and characterization of protocatechuate 2,3-dioxygenase from *Bacillus macerans*: A new extradiol catecholic dioxygenase, *J. Bacteriol. 175*, 4414-4426.
120. Cox, D. D., Benkovic, S. J., Bloom, L. M., Bradley, F. C., Nelson, M. J., Que, L., Jr., and Wallick, D. E. (1988) Catecholate LMCT bands as probes for the active sites of nonheme iron oxygenases, *J. Am. Chem. Soc. 110*, 2026-2032.
121. Anitha, N., and Palaniandavar, M. (2011) Mononuclear iron(III) complexes of 3N ligands in organized assemblies: spectral and redox properties and attainment of regioselective extradiol dioxygenase activity, *Dalton Trans. 40*, 1888-1901.
122. Stallings, M. D., Morrison, M. M., and Sawyer, D. T. (1981) Redox chemistry of metal-catechol complexes in aprotic media. 1. Electrochemistry of substituted catechols and their oxidation products, *Inorg. Chem. 20*, 2655-2660.
123. Chedekel, M. R., Land, E. J., Thompson, A., and Truscott, T. G. (1984) Early steps in the free radical polymerization of 3,4-

dihydroxyphenylalanine (dopa) into melanin, *J. Chem. Soc., Chem. Commun.*, 1170-1172.
124. Hartl, F., Stufkens, D. J., and Vlcek, A., Jr. (1992) Nature of the manganese(I)-dioxolene bonding as a function of the ligand oxidation state: UV-visible, IR, and resonance Raman spectroelectrochemical study of [Mn(CO)3Ln(Diox)]z (n = 0, 1; z = -2, -1, 0, +1) and [Mn(CO)2{P(OEt)3}m(Diox)]z (m = 1, 2; z = -1, 0, +1) complexes, *Inorg. Chem. 31*, 1687-1695.
125. Mialane, P., Anxolabeheremallart, E., Blondin, G., Nivorojkine, A., Guilhem, J., Tchertanova, L., Cesario, M., Ravi, N., Bominaar, E., Girerd, J. J., and Münck, E. (1997) Structure and electronic properties of (N,N'-Bis(4-Methyl-6-Tert-Butyl-2-Methyl-Phenolate)-N,N'-Bismethyl-1,2-Di Aminoethane)Fe-Iii (Dbsq) - spectroelectrochemical study of the red-Ox properties - relevance to Intradiol catechol dioxygenases, *Inorg. Chim. Acta 263*, 367-378.
126. Lynch, M. W., Valentine, M., and Hendrickson, D. N. (1982) Mixed-valence semi-quinone catecholate iron complexes, *J. Am. Chem. Soc. 104*, 6982-6989.
127. Deeth, R. J., and Bugg, T. D. H. (2003) A density functional investigation of the extradiol cleavage mechanism in non-heme iron catechol dioxygenases, *J. Biol. Inorg. Chem. 8*, 409-418.
128. Girerd, J.-J., Banse, F., and Simaan, A. J. (2000) Characterization and properties of non-heme iron peroxo complexes, *Struct. Bonding 97*, 145-177.
129. Roelfes, G., Vrajmasu, V., Chen, K., Ho, R., Y. N., Rohde, J.-U., Zondervan, C., La Crois, R., M., Schudde, E., P., Lutz, M., Spek, A., L., Hage, R., Feringa, B., L., Münck, E., and Que, L., Jr. (2003) End-on and side-on peroxo derivatives of non-heme iron complexes with pentadentate ligands: models for putative intermediates in biological iron/dioxygen chemistry, *Inorg. Chem. 42*, 2639-2653.
130. Zang, Y., Kim, J., Dong, Y. H., Wilkinson, E. C., Appelman, E. H., and Que, L. (1997) Models for nonheme iron intermediates: Structural basis for tuning the spin states of Fe(TPA) complexes, *J. Am. Chem. Soc. 119*, 4197-4205.
131. Lehnert, N., Ho, R. Y. N., Que, L., Jr., and Solomon, E. I. (2001) Electronic structure of high-spin Iron(III)-alkylperoxo complexes and its relation to low-spin analogues: Reaction coordinate of O-O bond homolysis, *J. Am. Chem. Soc. 123*, 12802-12816.
132. Zang, Y., Elgren, T. E., Dong, Y., and Que, L., Jr. (1993) A high-potential ferrous complex and its conversion to an alkylperoxoiron(III) intermediate. A lipoxygenase model, *J. Am. Chem. Soc. 115*, 811-813.
133. Wada, A., Ogo, S., Watanabe, Y., Mukai, M., Kitagawa, T., Jitsukawa, K., Masuda, H., and Einaga, H. (1999) Synthesis and characterization of novel alkylperoxo mononuclear iron(III) complexes with a tripodal pyridylamine ligand: a model for peroxo intermediates in reactions catalyzed by non-heme iron enzymes, *Inorg. Chem. 38*, 3592-3593.

134. Namuswe, F., Hayashi, T., Jiang, Y., Kasper, G. D., Sarjeant, A. A. N., Moenne-Loccoz, P., and Goldberg, D. P. (2010) Influence of the nitrogen donors on nonheme iron models of superoxide reductase: High-spin FeIII-OOR complexes, *J. Am. Chem. Soc. 132*, 157-167.
135. Bukowski, M. R., Halfen, H. L., van den Berg, T. A., Halfen, J. A., and Que, L., Jr. (2005) Spin-state rationale for the peroxo-stabilizing role of the thiolate ligand in superoxide reductase, *Angew. Chem. Int. Ed. 44*, 584-587.
136. Lehnert, N., Fujisawa, K., and Solomon, E. I. (2003) Electronic structure and reactivity of high-spin iron-alkyl- and -pterinperoxo complexes, *Inorg. Chem. 42*, 469-481.
137. Skrzypczak-Jankun, E., Bross, R. A., Carroll, R. T., Dunham, W. R., and Funk, M. O. Jr. (2001) Three-dimensional structure of a purple lipoxygenase, *J Am Chem Soc 123*, 10814-10820.
138. Zhang, Y., Gan, Q.-F., Pavel, E. G., Sigal, E., and Solomon, E. I. (1995) EPR definition of the non-heme ferric active sites of mammalian 15-Lipoxygenases: major spectral differences relative to human 5-lipoxygenases and plant lipoxygenases and their ligand field Origin, *J. Am. Chem. Soc. 117*, 7422-7427.
139. Li, F. F., Meier, K. K., Cranswick, M. A., Chakrabarti, M., Van Heuvelen, K. M., Münck, E., and Que, L. (2011) Characterization of a high-spin non-heme Fe^{III}-O intermediate and its quantitative conversion to an Fe^{IV} = O complex, *J. Am. Chem. Soc. 133*, 7256-7259.
140. Wada, A., Ogo, S., Nagatomo, S., Kitagawa, T., Watanabe, Y., Jitsukawa, K., and Masuda, H. (2002) Reactivity of hydroperoxide bound to a mononuclear non-heme iron site, *Inorg. Chem. 41*, 616-618.
141. Horner, O., Jeandey, C., Oddou, J. L., Bonville, P., and Latour, J. M. (2002) A Mössbauer study of [Fe(EDTA)(O-2)](3-) agrees with a high-spin Fe-III peroxo complex, *Euro. J. Inorg. Chem*.1186-1189.
142. Simaan, A. J., Banse, F., Mialane, P., Boussac, A., Un, S., Kargar-Grisel, T., Bouchoux, G., and Girerd, J. J. (1999) Characterization of a nonheme mononuclear peroxoiron(III) intermediate by UV Vis and EPR spectroscopy and mass spectrometry, *European Journal of Inorganic Chemistry*, 993-996.
143. Simaan, A. J., Banse, F., Girerd, J. J., Wieghardt, K., and Bill, E. (2001) The electronic structure of non-heme iron(III)-hydroperoxo and iron(III)-peroxo model complexes studied by Mössbauer and electron paramagnetic resonance spectroscopies, *Inorg Chem 40*, 6538-6540.
144. Jensen, K. B., McKenzie, C. J., Nielsen, L. P., Pedersen, J. Z., and Svendsen, H. M. (1999) Deprotonation of low-spin mononuclear iron(III)-hydroperoxide complexes give transient blue species assigned to high-spin iron(III)-peroxide complexes, *Chem. Commun.*, 1313-1314.
145. Horner, O., Jeandey, C., Oddou, J. L., Bonville, P., McKenzie, C. J., and Latour, J. M. (2002) Hydrogenperoxo-[(bztpen)Fe(OOH)](2+) and its deprotonation product peroxo-[(bztpen)Fe(O-2)](+), studied by EPR and

Mössbauer spectroscopy - Implications for the electronic structures of peroxo model complexes, *Euro. J. Inorg. Chem*. 3278-3283.
146. Hazell, A., McKenzie, C. J., Nielsen, L. P., Schindler, S., and Weitzer, M. (2002) Mononuclear non-heme iron(III) peroxide complexes: syntheses, characterisation, mass spectrometric and kinetic studies, *Journal of the Chemical Society-Dalton Transactions*, 310-317.
147. Burstyn, J. N., Roe, J. A., Miksztal, A. R., Shaevitz, B. A., Lang, G., and Valentine, J. S. (1988) Magnetic and spectroscopic characterization of an iron porphyrin peroxide complex. Peroxoferrioctaethylporphyrin(1-), *J. Am. Chem. Soc. 110*, 1382-1388.
148. Bukowski, M. R., Comba, P., Limberg, C., Merz, M., Que, L., Jr., and Wistuba, T. (2004) Bispidine ligand effects on iron/hydrogen peroxide chemistry, *Angew. Chem. Int. Ed. 43*, 1283-1287.
149. Horner, O., Mouesca, J. M., Oddou, J. L., Jeandey, C., Niviere, V., Mattioli, T. A., Mathe, C., Fontecave, M., Maldivi, P., Bonville, P., Halfen, J. A., and Latour, J. M. (2004) Mössbauer characterization of an unusual high-spin side-on peroxo-Fe^{3+} species in the active site of superoxide reductase from *Desulfoarculus baarsii*. Density functional calculations on related models, *Biochemistry 43*, 8815-8825.
150. Brausam, A., Maigut, J., Meier, R., Szilagyi, P. A., Buschmann, H. J., Massa, W., Homonnay, Z., and van Eldik, R. (2009) Detailed spectroscopic, thermodynamic, and kinetic studies on the protolytic equilibria of Fe(III)CYDTA and the activation of hydrogen peroxide, *Inorg. Chem. 48*, 7864-7884.
151. Homonnay, Z., Szilagyi, P. A., Vertes, A., Kuzmann, E., Sharma, V. K., Molnar, G., Bousseksou, A., Greneche, J. M., Brausam, A., Meier, R., and Eldik, R. (2008) Iron chelates: a challenge to chemists and Mossbauer spectroscopists, *Hyperfine Interact. 182*, 77-86.
152. Stallings, M. D., Morrison, M. M., and Sawyer, D. T. (1981) Redox chemistry of metal-catechol complexes in aprotic media .1. Electrochemistry of substituted catechols and their oxidation-products, *Inorg. Chem. 20*, 2655-2660.
153. Steenken, S., and Neta, P. (1982) One-electron redox potentials of phenols. Hydroxy- and aminophenols and related compounds of biological interest, *J. Phys. Chem. 86*, 3661-3667.
154. Duckworth, H. W., and Coleman, J. E. (1970) Physicochemical and kinetic properties of mushroom tyrosinase, *J Biol Chem 245*, 1613-1625.
155. Mason, H. S. (1948) The chemistry of melanin; mechanism of the oxidation of dihydroxyphenylalanine by tyrosinase, *J Biol Chem 172*, 83-99.
156. Ellis, S. (1943) Physostigmine and related substances. IV. Chemical studies on physostigmine breakdown products and related adrenaline derivatives, *J. Pharmacol. 79*, 364-372.
157. Mason, H. S., and Peterson, E. W. (1965) Melanoproteins. I. Reactions between enzyme-generated quinones and amino acids, *Biochim. Biophys. Acta, Gen. Subj. 111*, 134-146.

158. Kalyanaraman, B., Felix, C. C., and Sealy, R. C. (1985) Semiquinone anion radicals of catechol(amine)s, catechol estrogens, and their metal ion complexes, *EHP, Environ. Health Perspect. 64*, 185-198.
159. Neibergall, M. B., Stubna, A., Mekmouche, Y., Münck, E., and Lipscomb, J. D. (2007) Hydrogen peroxide dependent cis-dihydroxylation of benzoate by fully oxidized benzoate 1,2-dioxygenase, *Biochemistry 46*, 8004-8016.
160. Fielding, A. J., Kovaleva, E. G., Farquhar, E. R., Lipscomb, J. D., and Que, L., Jr. (2011) A hyperactive cobalt-substituted extradiol-cleaving catechol dioxygenase, *J. Bio. Inorg. Chem.16*, 341-355.
161. Frazee, R. W., Orville, A. M., Dolbeare, K. B., Yu, H., Ohlendorf, D. H., and Lipscomb, J. D. (1998) The axial tyrosinate Fe^{3+} ligand in protocatechuate 3,4-dioxygenase influences substrate binding and product release: evidence for new reaction cycle intermediates, *Biochemistry 37*, 2131-2144.
162. Valley, M. P., Brown, C. K., Burk, D. L., Vetting, M. W., Ohlendorf, D. H., and Lipscomb, J. D. (2005) Roles of the equatorial tyrosyl iron ligand of protocatechuate 3,4-dioxygenase in catalysis, *Biochemistry 44*, 11024-11039.